Electrochemistry of Single Entities and Ensembles of Metal-based Nanoparticles

Ruo-Chen Xie

Supervisor: Prof. Dr. Richard G. Compton

St John's College

A thesis submitted for the degree of Doctor of Philosophy in Physical and Theoretical Chemistry

Hilary Term 2021

Abstract

This thesis aims at both *electrochemically* investigating mainly *at the single entity level* the physicochemical properties of metal-based nanoparticles and seeking to study unusual *electrochemical activity* of metal nanoparticle ensembles by using mainly an optical approach. Three experimental stages are presented accordingly:

(1) Electrochemical detection and sizing of single metallic nanoparticles with a critical focus on the study of the quantitative methodology;

(2) Further investigations of the surfaces (composition, structure and catalytic activity) of metal-based core-shell nanoparticles both at the particle ensemble and single particle level;

(3) Opto-electrochemical investigation of a substrate-mediated electrochemical dissolution of metal nanoparticle ensembles.

To begin with, the first chapter briefly reviews the key basics of fundamental electrochemistry, and the second chapter introduces the metal-based nanoparticles, the major electrochemical technique of 'nano-impacts' and the alternative technique of dark field microscopy used in this thesis.

Chapter 3 reports a generic quantitative methodology for electrochemically detecting and sizing individual nanoparticles using the complete oxidation of silver nanoparticles in halide solutions as a model system. In particular, this established methodology of nano-impacts emphasises the use of lower filtering frequencies in the data acquisition (prior to any analysis) for the accurate description of the charge passed during a transient nano-event. For the critical comparison between electrochemical and electron microscopic measurements, the effect of the nanoparticle diffusion coefficient on the probability of it being observed in the electrochemical responses and the effects of

non-spherical shapes of nanoparticles visible in the microscopic images are also discussed. On this basis, Chapter 4 further shows the advantages of applying the nano-impact technique for sizing small (d < 30 nm), multimodal-sized nanoparticles that are inherently beyond the measuring capacity of the conventional light scattering methods of dynamic light scattering and nanoparticle tracking analysis.

Chapter 5 next demonstrates the electrochemical characterisation of the surface compositions of $Co@Co(OH)_2$ nanoparticles at the single particle level. By contrast, the very thin surface layer of $Co(OH)_2$ is not characterised by either X-ray diffraction or transmission electron microscopy. Moreover, the aggregation of the nanoparticles in aqueous solutions is implied *via* the impact electrochemistry. Chapter 6 focuses on the mechanistic study of the mediated hydroxide ion oxidation by Co_3O_4 nanoparticles in alkaline conditions. Hydrogen peroxide, rather than dioxygen, is found to be the predominant initial oxidation product of the electron transfer. The nano-impact results further point out the rate determining step and the limiting kinetics of the catalytic reaction. Furthermore, as the work next compares the electrochemical behaviour of bare Co_3O_4 with that of core-shell $Co_3O_4@SiO_2$ nanoparticles, the surface silica of the synthesised core-shell particles is inferred to be highly porous or broken. This is not otherwise easily distinguished, for example, by electron microscopy.

Chapter 7 reports a substrate-mediated electrochemical dissolution into aqueous solution of silver nanoparticles driven *via* electron transfer to trace dissolved oxygen. Investigation of a range of solid materials (glass, indium titanium oxide, glassy carbon and platinum) used to support the nanoparticles shows that conductive supports greatly catalyse the dissolution and by means of complementary and synergistic optical and electrochemical measurements it is inferred that the electron transfer can occur at locations on the support surface remote from the silver nanoparticles.

Acknowledgements

In this great university, my D.Phil., which is the very first few years of research in my life, gained me an even more important leap in the understanding of the world and life than that simply in research skills. Through studying science as a research worker and communicating with smart people around, I unravelled the university motto '*Lord is my light*'. I value this epiphany so I appreciate people who helped me along this 'tasteful' journey. Greatest gratitude to my supervisor Professor Richard Compton – I thank him for recognising my potential in the first place, and leading my way to approach true science so supportively and carefully. Deep gratitude to Dr. Christopher Batchelor-McAuley for helping me tremendously during my PhD with patient guidance especially in my first year. Also importantly, these two smart and dedicated figures impressed and inspired me on how a most professional researcher in the world does science. Dr. Bertold Rasche with his outstanding academic capacities and personal charm inspired me greatly on the general scientific thinking and habits. Dr. Xiuting Li impressed me much on her single-minded research lifestyle and acts also as a nice senior buddy who helped me a lot at the beginning of my PhD. Dr. Miriam Chung who is a retired Oxford staff in experimental psychology, though not participating in my research, inspired me a lot on why we should follow and explore the truth. As such, I have developed a great appreciation and a determined pursue of truth, for which I acknowledge the interactions with these very important people. Only with all these above is it possibly reasonable for myself to be awarded Doctor of Philosophy in Physical and Theoretical Chemistry, literally.

In terms of life, I understand 'Happiness only real when shared' a lot better (cited from a biography 'Into the Wild' which Bertold recommended). This mainly comes from my friendship with mature Jake, thoughtful Haonan, happy Danlei, and fun Ruiyang, with whom I shared quite a few of my feelings and thoughts. I won't forget to sincerely thank St John's college and all the kind and humorous personnel for providing such an ideal accommodation

and living conditions. I also thank the lucky chance encounter in Paris-Charles de Gaulle Airport with Mr. Luo who then became a close, inspiring friend of mine despite the difference in age. I therefore become fully aware of the indispensable role of simple, random joy in life besides profession.

Last but not least, my immense gratitude goes to my mother Mrs. Cao and my father Mr. Xie for their selfless support in terms of both mind and finance. I appreciate the precious love from and the great perseverance of my girlfriend Ms. Yuanyi Fan over the past couple of years, overcoming together any difficulty from the 8000 km-long distance relationship. If myself is compared to a chemical, my understanding of the world and life is compared to a reaction thermodynamics and my research abilities are compared to the reaction kinetics, then only with you, the stable chemical environment, is it possible for myself to react with the targets to generate wonderful products!

Dr. Ruo-Chen Xie

2021-04-16

Contents

Chapter 1

Fundamentals of electrochemistry

This chapter presents an overview of some key fundamental concepts involved in general electrochemistry, including electrochemical thermodynamics, the electrode double layer, electrode kinetics, electrochemical cells, and mass transport, as well as describing some basic electrochemical techniques, mainly chronoamperometry and cyclic voltammetry. This short chapter aims to aid the understanding of the subsequent chapters.

1.1. Electrochemical Thermodynamics

Fundamental electrochemistry focuses on electron transfers between an electrode and usually an electro-active molecular species, unlike general redox chemistry where electrons transfer between a pair of molecular species. It is straightforward in the context of general redox chemistry that electrons transfer from one molecule to another owing to the difference in their tendencies for electron exchange: one wants to gain electrons (become reduced) and the other to lose electrons (and become oxidised) such that consequently both may form new and more stable molecular species. The tendencies for the electron exchange of molecules are described by their specific *chemical potentials* (which will be explained below). However, the tendency for an electrochemical electron transfer of an electroactive species is quantified by *electrode potential* due to the introduction of the electrode phase. Therefore,

understanding electrochemical reduction and oxidation first requires an appreciation of the origin of electrode potentials.

Consider a simple one-electron-transfer electrochemical equilibrium established at a single electrode-solution interface,

$$O^z\ (aq) + e^-\ (m) \rightleftharpoons R^{z-1}\ (aq) \qquad (1.1)$$

where O (aq) and R (aq) are the oxidised and reduced species of a redox couple in aqueous solution with which this thesis exclusively deals, and *z* represents their charge number; e^- (m) is an electron present in the electrode phase (often a metal, m). The position to which the equilibrium lies relative to the initial thermodynamic state of the reaction system is indicative of the sign of the charge born by the electrode phase. If the equilibrium lies to the left in favour of the species O and e^- (m), the electrode bears a negative charge (as relatively electron 'rich') while the solution phase a positive charge. If the equilibrium lies to the right, the electrode bears a positive charge (as relatively electron 'deficient') while the solution a negative charge. Hence, in either case there exists a charge separation at the electrode-solution interface (which is discussed in more detail in Section 1.2). This charge separation brings about a difference in electrical potential between the two phases, where the electrical potential at a point is formally defined as the work required to bring a unit test charge (of one Coulomb) from infinity to the point. In other words, a resultant *interfacial potential difference* is established [1]. However, in practical electrochemistry where the quantity is made readily measurable and thus meaningful, another electrode needs to be introduced to the system to establish a potential difference of another electrode-

solution interface which serves as a reference level; relative to the latter, the interfacial potential difference is defined as 'electrode potential'. That said, the charge separation arising from the heterogeneous chemical process results in the electrode potential established across the interface.

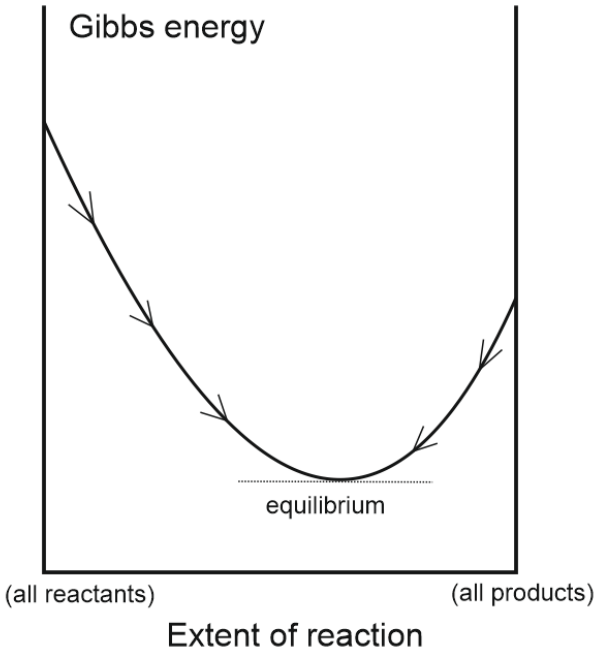

Figure 1.1. Gibbs energy of a system as a function of the extent of reaction. Arrows on the curve represents the direction of thermodynamically favoured reaction. The lowest point of the curve has the derivative of zero, denoted as the 'equilibrium' state.

The understanding above of the establishment of electrode potentials can be precisely described in thermodynamic terms. Nevertheless, before doing that directly, a brief review on thermodynamics in general is necessary. Thermodynamics states that any spontaneous chemical reaction tends to move towards a state of lower energy and finally reaches a dynamic equilibrium where there is no further tendency to undergo a net change. The tendency allows one to predict the direction of the reaction between

'reactants' and 'products'. Therein, the chemical change essentially reflects the transfer of chemical energy. The Gibbs energy is commonly used in *laboratory chemistry* (which is usually carried out under constant pressure) to describe the maximum available energy for a specified chemical change [2]. As such, the criterion for reaction spontaneity ($dG_{T,\,P} \leq 0$) predicts the reaction direction, at constant pressure and temperature, as decreasing the Gibbs energy of the overall system (See Figure 1.1) until it becomes the lowest and mathematically,

$$dG_{sys} \leq 0 \tag{1.2}$$

where dG_{sys} is the (infinitesimal) change of Gibbs energy of a whole system over an infinitesimal change in the extent of reaction and the case of $dG_{sys} = 0$ corresponds to equilibrium. More specifically [2],

$$dG_{sys} = \Sigma \nu\, dG_f(\text{products}) + \Sigma \nu\, dG_f(\text{reactants}) \tag{1.3}$$

where G_f is Gibbs energy of formation (of reactant or product species), ν is the generalised stoichiometric coefficient for a given reaction, and expressed by

$$dG_{f,i} = (\mu_i\, dn_i)_{\,T,\,p,\,n'} \tag{1.4}$$

where μ_i is the chemical potential of a given chemical species (J mol^{-1}) and is specific to the species, n is the mole of the species (mol), T is the absolute temperature (K), p is the pressure (Psi) and n' is the total number of moles of all the other species present in the system (mol). That said, Gibbs energy change depends on the change in the amount of the chemical species. It follows that the energy change of the system at a certain extent of reaction depends on the variation of the composition of this

system. As such, one can then look at electrochemical systems to solve the Equation 1.2 so as to move on to the electrochemical thermodynamics.

For electrochemical systems, the introduction of the electrode phase that conducts 'free' electrons leads to involvement of electrical energy in addition to chemical energy. Consequently, the (molar) Gibbs energy of an electrochemical system is described in terms of electrochemical potential that further includes electrical terms. For a given species *i* the electrochemical potential (J mol^{-1}) is defined as [3]

$$\overline{\mu_i} = \mu_i + z_i F \phi \tag{1.5}$$

where F is the Faraday constant (96485 C mol^{-1}), ϕ is the electric potential (V) of a particular phase (solution or electrode, denoted as ϕ_s and ϕ_m respectively).

Based on Equations 1.2-1.5, the Gibbs energy change of the system described in the equation 1.1 for the forward reaction is [3]

$$dG_{sys} = (\overline{\mu_R} + \overline{\mu_O} + \overline{\mu_e})\ dn = [\ \overline{\mu_R} - (\overline{\mu_O} + \overline{\mu_e})\ ]\ d\xi \tag{1.6}$$

$$\Delta_r G = \mu_R + (z\text{-}1) F \phi_s - (\mu_O + z F \phi_s + \mu_e - F \phi_m) \tag{1.7}$$

$$= \mu_R - \mu_O - \mu_e + F \phi_m - F \phi_s \tag{1.8}$$

$$= (\mu_R^{\ominus} + RT \ln \frac{a_R}{a_R^{\ominus}}) - (\mu_O^{\ominus} + RT \ln \frac{a_O}{a_O^{\ominus}}) - \mu_e + F(\phi_m - \phi_s) \tag{1.9}$$

Rearrangement gives

$$\Delta_r G = F(\phi_m - \phi_s) + d\mu^{\ominus} + RT \ln (\frac{a_R}{a_O}) \tag{1.10}$$

where $d\mu^\circ = \mu_R^\circ - \mu_O^\circ + \mu_e$ and is the standard chemical potential change of the reduction, a_O and a_R are activity of O and R present in solutions respectively, and the term $\phi_m - \phi_s$ is the interfacial potential difference (V) mentioned earlier.

At equilibrium, $\Delta_r G = 0$, then

$$\phi_m - \phi_s = -\frac{d\mu^\circ}{F} - \frac{RT}{F} \ln\left(\frac{a_R}{a_O}\right) \tag{1.11}$$

This is the Nernst equation [4] associated with the system of a single electrode-solution interface. As such, one is able to *theoretically* locate the position of equilibrium of the electrochemical process. However, μ_e is not measurable and the absolute value of $\phi_m - \phi_s$ is often very difficult to be experimentally measured. Therefore, a reference electrode system, with an experimentally pre-determined $\Delta\phi$ (exclusively standard hydrogen electrode as formally recommended by IUPAC[5]), assumed as

$$O' + e^- \rightleftharpoons R' \tag{1.12}$$

is required for giving a *ready* measure of the electrode potential in a *relative* sense, which can be written as

$$E = (\phi_m - \phi_s)_{study} - (\phi_m - \phi_s)_{ref} \tag{1.13}$$

Similarly for the reference electrode system,

$$(\phi_m - \phi_s)_{ref} = -\frac{d\mu'^\circ}{F} - \frac{RT}{F} \ln\left(\frac{a_{R'}}{a_{O'}}\right) \tag{1.14}$$

One essential requirement is that the reference electrode potential has to be stable – the activity of all the composition is constant, independent of the extent of the reaction under study, such that

$$(\phi_m - \phi_s)_{ref} = -\frac{d\mu'^\circ}{F} - c \tag{1.15}$$

where $c = \frac{RT}{F} \ln(\frac{a_{R\prime}}{a_{O\prime}})$. Then, based on the equations 1.11-1.15,

$$E = E^{\ominus} - \frac{RT}{F} \ln(\frac{a_R}{a_O}) + c \quad (1.16)$$

where $E^{\ominus} = -\frac{d\mu^{\circ} - d\mu\prime^{\circ}}{F}$ and is the electrode potential under standard conditions (i.e. 25 ºC, 1 atm and 1 mol L^{-1} of concentration for all soluble species); the term c reflects that practically the activity of solutes used in a reference electrode affects the electrode potential. In this form the Nernst equation becomes a lot more useful as the equation can be used to directly link the electrode potential under experimental conditions to the ones under standard conditions. A list of standard electrode potentials can be found in Ref [6], where the reference electrode is by internationally agreed convention of the standard hydrogen electrode with c being zero.

It should be noted for the equations above that as 'concentration' is generally used in laboratory chemistry, the difference between activity (or 'effective concentration') and concentration should be accounted here for applying the equations above. For a given chemical species, activity is defined as [3, 7]

$$a = \gamma \frac{[i]}{[i]^{\circ}} \quad (1.17)$$

where γ is activity coefficient, $[i]$ is concentration (mol L^{-1}) and $[i]^{\circ}$ is the standard concentration (usually taken as 1 mol L^{-1}), respectively, of a given species i. Accordingly, the formal potential $E_f{}^{\circ}$ (V) is used for practical calculations regarding electrode potentials and is defined as [3]

$$E_f{}^{\circ} = E^{\circ} - \frac{RT}{F} ln(\frac{\gamma_R}{\gamma_O}) \quad (1.18)$$

Such that one can have

$$E = E_f^{\ o} - \frac{RT}{F} \ln\left(\frac{[R]}{[O]}\right) \tag{1.19}$$

Away from equilibrium, one may thermodynamically predict the occurrence of electrochemical reduction or oxidation based on the criterion $dG_{sys} < 0$. Herein, the G_{sys} refers to the Gibbs energy for a complete cell consisting of the two electrode-solution interfaces (the one under study and the other for reference), and

$$\Delta_r G = - F E \tag{1.20}$$

It follows that,

if $E > 0$, $\Delta_r G < 0$, the forward reaction of electrochemical reduction of species O tends to occur;

if $E < 0$, $\Delta_r G > 0$, the backward reaction of electrochemical oxidation of R tends to occur.

In this sense, the establishment of electrode potential dictates in which direction a decrease of the overall Gibbs energy should be expected, which thus explains the reason of an electrochemical electron transfer.

1.2. Electrode double layer

It is learnt from last section that fundamental electrochemistry is thermodynamically approached with the essential understanding of the concepts from electrode potentials, the potential-determining electrochemical equilibrium, to the origin of electron transfer, all occurring at the electrode-solution interface. One may then expect to get a picture

of the electrochemical interface before further examining the chemical processes there. In turn this section would also help further understand the essence of electrode potentials mentioned earlier – the charge separation at the electrode-solution interface.

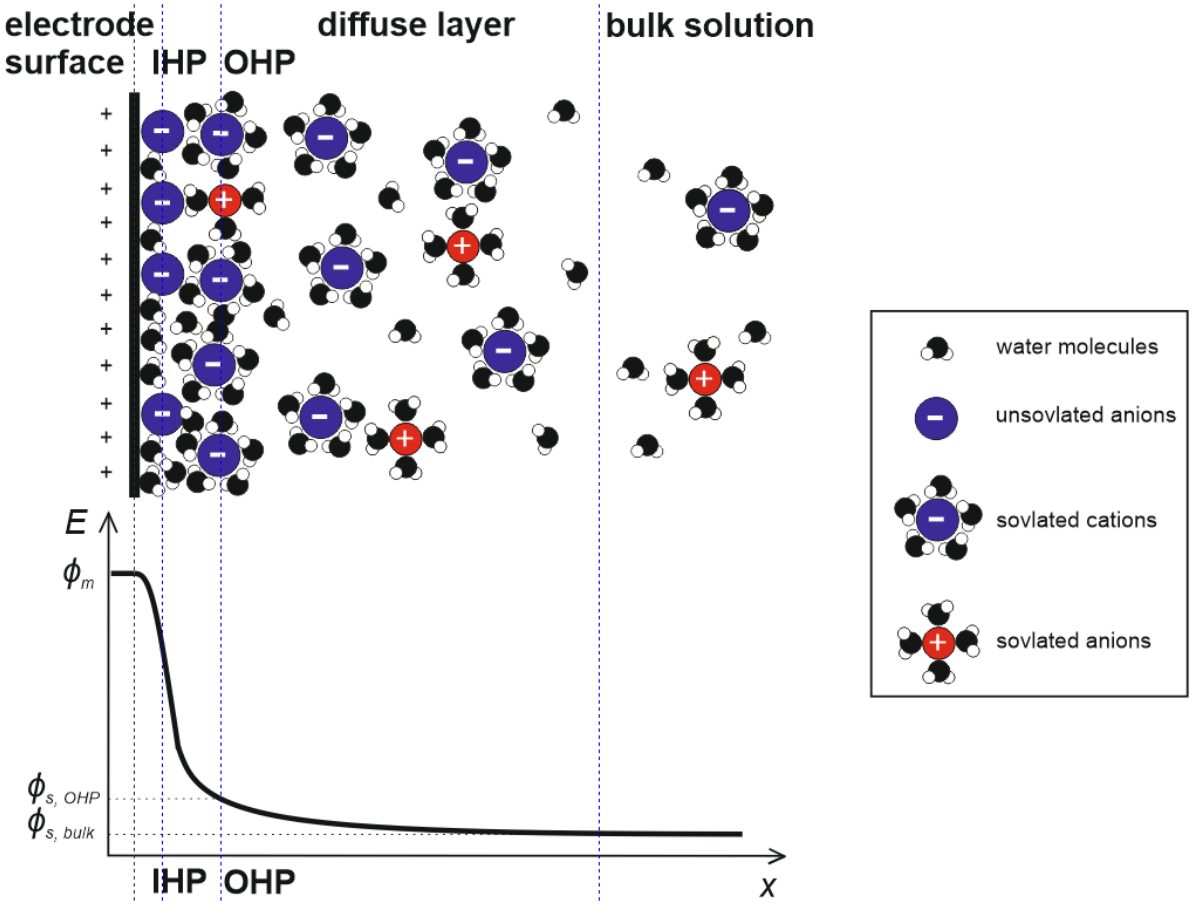

Figure 1.2. Schematic representation of electrode double layer in aqueous solutions and the corresponding electrical potential (E) as a function of distance (x) away from the electrode surface.

The interfacial site of electrochemical reaction is described by several dividing planes (parallel to the electrode surface, assumed flat) according to the widely accepted Stern model of electrode double layer [2, 8-9]. For an electrode at equilibrium with the solution, its surface may be electron deficient for example, presenting positive charges as shown in Figure 1.2. Note that the charge is confined to a very thin layer of < 0.1 Å.

To maintain a local neutral environment, the solution side of the electrode surface is occupied by solvent molecules of water and the ionic species of opposite charge to the electrode (anions herein) with no or partial solvation. These ions are considered specifically adsorbed on the electrode surface. The layer comprising these ions is called *inner Helmholtz plane* (IHP), or *Stern layer*. Adjacent to this plane are more counter ions in the *Outer Helmholtz plane* (OHP), usually the same as the ones in IHP but which are solvated. Due to the electrostatic repulsion from the specifically adsorbed ions and thermal agitation in solutions, these ions are less restricted spatially, allowing larger extent of solvation, and therefore are considered 'non-specifically adsorbed'. The locus of the electrical centres is a few Å, or a total length of a few ions, away from the electrode surface. Typically the electron transfer occurs around this location *via* quantum mechanical tunnelling within a distance of some 10-20 Å from the electrode. The weak electrostatic interaction between the electrode and the solution phase ions operates over a distance away from the electrode surface and this larger region is called the *diffuse layer*. For an electrolyte concentration of over 0.01 M, the diffuse layer is less than 100 Å thick [8]. Thus, in summary, the 'double layer' can be understood that the electrode-solution interface consists of one layer of specifically adsorbed species (i.e. IHP) and the other of non-specifically adsorbed ones (i.e. OHP and diffuse layer) and the charge in these layers balances that on the electrodes surface. Further away is the bulk solution where solvated ions and water molecules are considered spatially evenly distributed, exhibiting a net neutral charge everywhere macroscopically.

As a result of the fine structure of the double layer, the electrical potential varies in different ways in each region, as shown in the potential plot as a function of distance in Figure 1.2. Around the IHP, the electrical potential drops dramatically, due to the dominant presence of charges of opposite sign (to the electrode). Further through the OHP and the diffuse layer, the potential drop continues yet in an increasingly weaker way due to an increasingly lower density of the counterions. Ultimately beyond the diffuse layer, the electrical potential of the solution reaches a steady value as the electrostatic interaction from the electrode surface completely fades away over the 'long' distance so that the ions in the bulk solution are completely screened from the electrode charge by the double layer.

Thermodynamically, the double layer structure can affect an electrode reaction. Consider an electrochemical reaction of a non-specifically adsorbed solution phase species whose electron transfer can only happen at/around the OHP through tunnelling. It follows that the applied potential supposed ($\phi_m - \phi_{s,\,bulk}$) is actually $\phi_m - \phi_{s,\,OHP}$ with a value of smaller magnitude, as shown in Figure 1.3. For a solution of dilute electrolytes, the diffuse layer often extends over such a distance that the electrical potential $\phi_{s,\,OHP}$ deviates markedly from $\phi_{s,\,bulk}$. The discrepancy is therefore non-negligible and this may consequently affect the rate of electron transfer [8] since the driving force for the reaction is correspondingly reduced. This is also one of the major reasons why in many cases, a least concentration of inert supporting electrolyte (typically 0.1 M) is deliberately added into the solution to assure a high charge density, at and around the electrode surface, compressing the double layer to a thickness of

less than the tunnelling distance of 10-20 Å, such that the electron transfer of the species experiences a full potential drop applied [3].

An essential property of the electrode double layer as an interface is its capacitance. As with the interfaces of a common capacitor comprising a pair of conducting plates with a non-conducting medium in between (e.g. air), an electrode double layer does not allow electron transfer (in absence of Faradaic active species). The concept of double layer capacitance C_d (usually in μF cm^{-2}) is therefore raised and similarly defined as [8]

$$C_d = \frac{Q}{E \times A} \tag{1.21}$$

where Q is the charge accumulated on the either side of the interface (C), E is the electrode potential (V), and A is the electrode area (cm^2).

Unlike the common capacitors in physics whose capacitance is independent of electrical potential, the double layer capacitance is often a function of the electrode potential applied.

Current arises from double layer capacitance, regardless of the presence of Faradaic processes. Upon the polarisation of the electrode, charge is excessively accumulated on the electrode surface, while on the side of solution, ions of counter charge move towards the interface, resulting in a capacitive current. This electrode process is called *double layer charging*, which often happens very fast and typically over a timescale of milliseconds or microseconds depending on the electrode dimensions. Even so, the

induced capacitive current as opposite to the Faradaic currents in which experimentalist are actually interested, may sometimes dominate and can cause analytical difficulty in some cases where, for example, ultralow concentrations of analyte are used.

1.3. Electrode kinetics

Having understood why and where an electrochemical reaction occurs from the last two sections, one may next expect to see how the electron transfer processes are quantified and rationalised.

It has been pointed out that the process of electrochemical reactions is in essence the energy conversion between chemical energy and electrical energy. The general quantification of electrolysis, or the process of electrical energy being converted to chemical energy, was summarised by the great scientist Michael Faraday in 1833, who also proposed the terminology 'electrode' [10]

> '*The chemical power of a current of electricity is in direct proportion to the absolute quantity of electricity which passes.*'

The chemical power of a current of electricity here refers to the mass of the electro-generated species resulting from electrolysis, and the law is accordingly expressed as

$$m = \frac{M}{Fz}Q \tag{1.22}$$

where m, M and z are the mass (g), molar mass (g mol^{-1}) and electrical charge number, respectively, of the substance produced at the electrode surface, Q is the total electrical charge passing through the electrode surface (C), F is the *Faraday* constant (96485 C mol^{-1}).

For any electric current measured in the electrolysis, the total charge Q is precisely the integral of the current over time

$$Q = \int_0^t I(t)dt \tag{1.23}$$

Also often as applied in fundamental electrochemistry is the reverse process: the mass of reacted species at the electrode surface is proportional to the electrical charge produced.

Another significant discovery from early studies of electrochemistry is the Tafel equation, which relates electric current to electrode potential in the fashion [11]

$$\eta = a_0 + b_0 \log I \tag{1.24}$$

where η is the overpotential (E - $E_f{}^o$); a_0 and b_0 are constants. The logarithmic dependence implies the great sensitivity of current to electrode potential, although this simple model of electrode kinetics in fact only applies to the cases whose reaction rate is limited by that of the interfacial electron transfer. A more complete view of electrode processes will be discussed later in Section 1.4 by including the transport of materials from bulk solution to the electrode surface (i.e. mass transfer, see Section

1.5). The justification of the Tafel relation between current and electrode potential is underpinned by several key theories that are discussed next.

First, of essential importance is the dynamic nature of electrochemical equilibrium. As mentioned in Section 1.1, the state of equilibrium does not mean that no molecules react. Instead, the rate of the forward and backward reaction equals each other. Consider again the following processes

$$O^z\ (aq) + e^-\ (m) \underset{k_a}{\overset{k_c}{\rightleftharpoons}} R^{z-1}\ (aq) \tag{1.25}$$

where k_c and k_a are the rate constants (cm s^{-1} for the first order heterogeneous reaction), respectively, for the forward (reduction of O) and the reverse process (oxidation of R). According to the rate law

$$J = k_c[O] - k_a[R] \tag{1.26}$$

where J is the net reaction flux of the overall process (mol cm^{-2} s^{-1}). The corresponding amount of materials reacted at a uniformly accessible electrode is

$$n = J A t \tag{1.27}$$

and from Faraday's law of electrolysis (Equation 1.22, $z = 1$),

$$Q = n F \tag{1.28}$$

Combining equations 1.26-1.28 gives the expected current

$$I = F A (k_c[O] - k_a[R]) \tag{1.29}$$

which should be zero at equilibrium, and therefore

$$\frac{k_c}{k_a} = \frac{[R]}{[O]} \tag{1.30}$$

consistent with the definition of an equilibrium constant:

$$\mathrm{K} = \frac{[R]}{[O]} \tag{1.31}$$

so that

$$\mathrm{K} = \frac{k_c}{k_a} \tag{1.32}$$

As such, the rate law of electrode kinetics collapses at equilibrium to the thermodynamic form, in turn confirming the concept of dynamic equilibrium.

Second, building on the generic framework above of electrochemical kinetics, it is next important to further explore what determines the rate 'constant'. Empirical evidence shows a logarithmic dependence of the rate 'constant' on the reciprocal of temperature, $\ln k \propto -\frac{1}{T}$, as discovered by Arrhenius [12]. The rate constant for electrode reactions can be expressed in an Arrhenius form

$$k = A_f \cdot e^{-\frac{\Delta G^{\ddagger}}{RT}} \tag{1.33}$$

where $\Delta G^{\ddagger}$ is the *standard Gibbs energy of activation*[1] (J mol^{-1}), while the whole exponential factor may reflect the probability of molecules passing over an activation barrier, and A_f can be accordingly considered a frequency factor (has units of k) of the molecules attempting to climb over the energy barrier; R is the gas constant (8.3145 J K^{-1} mol^{-1}) and T is the temperature (K).

[1] Herein *standard* thermodynamic properties are used, because the Gibbs Energy (as opposed to the Standard Gibbs Energy) of a species is concentration dependent whereas the rate constant does not depend on the concentrations in dilute systems. Hence, the discussion, including the following of the section, is developed in terms of the standard state of a solution. To simplify the notations, the conventional superscript 'o' is omitted.

Third, the concept of activation energy can be explained with the picture of reaction paths following the Gibbs energy curves in a reaction coordinate and the assumption of existence of a well-defined transition state, as illustrated in Figure 1.3. The reaction coordinate often refers to a particular structural parameter of a reactive species, for example, a bond length or angle [13]. Accordingly, the potential energy curve at each point of coordinate corresponds to the potential energy of the molecules at that particular molecular configuration. Most reactant and product molecules are considered to stay at the minima of the energy distribution curves.

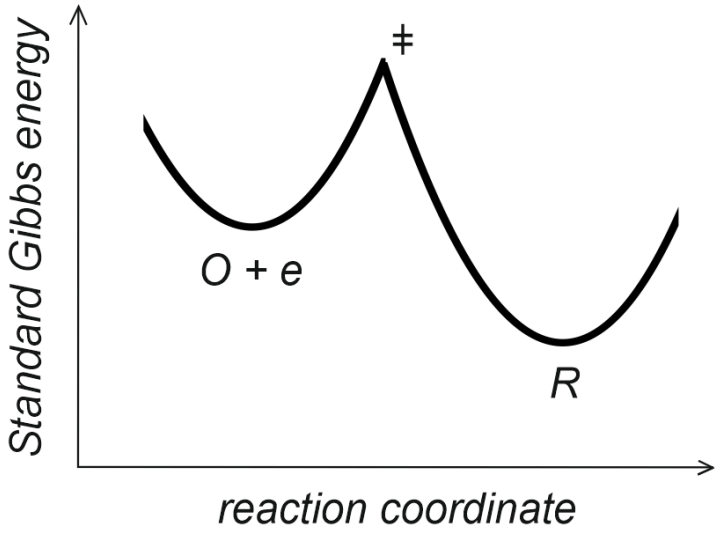

Figure 1.3. Gibbs energy curve as a function of reaction coordinate for the reaction O + e = R, where the symbol ‡ stands for the transition state. Note that O and R are solution phase species; the electron, e, is located in the metal. In the solution phase, the energy is discussed in terms of Gibbs energy as both enthalpy and entropy change of the reaction are considered.

With thermal motion in the solution at the molecular scale, however, some molecules may temporarily gain energy to have a distorted and less stable configuration. When

the energy of reactant molecules reaches the cross-over point of the two curves, which is the assumed transition state that has a transitional molecular configuration in between the reactant and product species, the molecules may surmount the energy barrier to the zone of products. As such, the energy required for this process, or the difference between the energy maxima and one of the minima, is called the *activation energy* or more precisely for an electrode reaction, the Gibbs energy of activation.

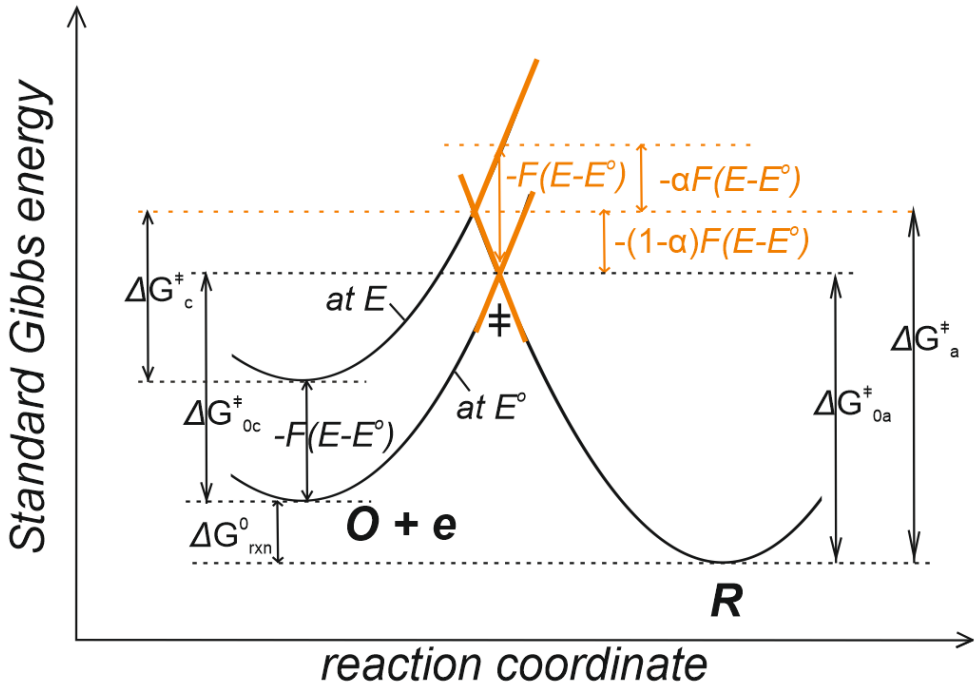

Figure 1.4. Effects of a negative polarisation on the standard Gibbs energy change of activation (‡) for the cathodic and the anodic processes [8]. ΔG^0_{rxn} is the standard Gibbs energy change for the reaction O + e = R at E_0. The thick orange lines denote a linear approximation of the energy curves near the transition state.

Last, the relationship between $\Delta G^{\ddagger}$ and electrode potential E, and the term of pre-exponential factor A_f are explained with the most successful and widely accepted

Butler-Volmer model of electrode kinetics. In developing this theory, suppose the standard Gibbs energy profiles along the reaction coordinate for the reaction O + e ⇌ R have the parabolic shapes as shown in Figure 1.4, and the standard potential of the system is used as a reference point for the following discussion. Accordingly, suppose the lower curve of O + e applies when the electrode potential is E^o. If the electrode is then polarised to a more negative potential E, one knows from Section 1.1

$$G(R) = z F \phi_s - F \phi_m + \mu_e + \mu_O \tag{1.34}$$

(where G(R) refers to the standard Gibbs energy of the reactants, while μ_e and μ_O are two constants under the standard conditions) that the Gibbs energy of the reactants is expected to increase as the ϕ_m containing the electrons becomes more negative. Consequently, the Gibbs energy parabola of reactant O + e is raised by a difference of $-F(E - E^o)$.

A key consequence of this polarisation is the shift in the coordinate of the transition state. To simplify the change of the position of transition state, the energy curves around the cross-over points are approximated to straight lines, as shown with the orange lines in Figure 1.4. $\Delta G_{0c}^{\ddagger}$ and $\Delta G_{0a}^{\ddagger}$ are the standard activation energies (energy differences between the transition state and the reactants or products) at the electrode potential of E_0 for the cathodic and anodic processes respectively; $\Delta G_c^{\ddagger}$ and $\Delta G_a^{\ddagger}$ are those at the applied reducing potential E. Consequently, the change in standard Gibbs energy of activation for the reduction or oxidation turns out to be not the same as $-F\Delta E$ but rather a fraction of it

$$\Delta G_c^{\ddagger} = \Delta G_{0c}^{\ddagger} - \alpha F(E - E^o) \tag{1.35}$$

$$\Delta G_a^{\ddagger} = \Delta G_{0a}^{\ddagger} + (1 - \alpha) F(E - E^o) \tag{1.36}$$

where α denotes the fraction of the change ($0 < \alpha < 1$) and is formally called the *transfer coefficient*, which represents a measure of symmetry of the energy barrier (will be discussed soon later regarding the *Tafel plot*). For the reverse process (reduction), the transfer coefficient is the complementary fraction $1 - \alpha$ and conventionally replaced by β, with, for a one electron process

$$\alpha + \beta = 1 \tag{1.37}$$

Furthermore, substituting Equations 1.35-1.37 into the Arrhenius form of rate constants k_c and k_a

$$k_c = A_c \cdot e^{-\frac{\Delta G_{0c}^{\ddagger} - \alpha F(E - E^O)}{RT}} \tag{1.38}$$

$$k_a = A_a \cdot e^{-\frac{\Delta G_{0a}^{\ddagger} + \beta F(E - E^O)}{RT}} \tag{1.39}$$

Next, consider the special case where the system is right at equilibrium with $C_O = C_R$ at the electrode-solution interface, this leads to $k_c = k_a$. That said, the cathodic and anodic processes have the rate constants of the same value, which is formally defined as the *standard electrochemical rate constant* k_0. Since at equilibrium both $\Delta G_{0c}^{\ddagger} = \Delta G_{0a}^{\ddagger}$ and $E = E^o$ apply, one can obtain $A_c = A_a$. Therefore, it follows that

$$k_0 = A_c \cdot e^{-\frac{\Delta G_{0c}^{\ddagger}}{RT}} = A_a \cdot e^{-\frac{\Delta G_{0a}^{\ddagger}}{RT}} \tag{1.40}$$

Since the rate constant for an elementary process is fixed for a given temperature and pressure and does not depend on the concentrations of O and R, this equation

is a general expression. As it holds at equilibrium, it also holds away from equilibrium. Combining Equations 1.38–1.40 with Equation 1.29 gives the final form of the Bulter-Volmer equation

$$I = F A (k_0 e^{\frac{-\alpha F(E-E^O)}{RT}} [O] - k_0 e^{\frac{+\beta F(E-E^O)}{RT}} [R]) \quad (1.41)$$

which relates the Faradaic current directly to the electrode potential, and also to the surface concentration of the chemical species.

So far, one is able to justify the Tafel equation described at the beginning of this section using the derived Butler-Volmer equation [3]. Consider the simple electrode reduction of O to R with a small k_0, when the rate of the overall reaction is dominated by the interfacial kinetics (rather than the mass transport), the applied electrode potential E is more negative than the standard formal potential E_f^o, namely $E < E_f^o$, leading to

$$-\left(E - E_f^o\right) > E - E_f^o \quad (1.42)$$

and this results in the further inequality

$$e^{-(E-E_f^O)} \gg e^{(E-E_f^O)} \quad (1.43)$$

For this reduction, given that $\alpha \sim \beta$ often holds, the second term in Equation 1.41 can be omitted as

$$I_{red} \sim F A k_0 e^{\frac{-\alpha F(E-E_f^O)}{RT}} [O] \quad (1.44)$$

Taking the natural logarithm of both sides, followed by rearrangement, gives

$$\eta = -\frac{RT}{\alpha F}\ln|I_{red}| + C \tag{1.45}$$

where

$$C = \frac{RT}{\alpha F}\ln(F\ A\ k_0\ [\mathrm{O}]) \tag{1.46}$$

As such, the linear relation between electrode potential and logarithm of current is derived. However, it is clear that Equation 1.45 above holds within accuracy only when [O] stays almost constant. This prerequisite limits the application of Tafel equation to the electrode reactions when mass transfer effects are not important [3].

Often use of the Tafel equation is to evaluate the transfer coefficients as fundamental kinetic parameters. The equation for the reduction process O^z (aq) + e^- (m) ⇀ R^{z-1} (aq) can be rewritten as

$$\ln|I_{red}| = \frac{-\alpha F}{RT}E + C' \tag{1.47}$$

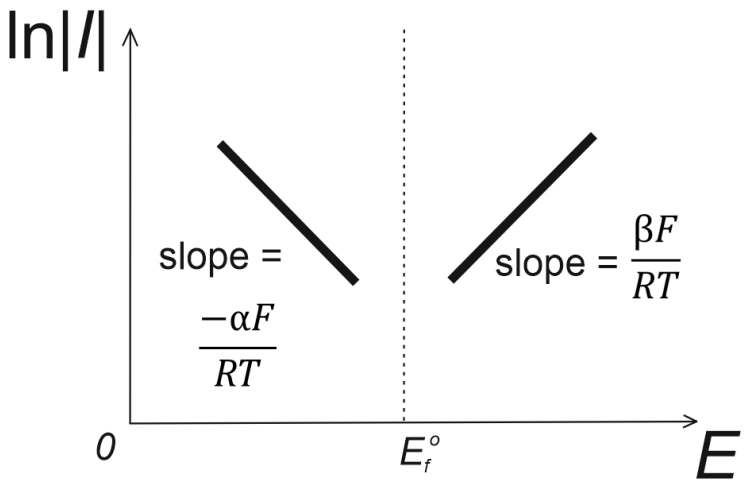

Figure 1.5. Tafel plots for reduction and oxidation at the corresponding overpotential regions. Note that the current is the absolute value of the Faradaic current of the reduction or oxidation.

Similarly, for the complementary oxidation process R^{z-1} (aq) ⇀ O^{z} (aq) + e^{-} (m)

$$\ln|I_{ox}| = \frac{\beta F}{RT} E + C'' \qquad (1.48)$$

The corresponding *Tafel plots* can be seen in Figure 1.5. From the slope of these plots, one can estimate the values of the transfer coefficients. Theoretically, when $\alpha = \frac{1}{2}$, the energy barrier is considered to be symmetric. This implies a similar difference in terms of the reaction coordinate from the transition state to the reactant and to the product species, and therefore the structure of transition state resembles neither of them. When $\alpha < \frac{1}{2}$, the transition state is, for a reduction reaction, product-like, while $\alpha > \frac{1}{2}$ implies a reactant-like transition state, which means kinetically the reactants surmount the energy barrier in a relatively facile way. In other words, transfer coefficients are the indicators of the relative position of the transition state along the reaction path which imply the ease of electron transfer. As such, Tafel plots may provide mechanistic implications.

The Butler-Volmer model of electrode kinetics explains based on macroscopic concepts the dependence of the heterogeneous rate constant, k_c and k_a, on the reaction Gibbs energy with the introduction of the phenomenological parameters of standard rate constants k_0 and transfer coefficients α (or β). However, those parameters offer little *physical* insight at the molecular level into the reaction mechanisms with extremely different values of k_0 that can even span over ten orders of magnitude [14]. Therefore, one may seek for a microscopic theory to rationalise this difference. Marcus-Hush theory, another widely accepted model of electrode

kinetics, comes to the aid as it elaborates how the molecular geometry of reaction species and the surrounding solvent environment affect the rate constants [15-16].

Consider the process of O being reduced to R, as discussed above. According to the Franck-Condon principle, the timescale of molecular nuclear motion (*ca.* 10^{-13} s) is far slower than that of electron transfer (*ca.* 10^{-15} s) [3]. The molecules involved in the reaction, including both the reaction species O and R and the solvation molecules, are therefore considered to be 'frozen' at the moment of electron transfer. This constraint requires that prior to the electrode transfer the reactant species has to be activated to a highly excited state to match the same molecular geometry as that of the transition state, which is afterwards deactivated to the ground state of product molecules. This can be achieved *via* thermal interaction with other molecules in the solution. Also, the solvent molecules need to be rearranged to a favourable state for the moment of electron transfer *via* thermal activation.

On the other hand, since the chemical electron transfer is radiationless, no energy gain or loss is thought to happen then. Consequently, the simultaneous operation of both constraints imply that the rate of rearrangements of relevant molecules for the right match in terms of the geometry and local chemical environment dictates the rate of electron transfer. It may thus give rise to a simple rule that if the molecular geometry and the solvation of species O both resemble those of R, a fast electrode reaction will occur [17]. One example is the reduction MnO_4^- (aq) + e^- ⇌ MnO_4^{2-} (aq), which shows rapid electrode kinetics (k_0 ~ 0.2 cm s^{-1}) since both anions are

tetrahedral in shape and the Mn-O bond lengths are very similar - MnO_4^- (1.63 Å) and MnO_4^{2-} (1.66 Å). Moreover, their charges are highly delocalised, leading to little changes in solvation from the reduction. The converse is also true: a major difference in the bond length of Fe-O between $Fe(H_2O)_6^{3+}$ (2.05 Å) and $Fe(H_2O)_6^{2+}$ (2.21 Å) leads to relatively sluggish kinetics with k_0 of 7×10^{-3} cm s^{-1} at 25 °C for the reaction $Fe(H_2O)_6^{3+}$ (aq) + e^- ⇌ $Fe(H_2O)_6^{2+}$ (aq).

1.4. Electrochemical cells and electrode processes

From the last three sections, one may have obtained an adequate theoretical understanding of the central step of electrode processes, the interfacial electron transfer, which allows the prediction of current-potential behaviour. To measure the latter in practice, electrochemical experiments of fundamental studies are typically carried out with a three-electrode potentiostat. A highly simplified sketch of the equipment is presented in Figure 1.6. The electrode where the reactions of interest occur at its interface with solution is called the *working electrode* (WE). To impose a potential upon this electrode, a *reference electrode* (RE) is needed, as discussed in Section 1.1. The potential of this electrode is required to be constant and stable, or at least predictable, throughout the experiments. Between WE and RE is a voltmeter (or its modern equivalent) that can record the potential difference applied across the two electrode-solution interfaces.

A third electrode called the *counter electrode* (CE), or *auxiliary electrode*, is connected also to the WE. The auxiliary nature of CE requires itself to ideally be

chemically inert, and to have a large surface area and good conductance to avoid additional resistance to the electrode reactions. An amperometer is loaded in this part of the circuit to record the current flowing through the WE, as a result of the fact that the significantly lower impedance of the amperometer than that of the voltameter directs the electrons to flow almost only between the WE and the CE. Consequently, given that the main function of potentiostat is to precisely control the electric potential applied on the WE, the inclusion of CE leads to two advantages.

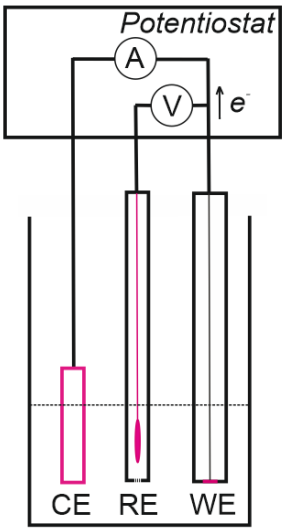

Figure 1.6. Schematic presentation of a three-electrode potentiostat. Below the dashed line is the solution phase.

First, the resultant negligible current flowing through the RE assures a stable reference potential and second, the unwanted ohmic drop ΔE_s across the solution phase, which is intrinsic to this type of measurement, is kept to a minimum level:

$$E_{appl} = (\phi_m - \phi_s)_{WE} + \Delta E_s - (\phi_m - \phi_s)_{RE} \quad (1.49)$$

with

$$\Delta E_s = I_{WR} \times R_{s,WR} \quad (1.50)$$

where I_{WR} and $R_{s,WR}$ are the current flowing (A) and the resistance of the part of solution (Ω), respectively, between the WE and RE. It is often true that I_{WR} « 10 μA and $R_{s,\,WR}$ < 100 Ω, so the ohmic drop is far less than 1 mV [8]. Alternatively, if the working electrode is a microelectrode (i.e. electrodes with at least one dimensions at a scale of micrometres), the current level is often in the order of nA, so that the reference electrode is easily assured stable and a solution resistance of even MΩ might still be accepted. In this situation, a two-electrode system of WE and RE may operate with desired accuracy.

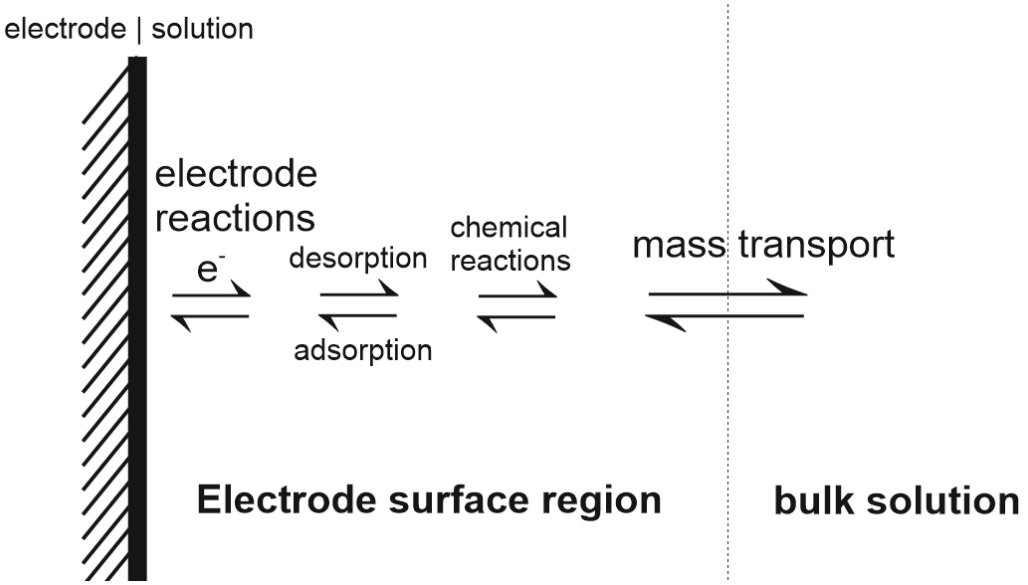

Figure 1.7. Possible common electrode processes of an electrochemical reaction. Not to scale.

In many conditions, the actual measurements yield a dependence of current on electrode potential that is not simply logarithmic as predicted from the Butler-Volmer theory. This can arise from other processes related to the electrochemical reactions. It is therefore necessary to have an overview of electrode processes before

proceeding to subsequent sections. Different from Section 1.2 of introducing the electrode double layer where no reaction is driven at the electrode-solution interface, the scenario here (see Figure 1.7) for the electrode processes is with the start of an electrochemical reaction.

Overall, the electro-active species are depleted at or near the electrode surface over time, and subsequently the materials are supplied by mass transport from the bulk solution to the electrode surface (which will be discussed in detail in the next section). However, if looking closer at the electrode surface region, one may find that the electrode reactions are accompanied by many other *non-Faradaic* (i.e. no electron transfer with the electrode) types of interactions. At the electrode, there might be surface adsorption or desorption (e.g. the adsorption of silver nanoparticles onto a carbon electrode[18]), while in the solution phase homogeneous reactions may couple (e.g. electro-generated silver ions react with halide ions to form silver halide solids[19]), before or after the interfacial electron transfer. The rate constants for some of these 'additional' processes may be potential dependent and therefore, also depending on which process is the *rate determining step*, alter the magnitude and shape of the measured current-potential curves.

1.5. Mass transport

It has been seen above that the interfacial kinetics of electrode processes largely depends on the potentials applied and even an initial sluggish electrode reaction (with a small k_0) can become extremely fast if subjected to a vast overpotential. On the

other hand, what is measured using an electrochemical cell actually results from a competition of different electrode processes involved. There, whichever step is the slowest dictates the overall rate of electrode reactions. As discussed in Section 1.4, *mass transport* of solution phase species almost always participates in the overall process and one major means of mass transport, *diffusion*, tends to be a rather slow process. The diffusion of the materials between the bulk solution and the electrode surface necessarily follows the consumption of reactive species at/near the electrode surface. Therefore, it is important to look into this fundamental phenomenon.

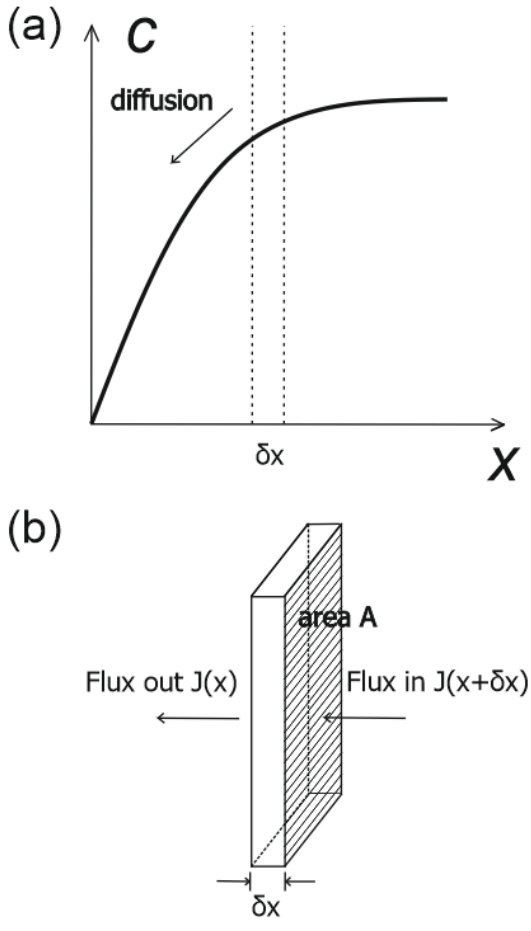

Figure 1.8 (a) Diffusion along an arbitrary concentration gradient established across a spatial dimension. (b) Diffusional fluxes in and out a 'slab' of solution.

Diffusion of a species always occurs from a point of a high concentration to a lower one. The concentration difference is the sole driving force. Fick's 1st law of diffusions[20] defines the diffusional flux J of a species along a linear dimension in a solution (see Figure 1.8a) as

$$J(x) = -D\frac{\partial c}{\partial x} \tag{1.51}$$

where D ($cm^2\ s^{-1}$) is the diffusion coefficient of a species, c (mol L^{-1}) is its concentration at a point x (cm). Note that the minus sign denotes the direction down the concentration gradient. Diffusion coefficients of a molecule often fall in the range of $10^{-5} \sim 10^{-6}$ $cm^2\ s^{-1}$ and physically reflect how far a molecule diffuses per unit time as

$$D = \frac{(\partial x)^2}{2\partial t} \tag{1.52}$$

Or for the one dimensional displacement x driven solely by diffusion

$$x = \sqrt{2Dt} \tag{1.53}$$

For example, a molecule with a diffusion coefficient of 10^{-5} $cm^2\ s^{-1}$ is therefore estimated to move merely 50 μm in one second. This is an extremely short distance as compared to the dimension of a macroelectrode (~1 mm). Importantly, diffusion coefficients are highly sensitive to temperature, and similar to rate constants, often display an Arrhenius type of dependence of $\ln D \propto -\frac{1}{T}$. The strong temperature sensitivity dictates careful thermostating to ensure reproducible experiments.

Fick's 2nd law[20] gives the consequence of diffusion – the concentration variation with time for a given position. Consider the fluxes to $J(x+\delta x)$ and away $J(x)$ from a

cuboidal 'slab' of solution with dimensions of a width δx and a lateral area A (see Figure 1.8b). The net flux through the slab

$$J(\delta \mathrm{x}) = J(x) - J(x + \delta \mathrm{x}) \tag{1.54}$$

Mathematically, using a Taylor expansion

$$J(x + \delta \mathrm{x}) \sim J(x) + \delta \mathrm{x} \frac{\partial J(x)}{\partial x} \tag{1.55}$$

So

$$J(\delta \mathrm{x}) = -\delta \mathrm{x} \frac{\partial J(x)}{\partial x} \tag{1.56}$$

Then in light of Fick's 1st law

$$J(\delta \mathrm{x}) = \delta \mathrm{x}\, D \frac{\partial^2 c}{\partial x^2} \tag{1.57}$$

On the other hand (n is the number of moles of the diffusing species),

$$J(\delta \mathrm{x}) = \frac{\delta n}{A\, \delta t} \sim \frac{\partial n}{A\, \partial t} = \frac{\partial n}{A \times \delta \mathrm{x}} \times \frac{\delta \mathrm{x}}{\partial t} = \delta \mathrm{x} \frac{\partial c}{\partial t} \tag{1.58}$$

Equating gives

$$\frac{\partial \mathrm{c}}{\partial t} = D\, \frac{\partial^2 c}{\partial x^2} \tag{1.59}$$

which is the final equation of Fick's 2nd law in one dimension that correlates the concentration change over time to the curvature of concentration change over space, and to the diffusion coefficient.

Based on the Fick's laws of diffusion, the current-time response may be predicted for a diffusion-controlled process. A classic example is given by Cottrell for the case of

potential step chronoamperometry imposed on a planar macroelectrode where the potential is stepped from a value at which no current flows to one at which the transport is fully controlled by diffusion. The features of this scenario are the boundary conditions

$$t = 0, \text{ all } x, c = c^*$$

$$t > 0, x = 0, c = 0$$

$$t > 0, x \to \infty, c = c^*$$

resulting in the Cottrell equation[21]

$$I = \frac{nFA\sqrt{D}c^*}{\sqrt{\pi t}} \tag{1.60}$$

which shows that the current has an inverse square root decay with time. Microscopically, the decrease of the current is because the diffusion layer where a concentration gradient exists across the x axis keeps expanding over time, and therefore the diffusional flux is slowed down. However, in reality, the diffusion layer will not infinitely expand – it tends to have a finite thickness after a certain period of time. This leads to the concept of a Nernst diffusion layer (see Figure 1.9), on which another type of mass transport, *natural convection*, (which will be discussed in detail later) has significant effects. Specifically, electrode reactions very likely result in a product species of a different density, and this will induce a conventional mixing of all the molecules present in the solution. Also, regional temperature variations throughout the solution contributes to the mixing of the molecules of interest. That said, as a result, at some point of $x = \delta$, the concentration difference becomes so small and easy

to eliminate by the convectional mixing that a bulk concentration will always be sustained.

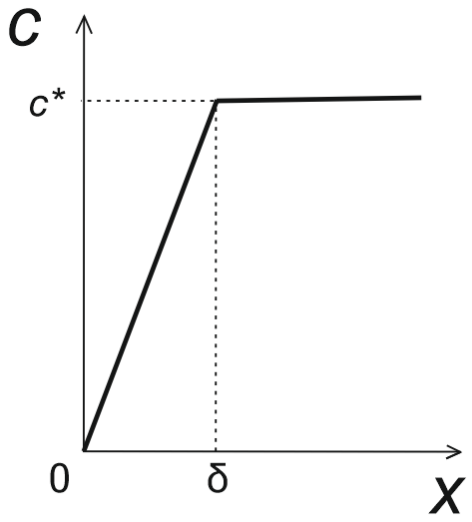

Figure 1.9. Nernst model of the diffusion layer, although in practice the transition from the diffusion region to the bulk region is gradual, similar to Figure 1.8a.

When the diffusion layer expansion stops, a steady-state diffusion in the layer may operate, which means

$$\frac{\partial c}{\partial t} = 0 \tag{1.61}$$

So according to Fick's 2nd law,

$$\frac{\partial^2 c}{\partial x^2} = 0 \tag{1.62}$$

Assuming that

$$c(x = 0) = 0 \tag{1.63}$$

$$c(x = \delta) = c^* \tag{1.64}$$

Combining equations 1.62 ~ 1.64, for $0 < x < \delta$,

$$c(x) = \frac{c^*}{\delta} x \tag{1.65}$$

Then according to Fick's 1st law, the absolute steady-state diffusional flux is

$$J(x) = D\frac{\partial c}{\partial x} = D\frac{c^*}{\delta} \tag{1.66}$$

Since this has the same form of the rate law for electrode kinetics, an analogous (diffusional) mass transport coefficient m_T can be defined as

$$m_T = \frac{D}{\delta} \tag{1.67}$$

which has the same units (cm s^{-1}) of and therefore can be directly compared with the electrochemical rate constant, *k*. This parameter is of great use in the development of voltammetry theories and will be further involved in the discussion in the next section.

Apart from diffusion, there are other forms of mass transport in solution: *convection* and *migration*. Specifically, *convection* is usually categorised into two different types: *natural* and *forced*. Natural convection is intrinsic to the process of electrolysis, and as mentioned, often arises from a density difference between the electro-generated species and the existing ones, or from temperature variations that may result from the heat transfer as a result of the electrode processes or from non-ideal thermostating. Natural convection at macroelectrodes usually starts to operate after tens of seconds following the outset of the diffusion layer evolution. By contrast, *forced convection* requires artificial control of fluid motion. For example,

electrochemical experiments using rotating disc electrodes utilise the forced convection induced by the electrode rotation to create a controlled mass transport rate depending on the rotation speed. In this thesis, stationary electrodes and well thermostatted static solutions are used to exclude the consideration of this type of mass transport.

The other type of mass transport, *migration*, or more precisely *electro-migration*, almost inevitably occurs in the context of an electrode reaction. It refers to the migration of charged species in an electric field that is always present at/near the electrode surface except at the point of zero charge where the electrode surface exhibit electrical neutrality. The movement of the charged species may be towards or away from the electrode surface depending on the sign of the charge of the species. The *Debye length* κ^{-1} (Å) is used to estimate how far the induced electric field of a charged electrode can persist[22]

$$\kappa^{-1} = \frac{1}{\sqrt{8\pi\lambda_B N_A \times 10^3 I_{ion}}} \tag{1.68}$$

where λ_B is the Bjerrum length of the medium (Å) (is 7 Å for water at room temperature), and I_{ion} is the ionic strength of the electrolyte (mol L^{-1}). Supporting electrolyte is used to 'screen' the effect of electrostatic interaction between the electrode and the species of interest. Theoretically, when the supporting electrolyte in the solution increases from 1 mM to 0.1 M, the Debye length is reduced from 100 Å to 10 Å. This eliminates migration except very close to the electrode and is a major reason for adding an excess amount of supporting electrolyte (> 0.1 M). In addition,

as discussed in Section 1.2 the supporting electrolyte confines the electron transfer within the quantum tunnelling distance.

1.6. Basics of some classic electrochemical techniques

Following the description of the fundamental theories of electrode processes and basic instrumentation, this section introduces two classic electrochemical methods: *chronoamperometry* and *cyclic voltammetry*. For both methods, the potential (of the working electrode) is controlled in a pre-determined manner as a function of time using a potentiostat, and the resulting current is recorded as a function of time or potential. As only the stationary electrodes are used in this thesis, diffusion is assumed as the sole way of mass transport in solution in introducing the ideas of those methods. Moreover, the presence of a constant bulk concentration is assumed. With well-established correlations between the experimental parameters and kinetic parameters, these potential-controlled methods are considered as the most powerful approaches available to fundamental electrochemistry.[8]

1.6.1. Chronoamperometry

The simplest way of varying an electrode potential is to apply a single potential step. Chronoamperometry is such a potential step method as shown in Figure 1.10a, in which the potential of the working electrode is polarised from a potential E_1 where typically no reaction is driven, *abruptly* to another E_2 where the solution phase reaction is driven so hard that the rate of electron transfer is limited by that of the diffusional mass transport. The resulting current density is then recorded as a

function of time. Apart from the Faradaic process, the current response for the potential step also necessarily comprises the capacitive current due to the electrode double layer charging as described in Section 1.2 and depicted in the Figure 1.10b (red curve), whilst this current component operates for typically only the first tens of milliseconds following the step.[3]

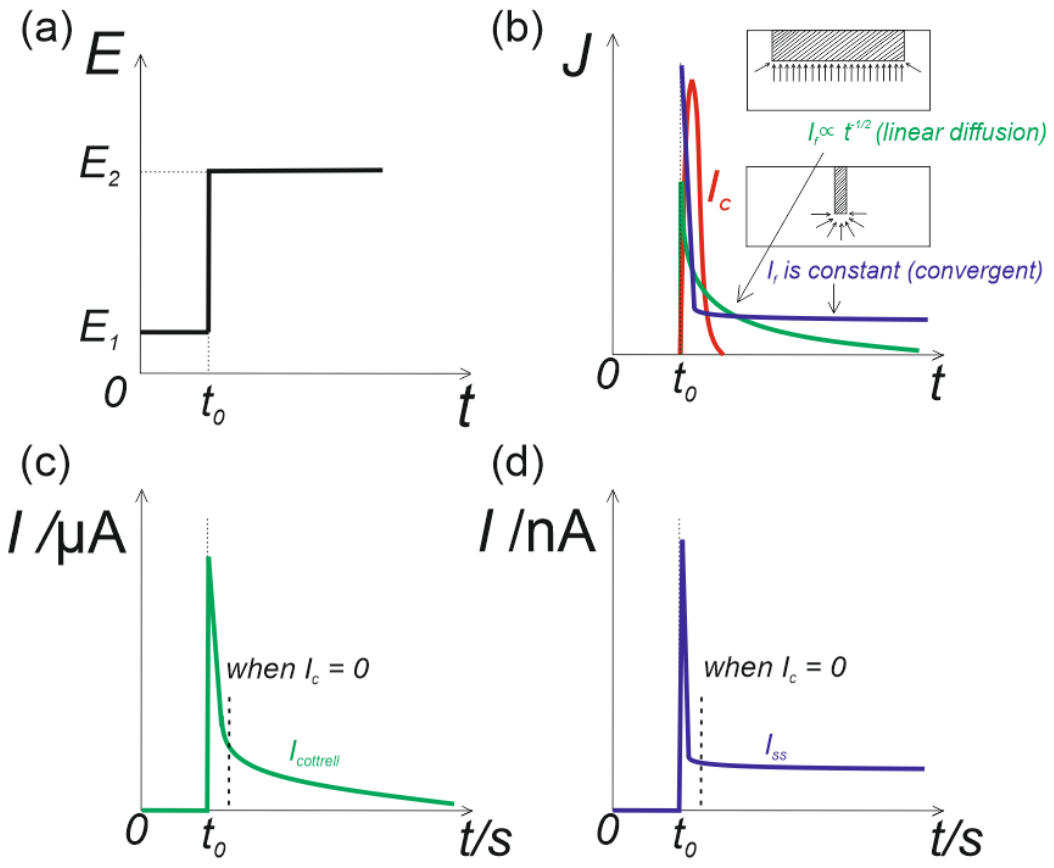

Figure 1.10. (a) Potential step in the chronoamperometric experiments. (b) Potential step polarisation leading to the Faradaic (green for the macrodisc electrode limit and blue for the microdisc electrode limit) and capacitive (red) current density. The inlay illustrate the diffusion regimes for the two cases typically after the capacitive processes finish. (c) and (d) Resulting overall current on macro- and micro-disc electrodes respectively.

Due to the selection of E_2, the Faradaic current is determined by the diffusional flux of the electroactive species from the bulk solution towards the electrode surface. Consider the case of a disc electrode (only this electrode geometry is used in this thesis), the temporal transport-limited current is fully described by the equation[3]

$$I = 4nFc^*Dr_e f(\tau) \tag{1.69}$$

where r_e is the electrode radius (m) and the dimensionless time,

$$\tau = \frac{4Dt}{r_e^2} \tag{1.70}$$

which can be understood as the ratio of the lengthscale ($\sim\sqrt{\pi Dt}$) of the diffusion layer developed over time to the electrode dimension (radius). Calculations have been made to show that

$$f(\tau \ll 1) \rightarrow (\frac{\pi}{4\tau})^{1/2} \tag{1.71}$$

$$f(\tau \gg 1) \rightarrow 1 \tag{1.72}$$

On this basis, two limiting cases of macro and micro-(disc) electrode are considered. For a macroelectrode with large electrode radii (green curve in Figure 1.10b), $\tau \ll 1$ always holds (assuming $D \sim 10^{-5}$ cm^2 s^{-1}), and this means the diffusion layer is thin as compared to the electrode size, so that linear diffusion operates. Correspondingly, the Faradaic current is calculated to be exactly Cottrellian ($I \propto \frac{1}{\sqrt{t}}$) as described in Euqation 1.58. More precisely, the Cottrellian behaviour will gradually cease and turn to a steady state after *ca.* 20 seconds when the natural convection starts to have an effect.

For a microelectrode with a rather small radius (blue curve in figure 1.10b), the Faradaic current is still Cottrellian for the first tens of milliseconds, but overlaps with the capacitive current. Soon over time, $\tau \gg 1$ becomes true, corresponding to the expansion of the diffusion layer over the length scale of the electrode. At this point, the edge of the disc becomes significant and induces predominantly convergent diffusion, leading to

$$I = 4nFc^{*}Dr_{e} \tag{1.73}$$

which is a constant current regardless of time, namely a steady-state current (I_{ss}) and notably, scales with the electrode dimension. The overall chronoamperometric currents expected on macro and microdisc electrodes as a function of time are depicted in Figures 1.10c and d respectively.

The current-time responses are able to offer direct insights into the reaction mechanisms or the electrode systems. For example, in the case of a macrodisc electrode, the slope of the plot of current as a function of the inverse square root of time may allow extraction of the number of electron transferred or the diffusion coefficient of the species, if the other parameters are known. Similarly, the steady-state current in the case of a microdisc electrode is correspondingly insightful.

1.6.2. Cyclic voltammetry

The inherent simplicity limits the applications of potential step chronoamperometry; another method of *cyclic voltammetry* has been established with its improved

complexity of the way of controlling the electrode potential to offer significantly more insights into electrode systems, e.g. regarding the electro-generated species and electroactive intermediates.[23]

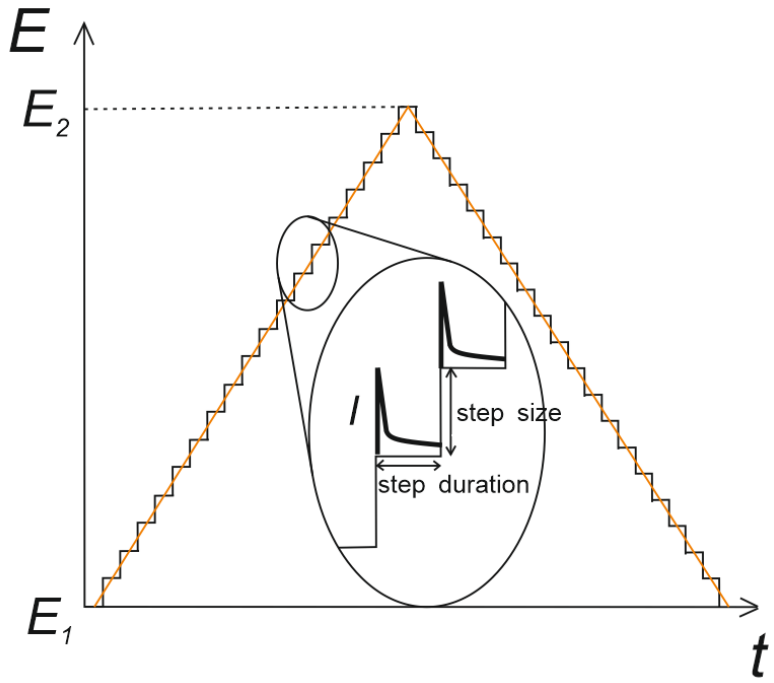

Figure 1.11. Potential sweep of staircase cyclic voltammetry: the black 'staircases' denote the real potential ramp whereas the orange lines present the approximated linear potential sweeps. The inlay shows the consequent current response of each potential steps.

Specifically, this method applies a potential sweep typically as depicted in Figure 1.11. The sweep starts from a value E_1 where no reaction of the solution phase species of study is driven, and then varied with a constant scan rate v (equal to the quotient of the step size and the step duration) in a way resembling a 'staircase', to another E_2 sufficiently oxidising or reducing to cause a diffusion-limited Faradaic current of interest. The forward potential ramp of the staircase voltammetry has the relationship $(E_1 \leq E \leq E_2)$

$$E = E_1 + vt \tag{1.74}$$

The potential step size should ideally be infinitely small to produce 'linear' potential ramps; nevertheless, in practice it is controlled as small and is often less than 1 mV. Finally, the potential is swept back to the initial potential E_1 with the same scan rate.

Within each step duration, diffusional Faradaic process of interest and electrode double layer charging both contribute to the overall current measured as with the case of the single potential step experiment discussed above. Studies suggest a sampling point at 30% along each step duration to be consistent with theoretical predictions based on linear ramps.[24] As such, the resulting current is measured once for each step and plotted as a function of potential, yielding a cyclic voltammogram.

The shape of a cyclic voltammogram reflects the kinetics of the rate determining step of the overall electrode processes. Consider the simplest electrode system of one electron transfer oxidation of solution phase species R to O with a (planar) disc electrode, and initially only species R is present in the solution. The electrode kinetics and diffusional mass transport are identified as the two principal, competing processes. Whichever is slower dictates the measured current-potential curve. The two processes vary differently with the potential sweep. In the forward potential sweep, it is clear that from Section 1.3 the rate of oxidative electron transfer increases near exponentially with the increasingly oxidising potential. The variation of diffusional flux with potential (or time in effect) is, however, not simple and primarily depends on the electrode size in a way similar to the discussion above

regarding chronoamperometry. For a disc electrode, the steady-state behaviour occurs after a timescale t_{ss} of $\sim\frac{r_e^2}{D}$, whereas the timescale t_{CV} for voltammetric experiments is approximately $\frac{RT}{Fv}$. A parameter p can be accordingly used to discriminate whether the diffusion would appear steady-state or not in the experimental timescale

$$p = \sqrt{\frac{t_{ss}}{t_{CV}}} = \sqrt{\frac{Fr_e^2 v}{RTD}} \tag{1.75}$$

where $p \gg 1$ corresponds to the case where the experimental timescale is much shorter than that required to reach a steady-state diffusional flux, which is therefore not observed. This is true for the macroelectrode limit. A value of $p \ll 1$ suggests a diffusion transition to convergent mode can be observed, which holds for the microelectrode limit. Correspondingly, the following discussions on the characteristics of cyclic voltammograms are divided to the two limiting cases of macro and micro-(disc) electrodes.

1.6.2.1. Voltammetry at macroelectrodes

On the timescale of macroelectrode voltammetry, the diffusion regime is constantly linear. Therefore, after the current rises with the increasing potentials and at some overpotential the species R at the electrode surface is near depleted (i.e. [R] = ¼ [R]* in the reversible limit), the current starts to decrease in an approximately Cottrellian way ($I \propto \frac{1}{\sqrt{t}}$). As such, a peak of current is seen as shown in Figure 1.12 below. From the forward scan, the oxidised species O accumulates at the electrode surface and, following the reverse scan, is reduced back to R with again the

competition between the electrode kinetics and diffusion, resulting now in a reduction peak.

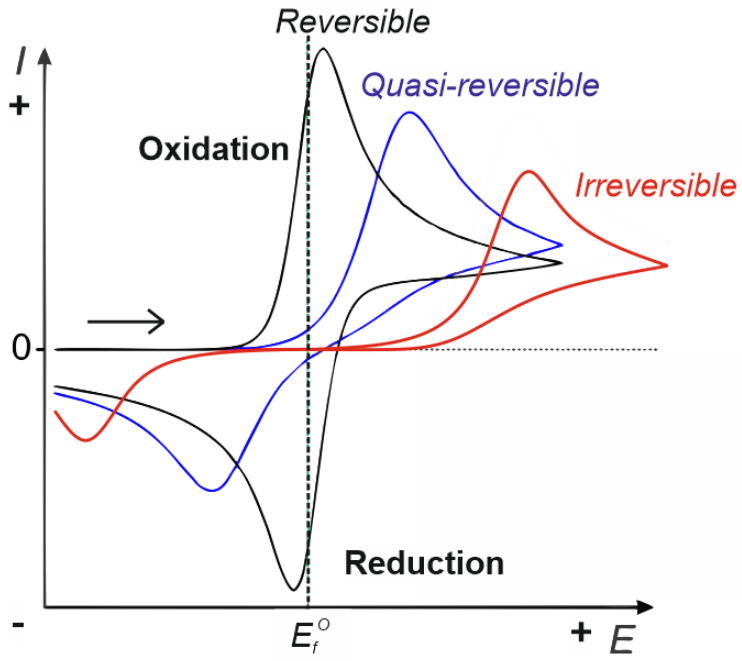

Figure 1.12. Representative cyclic voltammograms using a macrodisc electrode under the reversible, quasi-reversible and irreversible limits for a single-step one-electron transfer solution phase process, with initially only species R present in the solution.

The characterisation of the macroelectrode voltammetry is based on the reversibility of the electrochemical behaviour of the electrode system. 'Reversible' voltammetry is observed for 'fast' electrode kinetics where the electrode reaction appears constantly at equilibrium (thus reversible) and can be described by thermodynamics, whereas 'irreversible' voltammetry is observed for 'slow' electrode kinetics in which the signs of disequilibrium are detected. However, 'fast' or 'slow' is termed relative to the rate of diffusional mass transport, which in turn is described by the mass transport

coefficient m_T ($=\frac{D}{\delta}$). As the diffusion layer thickness depends on the experimental timescale ($\delta \sim \sqrt{Dt}$) which primarily depends on the voltage scan rate ($t \sim \frac{RT}{Fv}$), one has

$$m_T \sim \sqrt{\frac{FDv}{RT}} \tag{1.76}$$

As such, a direct comparison with the rate constant of electron transfer can be made using the parameter Λ as proposed by Matsuda and Ayabe[25]

$$\Lambda = \frac{k_0}{\sqrt{\frac{FDv}{RT}}} \tag{1.77}$$

where

Reversible: $\Lambda > 15$

Quasi-reverisble: $10^{-3} < \Lambda < 15$

Irreversible: $\Lambda < 10^{-3}$

The electrochemical reversibility is therefore shown to be largely dependent on the voltage scan rate. The faster the potential sweep is scanned, the thinner the diffusion layer and therefore the faster diffusional fluxes. With an extreme scan rate that is easily achievable at > 10^3 V s^{-1}, no known electrode systems would exhibit reversible behaviour (the fastest known electrochemical rate constant k_0 is ~10 cm s^{-1} [26]). Conversely with a sufficiently slow scan rate, all electrode processes can appear electrochemically reversible in principle.

The characteristics of well-defined reversible and irreversible voltammetry significantly differ as shown in Figure 1.12. Importantly, in reversible voltammetry,

the relationship between the surface activity of the reactive species and the electrode potential can be described by Nernst equation, but this does not hold for irreversible voltammetry. Further in detail, the characteristics of the two types of voltammetry is discussed in terms of peak current, mid-point potential, peak-to-peak separation and importantly their dependence on the voltage scan rates. The peak current I_p for a one-electron oxidation of the species R is given by the Randles-Ševčík equations for the reversible and irreversible limits respectively (at 298 K)[3]

$$I_p = 0.446\, FA[R]^* \sqrt{\frac{FDv}{RT}} \quad (reversible) \tag{1.78}$$

$$I_{p,a} = 0.496\sqrt{\beta}\, FA[R]^* \sqrt{\frac{FDv}{RT}} \quad (irreversible) \tag{1.79}$$

It is therefore consistent with the feature observed in Figure 1.12 that the peak current for a reversible reaction tends to be a little higher than that for an irreversible reaction (as β often $\sim$ 0.5). In terms of potential features, the peak-to-peak separation is defined as

$$\Delta E_{pp} = |\, E_{p,a} - E_{p,c}| \tag{1.80}$$

and is calculated to be *ca*. 57 mV (298 K, and $\frac{57}{n}\ mV$ for a n-electron process) for a pair of reversible redox peaks, independent of scan rate. However, at high scan rates, in the irreversible limit, a logarithmic dependence on the scan rate is expected

$$\Delta E_{pp}\ (\mathrm{mV}, 298\ \mathrm{K}) = \frac{59}{\beta} log_{10} v + constant \tag{1.81}$$

which is for the one-electron oxidation process and exceeds at least *ca*. 200 mV.

The mid-point potentials $E_{1/2}$ regardless of scan rate for both reversible and irreversible limits, assuming $D_O = D_R$, match the standard formal potential

$$E_{1/2} = \frac{E_{p,a} + E_{p,c}}{2} = E_f^o \quad (1.82)$$

1.6.2.2. Voltammetry at microelectrodes

The cyclic voltammograms observed using a microelectrode exhibits very different voltammetric features from that using a macroelectrode. This is because in the microelectrode limit, the diffusion regime rapidly changes, within the experimental timescale, from linear above the flat surface to predominantly convergent towards the edge of the disc. A steady-state, rather than peaked, current is seen as in Figure 1.13, presenting a sigmoidal shape of the voltammograms. Moreover, due to the greatly enhanced rate of diffusional mass transport, the electro-generated oxidised species O is rapidly removed from the electrode surface and therefore no reduction current is measured on a reverse sweep except at extremely fast scan rates.

The reversibility of microelectrode voltammetry is estimated again based on the direct comparison between the reaction rate constant and the mass transport coefficient. Different from the macroelectrode limit, the steady-state mass transport coefficient in this case is approximately

$$m_T \sim \frac{D}{r_e} \quad (1.83)$$

Therefore, the diagnostic parameter can be defined as[8]

$$\kappa = \frac{r_e k_0}{D} \tag{1.84}$$

where similarly,

$$\text{Reversible: } \kappa > 10$$

$$\text{Quasi-reverisble: } 10^{-2\beta} < \kappa < 10$$

$$\text{Irreversible: } \kappa < 10^{-2\beta}$$

in which β is the transfer coefficient.

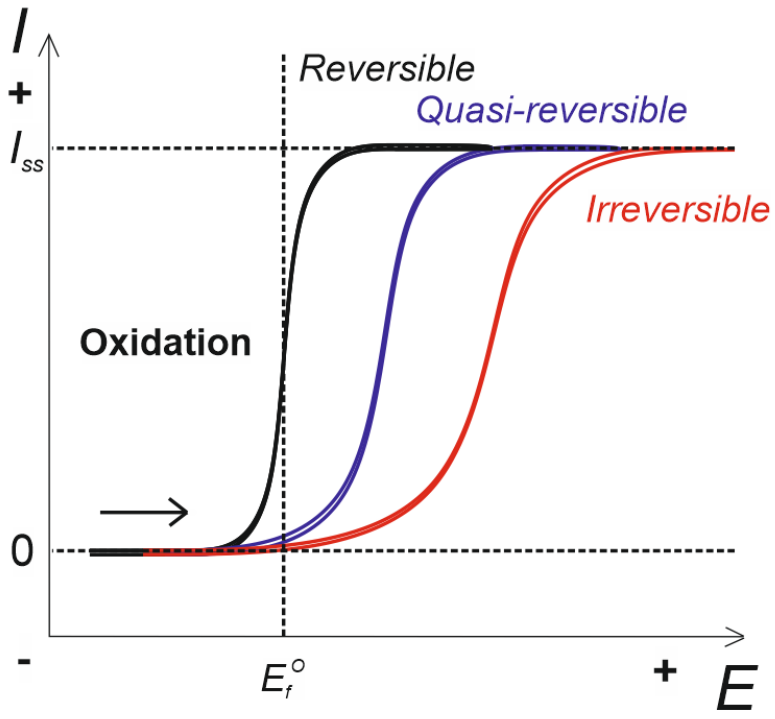

Figure 1.13. Representative cyclic voltammograms using a microdisc electrode in the reversible, quasi-reversible and irreversible limits for a single-step one-electron transfer solution phase process, with initially only species R present in the solution.

The microelectrode voltammetry is further characterised mainly by the steady-state current and half-wave potential. It is noteworthy that the steady state of the current

indicates a limiting current condition where the diffusion layer stops expanding. Since the upper limit of the diffusion layer thickness depends solely on the disc electrode size, not on the interfacial kinetics (i.e. $\delta = r_e \frac{\pi}{4}$)[27], the magnitude of the steady-state current is independent of the electrochemical reversibility as described by Equation 1.73.

However, due to the slowness of the reaction kinetics in the irreversible voltammetry, the current rises not as fast as in the case of a reversible voltammetry, requiring a large overpotential to reach the steady state. The half-wave potentials $E_{1/2}$, or the potential at which half of the steady-state current is found, are therefore different for the reversible and irreversible limits (assuming $D_O = D_R$)

$$E_{1/2} = E_f^o \quad (reversible) \tag{1.85}$$

$$E_{1/2} = E_f^o + \frac{RT}{\beta F} \ln\left(\frac{r_e k_0}{D}\right) \quad (irreversible) \tag{1.86}$$

1.6.2.3. Voltammetry of (ideally) adsorbed species

The discussion above of this section so far is exclusively based on solution phase reactions. However, adsorption of reaction species is not uncommon. Consider the ideal case of a one-electron oxidation

$$R_{(ad.)} - e^-_{(m)} \rightleftharpoons O_{(ad.)} \tag{1.87}$$

where 'ad.' denotes the adsorbed state on the electrode surface of the reactive species. A few assumptions must be met if the adsorption can be viewed as 'ideal'.[28]

First, all the adsorption sites must be equivalent. Second, there are no interactions between the adsorbed species. Third, the surface activity is equivalent to the surface coverage. Last, the total surface coverage is independent of the applied potential. In many cases, and regardless of any ideality or otherwise, the rate of the overall reaction may be dominated by the finite amount of the surface-bound species, and therefore no diffusional tail is present. Consequently, this results in another vastly different type of voltammograms as shown in Figure 1.14.

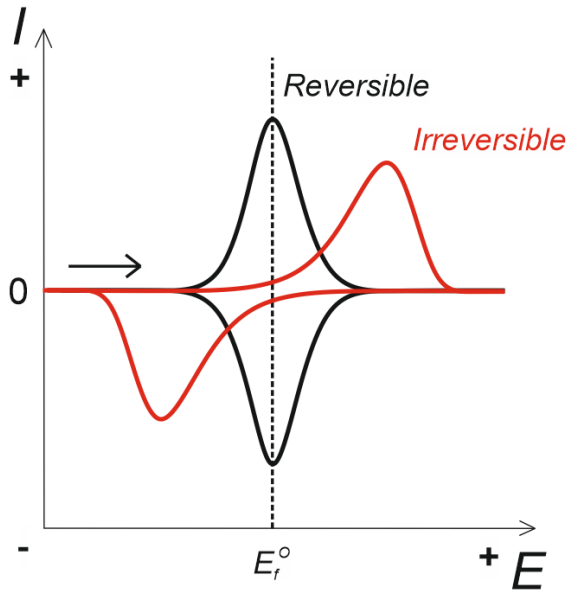

Figure 1.14. Representative cyclic voltammograms of adsorbed species in the reversible and irreversible limits for a single-step one-electron transfer process, with initially only species R adsorbed at the electrode surface.

The shape of the voltammograms above is solely determined by the rate of interfacial electron transfer and its reversibility. Initially, abundant surface-bound species R is present and upon polarisation the current rises with increasingly oxidising potentials, leading to fewer R. Then at the potential where the surface concentration of the

species becomes so low that the overall electron transfer rate starts to drop despite the increasing oxidation rate constant, a peak forms. Eventually, the current decreases to zero, corresponding to the depletion of the adsorbed R and full oxidation to the species O. On the reverse scan, the same processes happen to the oxidised species.

The voltammetry of adsorbed species is mainly characterised by the peak potential and peak current. The peak potential is the major difference between reversible and irreversible limits[3]

$$E_{p,a} = E_{p,c} = E_f^o \quad (reversible) \tag{1.88}$$

$$E_{p,a} = E_f^o + \frac{RT}{\beta F}\ln\left(\frac{\beta F v}{RTk_0}\right) \quad (irreversible) \tag{1.89}$$

while the peak current is given by[3]

$$I_p = \frac{F^2}{4RT} vA\Gamma_{tot} \; (reversible) \tag{1.90}$$

$$I_p = \frac{\beta F^2}{2.718RT} vA\Gamma_{tot} \; (irreversible) \tag{1.91}$$

where Γ_{tot} is the total surface concentration (mol m^{-2}) of the species R. It is seen that the peak current is directly proportional to the voltage scan rate for both reversibility limits, as opposed to the square root dependence seen in the solution phase voltammetry (see Equations 1.78-1.79). This will be found very useful in this thesis for discriminating the type of reactions for unknown systems.

1.7. Voltammetry at nanoparticle-modified electrodes

Nanoparticle-modified electrodes have found important applications especially in the field of electrocatalysis [29] and sensors [30]. Also, studying nanoparticles at an electrode surface has proven fundamentally insightful for understanding their altered properties from their bulk counterparts [31]. As such, voltammetry at electrodes modified with an array of nanoparticles is of great interest. However, such voltammetry may be essentially very different from that at bare electrodes studying molecular species (as introduced in the last section), due to the changes in the active electrode surface area and associated diffusion regimes. Specifically, metal-based nanoparticles themselves can be viewed as individual 'nanoelectrodes' in electrical contact with the support electrode beneath. In most cases, the nanoparticles of study are expected to exhibit significantly higher electro-activity compared to the support electrode, especially if the latter is selected carefully, so the 'actual' electrode active surface may be approximated to the total surface of the nanoparticle array exclusively. These surface can be extremely curved. This sometimes leads first to the surface atoms themselves far more active compared to those in a bulk layer due to the increase in their surface Gibbs energy. Consequently, in the case of a nanoparticle redox reaction, the electrode potential of a metal-based nanomaterial may differ from that of the bulk form. Second, more importantly, the array of these curved surface areas causes vastly different diffusion regimes of relevant molecular species from that on an electrode made of the same material. As learnt from previous sections, this would in turn induce, in both cases of nanoparticle redox chemistry and catalysis, alteration in the features of the resulting voltammetry. It is therefore worthwhile examining these fundamental differences.

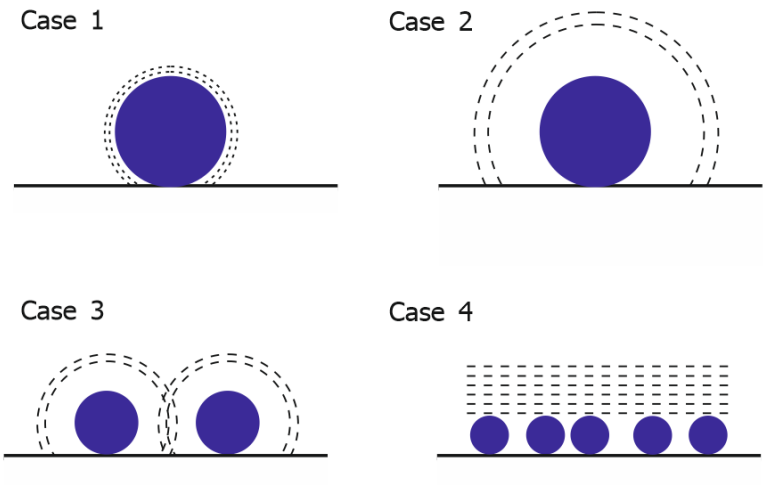

Figure 1.15. Four limiting cases of the diffusion regimes at an array of spherical nanoparticles of an equal size.

The foremost change of diffusion regimes to or from the modified electrode surface as a function of nanoparticle coverage can be readily understood with the general categorisation of four limiting cases for an array of monodisperse spherical nanoparticles [32], as depicted in Figure 1.15. Herein for exemplification, the molecular diffusion is considered to be the diffusion of an electro-active molecular species to a catalytic nanoparticle. Four cases of voltammetrric responses have been accordingly categorised [32]. In Case 1 and 2, nanoparticles have a low coverage. Similar to the evolution in the diffusion on a microdisc electrode, Case 1 corresponds to the time of the start of the diffusion evolution, showing a spatially tiny linear diffusion zone over each single nanoparticle surface, whereas in Case 2 the diffusion at the 'nanoelectrode' is still isolated from the adjacent particle's but has reached a fixed radial regime. In reality, the transition between the two limiting cases takes a very short time of ~ r_{np}^2/D. In Case 3, the nanoparticles have a larger coverage where the developed

Nernstian diffusion layers of adjacent particles slightly overlap with each other. This corresponds to an inter-particle distance comparable to the nanoparticle size. Case 4 describes an array of nanoparticles that are very close to each other. In this limiting case, the diffusion layer heavily overlaps between adjacent nanoparticles and thus collectively exhibits an effectively one-dimensional linear diffusion regime of the molecules across the *whole* array and the current reflects the geometric area of the electrode whereas in Case 1 it reflects the total surface area of the nanoparticles.

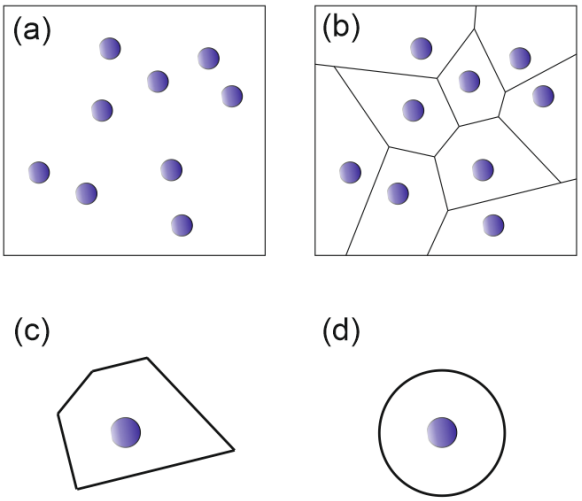

Figure 1.16 Top view of randomly distributed nanoparticles (a) on a sectional area of an electrode surface, which is then (b) divided into Voronoi cell. (c) One single Voronoi cell and (d) a round cell of an equivalent area derived from diffusion domain approximation.

It is possible to model the four cases for regularly spaced nanoparticles [33-34] but, in practice, no matter whether the nanoparticles are deposited or dropcast on to an electrode surface, a random array is typically formed. Consequently, simulations adopt a Voronoi cell for analysing the irregular arrangements of nanoparticles [35]. In doing so, boundaries are drawn midway between any adjacent two nanoparticles in the perpendicular direction as shown in Figure 16a. Next, the diffusion domain

approximation [34] is applied where each divided area is approximated to an equivalent circular area (Figure 16b), the sizes of which follow a Poisson distribution. Meanwhile and importantly, since both adjacent particles are equidistant from the boundary, there would not be a significant difference between the concentrations of the same diffusing species from the two sides, and therefore it is reasonable to assume zero net fluxes across the boundaries. As such, the approximated diffusion domains are diffusionally independent from each other and simulated separately, and the final voltammogram is simply the sum of all the voltammograms from each Voronoi cell. This has been demonstrated to be accurate by comparison with experiment for all but very high coverages [34].

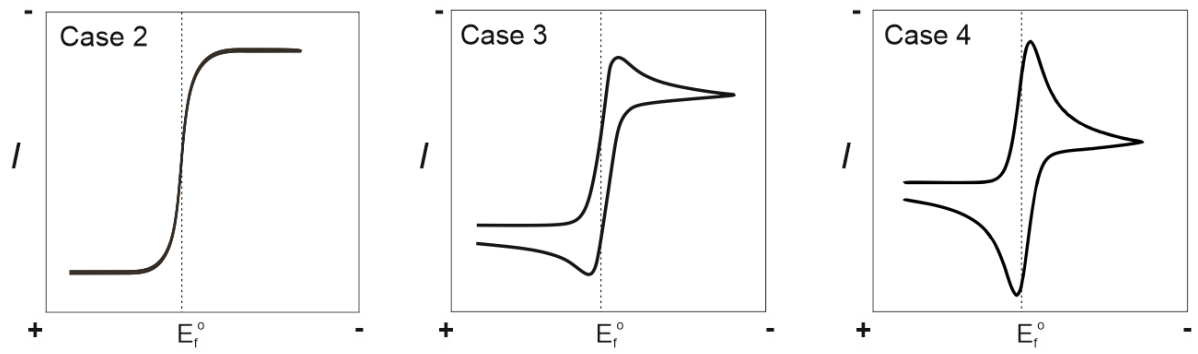

Figure 1.17. Voltammetry at electrodes modified with a random array of catalytic nanoparticles in the three limiting cases, 2, 3 and 4 for a reversible couple.

To characterise the voltammetry at these nanoparticle-modified electrodes, the categorisation needs to be further discussed separately in the cases of nanoparticle catalysis and redox chemistry in both reversible and irreversible limits [32]. For the study of a nanoparticle-mediated reversible reaction (e.g. $O_{(aq)} + e^-_{(m)} = R_{(aq)}$), Figure 1.17 shows that at low particle coverages (Case 2), the nanoparticles are diffusionally

independent, and the radial diffusion of the solution phase reactive species leads to a steady-state current with a magnitude of

$$I_{lim} = 4\pi(ln2)F[i]D_i r_p \quad (1.92)$$

where *[i]* and D_i are the concentration and diffusion coefficient of the electroactive species *i* (herein O or R) respectively; r_p is the nanoparticle radius. By contrast, at higher coverages (Case 3) a Faradaic peak current would be observed due to the overlapping of the diffusion layers that slows the overall diffusion. In Case 4, the *effective* linear diffusion regime renders the voltammograms similar to that using an electrode of the same geometric size as the substrate and made of the same material as the nanoparticles. In irreversible limits, the features would be altered in a qualitatively similar way to those observed in the voltammetry at a single macro- or microelectrode as described in Section 1.6.2.1; for instance, in Case 4 an irreversible electrode kinetics would lead to a larger peak-to-peak separation (than 57 mV at 298 K in a reversible limit) as a function of electrode potential, and the magnitude of the current would be slightly smaller.

References

[1] R. G. Compton, G. H. Sanders, *Electrode Potentials*, Oxford University Press Oxford, **1996**.

[2] P. W. Atkins, J. De Paula, J. Keeler, *Atkins' Physical Chemistry*, 11th ed., Oxford University Press, **2018**.

[3] R. G. Compton, C. E. Banks, *Understanding Voltammetry*, 3rd ed., World Scientific, New Jersey, **2018**.

[4] W. Nernst, *Z. Phys. Chem.* **1889**, *4*, 129-181.

[5] S. Trasatti, *Pure Appl. Chem* **1986**, *58*, 955-966.

[6] P. Vanysek, in *CRC Handbook of Chemistry and Physics, Vol. 8*, 93rd ed., CRC Press, **2000**.

[7] G. N. Lewis, in *Proc. Am. Acad. Arts Sci., Vol. 43*, **1907**, pp. 259-293.

[8] A. J. Bard & L. R. Faulkner, Electrochemical Methods: Fundamentals and Applications, 2nd ed., Wiley New York, 2001.

[9] O. Stern, *Zeitschrift für Elektrochemie und Angewandte Physikalische Chemie* **1924**, *30*, 508-516.

[10] M. Faraday, *Philos. Trans. R. Soc. London* **1834**, 77-122.

[11] J. Tafel, *Z. Phys. Chem.* **1905**, *50*, 641-712.

[12] S. Arrhenius, *Z. Phys. Chem.* **1889**, *4*, 96-116.

[13] K. J. Laidler, *Pure Appl. Chem.* **1996**, *68*, 149-192.

[14] E. E. Tanner, E. O. Barnes, P. Goodrich, C. Hardacre, R. G. Compton, *J. Phys. Chem. C* **2015**, *119*, 3634-3647.

[15] R. A. Marcus, *J. Chem. Phys.* **1965**, *43*, 679-701.

[16] N. Hush, *J. Electroanal. Chem.* **1999**, *460*, 5-29.

[17] A. C. Fisher, *Electrode Dynamics*, Oxford University Press, **1996**.

[18] K. Tschulik, C. Batchelor-McAuley, H.-S. Toh, E. J. Stuart, R. G. Compton, *Phys. Chem. Chem. Phys.* **2014**, *16*, 616-623.

[19] K. Ngamchuea, R. O. Clark, S. V. Sokolov, N. P. Young, C. Batchelor - McAuley, R. G. Compton, *Chem. Eur. J.* **2017**, *23*, 16085-16096.

[20] A. Fick, *J. Membr. Sci.* **1995 (reprinting year)**, *100*, 33-38.

[21] F. Cottrell, *Z Physik Chem* **1902**, *42*, 385.

[22] D. Davis, *Physical Review B* **1973**, *7*, 129.

[23] R. S. Nicholson, I. Shain, *Anal. Chem.* **1964**, *36*, 706-723.

[24] C. Batchelor-McAuley, M. Yang, E. M. Hall, R. G. Compton, *J. Electroanal. Chem.* **2015**, *758*, 1-6.

[25] H. Matsuda, Y. Ayabe, *Zeitschrift für Elektrochemie, Berichte der Bunsengesellschaft für physikalische Chemie* **1955**, *59*, 494-503.

[26] R. F. Martin, D. G. Davis, *Biochemistry* **1968**, *7*, 3906-3912.

[27] A. Molina, J. Gonzalez, M. Henstridge, R. Compton, *Electrochim. Acta* **2011**, *56*, 4589-4594.

[28] R. G. Compton, C. Batchelor-McAuley, E. J. Dickinson, *Understanding Voltammetry: Problems and Solutions*, World Scientific Publishing Company, **2011**.

[29] J. Zhu, L. Hu, P. Zhao, L. Y. S. Lee, K.-Y. Wong, *Chem. Rev.* **2019**, *120*, 851-918.

[30] M. Pumera, S. Sanchez, I. Ichinose, J. Tang, *Sensors and Actuators B: Chemical* **2007**, *123*, 1195-1205.

[31] F. W. Campbell, R. G. Compton, *Analytical and bioanalytical chemistry* **2010**, *396*, 241-259.

[32] S. R. Belding, R. G. Compton, *The Journal of Physical Chemistry C* **2010**, *114*, 8309-8319.

[33] F. W. Campbell, S. R. Belding, R. Baron, L. Xiao, R. G. Compton, *The Journal of Physical Chemistry C* **2009**, *113*, 9053-9062.

[34] T. J. Davies, C. E. Banks, R. G. Compton, *J. Solid State Electrochem.* **2005**, *9*, 797-808.

[35] F. W. Campbell, S. R. Belding, R. Baron, L. Xiao, R. G. Compton, *The Journal of Physical Chemistry C* **2009**, *113*, 14852-14857.

Chapter 2

Advancing nanoparticle electrochemistry

The electrochemistry of nanoparticles (NPs) is currently of significant interest not only because of its important applications in catalysis, energy and sensor technologies, but also for it offers fundamental insights into the physical world. Whilst continuously developing relevant theories applicable at the nanoscale, it is necessary to establish and apply more effective experimental methods for advancing the field of fundamental nanoparticle electrochemistry. The electrochemical activity of NPs depends strongly on their size, shape and surface properties. However, the NP samples used in most reported kinetic measurements inevitably exhibit, within the sample, some degree of both size and shape polydispersity and further different NP crystal orientations. Consequently, many conventional methods for studying the responses of a large number of particles often involve an averaging of the NP properties. Separating the individual responses from the ensemble would thus be desired to decipher the structure-activity relationship at the single entity level for better understanding, design and manipulation of the functional nanoparticles. In addition, single particle electrochemistry also enables important insights into microscopic mechanism and kinetics of nanoparticle reactions. For instance, in the formate and methanol fuel cells using palladium-based nanoparticle as the electro-catalyst, the occurrence of the competitive reaction of palladium oxide formation with formate or methanol oxidation is considered to be detrimental to the catalyst stability. However, this unwanted reaction is revealed to be greatly inhibited at isolated single Pd-decorated carbon nanotubes as compared to the particle ensembles where the mass transport of the

organic molecules is significantly faster than that for the ensembles,[1] which provides mechanistic insights at the microscopic level for improving the electro-oxidation efficiency of the organic fuels.

To essentially improve the methodological resolution to a single particle level, the electrochemical tools are required to reach the precision needed for characterising at dimensions comparable to or even smaller than those of nanoparticles. One foremost success is the development of microelectrodes with at least one geometric dimension of micrometers,[2] and due to its inherent low noise and small double layer capacitance the minute electrochemical signals associated with nanoparticles are allowed to be investigated. The design of the potentiostat system is also crucial. Currently the sampling rate can reach tens of kiloHertz, allowing nanoparticle dynamics occurring at a timescale of microseconds to be explored,[3] whilst the ability of the potentiostat to measure femto-coulombs (i.e. 10^{-15} C) of charge leads to direct investigations of the charge transfer event of a single 3 nm-radius nanoparticle.[4] As such, studying each nanoparticle within the sample is technically feasible and attracts numerous recent efforts, including probing single immobilised NPs with the tip of a scanning electrochemical microscope,[5] monitoring the collisions between a NP and a carbon nanopipette[6] or a microelectrode surface.[7] The latter is mainly discussed in this thesis. In addition, however, in order to fully investigate the electrochemistry of nanoparticles alternative techniques to electrochemical methods may be required to study the non-Faradaic steps involved in the electrode processes. Accordingly in the last chapter, a work mainly using an optical approach to study the redox chemistry of nanoparticles will be demonstrated.

Herein in this chapter, metal-based nanoparticles, as a widely studied type of nano-entities chosen for this thesis, are first introduced in Section 2.1. Next, with the fundamental theories described in the first chapter, the electrochemical technique of 'nano-impacts' based on NP impacts with an electrode surface is introduced in Section 2.2 as the core methodology used in this thesis to study nanoparticles. This method will be shown in the subsequent chapters to be a powerful analytical approach for both, at single entity level, characterising nanoparticles *in situ* and providing mechanistic insights into reactions with or on the nanoparticles. Last, in section 2.3, dark field microscopy is introduced for accessing the insights into the redox chemistry of metal nanoparticles beyond electrochemistry.

2.1. Metal-based nanoparticles

Nanoparticles (NPs) are defined, according to International Union of Pure and Applied Chemistry (IUPAC), as the entities of any shape with dimensions between 1 and 100 nm.[8] Metals may be most accurately defined as substances whose electrical conductivity tends to a finite value at the absolute zero of temperature[9]; nevertheless, for this thesis, one can resort to the conventional though somewhat empirical definition – elements that under ambient conditions readily conduct electricity by electron transfer, and have metallic lustre, opacity and malleability.[10] As such, metal-based nanoparticles refers to the broad family of nanoparticles containing the nominally metallic elements, namely those made of either pure metals (e.g. silver, gold, cobalt) or their compounds (e.g. oxides, hydroxides, chlorides).

Despite huge activity via modern synthetic laboratory approaches, metal-based nanoparticles actually have long existed in nature produced from, for example, volcanic eruptions and microbial processes.[11] Applications of metal-based nanoparticles can even be found in ancient times, mainly as colour pigments in art works. Metallic gold nanoparticles, for example, were used in the *Lycurgus cup*, which was produced in the 4th century and now displayed in the British Museum.[12] As a result, the cup appears ruby red when illuminated from inside and green when exposed to daylight (see Figure 2.1), different from the golden yellow of bulk metallic gold. However, the scientific understanding of the properties of nanoparticles came a lot later only in the year 1857 when Michael Faraday first systematically studied and related the unusual optical properties of gold nanoparticles to the *minuteness* of their sizes.[13] This date can be marked as the emergence of nanoscience.[14] Many tens of years later, underpinned by the advances in quantum theory and in the corresponding experimental validation mainly using electron microscopy[15] and X-ray diffraction[16] for visualisation and structural analysis respectively, the science of metal-based nanoparticles surges.

Figure 2.1. Unusual optical appearances of the Lycurgus cup, illuminated from inside (left) and from outside (right). © Trustees of the British Museum.

It is recognized that at the nanoscale, size starts to dictate properties which differ significantly from those of the bulk materials (which have dimensions above the microscale). Essentially, the interactions between the nanoparticles and the surroundings are dominated by electromagnetic forces, whereas gravitation is not important, such that Brownian motion is observed and enables studies of nanoparticles in the solution phase. Moreover, when size changes down to nanoscale, the electronic energy levels of the material become prominently discrete, such that electrons may

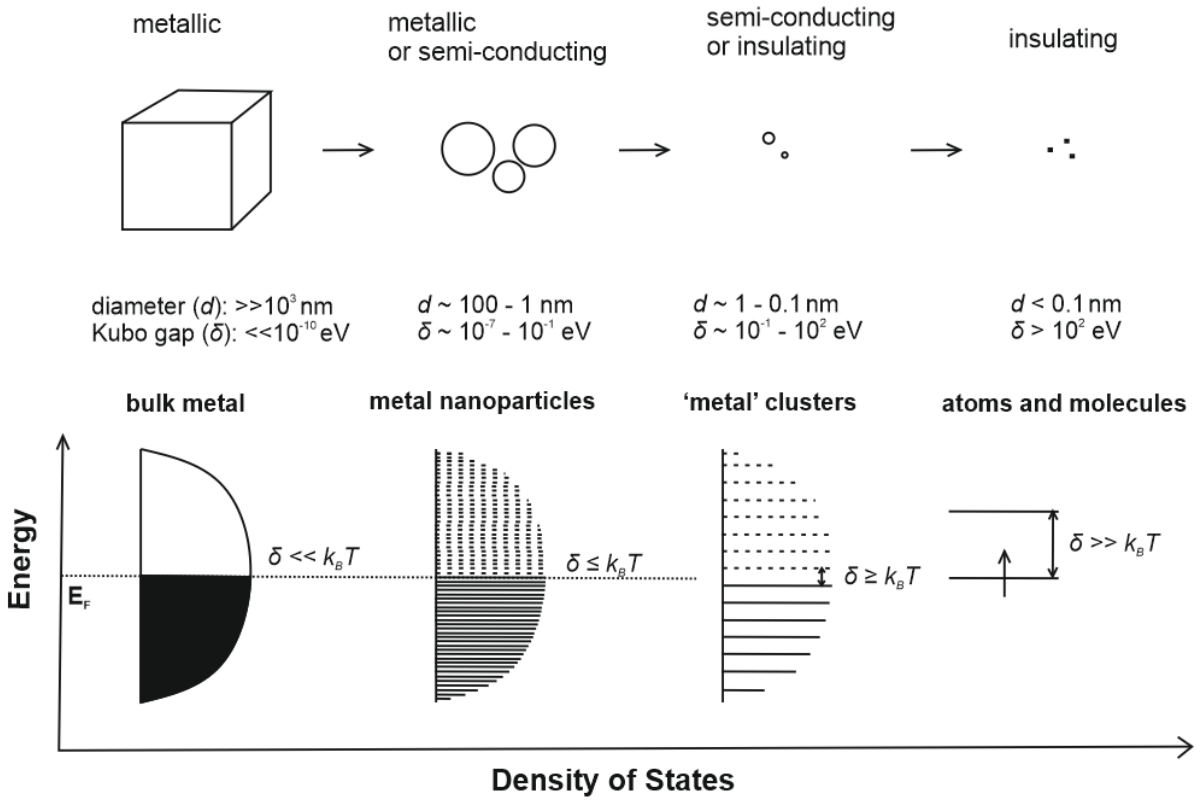

Figure 2.2. Schematic illustration of the size-induced metal-insulator transition. The diameter range and corresponding Kubo gaps are presented. The lower figure depicts the energy level diagram of the bulk metal and of those at smaller dimensions. Dashed and solid horizontal lines in the middle two sketches (for metal nanoparticles and 'metal' clusters) represent respectively unfilled and filled atomic/molecular orbitals.

undergo quantum confinement in these very small particles. This may in turn lead to changes in their electrical properties as shown in Figure 2.2.[17] Specifically, assuming a substance is a metal in its bulk form at room temperature, the continuum of the electronic structure ensures a facile electronic transition from the metal's valence band to its conduction band. As the dimensions of the metal decrease to nanometers, the energy gap between the two bands increases drastically and is no longer continuous. Consider a 20 nm-diameter silver nanoparticle (the smallest Ag nanoparticles studied in this thesis), it is estimated to contain a total number of 2.5×10^5 atoms. This corresponds to a Kubo gap δ, which is the average spacing between successive electronic energy levels (defined as below), of *ca* 3 μeV.

$$\delta = \frac{4E_F}{3n}$$

where E_F is the Fermi level of the metal (i.e. 5.48 eV for silver), n is the number of valence electrons. Even so, the thermal energy of the electrons, with a magnitude of $k_B T$ (k_B is Boltzmann constant) ~ 26 meV at room temperature,[18] is still far larger than the Kubo gap, and thus a 20 nm silver nanoparticle would remain metallic. However, 2 nm diameter silver particles are expected to have a Kubo gap of around 24 meV, which is very comparable to $k_B T$, rendering them semi-conducting. At lower temperature or even smaller sizes of the 'metal' (e.g. a cluster or a single atom), the element would become insulating. Such a vast size-induced change can also be found in the magnetic susceptibility, which closely relates to the dimensions of the magnetic domains. As such, the quantum confinement effects allows tuneable electrical and magnetic properties of metal-based nanoparticles. [18-21]

Of particular interest for chemists are the unusual *surface* physical and chemical properties. Optically, with dimensions far smaller than the wavelength of visible light, the surface plasmon resonance of metallic nanoparticles becomes localised, and therefore the particles show an absorption maximum at the plasmon resonant frequency that is strongly dependent on size.[22] Also, the particles have optical cross sections which are much larger than their geometrical size, and more than 5 orders of magnitude larger than those of dye molecules.[23] Consequently, metal nanoparticles tend to have large extinction and scattering coefficients. Chemically, the inherent large surface-to-volume ratios indicate a significant fraction of surface atoms with relatively high energy/activity, which renders them more chemically active. In particular, this also means a large density of catalytically active sites on the surfaces of metal nanoparticles. As such, many metal-based nanoparticles show exceptional catalytic activities in contrast to their bulk counterparts. For instance, bulk gold is often inert but gold NPs can catalyse many reactions (e.g. CO oxidation) under mild conditions,[24] and similar contrasts also occur for Cu_2O towards the clock reaction between hydrazine and methylene blue.[25] On the other hand, however, more unstable surface atoms inevitably cause the inherently lower stability than the bulk state, leading to the fact that nanoparticles are prone to agglomeration or aggregation in solution. Nevertheless, surfactants are often used to overcome this issue.[19] On the whole, the different and sometimes unique properties have triggered a myriad of research and applications of these nanoparticles.

Metallic silver nanoparticles are probably the most widely used metal-based nanoparticles.[26-27] While applied in microelectronics as electrical contact materials

due to their excellent conductivity and large specific surface area,[28] and in bio-diagnostics (e.g. for Alzheimer's disease[29]) due to the special optical properties (i.e. localised surface plasmon resonance), silver nanoparticles are most particularly known for their biocidal uses in consumer products such as textiles and plastics.[30] The biocidal activity is considered to originate very likely from the strong affinity of silver ions released from the nanoparticles towards sulphur and phosphorous-containing groups which are present in DNA and some proteins, and/or the capability to generate free radicals and reactive oxygen species.[31]

On the other hand, however, the biocidal property indicates a great potential of nano-toxicity as possibly causing disruption of enzyme functions and DNA replication processes upon uptake by human cells.[26] It has been found that silver tends to bioconcentrate in organisms probably because Na^+ and Ag^+ share a similar uptake pathway.[32] Moreover, a total weight of 65 tons of silver ions per year were released from silver nanoparticle consumer products alone into freshwater ecosystems globally in 2010 as estimated based on predictive models.[30] Hence, the potential nano-toxicity of silver nanoparticles is being studied worldwide with the analysis of the particulate behaviours and fate especially in the solution phase.

The analysis of nanoparticles requires basic characterisation of their size, shape and agglomeration/aggregation states. In principle, some of this information can be achieved by electrochemistry and this is encouraged for silver nanoparticles by the

fact that silver has relatively straightforward electrochemical behaviour in solution due to the predominant +1 oxidation state

$$\mathrm{Ag(s) - e^- \rightarrow Ag^+(aq)} \tag{2.1}$$

whilst in the presence of halides X^- (X = F, Cl, Br, I)

$$\mathrm{Ag(s) - e^- + X^-(aq) \rightarrow AgX(s)} \tag{2.2}$$

which is much more thermodynamically favourable (e.g. $E^o_{Ag/AgCl} = 0.22\,V$) than without halides ($E^o_{Ag/Ag+} = 0.80\,V$). The amount of charge transferred can be directly related to the number of silver atoms. This simple fundamental relation offers exciting opportunities for *in situ* characterisation of silver nanoparticles from an electrochemistry point of view which will be further described in Section 2.2.

Despite the fact, but possibly because of it, that cobalt has far more complicated electrochemistry than silver in aqueous solutions (refer to the Pourbaix diagram in Figure 5.2 of Chapter 5), cobalt-based nanomaterials have found many important applications particularly in the field of electrochemical energy generation and storage.[33] The category includes Co-N-C composites, Co oxides and hydroxide, Co chalcogenides, Co phosphides and phosphates.[33] Amongst them, the spinel oxide Co_3O_4 nanoparticles has been extensively studied and show excellent catalytic activity towards oxygen evolution reaction – giving a Tafel slope of *ca.* 60 mV dec^{-1} in many cases regardless of their preparation methods and the nature of the supports[34]. The slope may suggest that assuming a four-electron pathway for the formation of each O_2 molecule, there are three successive fast electron transfers preceding the last rate

determining step.[35] The high chemical stability in alkaline media and earth abundance render the material a promising alternative to the most efficient noble-metal based electrocatalysts (e.g. Pt and Ir) in the field. Further advances in improving the catalytic activity of Co_3O_4 NPs to compete with that of noble material-based catalysts includes creating more oxygen vacancies and active surface areas by plasma engraving,[36] increasing the surface density of catalytic sites by nano-structuring of gold-core Co_3O_4-shell,[37-38] decreasing the interfacial ohmic drop by the use of carbon supports[39].

Another cobalt material $Co(OH)_2$ is also very interesting due to its layered crystal structure and the large interlayer spacing that confers large surface area and a fast (de-)intercalation rate.[40] Accounting for the latter, the oxidative electrode reaction associated with the material

$$Co(OH)_2 + OH^- \rightarrow CoOOH + H_2O + e^- \quad (2.3)$$

involves merely a proton transfer from the cobalt (II) hydroxide for the electron transfer, which leads to a rapid kinetics. With these excellent properties, $Co(OH)_2$ NPs have been further shown to be a potential electrode material for pseudo-capacitors of both large specific capacitance and high power density when combined with zeolite as a nanocomposite.[41]

In the subsequent chapters, we report the investigation on the detection and sizing (Chapter 3& 4), and a substrate-mediated dissolution (Chapter 7) of silver nanoparticles, the characterisation of surface composition and aggregation of

$Co@Co(OH)_2$ nanoparticles (Chapter 5) and the catalytic reaction mechanism of oxygen evolution reaction on Co_3O_4 and $Co_3O_4@SiO_2$ nanoparticles (Chapter 6).

2.2. Single entity electrochemistry: Nano-impacts

It is clear from the last section that both the characterisation of nanoparticles, and their optimisation in terms of material design and engineering, requires fundamental physicochemical insights into these nano-systems. To this end, several methods have been well-established that for instance include the sizing techniques based on light scattering of nanoparticles. As shown in Figure 2.3, dynamic light scattering (DLS) measures the collective, scattered light intensity from the moving particles in the whole volume of the suspension within the path of a laser beam through the sample as a function of time. The analysis of the measured intensity then applies an autocorrelation function (ACF) that decays with delay time due to the temporal shifts in the positions of the particles. Smaller particles move faster according to the generic Stokes-Einstein equation below[42], resulting in a shorter decay time of the ACF.

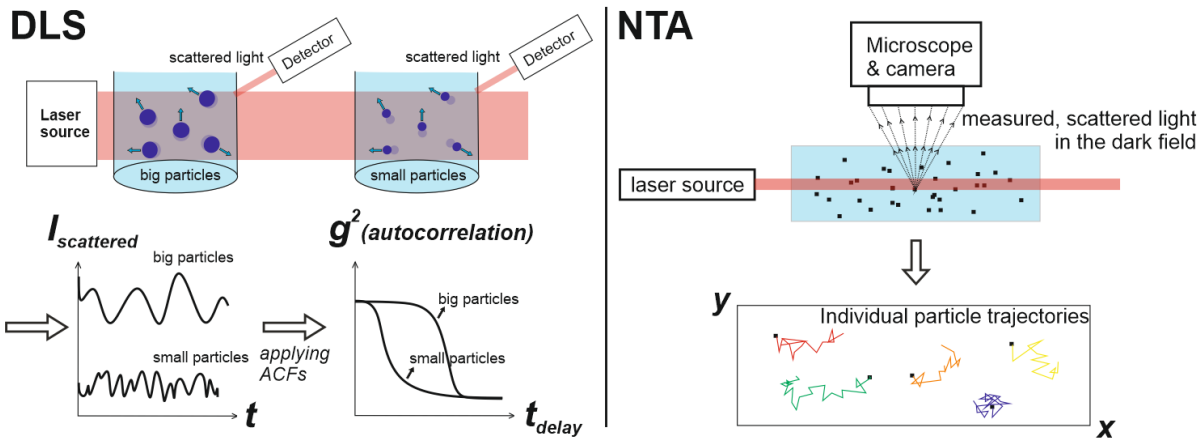

Figure 2.3. Sizing principles of dynamic light scattering (DLS) and nanoparticle tracking analysis (NTA).

$$D = \frac{k_B T}{6\,\pi\,\eta_S\,R_h} \tag{2.4}$$

where D is the translational diffusion coefficient ($m^2\ s^{-1}$) of a particle with a hydrodynamic radius of R_h (m) assuming perfect spheres, k_B is the Boltzmann's constant (1.38×10^{-23} J K^{-1})[43], T is the absolute temperature (K), η_s is the viscosity of the aqueous solution (approximately that of water, 8.9×10^{-4} Pa S at 298 K)[44]. However, for nanoparticles of other shapes than spherical, the equation needs to be corrected. For instance, the correction factor R_L/R_h (where R_L is the lateral radius, namely the length for a cuboid shape or diameter for a circular sheet) for a 2D nanoparticle with an aspect ratio of greater than 3 would be approximately 2 for a cuboid shape, and 2.7 for a circular-sheet shape[45]. On this basis, the average radius of the whole particle size distribution can be estimated.

Another light scattering technique, Nanoparticle Tracking Analysis (NTA) measures displacements due to Brownian motion, as a function of time, of the individual particles visualised within the path of a laser beam. This leads to the determination of their diffusion coefficients (*via* the 2D form of Equation 1.53 in which 2 is replaced by 4) and thus of the sizes for each particle assuming that they have a spherical shape. DLS is restricted to samples with sizes of high monodispersity while NTA sizing is inherently limited to particles bigger than 20-30 nm in diameter by the wavelength of visible light.[46]

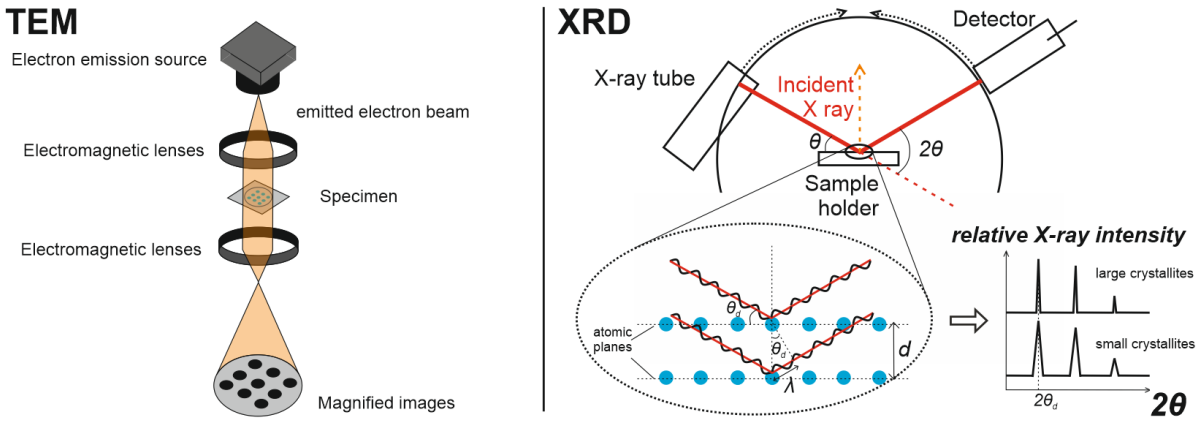

Figure 2.4. Sizing principles of transmission electron microscopy (TEM) and powder X-ray diffraction (XRD).

By contrast, transmission electron microscopy, TEM, uses an accelerated electron beam of short de Broglie wavelengths, « 1 Å at kinetic energies above 20 keV[47], that passes through the particles as shown in Figure 2.4. The method measures the loss of the electrons due to their interactions with the particles and with the substrate, which significantly differs due to the differences in their electron densities. As such, the contrast in the transmittance electron intensity allows a magnified visualisation of the two dimensional sizes and shapes of particles with a resolution well below 1 nm.[48] In addition, the use of the diffraction of varying-angle X rays of atomic-scale wavelengths (typically 1.5 Å[49]) in crystallography may enable the determination of the sizes of metal-based nanoparticles. According to the Bragg's model of diffraction[50], at certain angles θ_d of incident rays, complete constructive interference operates and the behaviour of the X-ray diffraction approximates specular reflection as illustrated in Figure 2.4. This results in the observation of a diffraction peak, which is predicted to be wider for a smaller crystallite as it has fewer atomic planes and a smaller magnitude

of the constructive interferences (see Figure 2.4). This quantitative relationship is described by the Scherrer equation[51]

$$d = \frac{K\lambda}{\beta cos\theta} \tag{2.5}$$

which relates the diameter *d* of a crystallite to the width of the diffraction peak at half of its height (β), with the Scherrer constant *K* (e.g. 0.94 for a spherical shape) and the wavelength (λ) of the applied X rays. It should be noted that the crystalline domain size is usually smaller than the particle size except for the case of a single crystal. Even so, both TEM and XRD are commonly *ex situ*, unable to provide direct information about the state and behaviour of nanoparticles suspended in solution.

Accordingly, the *operando* technique of liquid phase TEM has emerged recently. The idea of TEM studies in solution is realised by trapping a small volume of a liquid using an airtight liquid cell that is highly electron transparent in the path of the electron beam. To this end, typical liquid cells exploit micro-electromechanical systems for fabricating the cells with the use of Si_3N_4 membranes that are merely 10-100 nm thick to ensure high transmittance of the electron beam, or simply two graphene sheets that sandwich the liquid.[52] As such, the electron microscope is able to image through liquids with sub-nanometre resolution.[53] Recent work on liquid phase TEM focuses on visualising the dynamic phenomena at liquid-solid interfaces to gain fundamental insights into structural and chemical evolution of nanomaterials.[54] For instance, the electrochemically induced nucleation and growth of copper nanoparticles on a polycrystalline gold electrode in an aqueous solution has been observed in real-time and compared with theoretical modelling.[55] Also, Gu and co-workers[56] visualised the

lithiation and de-lithiation of silicon nanowire electrodes under the same electrolyte conditions with a commercial battery system.

On the other hand, however, the application of this technique is impeded by its high expense (which has been estimated as $10 in 2009 in total per eV of energy in the beam that ranges usually from 100 to 400 keV)[57] and the difficulty of operation,[58] as well as the currently limited understanding of the unwanted radiolytic effects on the solution chemistry that are incurred by the interactions of the high-energy electron beam with the sample and the chemical environment.[59] In addition to the generation of gas bubbles (e.g. H_2)[60] and reactive species such as H•, HO• and e_h (hydrated electrons), one extremely influential consequence of irradiation is the massive change in the local pH of the irradiated volume.[61] In particular, the effects are more profound in alkaline conditions which may become locally acidic within milliseconds. It follows that the pH change can in turn possibly cause other side effects such as the aggregation of colloidal nanoparticles.[61]

Another emerging electrochemical technique developed in recent years based on impacts between particles and an electrode, called 'nano-impacts', has been extensively shown to be a rapid, powerful analytical method for, not only size, but also with which to study many other physicochemical properties of nanoparticles in solution.[62] In a typical experiment (detailed schemes, including that for particle sizing, are shown later in Figure 2.6), insoluble solid nanoparticles are dispersed in solution and randomly move in virtue of Brownian motion. The particles near the electrode-

solution interface may impact on the electrode surface. During the impact duration, the nanoparticle may undergo a chemical change, or catalyse a reaction of a solution phase electroactive species under suitable electrolyte and potential conditions. Depending on the timescale of the residence, the electron transfer between the particle and the electrode surface may result in 'spike' or 'step'-like current signals, from which information about the particles themselves and/or the catalysed reaction may be extracted. As such, *in situ* characterisation and analysis of nanoparticles are possible.

The concept of particle-electrode impacts was initiated by the pioneering work of Micka[63] in 1956 who studied insoluble metal sulphide (e.g. HgS and CuS) particles suspended in an aqueous solution using polarography. He stirred the microparticles that otherwise tend to precipitate, and observed a cathodic wave in comparison with no current in absence of stirring, as shown in Figure 2.5a. This result therefore evidenced the simultaneous collisions of many particles on the dropping mercury electrode surface. Later in 1971 the practical application of particle-electrode collision was first proposed by Moller[64] and significantly advanced by Holland and co-workers[65-66] leading to the invention of a device for grain size analysis based on electrolytic reduction of AgBr crystals. This utilised a platinum microwire electrode with a diameter of *ca*. 5 μm and the immobilisation of the crystals on a piece of fine-pore filter paper with an inter-distance of *ca*. 3 μm. The modified filter paper is stuck on a turntable and immersed in solution. As the turntable moves slowly, the vertically placed platinum microelectrode makes contacts with the AgBr grains and reduces the individual particles. Consequently, series of sharp reduction peaks are observed (see

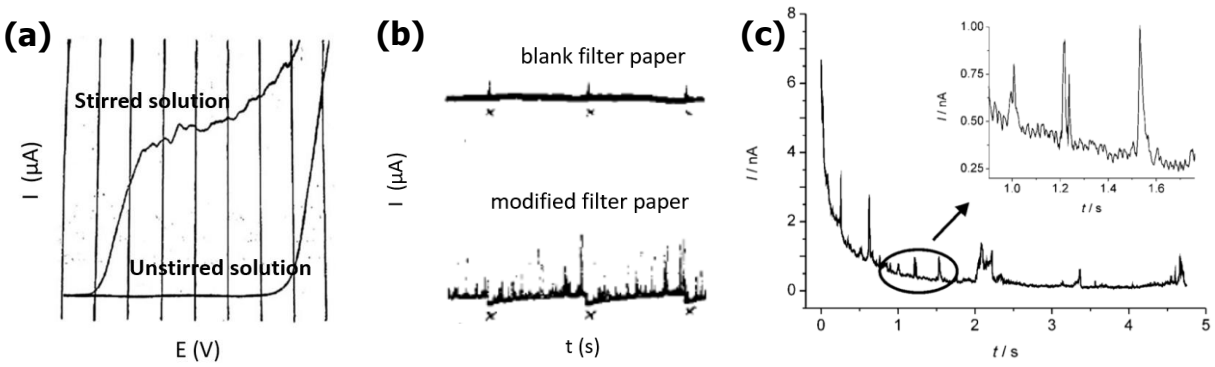

Figure 2.5. Advances in the particle-electrode impacts. (a) Polarograms of HgS particles in stirred and unstirred solution respectively. Data recorded by Micka.[63] (b) Reduction voltammograms of immobilised AgBr particles on a filter-paper-paved turntable when contacting a Pt wire microelectrode, in contrast to that using a blank filter paper. Data recorded by Holland and Feinerman.[66] (c) Chronoamperogram using a carbon microelectrode of the impact oxidation of metallic Ag NPs in a citrate solution. (Reprinted from [7], Copyright 2011, with permission from Wiley. It is observed that the voltammgrams a& b used the past convention that the upward direction refers to reduction current instead.

Figure 2.5b). Based on Faraday's first law (Equation 1.22), the amount of charge measured during each impact event gives the total number of atoms contained in each particle and therefore their volumes. As such, particle with diameters as small as 0.1 ~ 0.2 μm can be accurately sized. This invention was subsequently widely used in the chemical photographic industry for characterising the ultrasmall photo-sensitive particles.

Since the start of the 21st century, particle-electrode impact electrochemistry has witnessed a significant growth of interest along with the rise of nanoscience and nanotechnology. To study the collisions between nanoparticles and an electrode

surface, the current noise is controlled to a low level, usually but not always, in a static solution such that the mechanical noise (in the grain size analyser) is avoided, whereas the collisions can still be triggered by Brownian motion of colloidally stable nanoparticles. The use of microelectrodes as developed by Fleischmann and Wightman[67] also contributes to the significant decrease in noise as compared to macroelectrodes. Moreover, with the potentiostated three-electrode system (the early studies described above used only two electrodes), the potential control of the working electrode is of a greatly improved precision. As such, single nanoparticle impacts were first observed by Bard's group[68] in 2007 with the aid of catalytic current amplification of Pt NPs while importantly, Compton's group first achieved the direct characterisation of single Ag NPs using the technique in 2011 (see Figure 2.5c).[7] So far, the electrochemical impacts have been shown as a powerful analytical approach for studying a large variety of NPs, including metals,[69] organics,[70] polymers,[71] micelles[72], carbon[73-74] and metal-carbon composites[75]. Recent development of the nano-impact technique has been reviewed.[62, 76-77]

The origin of the current resulting from a nano-impact event is commonly charge transfer between the impacting particle and the electrode surface, or simply the surface charge displacement of the electrode. As bare metal-based nanoparticles have minimal surface area as compared to that of a microelectrode, the charge displacement towards the solution phase or the particle surfaces, because of the perturbation of the electrode double layer upon particle arrivals, is negligible. Therefore, according to whether the transferred charge comes from the particles themselves or redox species in solution, the nanoparticle-electrode impacts can be

categorised into two types: *direct* and *mediated Faradaic* impacts (see Figure 2.6 taking 'metal nanoparticles' for example), which are primarily studied in this thesis.

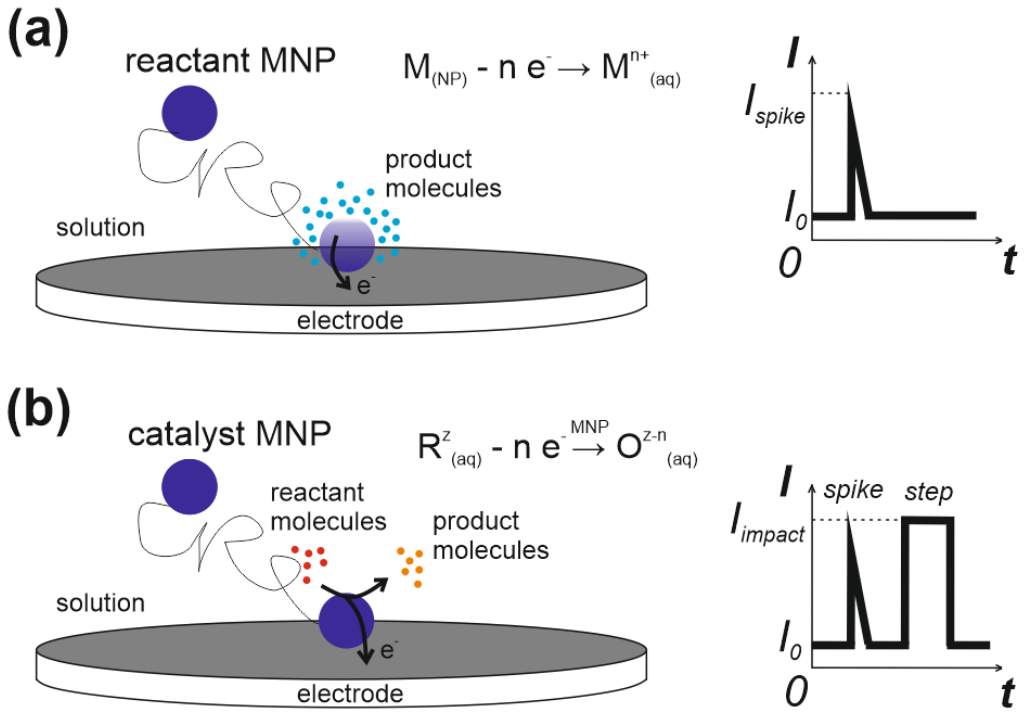

Figure 2.6. Schematic illustration of (a) direct and (b) mediated Faradaic impacts between a microelectrode and, for example, a metallic nanoparticle (MNP). Note that M is the metal species, R and O are the reduced and oxidised form of the redox couple.

In a direct Faradaic impact event, the charge transfer is directly between the impacting particle and the electrode surface as shown in Figure 2.6a. Under suitable potential and electrolyte conditions, the metal particle may be oxidised to form dissolved molecular or ionic species, resulting in Faradaic current spikes in the current-time measurements. The threshold potential of the observed current spikes is often a strong indication of the chemical identity of the particle due to the specificity of metal redox electrochemistry. Most importantly, the current spikes record the electrolysis

process at the single particle level. One significant outcome in the cases of complete particle oxidation is that from the integral of the current, the amount of charge transferred during each impact can be directly related to the total number of atoms/molecules contained in the particular particle, or the precise particle volume, according to Faraday's 1st law. If the shape and density (assuming the same as the bulk condition) are known, the particle dimensions can be further derived. As such, the 'destructive' impacts have been used to size metallic NPs such as silver,[46] gold,[78] copper[79] and nickel[80]. In the case of silver, NPs as small as 4 nm in diameter can be accurately sized.[4]

In a mediated Faradaic impact event, however, the electron transfer occurs between solution phase electroactive molecules and the electrode surface through a conductive metal nanoparticle within the time of its impacting duration (see Figure 2.6b). In this scenario, the particle can be regarded as a transiently formed nano-electrode that only catalyse the redox reaction of the molecules (whereas the reaction barely occurs on the microelectrode beneath due to kinetic limitations). As a result, a 'spike' or 'step'-like current signal is observed depending on the timescale of the particle residence. While the occurrence of the impact signals can therefore be used to detect metal nanoparticles[81-82], the magnitude of the current allows to resolve the rate of catalytic electron transfer at the individual nanoparticle surfaces[1]. In addition, the mediated Faradaic impact method has been shown to be insightful for studying catalytic reaction mechanisms [83-86] and surface dynamics of nanoparticles [75, 87].

2.3. Alternative method: Dark field Microscopy

A full understanding of many electrochemically driven processes, e.g. spontaneous metal corrosions or those involving important non-Faradaic processes, demands the use of complementary techniques, especially spectroscopy and microscopy so as to elucidate the interfacial processes. The latter is used in this thesis to image nanoparticles. In the context of studying aqueous electrochemical reactions of nanoparticles, current liquid cell electron microscopy is still experimentally limited in several aspects. First, the measurements of nanomaterials under the atmospheric conditions require the attainment of a stable volume of liquid within the microscope vacuum by using a microfabricated closed liquid cell, which allows the encapsulation of a liquid layer. This layer must be sufficiently thin so as to be transparent to the electron beam and hence provide an adequate signal-to-background ratio for the spatial resolution to be in the nanometre range. The thickness of thin liquid layer achieved to date ranges from up to 10s of microns[88] to a few nanometers.[52] Both nanoparticle nucleation and growth have been successfully monitored using this technique.[52, 55] Despite these recent varied attempts, the design and fabrication of the delicate liquid cell with adaption for the particular reaction system of interest still remain technically intricate.[53] Second, the use of thin electrochemical cells can largely affect the recording of electrochemical data as the thin electrolyte necessarily brings about a considerable ohmic drop[89] between the working and reference electrodes and therefore attaining a precise potentiostatic control is not straightforward. Moreover, for many electrochemical reactions where mass transport may play an important role at a micrometer scale from the electrode surface with a constant bulk concentration, such small solution layer thickness would severely deviate the mass

transfer condition from the 'real' phenomenon, discouraging relevant studies. Third, as mentioned in last section, the unwanted electron beam damage, inducing the formation of reactive radical species, will likely cause a significant local pH change and induce the degradation of the electrolyte and the nanomaterials in aqueous solution and hence demand further investigations on their suppression or control.

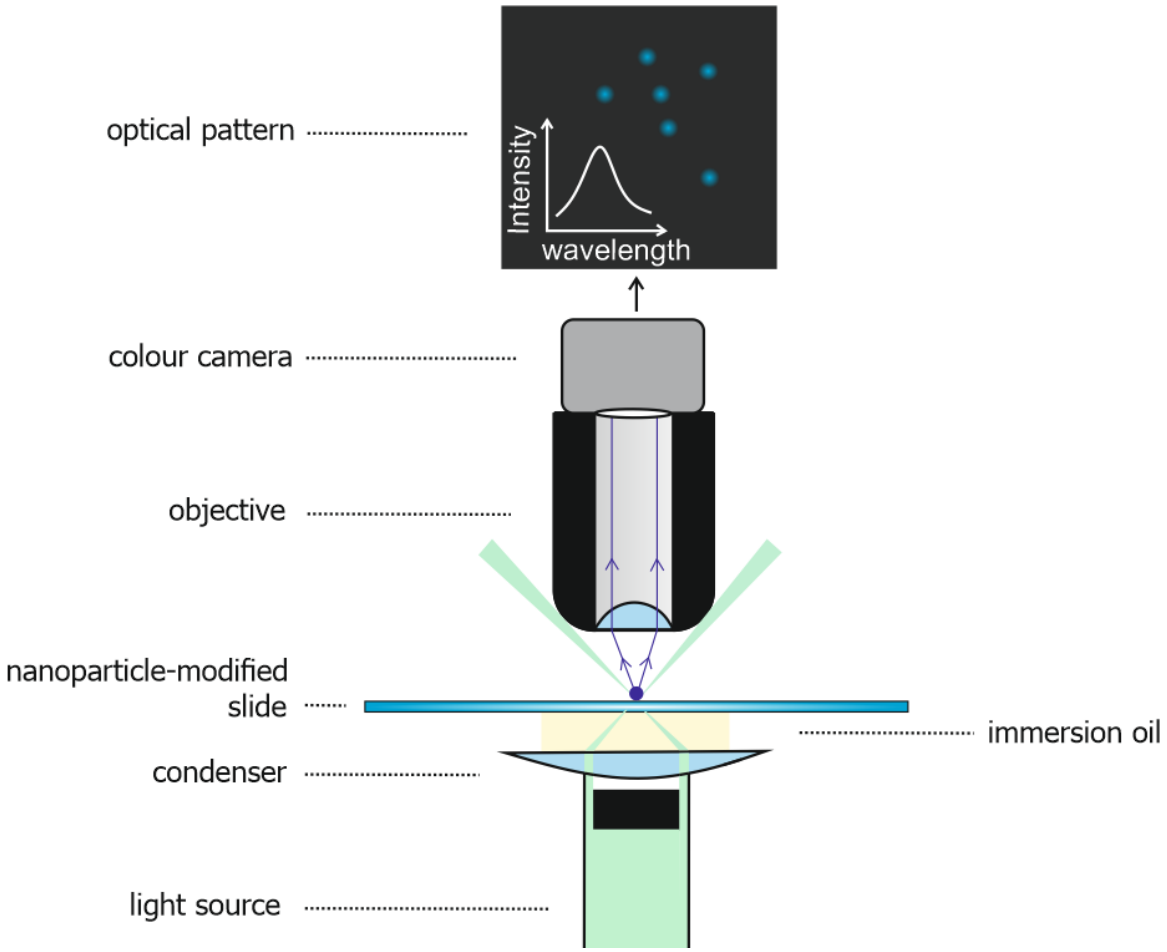

Figure 2.7. Schematic illustration of imaging plasmonic nanoparticles using dark field microscopy with a conventional optical configuration.

In contrast, optical microscopy uses a far less invasive visible light source. Optical microscopy has long been designed to magnify and resolve tiny objects based on light-matter interactions under common aqueous conditions. Among various types of optical

principles (e.g. fluorescence, Raman scattering and photothermal absorption),[90] dark field microscopy (DFM) has been developed to readily image single entities of metal nanoparticles in a wide optical field with good temporal and spatial resolutions.[91] In addition, when the microscopy is equipped with a spectrometer, the measured scattering spectrum of the nanoparticles can be analysed to allow complementary information regarding the local chemistry to be attained. This information comes from the spectral dependence on the particle size, morphology and the refractive index of the surface absorbates and surrounding medium.[92]

A DFM uses oblique illumination to ensure a minimum entry of the incident light into the objective, leading to a dark background (see Figure 2.7). In contrast, elastic scattering of light by metallic nanoparticles emits photons at all angles that partly enter the objective. More precisely, owing to the presence of the conduction electrons in the spatially confined surfaces of the subwavelength metal particles, their interactions with light result in localised surface plasmon resonance that leads to strong absorption and scattering (i.e. refraction and reflection) of light by the nanoparticles at the resonant frequencies. For instance, silver nanoparticles both absorb and scatter (i.e. refract and reflect) visible light in the spectrum region from visible to near-UV depending on their size, shape and agglomeration state. Under dark field illumination a single silver nanoparticle may thus be seen as a bright blue Airy disk (which is a two dimensional diffraction-limited spot of light that a perfect lens with a circular aperture can make). The radius of the latter can be approximately described by the equation

$$r_{Airy} = \frac{1.22\,\lambda}{2\,NA} \tag{2.6}$$

where λ is the wavelength of the light source (nm), NA is the numerical aperture of the objective lens. Such a diffraction pattern of the nanoparticle is typically in microns and thus *far* larger than the nanoparticle's geometric size, despite that the latter is significantly below the Abbe diffraction limited resolution of the microscopy (i.e. ~ 200 nm for conventional imaging modes, the minimum resolvable point-to-point distance of an optical system). For these nanoparticles the optical intensity of these scattering objects varies approximately with the nanoparticle radius to the sixth power (as described by Rayleigh scattering theory) and consequently only nanoparticles of a fairly large size may scatter sufficient light, as compared to the solvent and the substrate, to be visible with a desired signal-to-background ratio. In routine experiments, plasmonic nanoparticles with a diameter > 30 nm can be imaged by a conventional DFM, whereas those as small as 10 nm in diameter may be observed using innovative optical configurations.[93] On this basis, dark field microscopy can be applied to monitor the presence and the position of metal nanoparticles both in the solution phase[94] and adsorbed on an electrode surface[95] for assisting to explore nanoparticle electrochemistry. A work of the latter will be demonstrated in detail in chapter 7.

In the subsequent chapters, we report investigations on the establishment of a quantitative methodology for nano-impact experiments (Chapter 3), the comparison of the technique with conventional light-scattering methods for *in situ* sizing (Chapter 4), the characterisation of nanoparticle surface composition and aggregation (Chapter

5), a mechanistic study of a nanoparticle-catalysed reaction (Chapter 6) using the nano-impacts, and of a substrate-mediated reaction using a synergistic opto-electrochemical approach (Chapter 7).

References

[1] X. Li, H. Hodson, C. Batchelor-McAuley, L. Shao, R. G. Compton, *ACS Catal.* **2016**, *6*, 7118-7124.

[2] M. Edwards, D. Robinson, H. Ren, C. Cheyne, C. Tan, H. White, *Faraday Discuss.* **2018**, *210*, 9-28.

[3] C. A. Little, R. Xie, C. Batchelor-McAuley, E. Kätelhön, X. Li, N. P. Young, R. G. Compton, *Phys. Chem. Chem. Phys.* **2018**, *20*, 13537-13546.

[4] C. Batchelor-McAuley, J. Ellison, K. Tschulik, P. L. Hurst, R. Boldt, R. G. Compton, *Analyst* **2015**, *140*, 5048-5054.

[5] T. Sun, Y. Yu, B. J. Zacher, M. V. Mirkin, *Angew. Chem. Int. Ed.* **2014**, *53*, 14120-14123.

[6] Y. Wang, H. Cai, M. V. Mirkin, *ChemElectroChem* **2015**, *2*, 343-347.

[7] Y. G. Zhou, N. V. Rees, R. G. Compton, *Angew. Chem.* **2011**, *123*, 4305-4307.

[8] M. Vert, Y. Doi, K.-H. Hellwich, M. Hess, P. Hodge, P. Kubisa, M. Rinaudo, F. Schué, *Pure Appl. Chem.* **2012**, *84*, 377-410.

[9] P. P. Edwards, M. Lodge, F. Hensel, R. Redmer, *Philos. Trans. R. Soc., A* **2010**, *368*, 941-965.

[10] F. Hensel, D. R. Slocombe, P. P. Edwards, *Philos. Trans. R. Soc., A* **2015**, *373*, 20140477.

[11] J. R. Lead, K. J. Wilkinson, *Environ. Chem.* **2006**, *3*, 159-171.

[12] F. J. Heiligtag, M. Niederberger, *Mater. Today* **2013**, *16*, 262-271.

[13] M. Faraday, *Philos. Trans. R. Soc. London* **1857**, 145-181.

[14] P. P. Edwards, J. M. Thomas, *Angew. Chem. Int. Ed.* **2007**, *46*, 5480-5486.

[15] J. Turkevich, P. C. Stevenson, J. Hillier, *Discuss. Faraday Soc.* **1951**, *11*, 55-75.

[16] W. L. Bragg, *The London, Edinburgh, and Dublin Philosophical Magazine and Journal of Science* **1914**, *28*, 355-360.

[17] C. R. Rao, G. U. Kulkarni, P. J. Thomas, P. P. Edwards, *Chem. Soc. Rev.* **2000**, *29*, 27-35.

[18] P. P. Edwards, S. Johnson, M. Jones, A. Porch, R. Johnston, *Stud. Surf. Sci. Catal.* **2001**, *132*.

[19] D. L. Fedlheim, C. A. Foss, *Metal Nanoparticles: Synthesis, Characterization, and Applications*, CRC press, **2001**.

[20] C. Rao, G. Kulkarni, P. J. Thomas, P. P. Edwards, *Chem. Eur. J.* **2002**, *8*, 28-35.

[21] D. Duff, A. Curtis, P. P. Edwards, D. Jefferson, B. F. Johnson, A. Kirkland, D. Logan, *Angew. Chem. Int. Ed.* **1987**, *26*, 676-678.

[22] K.-S. Lee, M. A. El-Sayed, *J. Phys. Chem. B* **2005**, *109*, 20331-20338.

[23] P. K. Jain, K. S. Lee, I. H. El-Sayed, M. A. El-Sayed, *J. Phys. Chem. B* **2006**, *110*, 7238-7248.

[24] G. J. Hutchings, M. Haruta, *Applied Catalysis A: General* **2005**, *291*, 2-5.

[25] S. Pande, S. Jana, S. Basu, A. K. Sinha, A. Datta, T. Pal, *J. Phys. Chem. C* **2008**, *112*, 3619-3626.

[26] M. Akter, M. T. Sikder, M. M. Rahman, A. K. M. A. Ullah, K. F. B. Hossain, S. Banik, T. Hosokawa, T. Saito, M. Kurasaki, *J. Adv. Res.* **2018**, *9*, 1-16.

[27] J. Fabrega, S. N. Luoma, C. R. Tyler, T. S. Galloway, J. R. Lead, *Environ. Int.* **2011**, *37*, 517-531.

[28] H. Wu, J. Liu, X. Wu, M. Ge, Y. Wang, G. Zhang, J. Jiang, *Int. J. Adhes. Adhes.* **2006**, *26*, 617-621.

[29] A. J. Haes, W. P. Hall, L. Chang, W. L. Klein, R. P. Van Duyne, *Nano Lett.* **2004**, *4*, 1029-1034.

[30] S. A. Blaser, M. Scheringer, M. MacLeod, K. Hungerbühler, *Sci. Total Environ.* **2008**, *390*, 396-409.

[31] N. Durán, M. Durán, M. B. De Jesus, A. B. Seabra, W. J. Fávaro, G. Nakazato, *Nanomedicine: Nanotechnology, Biology and Medicine* **2016**, *12*, 789-799.

[32] N. R. Bury, C. M. Wood, *American Journal of Physiology-Regulatory, Integrative and Comparative Physiology* **1999**, *277*, R1385-R1391.

[33] J. Wang, W. Cui, Q. Liu, Z. Xing, A. M. Asiri, X. Sun, *Adv. Mater.* **2016**, *28*, 215-230.

[34] M. Hamdani, R. Singh, P. Chartier, *Int. J. Electrochem. Sci.* **2010**, *5*, 556-577.

[35] T. Shinagawa, A. T. Garcia-Esparza, K. Takanabe, *Sci. Rep.* **2015**, *5*, 13801.

[36] L. Xu, Q. Jiang, Z. Xiao, X. Li, J. Huo, S. Wang, L. Dai, *Angew. Chem. Int. Ed.* **2016**, *55*, 5277-5281.

[37] B. S. Yeo, A. T. Bell, *J. Am. Chem. Soc.* **2011**, *133*, 5587-5593.

[38] Z. Zhuang, W. Sheng, Y. Yan, *Adv. Mater.* **2014**, *26*, 3950-3955.

[39] S. Liu, L. Li, H. S. Ahn, A. Manthiram, *J. Mater. Chem. A* **2015**, *3*, 11615-11623.

[40] G. Wang, L. Zhang, J. Zhang, *Chem. Soc. Rev.* **2012**, *41*, 797-828.

[41] L. Cao, F. Xu, Y. Y. Liang, H. L. Li, *Adv. Mater.* **2004**, *16*, 1853-1857.

[42] K. A. Dill, S. Bromberg, Garland Science, New York, **2003**, pp. 327-328.

[43] The NIST Reference on Constants, Units, and Uncertainty. Online source: https://physics.nist.gov/cgi-bin/cuu/Value?k (Accessed on 28 July 2020)

[44] L. Korson, W. Drost-Hansen, F. J. Millero, *J. Phys. Chem.* **1969**, *73*, 34-39.

[45] Y. Yue, Y. Kan, H. Choi, A. Clearfield, H. Liang, *Appl. Phys. Lett.* **2015**, *107*, 253103.

[46] R. Xie, C. Batchelor-McAuley, N. P. Young, R. G. Compton, *Nanoscale* **2019**, *11*, 1720-1727.

[47] L. De Broglie, Doctoral thesis, Migration-university under assignment (France), **1924**.

[48] S. J. Pennycook, M. Varela, C. J. Hetherington, A. I. Kirkland, *MRS Bull.* **2006**, *31*, 36-43.

[49] R. Sharma, D. Bisen, U. Shukla, B. Sharma, *Recent Res. Sci. Technol.* **2012**.

[50] W. H. Bragg, W. L. Bragg, in *Proceedings of the Royal Society of London. Series A, Containing Papers of a Mathematical and Physical Character, Vol. 88*, **1913**, pp. 428-438.

[51] P. Scherrer, *Gottinger Nachr Math Phys* **1918**, *2*, 98-100.

[52] J. M. Yuk, J. Park, P. Ercius, K. Kim, D. J. Hellebusch, M. F. Crommie, J. Y. Lee, A. Zettl, A. P. Alivisatos, *Science* **2012**, *336*, 61-64.

[53] B. H. Kim, J. Yang, D. Lee, B. K. Choi, T. Hyeon, J. Park, *Adv. Mater.* **2018**, *30*, 1703316.

[54] Z. Zeng, W. Zheng, H. Zheng, *Acc. Chem. Res.* **2017**, *50*, 1808-1817.

[55] M. Williamson, R. Tromp, P. Vereecken, R. Hull, F. Ross, *Nat. Mater.* **2003**, *2*, 532-536.

[56] M. Gu, L. R. Parent, B. L. Mehdi, R. R. Unocic, M. T. McDowell, R. L. Sacci, W. Xu, J. G. Connell, P. Xu, P. Abellan, *Nano Lett.* **2013**, *13*, 6106-6112.

[57] D. B. Williams, C. B. Carter, C. T. E. Microscopy, *Transm. Electron Microsc.* **2009**.

[58] H. Martínez-Tejada, *Acta Microsc.* **2014**, *23*.

[59] N. M. Schneider, *Liquid Cell Electron Microscopy* **2016**, 140-163.

[60] J. M. Grogan, N. M. Schneider, F. M. Ross, H. H. Bau, *Nano Lett.* **2014**, *14*, 359-364.

[61] N. M. Schneider, M. M. Norton, B. J. Mendel, J. M. Grogan, F. M. Ross, H. H. Bau, *J. Phys. Chem. C* **2014**, *118*, 22373-22382.

[62] S. V. Sokolov, S. Eloul, E. Kätelhön, C. Batchelor-McAuley, R. G. Compton, *Phys. Chem. Chem. Phys.* **2017**, *19*, 28-43.

[63] K. Micka, O. Kadlec, *Allgemeine Beobachtungen. Collect. Czech. Chem. Commun* **1956**, *21*, 647-651.

[64] G. Moller, in *International Congress on Photographic Science*, Moscow, **1971**.

[65] A. Holland, J. Sawers, *Photogr. Sci. Eng* **1973**, *17*, 295.

[66] A. B. Holland, A. D. Feinerman, *J. Appl. Photogr. Eng.* **1982**, *8*, 165-167.

[67] J. Heinze, *Angew. Chem. Int. Ed.* **1993**, *32*, 1268-1288.

[68] X. Xiao, A. J. Bard, *J. Am. Chem. Soc.* **2007**, *129*, 9610-9612.

[69] G. Zampardi, J. Thöming, H. Naatz, H. M. Amin, S. Pokhrel, L. Mädler, R. G. Compton, *Small* **2018**, *14*, 1801765.

[70] W. Cheng, X. F. Zhou, R. G. Compton, *Angew. Chem.* **2013**, *125*, 13218-13220.

[71] X. F. Zhou, W. Cheng, R. G. Compton, *Angew. Chem. Int. Ed.* **2014**, *53*, 12587-12589.

[72] H. Toh, R. Compton, *Chem. Sci.* **2015**, *6*, 5053-5058.

[73] J. Poon, C. Batchelor-McAuley, K. Tschulik, R. G. Compton, *Chem. Sci.* **2015**, *6*, 2869-2876.

[74] X. Li, C. Batchelor-McAuley, L. Shao, S. V. Sokolov, N. P. Young, R. G. Compton, *J. Phys. Chem. Lett.* **2017**, *8*, 507-511.

[75] X. Li, C. Batchelor - McAuley, S. A. Whitby, K. Tschulik, L. Shao, R. G. Compton, *Angew. Chem. Int. Ed.* **2016**, *55*, 4296-4299.

[76] W. Xu, G. Zou, H. Hou, X. Ji, *Small* **2019**, *15*, 1804908.

[77] J.-H. Zhang, Y.-G. Zhou, *TrAC, Trends Anal. Chem.* **2020**, *123*, 115768.

[78] Y.-G. Zhou, N. V. Rees, J. Pillay, R. Tshikhudo, S. Vilakazi, R. G. Compton, *Chem. Commun.* **2011**, *48*, 224-226.

[79] B. Haddou, N. V. Rees, R. G. Compton, *Phys. Chem. Chem. Phys.* **2012**, *14*, 13612-13617.

[80] Y.-G. Zhou, B. Haddou, N. V. Rees, R. G. Compton, *Phys. Chem. Chem. Phys.* **2012**, *14*, 14354-14357.

[81] A. Fernando, S. Parajuli, M. A. Alpuche-Aviles, *J. Am. Chem. Soc.* **2013**, *135*, 10894-10897.

[82] A. Karimi, S. Andreescu, D. Andreescu, *ACS Appl. Mater. Interfaces* **2019**, *11*, 24725-24734.

[83] M. Kang, D. Perry, Y.-R. Kim, A. W. Colburn, R. A. Lazenby, P. R. Unwin, *J. Am. Chem. Soc.* **2015**, *137*, 10902-10905.

[84] X. Li, C. Lin, C. Batchelor-McAuley, E. Laborda, L. Shao, R. G. Compton, *J. Phys. Chem. Lett.* **2016**, *7*, 1554-1558.

[85] R.-C. Xie, M. Volokhova, A. Boldin, L. Seinberg, M. Tsujimoto, M. Yang, B. Rasche, R. G. Compton, *ChemElectroChem* **2020**, *7*, 1216-1276.

[86] K. Ngamchuea, R. O. Clark, S. V. Sokolov, N. P. Young, C. Batchelor - McAuley, R. G. Compton, *Chem. Eur. J.* **2017**, *23*, 16085-16096.

[87] H. Hodson, X. Li, C. Batchelor-McAuley, L. Shao, R. G. Compton, *J. Phys. Chem. C* **2016**, *120*, 6281-6286.

[88] S. Pu, C. Gong, A. W. Robertson, *R. Soc. Open Sci.* **2020**, *7*, 191204.

[89] I. B. Goldberg, A. J. Bard, S. W. Feldberg, *J. Phys. Chem.* **1972**, *76*, 2550-2559.

[90] W. Wang, *Chem. Soc. Rev.* **2018**, *47*, 2485-2508.

[91] J.-M. Noël, J.-F. Lemineur, *Curr. Opin. Electrochem.* **2020**, 100647.

[92] S. Schultz, D. R. Smith, J. J. Mock, D. A. Schultz, *Proc. Natl. Acad. Sci.* **2000**, *97*, 996-1001.

[93] A. Weigel, A. Sebesta, P. Kukura, *ACS Photonics* **2014**, *1*, 848-856.

[94] C. A. Little, C. Batchelor - McAuley, K. Ngamchuea, C. Lin, N. P. Young, R. G. Compton, *ChemistryOpen* **2018**, *7*, 370-380.

[95] V. Brasiliense, A. N. Patel, A. Martinez-Marrades, J. Shi, Y. Chen, C. Combellas, G. Tessier, F. Kanoufi, *J. Am. Chem. Soc.* **2016**, *138*, 3478-3483.

Chapter 3

A quantitative methodology for the study of particle–electrode impacts

In this first work, a generic framework is established for use in the acquisition and analysis of the electrochemical responses of individual nanoparticles, summarising aspects that must be considered to avoid mis-interpretation of data. Specifically, we threefold highlight the importance of the nanoparticle shape, the effect of the nanoparticle diffusion coefficient on the probability of it being observed and the influence of the used measurement bandwidth. Using the oxidation of silver nanoparticles as a model system, it is evidenced that when all of the above have been accounted for, the experimental data is consistent with being associated with the complete oxidation of the nanoparticles (50 nm diameter). The duration of many single nanoparticle events are found to be *ca.* milliseconds in duration over a range of experiments. Consequently, the insight that the use of lower frequency filtered data yields a more accurate description of the charge passed during a nano-event is likely widely applicable to this class of experiment; thus we report a generic methodology. Conversely, information regarding the dynamics of the nano redox event is obscured when using such lower frequency measurements; hence, both data sets are complementary and are required to provide full insight into the behaviour of the reactions at the nanoscale.

This work has been published in *Physical Chemistry Chemical Physics*, 2018, Royal Society of Chemistry,[1] and was realised in collaboration with Mr.s Christopher A. Little, Dr. Christopher Batchelor-McAuley, Dr. Enno Kätelhön, Dr. Xiuting Li, all from Department of Chemistry, University of Oxford and Dr. Neil P. Young, from Department of Materials, University of Oxford. MSc. Little collected some important experimental data and discussed with me throughout the research. Dr. Batchelor-McAuley helped us with the experimental design and the interpretation of the results. Discussions with Dr. Kätelhön and Dr. Li were helpful. Dr. Young helped with the TEM measurements of silver nanoparticles.

3.1. Introduction

The technique of particle coulometry has continued to evolve in the last 50 years;[2-3] the last decade in particular has seen rapid development in this field with research focusing on the characterisation of individual nanoparticles.[4-5] The technique has been applied to the study of a variety of nanomaterials including gold, silver, copper, iron oxide and liposomes. In general, an electrode is immersed into a solution containing a redox active nanoparticle suspension. The nanoparticles move around in solution by virtue of their Brownian motion. Upon making electrical contact with or 'impacting' a suitably potentiostated electrode, the particle may be oxidised or reduced, resulting in its destruction. These nanoparticle–electrode impacts are herein referred to as 'nano-impacts'. The oxidation or reduction of a single nanoparticle results in a single oxidative or reductive transient feature in the current–time trace. In this work, such current transients will be referred to as 'spikes'. Due to the often small size (*ca.*

picoamperes) of current involved in these reactions, consideration of the signal-to-noise ratio is important and can limit the size of the smallest observable features.[6] Measurement of the current passed during this redox event yields a direct measure of the number of electrons transferred during the process. For a redox reaction of known stoichiometry, with the use of Faraday's 1st law and often under the assumption that the density of the material is the same as that of the bulk, a direct estimate for the volume of material oxidised during the event can be obtained. The measurement of the charge passed during the event facilitates the estimation of the volume of material oxidised or reduced; this electrochemically determined volume can be compared to other particle sizing techniques in order to establish the extent of oxidation (or reduction) of the particle that has occurred during the course of a 'single' impact event.

Electron microscopy is widely accepted as the optimal method for particle sizing. The specific technique required depends on the size of the particles being studied. Whilst Scanning Electron Microscopy (SEM) is appropriate for larger particles, for diameters smaller than tens of nanometres the use of Transmission Electron Microscopy (TEM) is necessitated to ensure a higher level of accuracy. Moreover, as will be highlighted below, the requirement of obtaining and fully accounting for shape information regarding a nanoparticle sample subsequently means that only the family of TEM based techniques have sufficient resolution to enable comparison to be made with experimental electrochemical data. Even with the use of TEM, major ambiguities arise in the estimation of a nanoparticle volume distribution. Techniques are available for

the use of TEM to improve the 3D estimation of the particle shape either through tomography[7] or by 'counting'[8] the number of atoms present in individual particles. This affords an improved estimate of the particle volume distribution. Whilst this atom counting is well suited to very small particles, larger particles pose a greater challenge.

A number of subtleties in comparing conventional 2D microscopy and electrochemical data need to be highlighted. First, microscopy techniques are not devoid of error; the sizing information obtained is sensitive to both the magnification at which the images have been obtained, and the operator.[9] An intrinsic artefact of TEM imaging in this context is the presence of defocusing rings surrounding a particle. The ambiguity from the blurring of the edges of the particles is compounded by variations in contrast of the sample with the support, and the subsequent thresholding employed when analysing the images. The resultant error in radius measurement leads to an error in the estimated volume of a particle. Moreover, this error in the estimated volume is proportional to the cube of the error in the measured radius. Estimation of a particle volume from a 2D image necessarily requires assumptions to be made regarding the particle geometry. Challengingly for microscopy, the circularity of a 2D projection of a particle is not a good estimate of its sphericity. Consequently, even for a solid with a high degree of symmetry and circularity in its 2D projection such as an icosahedron, its volume can differ very markedly from that of the circumscribed sphere (60.5% in the case of an icosahedron).[10] The equilibrium particle shapes of crystalline solids are highly faceted and can be described by Wulff construction that assumes the growth of certain crystal planes is favoured over that of the others, giving thermodynamically determined crystal shapes with a minimised surface energy.[11] However, the actual morphology of a

particle sample depends on a wide variety of factors including synthesis method, aging and particle size. Even before the weak confinement limit (*ca.* <2 nm for metallic materials[12]) is reached, the properties of the solid may differ from that of the bulk material due to the increased surface energy.[13] Such surface curvature effects become influential for silver and gold particles at diameters approximately <20 nm.[14-15] As a result, nanoparticle samples often exhibit a wide variety of shapes and sizes. A given population of particles cast onto a TEM grid will consequently exhibit a diverse array of structural motifs, complicating statistical analysis of sizing. Ultimately, the pragmatic approximation of a particle as a sphere is a poor estimate of a particle's true 3D volume; this stems from the variation of polyhedral shapes and the presence of faceting of the particles.

Second, the electrochemical data reports on the events that have occurred at an electrochemical interface. The probability of a particle arriving at a surface is a function of its diffusion coefficient; for truly monodispersed samples this only serves to alter the expected impact frequency. However, for polydispersed nanoparticle populations (all nanoparticle populations exhibit some degree of heterogeneity) this leads to the electrochemical method being biased towards the observation of smaller particles. This arises due to the smaller particles moving faster within the solution and they are therefore more likely to impact the electrochemical interface. The issue is compounded to an extent by the propensity for nanoparticles to agglomerate in the solution phase in the presence of an electrolyte. Hence, such experiments are now sometimes performed using only millimolar salt concentrations.[16] A further related issue is the tendency for particles to adsorb on to surfaces (such as glass) surrounding the

electrode. This is especially important when considering sample contamination. Often, significant efforts need to be undertaken to avoid cross contamination of nano-particle samples.

Third, measurement and subsequent analysis of the electrochemical data can significantly influence the resulting volume distribution. Recent work in the literature has highlighted the benefits of recording the electrochemical impact data with relatively high bandwidths (*ca.* 10 kHz).[17-19] However – as a note of caution – it is highlighted that work utilising scanning electrochemical cell microscopy (SECCM) is potentially undermined by plausible nanoparticle contamination from the used quasi-reference electrode.[20-21] This caveat aside, at higher frequencies individual nanoparticle–electrode impact events are revealed to be comprised of multiple features. However, the shape of many of these events and the magnitude of the measurement noise are influenced by the used measurement and filtering system.[22] Any measurement system necessarily provides a non-perfect representation of the process it is recording. For electrochemical systems, one of the most important parts of the device is the current-amplifier. A transimpedance amplifier is often employed in the measurement of small currents, but the bandwidth of this device is often limited due to the high gains used.[23] The current-amplifier simultaneously acts in two ways. First, it behaves as an amplifier, converting the current into a voltage output at a predetermined gain, commonly ~1 GV A^{-1}. Second, it acts as a filter, the transfer function of which is often designed to be first order and low-pass. In the study of nanoparticle–electrode impact experiments, many nano-reactions occur at rates faster than can be accurately reported by the amplifier. Consequently, the

shape of the resulting measured nano-impact signal is often found to be influenced by the bandwidth and transfer function of the measurement system. In some cases, the nano-impact event may be so fast (relative to the bandwidth of the used electronics) that the resulting spike shape is that of the measurement systems impulse response.[22] However, although the spike shape can reflect the transfer function of the measurement system, the integral under the current trace, the value of which is equal to the charge passed during the impact, is conserved, assuming the system has been suitably designed.

Beyond considering how the representation of a nano-impact event changes with the used measurement frequency, it is important to consider how a system's electrical noise and hence the measured signal-to-noise ratio changes as a function of the signal bandwidth. As a simplified answer to this problem, assuming the background noise is solely the Johnson–Nyquist noise and similar to that found for an idealised resistor (*i.e.* the power spectral density is independent of the frequency), then the standard deviation of the noise current will vary linearly with the square-root of the signal bandwidth.[24] In contrast, the impulse response of a system is linearly proportional to the signal bandwidth. Consequently, one may anticipate the systems signal-to-noise ratio to improve as the measurement systems frequency (bandwidth) is increased. However, this will only hold true if first, the power spectrum is flat – for an electrochemical system the noise power spectral density will tend to be greater at higher frequencies due to the capacitive coupling of the electrode to the systems voltage noise.[6] Second, if the current measured for a nano-impact event is not that of the impulse response of the system, such that the kinetics of the nano-impact processes are at least partially

resolved by the measurement system, then the spike height will not increase linearly as a function of the measurement frequency. Consequently, as will be demonstrated in this chapter, in the most extreme case the use of high bandwidth measurement can result in the complete loss of information as the processes of interest are obscured by the noise of the system. Further considerations detailing the importance of signal-to-noise ratios in electrochemical measurements have been highlighted elsewhere.[25-26]

Aside from the issues of the measurement of the signal-to-noise ratio, the use of higher measurement frequencies also raises the questions of what constitutes a 'single' electrochemical event and how might the bandwidth at which the data is analysed influence the resulting size distribution? To further clarify terminology, as mentioned above, in this work the term 'spike' refers to a single transient oxidative feature observed in the current–time trace at a given data filtering frequency. During the course of the spike, the measured current does not pass through a pre-defined baseline, but a single spike may exhibit multiple maxima and minima. Like-wise, a single nano-impact event is taken to be one or more spikes in current that occur close to each other in time. The clustering of individual spikes into a single 'nano-event' may be justified on the basis of the known or expected frequency of the nano-impact events, such that the probability that two or more spikes are independent of each other can be defined statistically. The purpose of this chapter is to systematically explore the question of how the bandwidth at which the experimental data is presented and analysed influences both the qualitative and quantitative conclusions made for a nano-impact experiment. To answer this question, the oxidation of silver nanoparticles (Ag NPs) is taken as a model

nanoparticle coulometry system. However, the results have significant wider implications for a range of electrochemical single entity studies.

3.2. Experimental

3.2.1. Chemical reagents

Spherical citrate–AgNPs of *ca.* 50 nm diameter (NanoXact, 0.02 mg mL^{-1} silver, 2 mM sodium citrate) were purchased from nanoComposix, USA, whilst an average diameter of 41.5 ± 6.7 nm for these particles was measured by TEM with the images shown below. Potassium Chloride (≥99.0%) was obtained from Sigma-Aldrich and was used as received without further purification. Solutions were prepared using deionized water (Millipore) with a resistivity of 18.2 MΩ cm at 25 °C.

3.2.2. TEM images of silver nanoparticles

The silver nanoparticles were imaged by transmission electron microscopy (see Figure 3.1) using a JEOL JEM-3000F instrument with an accelerating voltage of 300 kV. Samples were prepared by drop casting nanoparticle suspensions (48 pM AgNPs, 2 mM sodium citrate) onto carbon grids (Agar Scientific) and allowing these to dry. Image extraction was subsequently performed using ImageJ software.

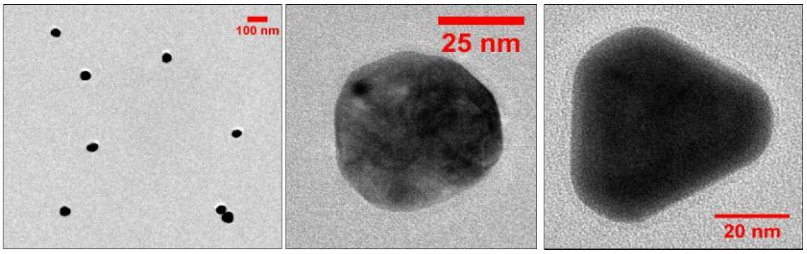

Fig. 3.1. Representative TEM images of commercial spherical citrate-capped silver nanoparticles of 50 nm diameter (NanoXact, 0.02 mg mL^{-1}, 2 mM sodium citrate)

3.2.3. Nano-impacts

Nano-impact experiments were carried out using a home-built in-house low noise potentiostat, as described previously.[6] A low-noise current amplifier (LCA-4K-1G, FEMTO Messtechnik GmbH, Germany) was filtered using two cascade analog RC-filters at 2000 Hz. The signal was then digitised at 100 kS s^{-1} *via* a USB data acquisition device (USB-6003, National Instruments, Texas, US). Finally, the signal was processed either in its raw form, or filtered digitally, *via* a 4-pole Bessel type of low-pass filter, to frequencies of 25, 50, 100, or 500 Hz using a script written in Python 3.5. The low-pass filter used in this work only passes signals with a frequency lower than the set cutoff frequency and attenuates signals with frequencies higher than the cutoff frequency using the Bessel transfer function. Measurements were carried out at a carbon microdisc (d = 33 µm, IJ Cambria Scientific Ltd, UK). We note that whilst this commercially supplied electrode nominally has a radius of 16.5 µm, on calibration it exhibited a radius of up to 22.6 ± 1.3 µm. A leakless Ag/AgCl (in 3.4 M KCl, eDaq) electrode was used as a reference electrode, and a platinum mesh was used as a counter electrode. Chronoamperometry was performed on solutions containing 12 pM AgNPs and 20 mM KCl using the carbon microdisc working electrode. The potential was held at 0.8 V (*vs.* leakless Ag/AgCl) for 20 s in each case. Nano-impact spikes were identified and analysed using a script written in Python 3.5.

3.3. Results and discussion

3.3.1. Individual Faradaic spikes measured from nano-impact experiments

A carbon microdisc electrode (radius = 16.5 μm) was immersed into a solution containing a 12 pM suspension of silver nano-particles and 20 mM KCl. Application of an oxidising potential to the electrode (+0.8 V *vs.* Ag/AgCl) and measurement of the current resulted in the observation of spikes in the time–current trace. Fig. 3.2 depicts a representative chronoamperogram, as measured over twenty seconds. In the absence of solution phase nanoparticles these fluctuations or spikes in the current were not observed. As has been previously documented,[27] these spikes in current are associated with the arrival and electrochemical oxidation of individual nano-particles at the electrochemical interface. In this experiment, the bandwidth of the analog signal was 2 kHz. The current amplifier had a bandwidth of 4 kHz and the output was subsequently low-pass filtered (analog) prior to digitalisation using two cascaded passive RC filters to limit the analog signals frequency to 2 kHz. The choice to filter a signal before it is digitised often arises due to limitations in the available sampling rate. As a minimum, the digitalisation sampling rate needs to be twice the systems measurement frequency (Nyquist–Shannon[28-30] sampling theorem); however, in the present case we are interested in the charge passed during a single nano-impact event. Consequently a far higher oversampling rate is required to ensure the analog signal is accurately represented in the digital data. In the present work, the 2 kHz analog signal is sampled at 100 kS s^{-1}, a factor of 50 times faster. It is important that the bandwidth (frequency) of a signal and the rate at which it is digitised (sampling rate) are not conflated. A flow diagram detailing the used

experimental measurement system is depicted in the Appendix section 1. Following digitisation, the signal is stored and can be digitally filtered (4-pole Bessel) as required following its acquisition. The use of a digital filter readily allows the same experimental data set to be viewed at different signal bandwidths and allows, in this work, for the influence of the filtering to be readily explored and exemplified.

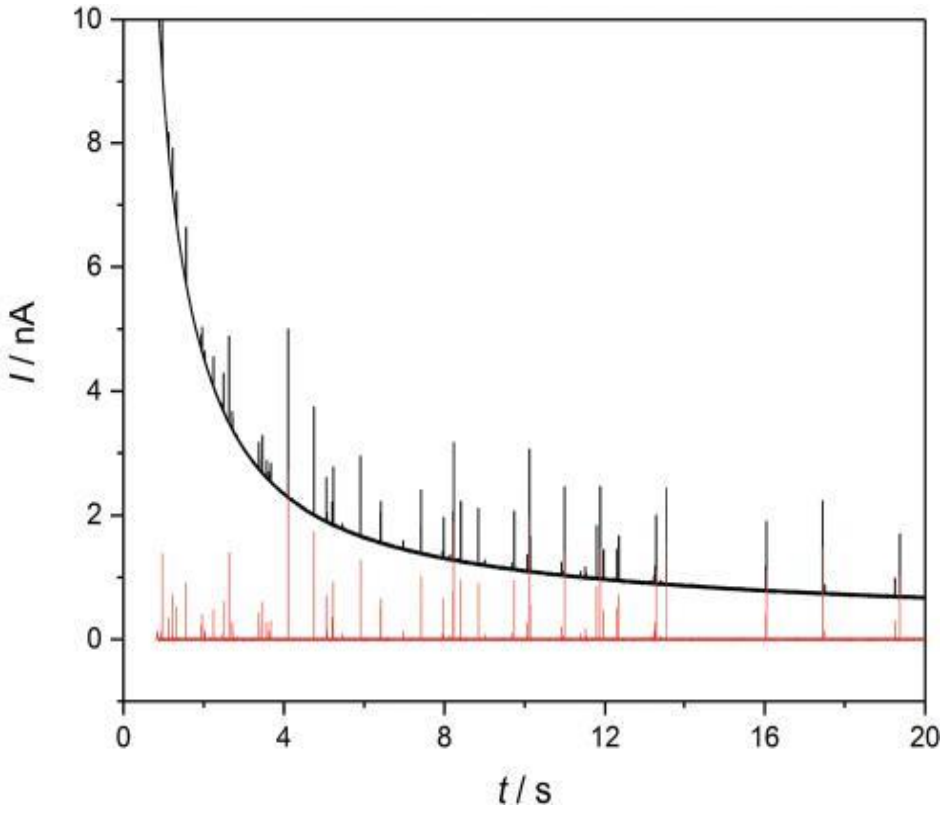

Fig. 3.2 Representative chronoamperogram of 12 pM AgNPs in 20 mM KCl at a 16.5 μm radius carbon microdisc electrode in which the potential is held at 0.8 V (*vs.* Ag/AgCl) for 20 s. The black line depicts the raw data, with the baseline subtracted data overlaid in red.

As shown in Fig. 3.2 (black line) the oxidative spikes in current are superimposed upon a relatively slowly changing background current. During the chronoamperogram, the background current value changes from ~10 nA at short times to less than 1 nA towards the end of the 20 second scan. This background current is ascribed to the capacitive

charging of the electrode and at higher electrode potentials also includes a noticeable Faradaic contribution arising from solvent breakdown. Analysis of individual spikes requires their delineation from the slowly-changing background current. A number of techniques and methods may be developed for this purpose; in the present work we utilise a method in which the local (windowed) variance of the current response is calculated and areas of high local variance are removed from the chrono-amperogram prior to estimation of the baseline. Baseline estimation is then achieved though low-pass filtering of the time–current transient. Further information on the employed methodology is provided in the Appendix section 2. Having obtained an estimate of the slowly varying background signal, this baseline transient is subtracted from the data, to give a baseline-subtracted time– current trace, as shown in Fig. 3.2 (red line). Notably the quantification of the integral of a spike is sensitive to the accuracy and quality of the baseline estimation and is an important factor in the analysis of the experimental data.

After removal of the low frequency baseline, the individual spikes are still superimposed upon a variable higher frequency (noisy) background. The specific origin of these high frequency background fluctuations in current depends upon the used experimental set-up; the electrical noise is commonly dominated by thermal fluctuations at the electrochemical interface or in the used current amplifier.[24] Having removed the slowly changing background, spike identification becomes a simpler task. In this work, a method is utilised in which a spike is identified and begins when the measured current passes through a threshold value, finishing when the current returns to the baseline. The magnitude of the used

threshold can be set by the user, but is most commonly taken as either three or five times the estimate of the standard deviation of the background noise current. The start and end of the spike are subsequently defined by the points at which the current passes through the calculated baseline.

3.3.2. Frequency, charge, multiplicity dependence of the spikes on the filtering bandwidth

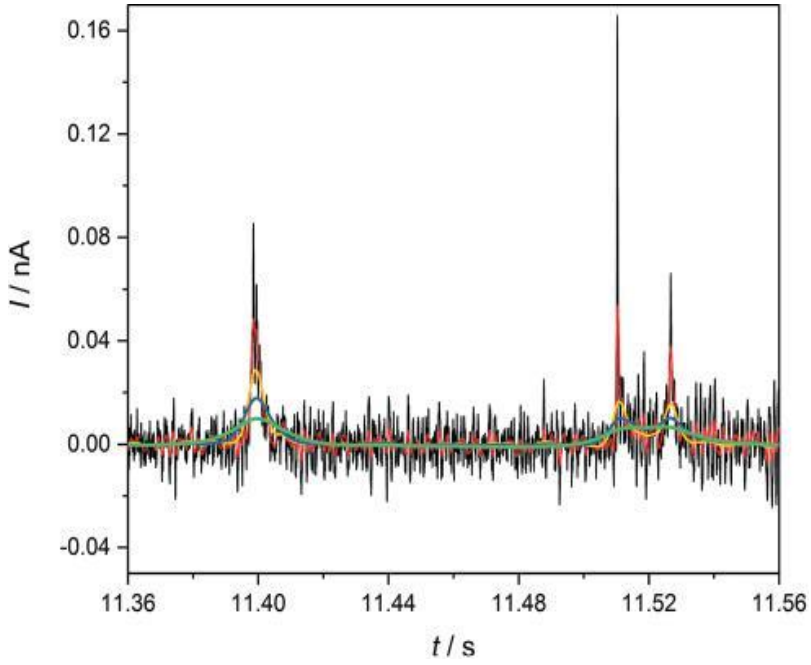

Fig. 3.3. Representative baseline-subtracted chronoamperogram impact spikes for 12 pM AgNPs in 20 mM KCl at a carbon microdisc electrode (33 μm diameter). The black line shows the raw data and the red, yellow, blue and green lines show the effect of filtering at 500, 100, 50 and 25 Hz, respectively.

Fig. 3.3 depicts a section of experimental raw data with the slowly-changing baseline removed, overlaid is the same data where it has been subsequently digitally low-pass filtered post-acquisition to 500, 100, 50 and 25 Hz using a four-pole Bessel filter.

Decreasing the signal bandwidth leads to a reduction in both the spike height and background noise. The width (duration) of the spike in current also increases with decreasing frequency, this is true to the extent that two individual spikes as seen in the raw data with maxima at 11.510 and 11.527 seconds are merged into a single event at 25 Hz.

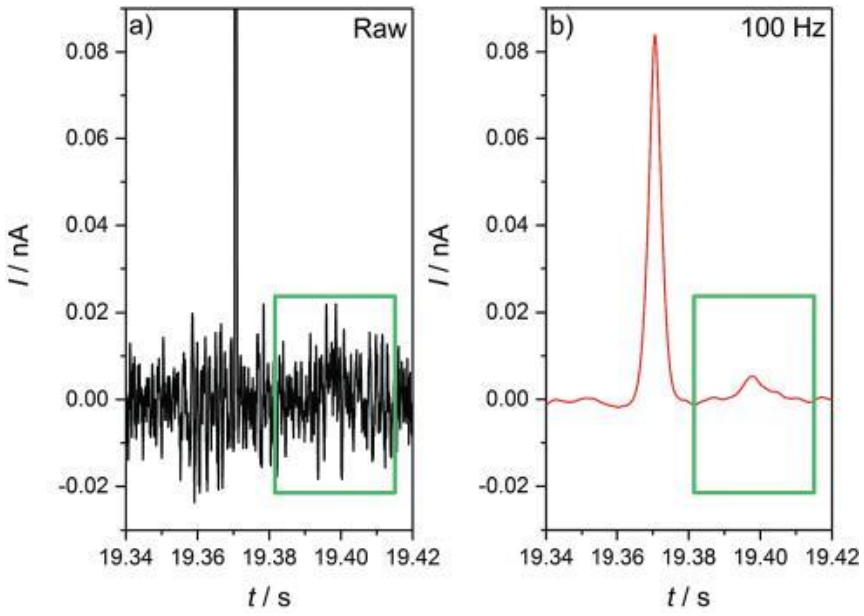

Fig. 3.4 Representative baseline-subtracted example of a 'vanishing' spike for 12 pM AgNPs in 20 mM KCl at a carbon microdisc electrode (33 µm diameter). The raw data is shown on the left with the region of the 'vanishing' spike outlined in green, and the same data filtered at 100 Hz is shown on the right. The charge of this 'vanishing' spike at 100 Hz is 0.038 pC.

This result highlights how filtering the data can lead to a loss of information as individual spike events can become merged into single events when filtered at a low frequency. Conversely, the use of higher filter frequencies can also lead to obfuscation of features in the data. Fig. 3.4 depicts more data both in its raw (not digitally filtered) state and the same data when filtered digitally to 100 Hz. In the

raw data shown in Fig. 3.4a, only one spike event can be identified on the basis of the current increasing significantly above the background noise; however, the same data when filtered to 100 Hz shows a secondary peak approximately 30 ms after the first (see Fig. 3.4b). This experimentally highlights how slow electrochemical processes can be lost (nominally 'vanish') into the data's noise when viewed at higher frequencies. Consequently, the experimental data can appear qualitatively different depending on the frequency at which it is viewed. Ultimately, as the measurement frequency is increased, at sufficiently high bandwidths all Faradaic data will become lost in the systems noise.

For many applications in particle coulometry, measurement of the charge passed during a single nano-impact event is of interest. If we take the duration of a single event to be defined as when the current leaves and returns to a pre-determined baseline, we can consider how the measured charge distribution alters as the data is analysed at different frequencies. Hence, the charge per spike event was measured for the same data set but where the data has been digitally filtered prior to spike identification and analysis of the spike integrals. Experimentally, three of the 20 s chronoamperograms that were recorded at a carbon fibre microelectrode in a solution containing 12 pM silver nanoparticles and 20 mM KCl were analysed at five different frequencies: raw (*ca.* 2 kHz), 500, 100, 50, and 25 Hz. The resulting charge distribution at each frequency is presented as the cumulative frequency as a function of the measured charge. First, the total number of spike features detected in the experimental data is sensitive to the filtering frequency; this is depicted visually in the inlay of Fig. 3.5. In the raw data a total of 254 individual events are detected but as the

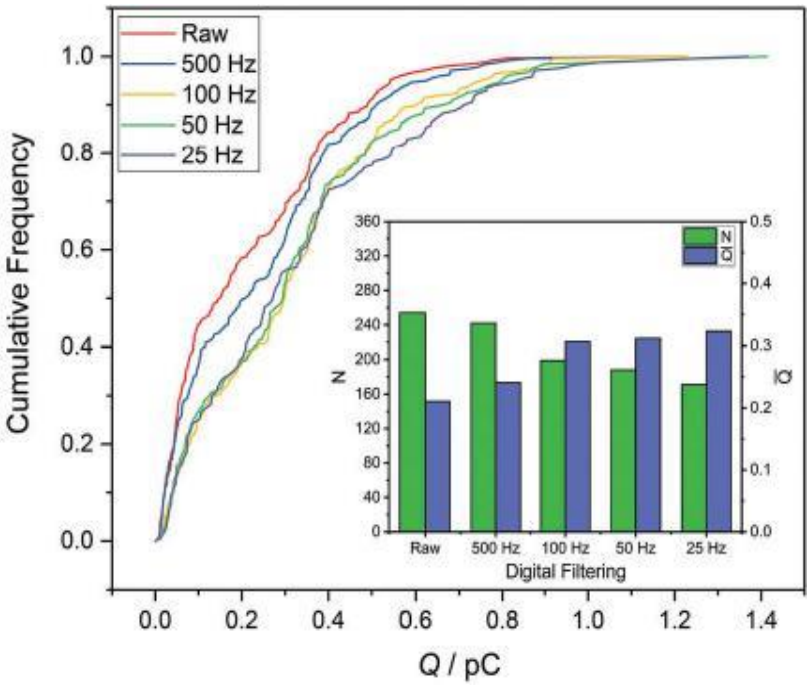

Fig. 3.5 Cumulative frequency plots of the charge transferred during nano-impacts of 12 pM AgNPs in 20 mM KCl at different filtering frequencies for 3 chronoamperograms. The red line depicts the distribution obtained from the raw data, whilst the blue, yellow, green and purple lines show the effect of filtering at 500, 100, 50 and 25 Hz respectively. The inlay shows the effect of the filtering frequency on the number of individual events observed (green) and the value of the mean charge (purple).

used filtering frequency is decreased, this number drops to 171 events at a filtering frequency of 25 Hz. This decrease in the number of spikes detected is attributed to the merging of individual spikes into single features when observed in the filtered data set, akin to the example presented in Fig. 3.3. Concomitantly, the merging of individual spikes together leads to an increase in the average charge passed per feature (see inlay of Fig. 3.5). As such the use of filtering serves to group spikes that occur close in time together as single features. For the presented experimental data this change in the average charge passed is significant where for the raw data 0.211 ± 0.012 pC of charge

is passed per electrochemical event and at a filter rate of 25 Hz this increases to 0.323 ± 0.020 pC. The standard deviations for the raw data and 25 Hz filtered data are 0.195 pC and 0.266 pC respectively. Note the standard deviation does not solely represent the measurement error but predominantly reflects the large variability of the magnitude of the impact events as anticipated for a heterogeneous nanoparticle sample. Importantly, due to the relatively large numbers of individual events measured, the standard error of the mean is comparatively small relative to the mean. This highlights the significance of the differences between the charge distributions measured at the different filtering frequencies.

The sensitivity of these results to the used low-pass filtering frequency raises a significant challenge. For data represented at high frequencies where individual electrochemical nano-impacts may exhibit multiple spikes, how can we determine which features correspond to the same interfacial event? Conversely, if the filtering frequency is too low do independent events become merged into being a single feature in the electrochemical data? Due to the arrival of the nanoparticles at the interface being a random event, it is impossible in the absence of more information to determine categorically if two spikes are associated with the same nano-impact or if they are independent. However, statistics may be employed to provide further insight. For a given particle concentration, known particle size and under the assumption the particles are consumed at the interface, the rate at which the nanoparticles are predicted to impact at a surface may be estimated. Under conditions of a steady-state flux to the electrochemical interface the rate of particle arrival is given by

$$J(t \to \infty) = 4DCr_d \tag{3.1}$$

In the above equation the particle diffusion coefficient can be estimated from the Stokes–Einstein equation (for a perfect sphere) as given by

$$D = \frac{k_B T}{6\pi\eta r_{NP}} \tag{3.2}$$

Assuming that the nano-impact events are independent, the Poisson distribution enables us to determine the probability of observing two or more independent events in a given time period. Alternatively, we can calculate a period of time for which there is a 95% or 99% probability that maximally only one event is predicted to occur. For a 12 pM solution of 50 nm diameter silver nanoparticles at room temperature and using an electrode of radius 16.5 μm, the predicted steady-state impact frequency is 4.7 Hz. Consequently, on the basis of the Poisson distribution, there is a 99% probability that one or zero spike events will occur within a 31.5 ms window. For the 4-pole digital Bessel filter used in this work and with a low-pass filter frequency of 100 Hz, the duration of the impulse response is *ca.* 15 ms. Consequently, on the basis of the above argument, it is a reasonable inference that the use of a 100 Hz filtering frequency, for this present nanoparticle concentration and size, will not lead to a significant number of individual nano-impact events being merged together as a single feature. It should be noted that due to the random and stochastic nature of the impact events it is impossible, no matter the measurement frequency used, to exclude the possibility that two or more events may occur simultaneously and independently at the electrochemical interface.

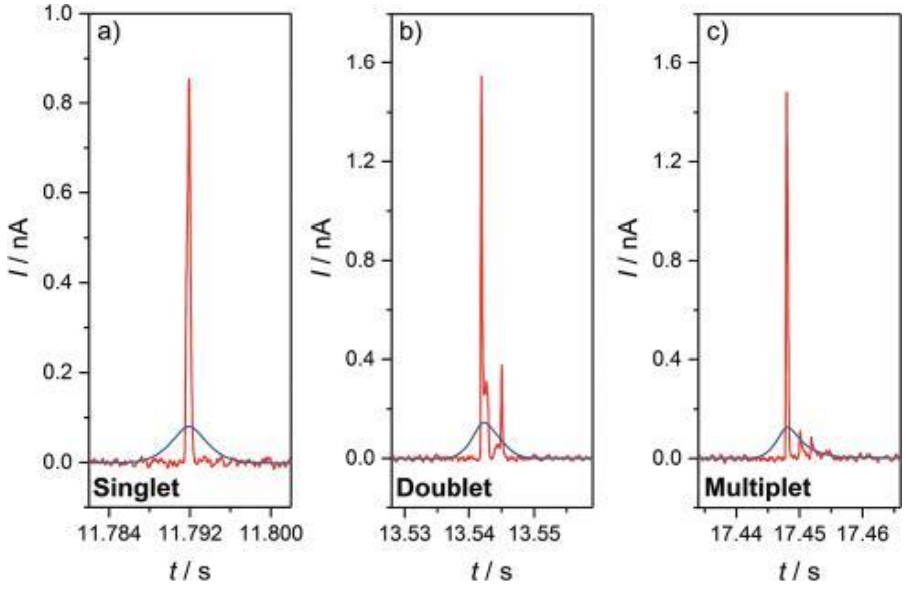

Fig. 3.6. Representative baseline-subtracted examples of 'singlet' (a), 'doublet' (b), and 'multiplet' (c) spikes for 12 pM AgNPs in 20 mM KCl at a carbon microdisc electrode (33 μm diameter). The raw data (red), is shown with the data filtered at 100 Hz (blue) overlaid. The singlet charge of 0.353 pC measured at 100 Hz is comparable with the raw charge of 0.351 pC. For the doublet, the charge of 0.747 pC measured at 100 Hz is also comparable with the raw charge of 0.752 pC, made up of two component charges of 0.603 pC and 0.149 pC. Finally, the multiplet charge measured at 100 Hz of 0.705 pC is slightly larger than the raw charge of 0.638 pC, made up of constituent charges of 0.522 pC, 0.062 pC and 0.054 pC.

Having ascertained that the use of a 100 Hz filter is acceptable for the present work, we next compare the same data set when viewed and analysed at its full (2 kHz) and filtered (100 Hz) frequencies. Fig. 3.6 represents 3 different individual nano-impact events; overlaid is the same data as represented in the raw data set and as reported after filtering to 100 Hz. In Fig. 3.6a, both the raw data and the 100 Hz-filtered data show a single spike. Moreover, the integral of these two peaks is near identical when measured at the two different frequencies (100 Hz charge: 0.353 pC, raw charge: 0.351 pC). Fig. 3.6b shows a single peak at 100 Hz but two separate

spikes in the raw data. Note, as before, a single spike is defined by the current not crossing the baseline. Again the integral of the feature measured at 100 Hz (0.747 pC) is comparable to the sum of the charge passed during the two individual events as measured from the raw data (total charge = 0.752 pC). Finally, and in contrast for the nano-impact event depicted in Fig. 3.6c, at 100 Hz a single spike is observed (charge passed 0.705 pC) but in the raw data 3 individual spikes are observed. A fourth possible spike is also shown but the height of this process is below the required threshold for spike identification and hence is not included in the charge summation. Summation of the charge for the three individual events leads to a calculated total charge of 0.638 pC, *i.e.* approximately 10% less than found for the event when analysed at 100 Hz. This issue of charge being partially underestimated for individual events when measuring data at a higher frequency and summing the charge passed during individual events is also reflected in the data analysis when performed on a larger population size. Appendix section 3 depicts comparative data where the charge distribution has been analysed from the detection of spike events in the raw data, then the raw data has subsequently been clustered together on the basis of a windowing method. Here, if further nano-events occur within 15 ms of the start of the first, the spikes are combined; this value is comparable to the duration of the impulse response of the filter. On average, measuring the data in this way at 2000 Hz results in the total mean spike charge being underestimated by approximately 5% compared to analysis of the data at 100 Hz, excluding those spikes which 'vanish'. However, in this population of events, the charge associated with some spikes is in very significant error (*ca.* 70%, see Appendix 4 for more information). Moreover, the use of high frequency data leads to some features not being identified. As highlighted in the

example shown in Fig. 3.4, this occurs when the electrochemical process is slower, with a longer spike duration leading to a broad and relatively poorly defined peak in the chronoamperometry. As a preliminary conclusion, when the dynamics and kinetics of the nano-event are of experimental interest, the use of higher frequency data is necessitated. Conversely, for situations in which the charge passed during the course of a nano-event is of interest, the analysis of data filtered to lower frequencies is more appropriate. Whilst the use of filtering to effectively cluster and merge spikes together as single events is challenging to justify on the basis of the statistics of the Poisson distribution (as compared to a windowing type method as exemplified in the Appendix section 3), the significant advantage of filtering the data set is the improvement in the signal-to-noise ratio for slow electrochemical events. Crucially, the use of digital filtering enables both data sets to be made available from a single experiment, allowing more complete analysis.

At higher measurement frequencies, the chronoampero-metric data reveals that individual nano-impact events are regularly comprised of multiple spikes in current; as has been exemplified in the data presented in Fig. 3.6. Comparison of the data at a given high and low frequency yields a route by which the multiplicity or the 'number of spikes per nano-impact event' can be systematically quantified. Here, the spike multiplicity gives a measure of the complexity of the current shape of the nano-impact event. In the following, the charge and duration of a nano-event is assessed from the data when it has been digitally filtered to 100 Hz. Subsequently, the number of spike-like features per event can then be assessed by comparison of this data to that obtained at a higher frequency. For example, using this definition,

the nano-impact events depicted in Fig. 3.6a-c are classified as a singlet, doublet and multiplet respectively, where a multiplet is defined as having 3 or more spike-like features per event.

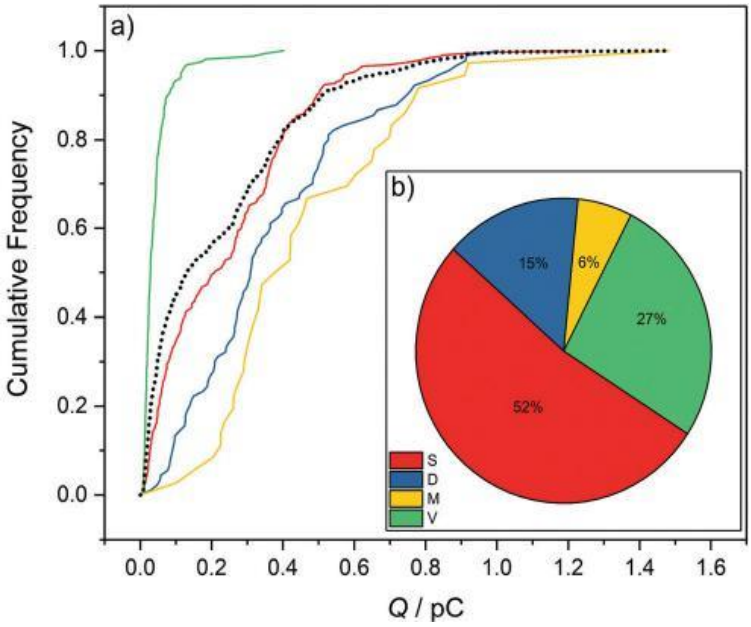

Fig. 3.7 (a) Cumulative frequency charge distributions of nano-impact events split by multiplicity by comparing raw data with that filtered at 100 Hz. Singlets, doublets, multiplets and vanishing spikes are depicted by red, blue, yellow and green lines respectively, with the dotted black line showing the overall distribution. (b) A pie chart showing the distribution of multiplicities of events when filtered at 100 Hz.

Fig. 3.7a shows the distribution of the nano-impact events as categorised by the above multiplicity definitions. Of the 601 nano-impact events considered in total, 52% are singlets when viewed in the raw data. Strikingly, of these nano-impact events, 26% of these features are not observable in the raw data (labelled 'vanished'); they are submerged by the noise of this system at the higher frequency. Fig. 3.7b presents the cumulative frequency for the four categories, showing the associated charge distributions. First, it can be seen that the features that are not detectable in the

high frequency data are on average significantly smaller (considering mean total charge passed, 0.0435 ± 0.0042 pC). This observation predominantly reflects the fact that the lower filter frequency has decreased the noise of the signal, enabling slow (and hence lower current magnitude) features to be resolved in the data set. However, the slow nature of these electrochemical features is of interest and may indicate that the processes leading to their detection differ markedly from other types of nano-impact events. Second, the charge distributions for the singlet, doublet and multiplet features are broadly comparable, but the average charge per event increases with the number of features present per event. Considering the data set in its entirety, the average charge passed for the whole population of events is found to be 0.223 ± 0.009 pC. The following section serves to evidence to what extent the individual nanoparticle oxidation processes goes to completion.

3.3.3. Sizing comparison with TEM

After experimentally obtaining the nano-impact data, filtering the raw data to group processes occurring close together in time, removing the slowly changing background from the chrono-amperometric data (baseline correction), identifying the individual nano-events and integrating the individual charges, it is vital to consider whether the observed individual nano-impact events are consistent with partial or total oxidation of the nanoparticles upon electrical contact with the electrode. To answer this question, one must consider not only the average charge passed per nano-impact event, but also the prospect of information being contained in the experimental nano-impact frequency data.

First, as highlighted in the introduction, it is important to recognise that the electrochemical nano-impact methodology is biased towards the detection of smaller nanoparticles due to their higher associated diffusion coefficient. If each nano-impact event is assumed to provide a measure of the impacting nanoparticles volume, we can also assume that this volume, *V*, gives a direct estimate of the diffusion coefficient of the particle (using a spherical approximation). Furthermore, if the probability of observing a nanoparticle is taken to be proportional to its diffusion coefficient (*i.e.* assuming a convergent steady-state mass-transport profile is operative), then the electrochemically measured charge distribution can be corrected by weighting each particle by the cube-root of the charge passed during the course of the individual nano-impact event ($Q^{1/3}$). This weighting derives from the Stokes–Einstein equation (given in Eqn (3.2)), where $D \propto \frac{1}{r}$ and, assuming a spherical nanoparticle, $V \propto r^3$, hence $D \propto \frac{1}{V^{1/3}}$. The influence of this diffusional correction is shown in Fig. 3.8 such that the weighted data gives – under the approximations made above – a non-biased estimate of the total charge per nanoparticle in the solution phase. This is equivalent to the estimation of the solution phase nanoparticle volume distribution under the assumption of a known material density and with the application of Faraday's 1st law. The above discussion explicitly highlights an assumption made in using the electrochemical method as a route to providing a size estimate of the solution phase nanoparticle volume distribution. Comparison of this estimated volume distribution to that of TEM requires the construction of a volume distribution from 2D representations of the nanoparticle population. As outlined above, in the absence of further topographical or 3D information, significant assumptions regarding particle geometry are required to make an estimate of the nanoparticle volume distribution. TEM images

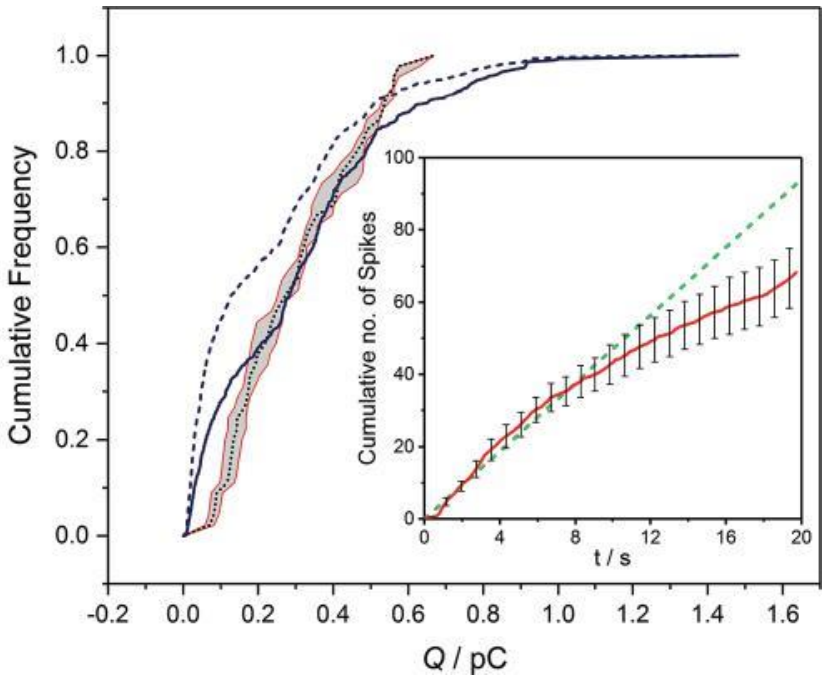

Fig. 3.8 Cumulative frequency charge distribution calculated from TEM sizing (assuming spherical nanoparticles) depicted as black dotted line with shaded area enclosed with a red line determined by the correction factor used. The purple dashed and solid lines show the unweighted and weighted charge distributions obtained from the chronoamperometry experiments respectively. Inlay depicts the mean cumulative number of impacts as a function of time for six chronoamperograms (red line) of 12 pM AgNPs in 20 mM KCl, with the associated standard error bars. The green dashed line portrays the expected cumulative number of spikes assuming a steady-state flux to the electrode.

of the nanoparticle sample used in this work demonstrate that this sample, as is commonly encountered in nano-particle populations, exhibits significant heterogeneity both in terms of the particle dimension and morphology. From these images an estimate of the particle volume distribution and hence oxidative charge per particle can be made. In making this estimate a correction factor (f), as defined in previous work,[31] is utilised and gives a guide to the possible error associated with the conversion of TEM images into a charge estimate per particle. The correction factors

used are further discussed in the Appendix section 4. To re-emphasise this point, the circularity of a 2D projection of a particle in an image does not provide a good estimate of the particles sphericity, even highly symmetric shapes can have significantly lower volumes as compared to the circumscribed sphere.

Fig. 3.8 depicts the TEM and electrochemical estimates of the equivalent charge distribution for the nanoparticle population. In accounting for the bias of the electrochemical technique towards the detection of smaller particles, the average charge per particle is determined to be 0.31 pC, with a standard deviation of 0.25 pC. Depending on the methodology used to estimate the charge per particle from the TEM data (see Appendix section 4), the expected charge per particle is in the range of 0.28 ± 0.02 to 0.32 ± 0.02 pC. The mean charge per particle, as estimated by the two techniques, is found to be in excellent agreement. A minor discrepancy arises in the fact that the electrochemical data estimates a wider size distribution as evidenced by the increase in the reported standard deviation from 0.16 pC (TEM) to 0.25 pC. Consequently, within the accuracy of the technique and the assumptions employed, the observed electrochemical data is consistent with the charge estimate made from the TEM data. This indicates that the nanoparticle oxidation goes to completion for this silver nano-particle population in the presence of 20 mM KCl. Previous work studying larger *ca.* 100 nm diameter particles has highlighted that in the larger size limit, the propensity for a particle to undergo complete or partial oxidation is likely dependent upon a variety of experimental factors, including the electrolyte identity and concentration.[32] Having accounted fully for all of the variables and biases in the system and having analysed the data thoroughly, there

is insufficient evidence to prove the nanoparticle population only undergoes partial oxidation at the electrochemical interface under these experimental conditions.

An alternate route to determine whether the nanoparticle oxidation goes to completion is to study the observed nano-particle impact frequency. The frequency of the nanoimpact events can be measured and compared to that expected on the basis of a diffusional model. Were the nanoparticles to undergo multiple partial oxidations, one may anticipate the measured nano-event frequency to be markedly higher than that predicted on the basis of a diffusion-only model. However, such analysis is complicated by the fact that a number of factors, including particle adsorption onto a supporting surface, agglomeration or chemical kinetic processes can lead to the observed nanoparticle impact frequency being significantly less than would be initially predicted utilising a diffusion-only model of the nanoparticle mass-transport to the electrode surface.[31, 33-34] The Fig. 3.8 inlay depicts the mean cumulative number of spikes observed as a function of time for 6 separately measured chronoamperograms with the associated mean standard error. Also depicted is the theoretically predicted cumulative number of spikes as estimated from assuming a steady-state flux of material to the electrode surface. Although at short-times (<8 seconds) the frequency of the nano-impacts is highly comparable to that predicted for a diffusion-only flux of material to the electrode surface, at longer times (48 seconds) the impact rate becomes significantly depleted. As has been previously reported,[31] the observed nano-impact frequency of the oxidation of silver nanoparticles is sensitive to both the identity and concentration of the halide anion. Notably, the lower the halide concentration the lower the nano-impact frequency is

observed to be (even in the presence of a constant ionic strength). Moreover, although the frequency of the impacts is sensitive to the halide concentration and identity, the magnitude of the average charge passed per event is found to be relatively invariant. This observation has been previously attributed to a nucleation growth type mechanism for the nanoparticle oxidation.[31] In conclusion, in accounting for the complications outlined above, the impact frequency data presented here is not inconsistent with the interpretation that the nanoparticle oxidation goes to completion, given that a wide number of factors can and do influence the observed electrochemical response.

3.4. Conclusions

In accordance with the literature, the use of high measurement frequencies (*ca.* kilo Hertz) reveals that individual nano-impact events tend to exhibit multiple maxima and in many cases are comprised of multiple spike features. This variation in the nano-impact event shape may in some cases reflect the underlying kinetics of the electrochemical reaction, or may reflect the nano-motion of the nanoparticle at the electrochemical interface. The value of the generic methodology employed in this work has been exemplified in the demonstration of the complete oxidation of silver nanoparticles of diameters as large as 50 nm, and such data has been correlated with TEM images to indicate the non-spherical geometry of such particles. However, when the charge per nano-event is of interest, this work demonstrates that the use of higher measurement frequencies tends, even with the use of appropriately fast electronics and sampling, to result in the underestimation of the charge passed per nano-impact event. This occurs due to the fact that at higher measurement frequencies individual nano-events can be comprised of multiple spike features and

the clustering of individual events together as single events is required to provide an estimate of the total charge passed per event. Moreover, higher signal bandwidths necessitate larger background noise and consequently slow and small processes can become 'lost' in the noise of the system. Consequently, in order to obtain more accurate information regarding the both the nano-impact event frequency and the charge passed per event, low-pass filtering the data to lower frequencies is advised prior to charge analysis. This filtering may be performed either prior to or after digitalisation of the signal. In order to exemplify the effect of the filtering system, this work has focused on digital filtering following data acquisition. The lowest suitable filtering frequency depends upon the expected nano-impact event frequency. Use of lower filtering frequencies will increase the probability of two independent events being counted as a single feature. However, for many experiments where frequencies of *ca.* <5 particle impact events are anticipated to occur per second, the use of a 100 Hz filtering frequency is acceptable and both reduces the electrochemical noise and facilitates quantitative analysis of the oxidative charge passed per event. Given the similarity of the duration of nanoparticle–electrode events in the same solvent, the results presented here have wider implications concerning the importance of considering the filtering frequency when pursuing quantitative charge information for a wide variety of nanoparticle systems. Namely, the use of a 100 Hz filtering frequency is widely suitable for charge analysis in this class of experiment.

Appendices

1. Flow diagram of experimental measurement system

The flow diagram in Fig. 3.9 depicts the key stages of the data acquisition process during a nano-impact experiment. Initially the working electrode is held at a virtual ground by the current amplifier, giving a low impedance pathway for the signal (a). The amplifier serves to both amplify the signal and convert it to a voltage (at a conversion of 1 GV/A), this amplification is done with bandwidth of 4 kHz, where the transfer function of the device closely approximates a first-order filter response. Then the voltage signal output of the amplifier is further filtered to 2 kHz using two cascaded passive RC filters (b). Following this, the filtered voltage signal is digitised by the data-acquisition device at a rate of 100 kS s^{-1} (c). Also of importance is the input resolution of the DAQ- in the present case a 16-bit device as been used. The device subsequently sends the digitised signal via a USB connection to the computer. Next, the computer receives and stores the digitised data (d), and this data can be loaded and analysed. If desired, it can be filtered prior to this using a digital low-pass filter, which limits the signals bandwidth (e).

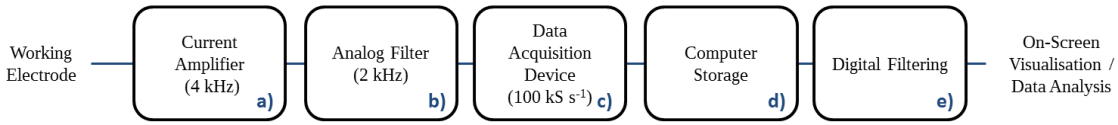

Fig. 3.9. Flow diagram outlining the used measurement and filtering procedure for nano-impact experiments.

2. Details of baseline estimation methodology

In order to analyse the electrochemical spike data an estimation of the baseline needs to be made. This may be done by an individual user on a per spike basis i.e. by manually selecting the 'start' and 'end' of a spike and assuming the background varies approximately linearly over the course of the event. Alternatively, more automated techniques for spike detection may be sought. A problem here lays in the large and relatively slowly changing experimental background signal. This leaves the development of such automated methodologies facing a number of complexities. In the present work the duration of a spike is defined by the points at which the current passes through this pre-defined baseline. Consequently, accurate estimation of the background is paramount to the validity of the analysis carried out. Automated spike identification has a propensity to underestimate the charge per event and requires validation against other analysis procedures prior to being employed.

The method utilised in this work briefly is outlined as follows:

Prior to estimation of the baseline, areas of the time trace containing impact events require removal. In this work we achieve this through analysing the local windowed variance. Using an adapted version of Welford's method (i.e. a single-pass method for computing the variance by looking at the differences between the sums of squared differences for N and N -1 samples) for the calculation of a dataset's variance, the rolling windowed standard deviation can be rapidly estimated with a high degree of accuracy. Having calculated the windowed regions of high variance likely to correspond to times at which a nano-event is occurring, data windows with a variance above a set threshold are removed from the data set. The threshold is

set by the user as a percentile across the whole dataset with values between 70 and 95% are commonly employed. In order to estimate the baseline the regions where data has been removed is filled by an estimate of the baseline. Note, simply filling the formed gaps in the dataset by linear interpolation is found to be insufficient in providing an accurate baseline estimate. Having filled the data gaps, the resulting dataset with the 'spikes' removed is digitally filtered to a very low frequency using a 4-pole Bessel filter (*ca.* 5 Hz). Note a two pass filtering is used first in the forward and then in the reverse direction to avoid phase shifting the resulting baseline. The final filtered response is used as the baseline for the spike detection algorithm. It should be noted that although the baseline estimation and spike identification is semi-automated, the developed script forces the user to validate the baseline and analysis of each individual spike prior to its use in the final data set.

3. Charge distributions using a windowing method

One method of obtaining a charge distribution is to measure data in its raw format, without applying a digital filter, and then clustering spikes together that occur within a given time window. In this case, if the current crosses the baseline more than once within a certain time window these multiple peaks will count as a single event, with the charge calculated by integrating over the whole range of these spikes. Fig. 3.10a depicts the cumulative frequency charge distributions obtained for suspensions of 12 pM AgNPs in 20 mM KCl over three chronoamperograms using this method. Window sizes from 0 ms to 50 ms are used, and the data filtered at 100 Hz overlaid. It can

be seen that a window size of 15 ms is in excellent agreement with the data filtered at 100 Hz, except at low charge (< 0.2 pC).

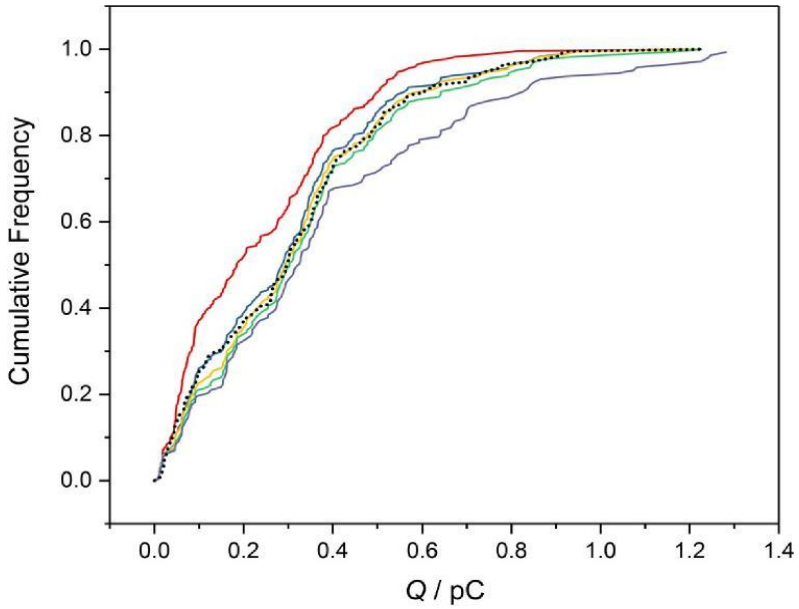

Fig. 3.10a. Cumulative frequency plots of the charge transferred during nano-impacts of 12 pM AgNPs in 20 mM KCl for three chronoamperograms. The data was obtained by detecting spikes from the raw, unfiltered data and then clustering spikes based on a window size. Window sizes of 0 ms, 10 ms, 15 ms, 20 ms and 50 ms are depicted as red, blue, yellow, green and purple solid lines respectively. Overlaid is the same charge distribution obtained from digitally filtering the data at 100 Hz prior to analysis (dotted black line).

As referenced in the main text, by using the high frequency raw data recorded at 2 kHz and clustering the spikes into events based on a 15 ms window size, the average spike charge is underestimated by approximately 5 %. Whilst the overall percentage error is relatively small in magnitude, the error-associated with individual spike events can be as high as 70 %. This data is presented in Fig. 3.10b, with Fig. 3.10bi depicting the correlation between 149 spikes measured by the two methods, excluding 21 'vanishing' spikes and 5 spikes that are split into doublets using the

window-size method. Fig. 3.10bii demonstrates that whilst there is a fairly small percentage change at higher charges (> 0.5 pC), the more extreme disparity comes with lower charge impacts; 10 % of the spike population show a 50 % or greater decrease in charge from the 100 Hz to window-size methods, and all of these are for spikes of magnitudes lower than 0.3 pC.

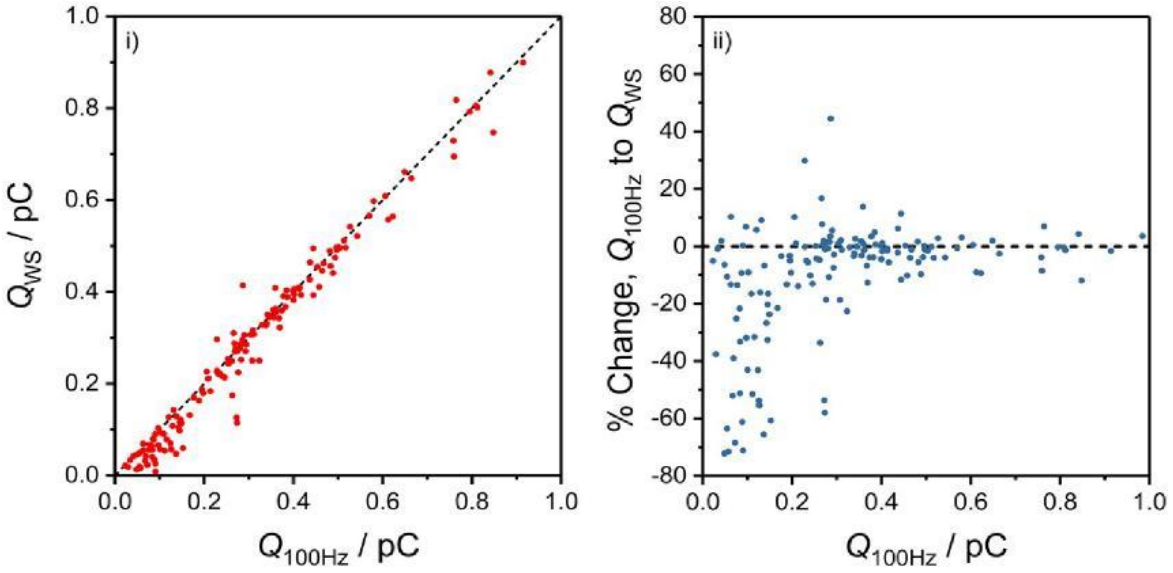

Fig. 3.10b. i) Correlation diagrams for the charge of nano-impact spikes measured with a post-acquisition 100 Hz digital filter applied (Q_{100Hz}) compared to the charge measured by detecting spike events in the raw data, and clustering them together based on a 15 ms window size (Q_{WS}). ii) Scatter plot showing the percentage change in measured charge from the method involving a post-acquisition 100 Hz digital filter applied (Q_{100Hz}) to the window-sizing method (Q_{WS}), plotted against the measured charge at 100 Hz.

4. Correction factors used in TEM

Without the use of tomography or other 3D techniques, attempting to obtain nanoparticle volume distributions from TEM images requires significant assumptions and approximations regarding the geometry of the particles. The TEM images in Fig.

3.11 depict the variation in shapes observed for this batch of silver nanoparticles, with the heterogeneity of the morphology clearly evident.

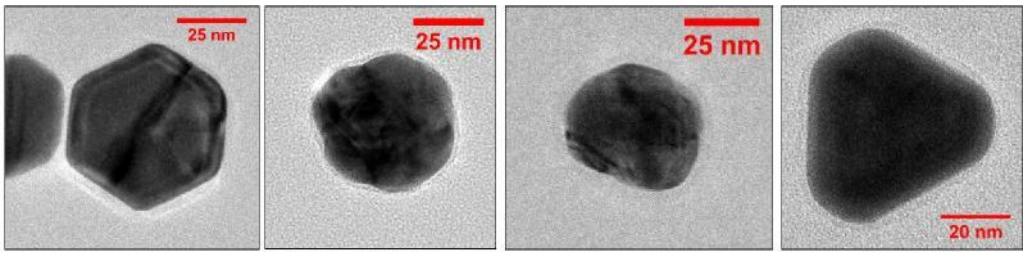

Figure 3.11. Representative TEM images showing the variability in dimension and morphology of nominally 50 nm diameter AgNPs.

As referenced in the main text, the estimation of the nanoparticle volume distribution and hence oxidative charge distribution must take into account a correction factor for their non-sphericity. The charge distribution presented in Figure 3.8 of the main text was constructed by calculating the volume of the nanoparticles as given below

$$V_{NP} = \frac{4\pi R_S^3}{3} \times f \tag{3.3}$$

where R_S is the radius of the sphere circumscribing the nanoparticle, and is taken to be the maximal radius for non-spherical particles (approximately 50 % of the sample). The value of f is taken to be 1 for spherical particles, and has previously been chosen semi-arbitrarily to be 0.5 for non-spherical particles.[31] Assuming complete oxidation of the nanoparticle, the charge transferred per nanoparticle Q_{NP} can then be calculated as given in the equation

$$Q_{NP} = \frac{\rho z F}{A_r} \times V_{NP} \tag{3.4}$$

where ρ is the density of silver (10.5×10^6 g m^{-3}),[35] z is the number of electrons transferred per atom (equal to 1 for silver oxidation), and A_r is the atomic mass of silver (107.9 g mol^{-1}).

Due to the large proportion of non-spherical particles in this sample, the choice of correction factor *f* can have a significant impact on the shape and mean of the charge distribution obtained from the TEM images. As a result, we have presented the distributions resulting from the range of correction factors 0.5-0.7, demonstrating the influence of *f*, and further highlighting the difficulties in using the circularity of a 2D projection to provide a good volume estimate.

References

[1] C. A. Little, R. Xie, C. Batchelor-McAuley, E. Kätelhön, X. Li, N. P. Young, R. G. Compton, *Phys. Chem. Chem. Phys.* **2018**, *20*, 13537-13546.

[2] K. Micka, O. Kadlec, *Allgemeine Beobachtungen. Collect. Czech. Chem. Commun* **1956**, *21*, 647-651.

[3] G. Moller, in *International Congress on Photographic Science*, Moscow, **1971**.

[4] P. H. Robbs, N. V. Rees, *Phys. Chem. Chem. Phys.* **2016**, *18*, 24812-24819.

[5] S. V. Sokolov, S. Eloul, E. Kätelhön, C. Batchelor-McAuley, R. G. Compton, *Phys. Chem. Chem. Phys.* **2017**, *19*, 28-43.

[6] C. Batchelor-McAuley, J. Ellison, K. Tschulik, P. L. Hurst, R. Boldt, R. G. Compton, *Analyst* **2015**, *140*, 5048-5054.

[7] B. D. Levin, E. Padgett, C.-C. Chen, M. Scott, R. Xu, W. Theis, Y. Jiang, Y. Yang, C. Ophus, H. Zhang, *Sci. Data* **2016**, *3*, 1-11.

[8] A. De Backer, L. Jones, P. D. Nellist, S. Van Aert, *Ultramicroscopy* **2017**, *177*, 69-77.

[9] P. M. Anderson, H. Guo, P. B. Sunderland, *J. Aerosol Sci* **2017**, *114*, 317-326.

[10] S. V. Sokolov, C. Batchelor-McAuley, K. Tschulik, S. Fletcher, R. G. Compton, *Chem. Eur. J.* **2015**, *21*.

[11] A. Kiejna, K. F. Wojciechowski, *Metal Surface Electron Physics*, Elsevier, **1996**.

[12] C. R. Rao, G. U. Kulkarni, P. J. Thomas, P. P. Edwards, *Chem. Soc. Rev.* **2000**, *29*, 27-35.

[13] W. Plieth, *J. Phys. Chem.* **1982**, *86*, 3166-3170.

[14] E. Villarreal, G. G. Li, Q. Zhang, X. Fu, H. Wang, *Nano Lett.* **2017**, *17*, 4443-4452.

[15] M. Asoro, J. Damiano, P. Ferreira, *Microsc. Microanal.* **2009**, *15*, 706-707.

[16] S. V. Sokolov, K. Tschulik, C. Batchelor-McAuley, K. Jurkschat, R. G. Compton, *Anal. Chem.* **2015**, *87*, 10033-10039.

[17] E. N. Saw, M. Kratz, K. Tschulik, *Nano Res.* **2017**, *10*, 3680-3689.

[18] J. Ustarroz, M. Kang, E. Bullions, P. R. Unwin, *Chem. Sci.* **2017**, *8*, 1841-1853.

[19] S. M. Oja, D. A. Robinson, N. J. Vitti, M. A. Edwards, Y. Liu, H. S. White, B. Zhang, *J. Am. Chem. Soc.* **2016**, *139*, 708-718.

[20] R. T. Perera, J. K. Rosenstein, *Sci. Rep.* **2018**, *8*, 1-10.

[21] A. Yakushenko, D. Mayer, J. Buitenhuis, A. Offenhäusser, B. Wolfrum, *Lab Chip* **2014**, *14*, 602-607.

[22] E. Kätelhön, E. E. Tanner, C. Batchelor-McAuley, R. G. Compton, *Electrochim. Acta* **2016**, *199*, 297-304.

[23] B. Sakmann, *Single-channel Recording*, Springer Science & Business Media, **2013**.

[24] J. Yao, K. D. Gillis, *Analyst* **2012**, *137*, 2674-2681.

[25] X.-S. Zhou, B.-W. Mao, C. Amatore, R. Compton, J.-L. Marignier, M. Mostafavi, J.-F. Nierengarten, E. Maisonhaute, *Chem. Commun.* **2016**, *52*, 251-263.

[26] C. Amatore, F. Grün, E. Maisonhaute, *Angew. Chem.* **2003**, *115*, 5094-5097.

[27] Y. G. Zhou, N. V. Rees, R. G. Compton, *Angew. Chem.* **2011**, *123*, 4305-4307.

[28] H. Nyquist, *Trans. Am. Inst. Electr. Eng.* **1928**, *47*, 617-644.

[29] C. E. Shannon, *The Bell System Technical Journal* **1948**, *27*, 379-423.

[30] C. E. Shannon, *Proc. IRE* **1949**, *37*, 10-21.

[31] K. Ngamchuea, R. O. Clark, S. V. Sokolov, N. P. Young, C. Batchelor - McAuley, R. G. Compton, *Chem. Eur. J.* **2017**, *23*, 16085-16096.

[32] T. R. Bartlett, S. V. Sokolov, R. G. Compton, *ChemistryOpen* **2015**, *4*, 600-605.

[33] K. J. Krause, F. Brings, J. Schnitker, E. Kätelhön, P. Rinklin, D. Mayer, R. G. Compton, S. G. Lemay, A. Offenhäusser, B. Wolfrum, *Chem. Eur. J.* **2017**, *23*, 4638-4643.

[34] K. J. Krause, A. Yakushenko, B. Wolfrum, *Anal. Chem.* **2015**, *87*, 7321-7325.

[35] R. C. Weast, *Handbook of Chemistry and Physics*, CRC Press, USA, **1974**.

Chapter 4

Electrochemical Impacts Complement Light Scattering Techniques for In-situ Nanoparticle Sizing

Having establishing a generic framework for the nano-impact technique in Chapter 3, we next show that the electrochemical method complements light scattering techniques for sizing both mono- and poly-disperse nanoparticles. It is found that established techniques – Dynamic Light Scattering (DLS) and Nanoparticle Tracking Analysis (NTA) – can accurately measure the diameters of '30 nm' silver particles assuming spherical shapes, but are unable to accurately size a smaller '20 nm' sample. In contrast, nano-impacts have a high accuracy (< 5% error in effective diameters) and are able to size both individual '20 nm' and '30 nm' silver NPs in terms of the number of constituent atoms. Further study of a '20 nm and 30 nm' bimodal sample shows that the electrochemical technique resolves the two very similar sizes well, demonstrating accurate sizing regardless of particle size polydispersity, whereas due to inherent limitations of light scattering measurements this is not possible for DLS and NTA. Electrochemical sizing is concluded to offer significant attractions over light scattering methods.

This work has been published in *Nanoscale*, 2019, Royal Society of Chemistry,[1] and was realised in collaboration with Dr. Christopher Batchelor-McAuley, from Department of Chemistry, University of Oxford and Dr. Neil P. Young, from Department of Materials, University of Oxford. Dr. Batchelor-McAuley helped me with

the experimental design and the interpretation of the results. Dr. Young helped with the TEM measurements of the silver nanoparticles.

4.1. Introduction

Size controls many physical and chemical properties of nanomaterials, including luminescence, catalytic activity and toxicity.[2-4] For nanoparticles (NPs) with well-defined geometries such as spheres or prisms, the particle size can be defined by simple parameters. However, most NPs exhibit a degree of irregularity in their shapes. Moreover, no NP samples contain truly monodisperse particles, which dictates a size distribution for the description of particle populations. Furthermore, efficient and precise sizing measurements of multimodal NP samples are desirable.[5-6] These facts present difficulties in the accurate determination of NP sizes for current analytical techniques based on light scattering.

Dynamic Light Scattering (DLS) and Nanoparticle Tracking Analysis (NTA) have been widely used as established techniques for size measurements of NPs in many fields involving environmental and biological studies.[7-8] As introduced in Chapter 2, both light scattering techniques provide an *in situ* measurement of the hydrodynamic radii of the NPs, assumed spherical. The measured quantities are often larger than the geometric radii. However, while it is well known that DLS can only resolve particles that differ in diameter by at least a factor of 3,[8] many studies have shown that for metal NPs such as silver and gold, the technique tends to yield markedly larger (> 50%) diameters than expected when the particle sizes are small (e.g. < 30 nm).[4, 9-

[13] The latter may in part reflect the significant effects of operational procedures on the measurement accuracy.[14] For NTA, due to individual visualization of particles, the technique has a much better size resolution (of two particles with less than 0.5 fold difference in diameter),[8] but for small NPs it may have difficulty in detecting them depending on the optical properties of the NPs and the type of laser used. This reflects a fourth-power dependence of scattered light intensity on the wavelength of incident light.[15] In addition to further improvements in the mature techniques themselves, this poses a question of how can these small NPs, especially when examined as polydisperse samples, be better sized using other sizing alternatives?

Among all the NP sizing techniques, transmission electron microscopy (TEM) offers excellent resolution in defining the particle size and shape based on projection images. However, TEM only measures samples in high definition when the particles are completely dry and clean. In addition, a recent study using electron tomography shows that even for some of the particles appearing to be almost spherical there is still an overestimation of *ca.* 8% in particle diameter.[16] As introduced in Chapter 2, an emerging technique in recent years, electrochemical particle-impact technique (or 'nano-impacts'), has been demonstrated as a volume-based sizing technique for many kinds of NPs such as metals,[17] organics[18] and polymeric NPs[19] using appropriate electrolytes and applied potentials. Recent developments of the nano-impact method have been reviewed.[20-22] In particular, a systematic quantitative methodology has been established for the technique in sizing NPs.[23] In this work, we aim to compare the electrochemical alternative with the light scattering techniques in sizing small NPs mainly in terms of measurement accuracy. To this end, the nominally '20 nm' and '30

nm'-diameter silver particles are selected and studied in both their individual dispersions as well as a bimodal sample. Insights into the strengths and limitations of the involved techniques are consequently obtained.

4.2. Experimental Section

4.2.1. Chemical reagents

Citrate-capped '20 nm' silver nanoparticles (Ag NPs) were synthesised by J. C. Lees following a seeded growth method as a 0.13 mg/mL particle dispersion containing 2 mM of sodium citrate.[24] The '20 nm' diameter and quasi-spherical shapes have been characterized by high-resolution SEM previously.[25] The '30 nm' silver nanoparticle suspension (NanoXact, 0.02 mg/mL silver, 2 mM sodium citrate) was purchased from NanoComposix, USA. Potassium Chloride (≥ 99.0%) was obtained from Sigma-Aldrich, and tri-sodium citrate (99.0%) from British Drug Houses. Solutions were prepared using deionized water (Millipore) with a resistivity of 18.2 MΩ cm at 298 K.

4.2.2. Electrochemical impacts

The nano-impact (or NI) experiments of both individual ('20 nm' and '30 nm') and mixed sizes were performed using an in-house low noise potentiostat as described previously.[26] Briefly, a low noise current amplifier (LCA-4K-1G, FEMTO Messtechnik GmbH, Germany) was used and filtered using two cascaded analogue RC-filters at 2K Hz. The filtered signal was then digitized at 100 kS s^{-1} via a USB data acquisition device (USB-6003, National Instruments, Texas, US). The low-pass digital filter was set to

100 Hz. The filter design used in this work has been demonstrated to conserve the overall charge transferred in such nano-impact events.[26-27] Current spikes were identified and analysed using a script written in Python 3.5.

The electrochemical measurements were carried out using a lab-built three-electrode system in a Faraday cage with temperature control at 25 °C. A 33 µm diameter[28] carbon disc electrode (IJ Cambria Scientific Ltd, UK) was used as the working electrode. A leakless Ag/AgCl (in 3.0 M KCl, eDaq) electrode was used as the reference electrode (+ 0.210 V vs. SHE), and a 0.5 × 4 × 8 mm^3 platinum mesh (Goodfellow, Cambridge, UK) as the counter electrode. The two silver particle dispersions, '20 nm' and '30 nm', were diluted and mixed with potassium chloride solution to a same particle concentration of 6 pM and 20 mM of KCl. The bimodal sample of '20 + 30 nm' was obtained by physically mixing the two stock individual samples with the chloride and citrate solution in a ratio that results in equal particle concentrations of 6 pM and 1.8 mM of citrate, 20 mM of KCl. Then chronoamperometry, with a step potential of + 0.80 V vs. Ag/AgCl for 60 seconds per scan, was performed to detect the particle impacts at the working electrode immersed in the three dispersions described above. The carbon microdisc electrode was polished between each scan with 0.3, 0.05 µm sized alumina in sequence and rinsed with deionized water.

4.2.3. Dynamic Light Scattering

The '20 nm' and '30 nm' particle diameter distributions with a concentration of 24 pM in 1.8 mM citrate were measured using a Nano ZS zetasizer system (Malvern Instruments). Measurement conditions mainly includes an irradiation wavelength of

632.8 nm (He laser) at a fixed backscatter angle of 173°, an equilibration time of 120 s, a measurement temperature of 298 K, a viscosity of 0.89 cP and refractive index of 1.3325 (of de-ionized water).[29] Prior to the measurement, the silver dispersions were filtered through a 0.22 µm polyvinylidene fluoride (PVDF) membrane. Three measurements of 10-20 scans each were performed for each sample in general purpose algorithm (with normal resolution). A forward scattering angle of 13° and a multiple narrow algorithm (with high resolution) was also attempted.

4.2.4. Nanoparticle Tracking Analysis

Nanoparticle Tracking Analysis (NTA) was performed using a NanoSight LM10 (NanoSight, UK), equipped with a sample chamber with a 405 nm or 642 laser. The samples were diluted to a concentration of *ca.* 1 pM and injected in the sample chamber with sterile syringes (BsD Discardit II, New Jersey, USA). All measurements were performed for five times at a temperature of 23.0 ± 1.0 °C. The samples were measured for 60 s with automatic exposure settings at 30 frames per second. The software used for video capture and data analysis was NTA 2.3. Dr. Tom Dennison and Mr. Liam Cole of Malvern Analytical are thanked for the NTA measurements using the 405 nm laser.

4.2.5. Transmission Electron Microscopy

The nominally '20 and 30 nm' silver nanoparticles were imaged by transmission electron microscopy (TEM) using a JEOL JEM-3000F instrument with an accelerating voltage of 300 kV. Imaging magnification was 120 to 300 thousandfold (kX). Samples

were prepared by drop-casting the nanoparticle suspensions (diluted 1/10 fold of the original stock suspension to 0.013 mg/mL Ag NPs, 0.2 mM sodium citrate for the '20 nm' particles; as-received 0.02 mg/mL Ag NPs, 2 mM sodium citrate for the '30 nm' particles) onto carbon grids (Agar Scientific) and allowing these to dry in air. Dr. Neil Young is thanked for operating the TEM for the acquisition of the images. Size information was subsequently extracted using ImageJ software.

4.3. Results and discussion

The diameters of Ag NPs were first measured using TEM to provide values of the diameters for the individual '20 nm' and '30 nm' samples. Next, to investigate how accurately the established in situ methods can size these small particles, the two NP dispersions were measured by NTA and DLS. As reported below, we find that both light scattering techniques measured diameters of 5-20% larger for the '30 nm' particles than the TEM reference values yet over 50% larger for the '20 nm' sample. To approach the question of how the electrochemical alternative performs in sizing these small NPs, the nano-impact (or NI) method is then applied to study the individual samples and further to investigate a mixed sample of the two particle sizes. The electrochemical measurements show an accuracy of within 5% error of the TEM results for both individual and the bimodal sizing. Advantages of the nano-impact methodology over the other involved techniques are discussed.

4.3.1. TEM analysis

TEM measurements were conducted for the silver NPs of both sizes. With high magnification of 120 to 300 kX, TEM images of '20 nm' (N=123) and '30 nm' (N=110) silver particles were obtained as shown in Figure 4.1. It was observed that for both sizes most particles appear to be quasi-spherical. As such, 2D areas of the particles were measured using a freehand tool for outlining the particle boundaries[30] and then converted to effective geometric diameters, where the median values were measured as 18.5 ± 0.3 nm and 28.9 ± 0.5 nm for later direct comparison (See Table 4.1). The standard deviations represent the measurement uncertainty as from defining the particle boundaries in the TEM images and were determined as 0.3 and 0.5 nm on average for the '20 nm' and '30 nm' particles respectively. This error estimation is described in detail in Appendix Section 1. This measurement uncertainty is of importance as compared to the other errors of typically some 0.5 nm (Table 4.1) in diameter obtained from reproducibility and would be more significant for images with lower resolution.

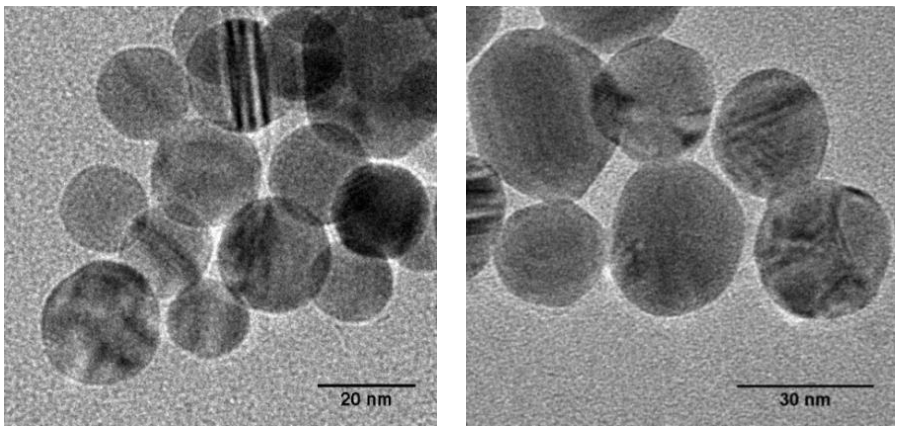

Figure 4.1. TEM images of the '20 nm' (left) and '30 nm' (right)-diameter silver particles.

4.3.2. Light scattering measurements

NTA measurements were performed to measure the diameters of the NPs in dispersions. This *in situ* technique uses a laser as the light source, illuminating the suspended particles to scatter light and allow individual entities to be visualized, tracked and analyzed. According to the Rayleigh Scattering theory, the scattered light intensity of NPs is inversely proportional to the fourth power of the wavelength of the laser.[15] Moreover, the light scattering of the metallic NPs is significantly affected by surface plasmon resonance (SPR). As such, the type of laser is crucial for these very small particles to be detected. Herein, a 642 nm and a 405 nm laser were used to study the two samples. It is noted that the 642 nm laser is commonly used in NanoSight instruments while the wavelength of 405 nm, which is also commercially available, is near the SPR wavelength of the silver NPs.[31] Diameter distributions (Figure 4.2) and the median diameters (Table 4.1) were obtained; the number of tracks per measurement was also recorded to represent the data statistics.

When using the 642 nm laser, few '30 nm' particles were observed in the microscopic view and consequently around 150 tracks per measurement were recorded with a measured median diameter as large as 49.6 ± 2.5 nm. Then using a 405 nm laser, approximately 18,000 tracks per measurement were measured and the diameter distribution of the '30 nm' particles is in overall good agreement with the TEM results though slightly larger (5%) than the reference values, considering that a hydrodynamic radius is often larger than the geometric radius of a particle. The significantly larger number of detected particles is due to far more scattered rays measured when using the shorter-wavelength laser.[15] For the smaller '20 nm'

particles, changing to use the 405 nm laser led the number of tracks to increase from *ca.* 100 to 5000 per measurement. Accordingly, the results of the median diameters showed, a decrease from 44.2 ± 1.6 nm to 27.8 ± 0.4 nm that is, however, still much larger (9 nm) than that of the TEM results. Although the technique measures hydrodynamic diameters, this 50% discrepancy is too significant to render the result accurate. It follows that the NTA is able to accurately measure the '30 nm' silver particles with the 405 nm laser but unable to do so for the smaller '20 nm' sample.

Next, the other light scattering technique DLS (equipped with a 633 nm laser) was used to size the particles. The technique measures the intensity fluctuation of scattered light of particle ensembles without the requirement of them being visualized individually as in NTA,[8] and thus is likely more sensitive in sizing small NPs. The intensity diameter distributions were obtained and herein converted to cumulative (intensity) frequency against diameter as shown in the Figure 4.2; conversion from the intensity plots to number- or volume-based diameter distribution can be significantly erroneous due to the inherent peak broadening of the intensity distributions[32]. Z-average diameters (i.e. intensity-weighted harmonic mean diameter) were measured, which can be expressed as[33]

$$D_z = \frac{\sum S_i}{\sum(\frac{S_i}{D_i})} \tag{4.1}$$

where D_z is the z-average diameter, S_i is the scattered light intensity from particle i and D_i is the diameter of particle i. Polydispersity indices (PDI) of the two samples were also recorded (Table 4.1).

Table 4.1. Summary of the sizing results of the four techniques for the '20 nm' and '30 nm'-diameter Ag NPs and their mixture.

Techniques	Measured Diameters (nm)/ Median Diameters (nm)[a)]	'20 nm'	'30 nm'	'20 + 30 nm'
DLS	Z-average diameter (nm)	31.1 (PDI = 0.222)[b)]	34.7 (PDI = 0.116)	×[c)]
	$d_{Intensity\ median}$ (nm)	**31.5 ± 0.8[b)]**	**34.7 ± 0.2**	
NTA	Modal diameter(nm)	26.6 ± 8.5	30.0 ± 6.0	×
	d_{median} (nm)	**27.8 ± 0.4**	**30.4 ± 0.1**	
TEM	Mean diameter (nm)	19.0 ± 4.2	29.2 ± 4.8	-
	d_{median} (nm)	**18.5 ± 0.3**	**28.9 ± 0.5**	
NI	Mean diameter (nm)	19.2 ± 3.9	30.2 ± 7.5	√[c)]
	d_{median} (nm)	**18.3 ± 0.5**	**28.7 ± 0.6**	

[a)] ('d_{median}' means the measured 'median diameters') [b)] (There are two types of standard deviations – the upper-row ones represent the width of the measured diameter distribution (otherwise, PDI is used for DLS results), while the lower-row ones indicate the reproducibility of the median diameters) [c)] ('√ or ×' means being able or not to discriminate the bimodal sample)

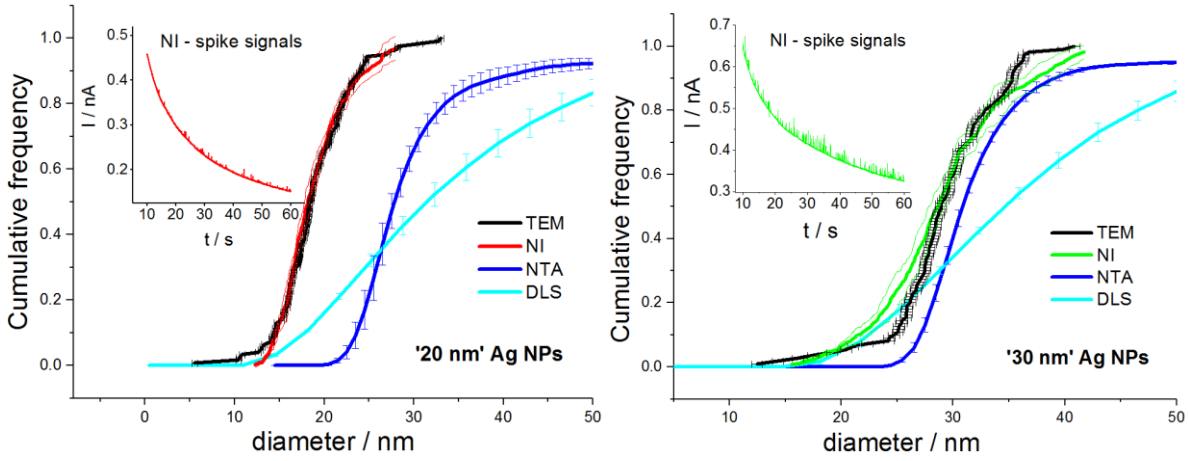

Figure 4.2. Inter-technique sizing comparison in cumulative frequency against diameter for the '20 nm' and '30 nm' silver particles in aqueous dispersions containing 20 mM KCl and 1.8 mM citrate. The inlay figures are chronoamperomogram examples (at + 0.8 V vs. Ag/AgCl, duration 60 seconds) with nano-impact (NI) spike signals for oxidation of the 6 pM '20 nm' (red) and '30 nm' (green) silver particles, respectively. Thin lines or error bars alongside the mainstream sizing curves denote the corresponding measure of uncertainty.

For the '30 nm' silver particles, DLS measured diameters of 6 nm (or 20%) larger than the reference value, which may reflect the measurement of a hydrodynamic quantity. A diameter distribution *shift* towards larger sizes is expected owing to a sixth-power dependence of scattered light intensity on the particle diameter.[15] Meanwhile, the PDI shows a narrow diameter distribution for the '30 nm' particles of 11.8 nm in width assuming a Gaussian distribution. However, for the '20 nm' particles there is a vast overestimation of 70% larger in the measured diameter than TEM while the diameter distribution is significantly biased towards larger sizes. It is noteworthy that that several studies have shown that for the DLS measurements of nanoparticles of a small size (e.g. 10 ~ 20 nm in diameter), a high particle concentration such as of the order of nanomolar (nM) may be essential for obtaining an accurate diameter distribution.[14, 34] Therefore, the NP sizes of the colloids with a particle concentration ranging from 6 pM to 4.8 nM were measured (see Appendix Section 2 for the details). However, the measured average diameters were shown to be still no less than 28 nm (corresponding to a 40% error) across this wide concentration range. Even so, the sizing results for the '20 nm' sample are in general agreement with other literatures[11-13] where typically an overestimation of over 50% in measured diameter is observed for silver particles of very small diameters (e.g. 10-20 nm). Therefore, the DLS measurements are able to size the '30 nm' sample but not the '20 nm' particles.

4.3.3. Electrochemical measurements

Having recognized the limited accuracy of the light scattering measurements, we next performed nano-impact (NI) experiments to size the two monomodal samples. A carbon microdisc electrode was immersed in a 20 mM KCl solution containing 6 pM

'20 nm' or '30 nm' silver nanoparticles and 1.8 mM citrate. At a step potential of + 0.8 V (vs. Ag/AgCl), five 60-second chronoamperograms were collected each for '20 nm' and '30 nm' silver particles (see the inlay of Figure 4.2), where 477 and 1203 spike signals were identified, respectively. The filter design used in this work has been demonstrated to conserve the overall charge transferred in such nano-impact events.[26-27] Consequently, the oxidative charge per impact event is then converted to number of silver atoms *via* Faraday's 1st law. The oxidative charge per impact event is converted to the number of silver atoms per particle *via* Faraday's 1st law. Specifically, if Q is the spike charge obtained by integrating current with time and carefully defining a baseline,[23] then

$$Q = Ne$$

where e is the electronic charge (1.60×10^{-19} C) and N is the number of silver atoms in the nanoparticle. This number is independent of the shape of the particle and the technique provides no shape information. However, it is possible to define an 'effective' diameter (d) of a perfect sphere containing the same number of atoms and having the same density, ρ in g m^{-3}, as bulk silver (10.5×10^{6} g m^{-3}),

$$\rho = \frac{\frac{N}{N_{Av}} \times A_r(Ag)}{\frac{4}{3}\pi\left(\frac{d}{2}\right)^3}$$

where N_{Av} is the Avogadro constant and $A_r\ (Ag)$ is the relative atomic mass of silver (107.9 g mol^{-1}). As such, the particle diameter distributions in form of cumulative frequency (i.e. normalized cumulative number of spikes) as a function of diameter were obtained. However, to obtain a 'true' diameter distribution, the impact data is first windowed to statistically reveal authentic numbers of spikes,[16] and then

weighted for diffusion to eliminate the effect of unequal probabilities of detecting the particles owing to their size-dependent mobility (See Appendix Section 3).[23] As a result, 443 ('20 nm') and 932 ('30 nm') spikes were confirmed as single features and the windowed- and weighted- diameter distributions were depicted in the Figure 4.2 with measured diameters in Table 4.1. The thin lines alongside the mainstream, thick sizing curves represent the standard deviations of the experimental reproducibility.

As depicted in Figure 4.2 (enlarged in Figure 4.3), the spike height of the '30 nm' impacting particles is observed nearly three times high as that of the '20 nm' sample. This ratio is the same as that for their impact charges, due to the sufficiently fast electrode kinetics at the applied high overpotential (η = 0.6 V) and thereof to similar durations of the spikes 18 ± 9 ms ('20 nm') and 22 ± 11 ms ('30 nm'). In terms of impact frequency, it was observed that the smaller '20 nm' particles, however, have a lower impact frequency than the '30 nm' particles. In the diffusion-only regime of particle movements in solution, the flux of NPs towards electrode surface is affected by the size of the particles as discussed above. However, the particles might not be immediately oxidized upon arrival given that the initiation of the oxidation events depends on the quality of electrical contact between the impacting particles and the electrode, which may be largely affected by the surface chemistry of the NPs and the electrolyte species and concentration.[35]

As seen from the Figure 4.2, the electrochemical measurements show excellent agreement with the TEM reference diameters for both '20 nm' and '30 nm' silver

samples. More precisely, the median diameters were measured as 18.3 ± 0.5 nm and 28.7 ± 0.6 nm for the '20 nm' and '30 nm' particles respectively, which both merely differ by 0.2 nm in diameter from the reference values. To facilitate the comparison of diameter distributions, D10, D25, D50, D75 and D90 percentile values of the TEM and electrochemical sizing curves were used to acquire a measure of accuracy. As a result, the nano-impact diameter distributions are within 2.0% error on average of the TEM results for the '20 nm' particles and within 5.4% error for the '30 nm' particles. In addition, the corresponding standard deviations as from the experimental reproducibility were found to be within less than 3.0% of the average diameters. It is thus concluded that the electrochemical technique provided highly accurate (< 5% error in effective diameters) sizing measurements of these small nanoparticles.

Building on the success of the accurate sizing of the individual NP dispersions, the nano-impact technique was further applied to size a bimodal sample of a mixture of the '20 nm' and '30 nm' Ag NPs. The carbon microdisc electrode was immersed in the 20 mM KCl solution containing deliberately mixed 6 pM '20 nm' and 6 pM '30 nm' silver nanoparticles with 1.8 mM citrate. Under the same conditions, five chronoamperograms were collected with 1391 spikes and then after windowing 1234 spikes. Figure 4.3c shows one chronoamperogram with nano-impact spikes for the bimodal sample. For ease of comparison, examples of the spikes for the individual samples are provided in Figure 4.3a& 3b. The impact frequencies of the '20 nm', '30 nm' and mixed '20+30 nm' particles are 1.5 s^{-1}, 3.1 s^{-1} and 4.1 s^{-1}, respectively. The cumulative frequency as a function of diameter is plotted as shown in Figure 4.3d for

the three experimental cases and the predicted mixture which is derived from the frequency-weighted sum of the two individual sizes.

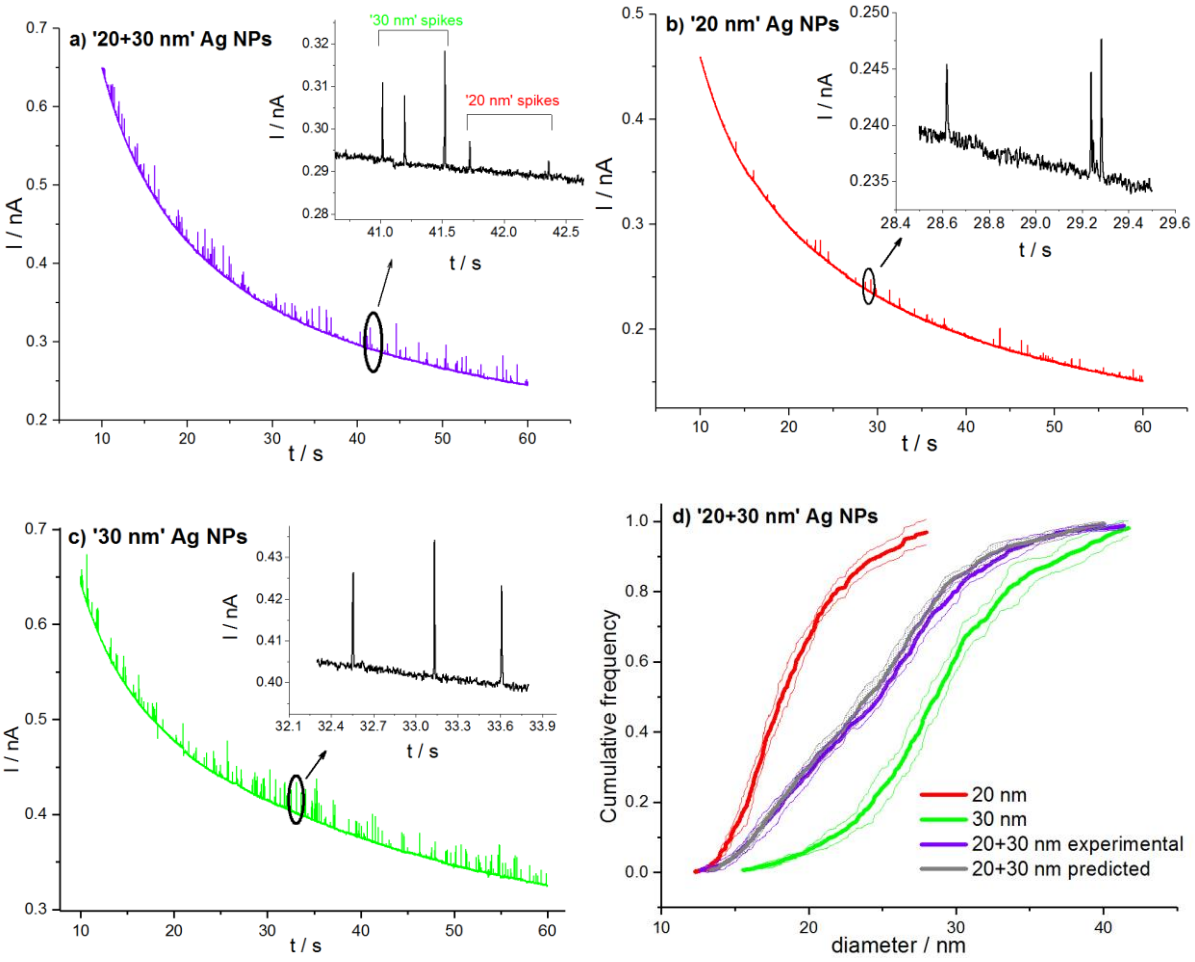

Figure 4.3. a) Chronoamperomograms at + 0.8 V vs. Ag/AgCl with a duration of 60 seconds show nano-impact spikes signals for the oxidation of the bimodal sample containing 20 mM KCl and 1.8 mM citrate. The enlarged figure show concurrent detection of the two distinct kinds of spikes. Similarly, the spike data are presented for the individual b) '20 nm' and c) '30 nm' samples. d) Nano-impact sizing curves for the individual '20 nm' (red), '30 nm' (green) particles, the mixed '20+30 nm' (violet) sample and the predicted diameter distribution for the mixture (gray). Thin lines alongside each thick curve denote the standard deviation of the measured diameters.

Figure 4.3 show that the two kinds of spikes for the individual '20 nm' and '30 nm' samples are observed together in the chronoamperograms of the bimodal sample. The measured diameter distribution lies in the middle of the two sizing curves for the individual samples with a median diameter of 24.8 ± 0.5 nm. An excellent agreement between the experimental curve and the predicted is observed. More precisely, by comparing the five D10-90 percentile values of the two diameter distributions for the mixture, the experimental results show an error of less than 2.0% of the predicted. In terms of impact frequency the '30 nm' sample rather than the bimodal sample appears to have the most spike signals. However, statistical analysis based on a Poisson distribution (see Appendix 3) reveals a number of 27% fewer single impact events by the data windowing as it was observed that many spikes came out so close that they are considered as single impact events composed of multiple collisions. Consequently, the '30 nm' sample actually has a lower impact frequency than the bimodal sample, and the measured and predicted impact frequencies, as being 4.1 and 4.6 s^{-1} respectively are consistent. It is concluded that the electrochemical detection and sizing measurements are able to discriminate two 10-nm-different sizes in high accuracy and are thereof essentially independent of the particle size polydispersity.

In terms of the measurement principle, nano-impacts have advantages over the other techniques to efficiently provide accurate information on particle sizes. It is highlighted that the electrochemical technique is a volume-based method as it *in situ* measures the total number of electrons transferred of each single particle upon collision at the electrode-solution interface. Subsequently, the charge data is, regardless of the particle shape, converted to a precise number of constituent atoms thus giving its

effective diameter for a perfect sphere containing the same number of atoms ($Q \propto d^3$). This, therefore, serves as a solid basis of discriminating particles of very similar sizes. One major requirement for such precise size determination is complete electrolysis of nanoparticles at the three phase boundary formed on impacts. Depending on the particle identity, this requires identification of suitable electrolyte species and their concentrations and the necessary potential applied. Specifically, previous research shows, under those conditions, an upper sizing limit of *ca.* 50 nm for silver NPs[36] but that 100 nm-diameter AgCl NPs can be readily sized.[37] To date, many metallic NPs (e.g. Cu,[38] Ni,[39-40] Au[41-42]), metal salt NPs (e.g. AgCl,[37] Hg_2Cl_2[43]), organic NPs (e.g. indigo[18]) and polymeric NPs (e.g. poly(*N*-vinylcarbazole)[19]) have been shown to undergo complete oxidation or reduction, or oxidative doping respectively, allowing accurate nano-impact sizing of themselves.

As to TEM measurements, size information tends to be skewed by the significant assumption based on 2D cross-section images especially for the particles with high irregularity. To obtain true volumes, electron tomography is required.[16] DLS and NTA techniques quantifying particulate movements in bulk are only able to measure hydrodynamic radii based on the Stoke-Einstein law assuming equivalently diffusing perfect spheres. They are unable to provide any related shape information. DLS is complex to interpret for non-spherical particles because of the need to quantify the contribution of rotational diffusion, although the electric birefringence methods can offer size distributions of non-spherical particles if a shape is assumed.[44] Also in many cases, the precise difference between a particle's hydrodynamic diameter and geometric diameter is difficult to know considering the uncertain effects of the often

used capping agents in NP systems. It is also well known that DLS can only resolve a diameter difference of two particles of at least a factor of 3. Even in presence of tiny portions (e.g. 5%) of larger particles smaller NPs are not possible to be detected; [8, 34] NTA heavily relies on a short-wavelength laser for smaller particles that is often inaccessible, both of which essentially root in the intrinsic scattering principle of these techniques. Therefore, especially in the case of sizing small, multimodal NPs, nano-impacts largely excel the light scattering techniques.

4.4. Conclusions

Accurate NTA sizing measurements require a shorter-wavelength 405 nm laser for the detection of the individual '30 nm' silver particles, while DLS shows biased diameter distributions for these particles towards larger sizes with 20% overestimation in diameter. Neither light scattering technique is able to accurately size the smaller '20 nm' particles. Moreover and fundamentally, these techniques only measure in hydrodynamic terms neglecting any shape information. In contrast, nano-impacts accurately measure geometric diameters in terms of the number of constituent atoms for *both* '20 nm' and '30 nm' particles. This electrochemical technique has further revealed its advantages as a volume-based method that is able to resolve these similar sizes in high accuracy, whereas due to inherent limitations of light scattering measurements this is not possible for the DLS and NTA. On these bases, we conclude that the nano-impact technique is an alternative, accurate way of sizing both nearly mono- and poly-disperse NP samples in the small-size range; particles as small as 4 nm have been successfully sized.[26]

Appendices

1. Uncertainty quantification of defining the particle boundary in TEM sizing

Limited resolution of TEM images leads to uncertainty in defining a particle's boundary, resulting in associated errors. This can be quantified by error function fitting on the intensity profile of the images. Specifically, the intensity profile as a function of distance was shown in Figure 4.4a, along the straight, yellow line drawn across a chosen '20 nm' particle in an image with a pixel size of 0.148 nm (corresponding to a magnification of 150 kX) as an example. One steep drop and then a sharp rise in the intensity curve at the particle boundaries were observed. Next, in the OriginPro 2017, a normal cumulative distribution function as described below was used as the error function and to fit the steep changes (the red curve).

$$y = y_0 + A\int_{-\infty}^{x} \frac{1}{\sqrt{2\pi}w} e^{-\frac{(t-x_c)^2}{2w^2}} dt \tag{4.2}$$

where y_0 is the offset in y direction, A is the amplitude of the curve, and x_c is the mean value and w is the standard deviation (STD). As illustrated in the Origin software, the standard deviation w is associated with the steepness of the amplitude change of the intensity curve as an equation is given that the inter-quarter range (IQR) in x axis, $IQR_x = 1.349\ w$, so the slope $\approx \frac{IQR_y}{IQR_x} = \frac{0.5\ A}{1.349\ w}$, and thus $w \propto \frac{1}{\text{slope}}$. This is consistent with the concept that the steeper the change, the less the uncertainty it has for defining a particle's boundary. As a result, the STDs for the left drop and the right rise in Figure 4.4a were 0.131 ± 0.099 nm and 0.091 ± 0.107 nm respectively, corresponding to one pixel size or so. Furthermore, to obtain a statistical measure of

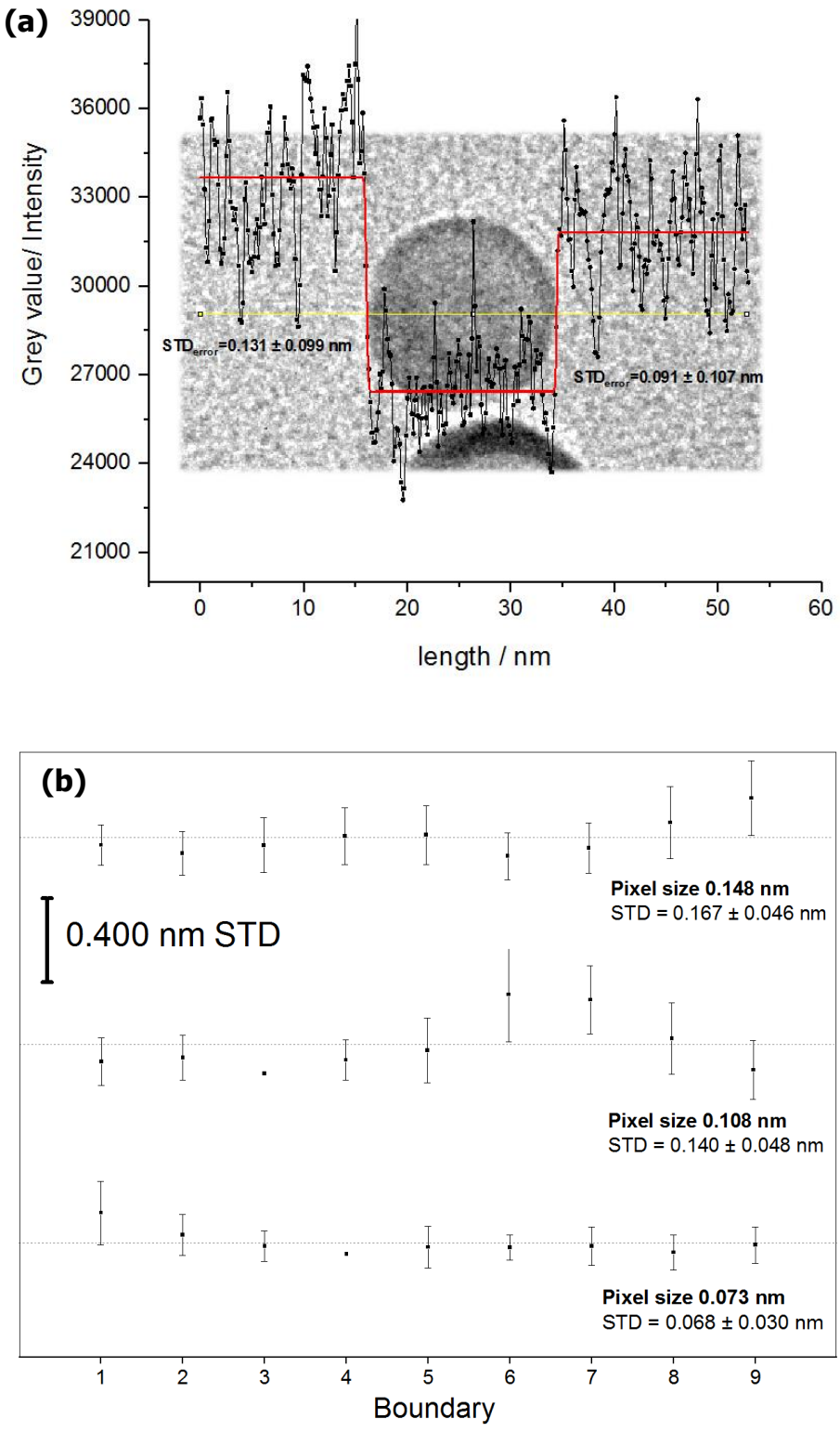

Figure 4.4. a) Representative superimposed TEM image of one '20 nm' silver particle with the intensity profile (black scatter + line) analysis along the yellow line. The red line represents the error function fitting, giving the standard deviation of defining the boundary position. b) Error analysis upon the TEM sizing for the images with different pixel sizes (0.148 nm, 0.108 nm and 0.073 nm).

the uncertainty for a fixed pixel size, 9 boundaries in total across a particle were analysed in the same way and the average were determined as the final uncertainty for this pixel size. As seen from the Figure 4.4b, the standard deviation ascends with increasing pixel size or decrease in image definition. For the '20 nm' silver particles, such measurement uncertainty was analysed for the TEM images of all the three pixel sizes 0.148 nm, 0.108 nm and 0.073 nm. As such, the mean STD was determined as 0.139 ± 0.028 nm, corresponding to 1.5 % error in diameter. Likewise, for the '30 nm' particles the 1D measurement uncertainty was found to be 1.6 %.

2. Concentration scaling for the DLS sizing

The stock dispersion with a concentration of as-synthesised 4.8 nM and the 2, 6, 10, 40, 100, 200, 400, 800-fold diluted dispersions were sized. Accordingly the Z-average diameters were recorded as shown in Fig 4.5. The figure shows an average mean diameter of 30.5 ± 1.5 nm from 12 pM to 2.4 nM, whereas *ca.* 10 nm higher measured diameters were observed for the 6 pM and the 4.8 nM samples. The latter may be explained that in the 6 pM dispersion the light scattered is so weak that the resulting low count rates of around 150 kcps (or 'thousand counts per second') and G1 correlation function intercepts of < 0.8 failed to interpret out a meaningful Z-average diameter. Note that the dense particles in the 4.8 nM dispersion probably results in multiple scattering that biases the results. Therefore, the experimentally measured diameters for the '20 nm' silver particles by DLS were confirmed as *ca.* 30 nm. Similarly, the average diameter of the nominally '30 nm' silver particles was determined as 34.5±0.3 nm from two particle concentrations, 24 pM and as-received 216 pM.

Consequently, it is shown that likely improvements in the measurement accuracy with a higher particle concentration does not apply to our silver nano-systems.

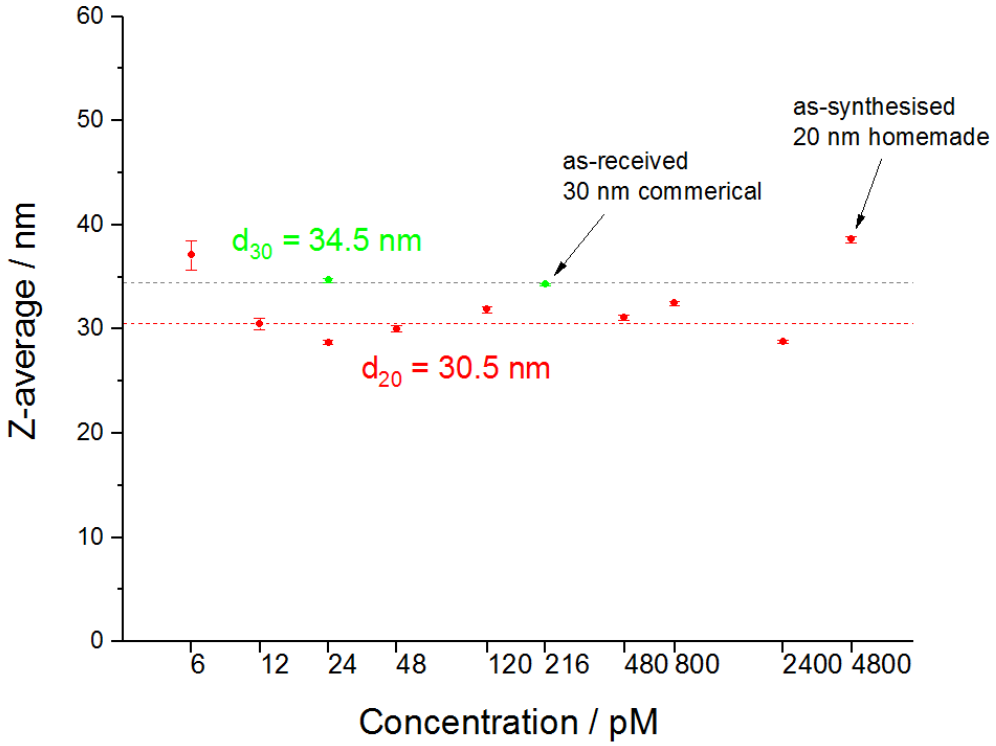

Figure 4.5. DLS sizing of the '20 nm' (red) and '30 nm' (green) Ag NPs with concentrations 6 to 4800 pM with near no salt presence (< 2 mM citrate).

3. Effects of windowing and weighting on the nano-impact sizing results

The measured spike signals need to be processed to reveal the 'true' diameter distributions by two-fold considerations based on the particulate motion in the dispersion. First, there is the question of the simultaneous collisions of two or more particles with the electrode and being detected at the same time. To statistically study the spike datasets, we define a time window during which only one impact event is allowed with 99% confidence. This can be quantified by probability theory of a Poisson

distribution. Under the assumption of independent impact events, a model of Poisson distribution as follows is provided,

$$P(k = \lambda t) = e^{-\lambda} \frac{\lambda^k}{k!} \tag{4.3}$$

where P is the probability, k is the number of events in a certain time interval t, and λ is the average occurrence rate of such events. Next, to calculate the time window t, assuming a steady-state diffusion flux of the particles to the microdisc electrode,[45]

$$J = 4\ D\ c\ r \tag{4.4}$$

where J is the steady-state flux (s^{-1}), D and c is the diffusion coefficient ($m^2\ s^{-1}$) and particle concentration (m^{-3}) of the nanoparticles, respectively, r is the microelectrode radius (m^{-1}). Herein, the calculated flux J is the average occurrence rate λ in the Poisson distribution equation. As a result, there would be 99% probability of up to one impact event that would occur within a time interval of 36 ms. Any two or more spikes detected within this time period were clustered as single features and their charges were summed. Similarly, such a time window was found to be 21 ms for the '20 nm' particles. Second, smaller particles move faster thus having higher probability of colliding with the electrode. Therefore, the windowed diameter distributions are further weighted for diffusion based on the diffusion coefficients of the individual particles. As a result, the Figure 4.6 shows that the impact frequencies of both samples stay almost unchanged; however, the charges of the larger '30 nm' sample increase to a larger extent as many spikes were observed occurring over twice within the window size of 36 ms due to its high impact frequency. In this way, the windowing effectively combines multiple impact signals that originate very likely from single impact event and reveals the 'true' sizes of the samples.

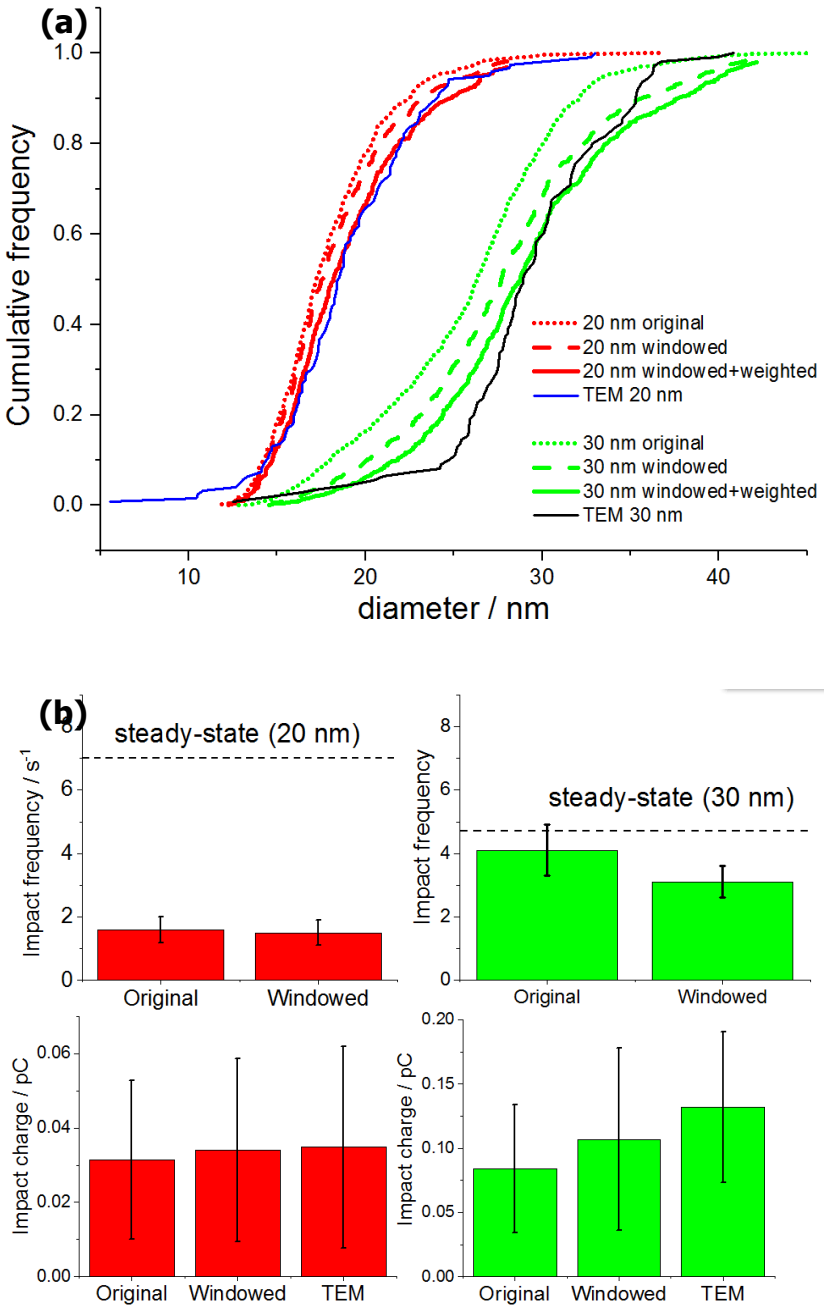

Figure 4.6. a) Cumulative frequency diameter distribution for nano-impact events of the '20 nm' and '30 nm' silver particles. Red dotted, dashed and solid lines represent the original (or not windowed) data of the '20 nm' silver particles, while the green lines are for the '30 nm' particles. Blue and black solid lines denote TEM sizing curves for the '20 and 30 nm' particles respectively. b) The second group of figures show impact frequencies before and after windowing for the '20 nm' (red) and '30 nm' (green) silver particles, with predicted steady-state frequencies shown as the dotted black lines; and impact charges before and after windowing as compared to the charges derived from TEM results.

References

[1] R. Xie, C. Batchelor-McAuley, N. P. Young, R. G. Compton, *Nanoscale* **2019**, *11*, 1720-1727.

[2] K. L. Kelly, E. Coronado, L. L. Zhao, G. C. Schatz, *J. Phys. Chem. B* **2003**, *107*, 668-677.

[3] X. Zhou, W. Xu, G. Liu, D. Panda, P. Chen, *Journal of the American Chemical Society* **2009**, *132*, 138-146.

[4] S. Kim, D. Y. Ryu, *Journal of Applied Toxicology* **2013**, *33*, 78-89.

[5] F. Laborda, E. Bolea, G. Cepriá, M. T. Gómez, M. S. Jiménez, J. Pérez-Arantegui, J. R. Castillo, *Analytica chimica acta* **2016**, *904*, 10-32.

[6] M. Gaumet, A. Vargas, R. Gurny, F. Delie, *Eur. J. Pharm. Biopharm.* **2008**, *69*, 1-9.

[7] S. K. Brar, M. Verma, *TrAC Trends in Analytical Chemistry* **2011**, *30*, 4-17.

[8] V. Filipe, A. Hawe, W. Jiskoot, *Pharm. Res.* **2010**, *27*, 796-810.

[9] F. Meli, T. Klein, E. Buhr, C. G. Frase, G. Gleber, M. Krumrey, A. Duta, S. Duta, V. Korpelainen, R. Bellotti, *Meas. Sci. Technol.* **2012**, *23*, 125005.

[10] P. Eaton, P. Quaresma, C. Soares, C. Neves, M. de Almeida, E. Pereira, P. West, *Ultramicroscopy* **2017**, *182*, 179-190.

[11] M. Ahamed, R. Posgai, T. J. Gorey, M. Nielsen, S. M. Hussain, J. J. Rowe, *Toxicol. Appl. Pharmacol.* **2010**, *242*, 263-269.

[12] S. A. Cumberland, J. R. Lead, *J. Chromatogr. A* **2009**, *1216*, 9099-9105.

[13] G. Singhal, R. Bhavesh, K. Kasariya, A. R. Sharma, R. P. Singh, *J. Nanopart. Res.* **2011**, *13*, 2981-2988.

[14] D. Langevin, O. Lozano, A. Salvati, V. Kestens, M. Monopoli, E. Raspaud, S. Mariot, A. Salonen, S. Thomas, M. Driessen, *Nanoimpact* **2018**, *10*, 97-107.

[15] H. Moosmüller, W. P. Arnott, *J. Air Waste Manage. Assoc.* **2009**, *59*, 1028-1031.

[16] C. A. Little, C. Batchelor-McAuley, N. P. Young, R. G. Compton, *Nanoscale* **2018**, *10*, 15943-15947.

[17] Y. G. Zhou, N. V. Rees, R. G. Compton, *Angew. Chem.* **2011**, *123*, 4305-4307.

[18] W. Cheng, X. F. Zhou, R. G. Compton, *Angew. Chem.* **2013**, *125*, 13218-13220.

[19] X. F. Zhou, W. Cheng, R. G. Compton, *Angewandte Chemie* **2014**, *126*, 12795-12797.

[20] S. V. Sokolov, S. Eloul, E. Kätelhön, C. Batchelor-McAuley, R. G. Compton, *Phys. Chem. Chem. Phys.* **2017**, *19*, 28-43.

[21] K. J. Stevenson, K. Tschulik, *Curr. Opin. Electrochem.* **2017**, *6*, 38-45.

[22] T. Albrecht, S. Horswell, L. Allerston, N. Rees, P. Rodriguez, *Curr. Opin. Electrochem.* **2017**, *7*, 138-145.

[23] C. A. Little, R. Xie, C. Batchelor-McAuley, E. Kätelhön, X. Li, N. P. Young, R. G. Compton, *Phys. Chem. Chem. Phys.* **2018**, *20*, 13537-13546.

[24] Y. Wan, Z. Guo, X. Jiang, K. Fang, X. Lu, Y. Zhang, N. Gu, *J. Colloid Interface Sci.* **2013**, *394*, 263-268.

[25] J. C. Lees, J. Ellison, C. Batchelor - McAuley, K. Tschulik, C. Damm, D. Omanović, R. G. Compton, *ChemPhysChem* **2013**, *14*, 3895-3897.

[26] C. Batchelor-McAuley, J. Ellison, K. Tschulik, P. L. Hurst, R. Boldt, R. G. Compton, *Analyst* **2015**, *140*, 5048-5054.

[27] E. Kätelhön, E. E. Tanner, C. Batchelor-McAuley, R. G. Compton, *Electrochim. Acta* **2016**, *199*, 297-304.

[28] Whilst the commercial working electrode is labelled as 33 μm in diameter, on calibration it exhbits 39.8 ± 0.6 μm. The measured value is later used in calcualtion of theoretical diffusion flux for the NPs.

[29] R. LeBel, D. Goring, *J. Chem. Eng. Data* **1962**, *7*, 100-101.

[30] In the TEM data analysis, a freehand tool in the ImageJ software was used to draw boundaries along the particle edges in the 2D images. As without any restrictions on the drawn shape it allows precise particle area to be measured.

[31] K. Ngamchuea, R. O. Clark, S. V. Sokolov, N. P. Young, C. Batchelor - McAuley, R. G. Compton, *Chem. Eur. J.* **2017**, *23*, 16085-16096.

[32] J. Stetefeld, S. A. McKenna, T. R. Patel, *Biophysical reviews* **2016**, *8*, 409-427.

[33] (1) International Standard ISO13321 Methods for Determination of Particle Size Distribution Part 8: Photon Correlation Spectroscopy, International Organisation for Standardisation (ISO) 1996. (2) International Standard ISO22412 Particle Size Analysis – Dynamic Light Scattering, International Organisation for Standardisation (ISO) 2008.

[34] E. Tomaszewska, K. Soliwoda, K. Kadziola, B. Tkacz-Szczesna, G. Celichowski, M. Cichomski, W. Szmaja, J. Grobelny, *J. Nanomater.* **2013**, *2013*, 60.

[35] K. Ngamchuea, R. O. Clark, S. V. Sokolov, N. P. Young, C. Batchelor - McAuley, R. G. Compton, *Chemistry-A European Journal* **2017**, *23*, 16085-16096.

[36] C. A. Little, X. Li, C. Batchelor-McAuley, N. P. Young, R. G. Compton, *J. Electroanal. Chem.* **2018**, *823*, 492-498.

[37] T. R. Bartlett, S. V. Sokolov, R. G. Compton, *ChemistryOpen* **2015**, *4*, 600-605.

[38] B. Haddou, N. V. Rees, R. G. Compton, *Phys. Chem. Chem. Phys.* **2012**, *14*, 13612-13617.

[39] E. J. Stuart, Y.-G. Zhou, N. V. Rees, R. G. Compton, *Rsc Advances* **2012**, *2*, 6879-6884.

[40] Y.-G. Zhou, B. Haddou, N. V. Rees, R. G. Compton, *Phys. Chem. Chem. Phys.* **2012**, *14*, 14354-14357.

[41] A. L. Suherman, G. Zampardi, S. Kuss, E. E. Tanner, H. M. Amin, N. P. Young, R. G. Compton, *Phys. Chem. Chem. Phys.* **2018**, *20*, 28300-28307.

[42] D. Qiu, S. Wang, Y. Zheng, Z. Deng, *Nanotechnology* **2013**, *24*, 505707.

[43] T. R. Bartlett, C. Batchelor - McAuley, K. Tschulik, K. Jurkschat, R. G. Compton, *ChemElectroChem* **2015**, *2*, 522-528.

[44] P. Arenas-Guerrero, Á. V. Delgado, K. J. Donovan, K. Scott, T. Bellini, F. Mantegazza, M. L. Jiménez, *Sci. Rep.* **2018**, *8*, 9502.

[45] R. G. Compton, C. E. Banks, *Understanding Voltammetry* (2nd edition), World Scientific, **2011**.

Chapter 5

Electrochemical characterisation of the surface composition of $Co@Co(OH)_2$ NPs and their aggregation in solution

In this chapter, core-shell $Co@Co(OH)_2$ nanoparticles are characterised electrochemically with a particular focus on the thin shell of cobalt (II) hydroxide which stabilises the metallic cobalt core against further oxidation in the presence of air. Voltammetric characterisation allows insights into the nature of the shell so both complementing and providing information unavailable using electron microscopy and X-ray diffraction. Moreover, the electrode reactions, occurring at particle ensembles, of the further oxidation of surface $Co(OH)_2$ to CoOOH under alkaline conditions are further evidenced at the single particle level using electrochemical particle-electrode impacts (or 'nano-impacts'). On this basis, the large extent of particle agglomeration/ aggregation of $Co@Co(OH)_2$ nanoparticles while suspended in the solutions is inferred.

This work has been published in *ChemElectroChem*, 2020, Wiley-Verlag Chemie, and was carried out in collaboration with Dr. Christopher Batchelor-McAuley, University of Oxford, Dr. Protima Rauwell and Dr. Erwan Yann Rauwell, both Estonian University of Life Sciences. Dr. Batchelor-McAuley helped me with the interpretation of the experimental results. Dr. Protima Rauwell and Dr. Erwan Yann Rauwell provided the

synthesised particles and performed the XRD and TEM characterisations of the material.

5.1 Introduction

Core-shell nanoparticles (NPs) are receiving rapidly increasing interest[1] because of their potential as highly and/or multi- functional materials that can be designed and manipulated for use in the catalysis,[2] biomedical[3] and electronics fields.[4-7] Hitherto, a vast variety of core-shell nanoparticles have been synthesised including metal@metal oxide,[8] organic@organic,[9] silica@metal,[10] and Au@polymer[11] core-shell particles. In particular, a number of studies focused on nanoparticles with cobalt cores have emerged due in part to the strong ferromagnetism of cobalt leading to their diverse uses as sensor materials,[12] drug delivery materials,[13] and retrievable catalysts,[14] in which the magnetic core allows the manipulation of the particles by magnetic fields. The designed structure of a cobalt core and an 'inert' coating layer (e.g. metal oxides,[15] silica[16] or carbon,[17-18]) overcomes a major issue of the chemical instability of metallic cobalt when exposed to air (which can be pyrophoric)[16] as the size shrinks to the nanoscale. Whilst the shell maintains the magnetic functionality of the cobalt core, the control of its chemical composition may lead to additional beneficial properties of the nanoparticles. For instance, the layered crystal structure of the $Co(OH)_2$ shell of $Co@Co(OH)_2$ NPs has been shown to have a large specific capacitance,[19] and the hydroxide is also electrocatalytically active towards the oxygen evolution reaction[20], the hydrogen evolution reaction[21] and the hydrogenation of nitrile/nitro compounds[21-22].

Transmission electron microscopy (TEM) almost fully dominates the characterisation of core-shell NPs mainly based on the differences in the electron density of the two compositions. There is often excellent contrast between the core and shell phases for the particles consisting of a metal core and a carbon shell, where the crystallinity difference also aids the phase contrast.[17-18, 23] With good crystallinity of the compositions, one may be able to further infer the specific chemical nature based on the measurements of lattice fringe spacing.[24] However, in some cases (e.g. Fe oxide@Au[25] and Co@$Co(OH)_2$[21]) a phase contrast may be not, or sometimes completely not, observed. Identification of such shells then remains a difficulty and limits the development of core-shell particles.

Spectroscopic methods such as energy-dispersive X-ray spectroscopy (EDS) and X-ray photoelectron spectroscopy (XPS) have been used to characterise the composition of the shells of core-shell NPs. A good example of the study using EDS is the work of Eichhorn and co-workders[26] who measured the line ED spectra across the 2D STEM image of the single Ru@Pt nanoparticles, and observed mono- and bi-modal atom distributions of the Ru core and Pt shell respectively, therefore demonstrating the core-shell structure and their compositions. However, this method is inherently limited to the core-shell particles with heavy atom compositions, especially in terms of inferring the specific chemical identities, as the accuracy of quantitative elemental analysis for light atoms (e.g. H and O) is significantly lower.[27] By contrast, the highly sensitive XPS, with a limited depth of analysis of less than 10 nm,[1] therefore is more commonly used for measuring the shell compositions. For instance, the work on organic-polymer-supported Co@$Co(OH)_2$ NPs[21] compares the XP spectra before and

after the sputtering removal of the thin shell of the nanoparticles, and consequently confirmed the chemical identity of the $Co(OH)_2$ shell. Nevertheless, both *ex situ* methods require an ultrahigh vacuum environment and can only measure particle ensembles.

The electrochemical method of stripping voltammetry has been successfully employed to investigate the binary composition of metal/metal oxide-based core-shell NPs.[28-30] Particles are simply drop-cast onto a macroelectrode to which cyclic voltammetry is applied to record the electrochemical responses. The composite particles with different core and shell compositions exhibit distinct voltammetric features, in which the initial electrochemical dissolution of the shell allows the subsequent quantitative analysis of the core. As a result, quantitative insights into the size and structure of the nanoparticles, including the shell composition, its integrity and thickness, may be inferred, as demonstrated in the work of Tschulik and co-workers on Fe_3O_4@Au and Au@SnO_2 nanoparticles.[28] Alternatively, for studying Ag@Ag_2O nanoparticles,[31] the shell of Ag_2O can be readily converted to metallic Ag with a reductive scan, and a subsequent oxidative scan is expected to measure significantly higher charge transferred during the process than the cathodic charge. Thus, the cyclic voltammetry is used to attempt the characterisation of Ag@Ag_2O nanoparticles and so derive the relative shell to core composition by comparison of measured charges. Moreover, a variant of stripping voltammetry compares the voltammetry for the catalysed electro-oxidation of adsorbed CO on the core-shell NPs, such as Ru@Pt, with those for the monophasic particles, such as bare Ru, Pt, and RuPt alloys.[25, 29]

Whilst voltammetry of dropcasted layers may allow the relative sizes and compositions of cores and shells to be investigated, problems can arise when investigating ensembles of particles mainly due to the incomplete stripping effects.[32-34] In particular for example, changes in the chemical nature of the surface species of the studied particles may induce different extents of incomplete stripping effects of the agglomerated/aggregated particles at the electrode surface, and together with the uncertainty of the extent of the electrical contact between the particles and the electrode makes the quantitative analysis challenging. To overcome this issue, the method of the particle-electrode impacts has been used based on the electrochemistry of individual single core-shell particles.[35-36] Therein, nanoparticles are dispersed in solutions and as they randomly move by virtue of Brownian motion, they may impact with the electrode held at suitable potentials. Meanwhile, current-time measurements are conducted and observe their electron transfer with an electrode so that the signal can be directly related to the chemical species involved in the corresponding electrode reactions driven by the applied potentials. Thus, for example,[35] gold-core, silver-shell particles show impact electrochemistry in which the shells are oxidatively dissolved in aqueous solution at significantly lower potentials than the gold cores. Given the complete oxidative dissolution seen for both compositions,[35, 37-38] the charges measured in the stripping of the shells and the cores upon impacts with the electrode allows their relative sizes to be found at the single particle level.

In the following, we infer *via* electrochemistry of the composition of Co@$Co(OH)_2$ nanoparticles and characterise the particles using both the stripping voltammetry and the particle-electrode impacts. The integrity (broken or not broken) of the shells is

considered. Moreover, the particle impacts provide insights towards the agglomeration state of the nanoparticles in solution useful for understanding the *in situ* performance of these NPs.

5.2 Experimental

5.2.1 Chemicals and instrumentation

Cobalt wire (purity 99.99+%; diameter 2.0 mm, length 25 mm) was purchased from GoodFellow, UK and used as received. 5 nm-diameter Co@$Co(OH)_2$ NPs were provided by PRO-1 NANOSolutions (100%), Estonia who state that "each individual Co nanoparticle's stability is ensured by the monolayer of oxide coating on their surfaces which turns them into non-pyrophoric and ultra-stable in air."[39] Co_3O_4 powder (diameter < 1 μm) was obtained from Sigma-Aldrich, UK. Potassium hydroxide (≥ 99.0%, Sigma-Aldrich, UK) solutions were prepared with a concentration of 20.0 mM (pH 12.22 ± 0.02) and thoroughly degassed before use. Solutions were prepared using deionised water (Millipore, USA) with a resistivity of 18.2 MΩ cm at 298 K.

The electrochemical measurements were carried out using a three-electrode system in a Faraday cage with a μAutolab TypeII potentiostat (Metrohm-Autolab BV, The Netherlands) at 298 K. For the CV measurements of bulk cobalt, a freshly polished cobalt disc electrode fabricated as described below was used as the working electrode, with a platinum foil as the counter electrode and a saturated calomel electrode (SCE; BASi, Japan) as the reference electrode (+0.241 V vs. SHE). For the CVs of Co_3O_4

particles, a glassy carbon (GC) electrode (diameter 3.00 mm, CH Instrument) was used as the working electrode and, before use, polished on three microcloth (Buehler, UK) pads with alumina of sizes 1.0, 0.3 and 0.05 μm.

The nano-impact experiments were conducted using an in-house low-noise potentiostat. The potentiostat is designed for nanoparticle-electrode impact detection and basically shares many of the specification requirements found with single-channel recording systems.[40] Most importantly, the design features in a highly stabilised three-electrode potentiostat circuit that confers the characteristic of low noise of the system itself and cosnequently a highly desirable, full potentiostatic control of the working electrode.[41] In particular, signals measured were filtered prior to data analysis, where the filter design used has been demonstrated to conserve the overall charge transferred in the nano-impact events detected.[42] Analysis of the spike transients was performed using a script written in Python 3.5. A 33 μm-diameter[43] carbon disc electrode (IJ Cambria Scientific Ltd, UK) was used as the working electrode and polished as above using the three grades of alumina.

The Nanoparticle Tracking Analysis (NTA) was performed using a NanoSight LM10 (NanoSight, UK), equipped with a sample chamber with a 642 nm-wavelength laser. Software for video capture. Data analysis used the version NTA 2.3.

X-ray diffraction (XRD) patterns were collected using a Panalytical Empyrean diffractometer with a Cu $K_{\alpha 1}$ radiation source (λ = 0.154 nm). The shape and size of $Co@Co(OH)_2$ nanoparticles were examined by Transmission electron microscope (TEM) on a probe corrected Titan 80-300 with a point to point resolution of 1.0 Å. Dr. Protima Rauwell and Dr. Erwan Yann Rauwell are thanked for both characterisation of the nanoparticles.

5.2.2 Cyclic voltammetry (CV) of 'cobalt' materials (bulk cobalt& Co_3O_4 particles)

For CV measurements of bulk metallic cobalt, a cobalt disc electrode was fabricated using the following procedure: 1) A pipette tip was sheared near the sharp top, leaving a small, flat opening; 2) a cobalt wire (d = 2.0 mm, l = 25 mm) was introduced into the small opening of the pipette tip; 3) the cobalt disc surface is adjusted to be level with the sheared tip surface; as such, the pipette tip acts as a 'leakless' sheath. Prior to the measurements, the cobalt disc electrode was successively polished using sandpaper (grit size 4000), a microcloth pad (Buehler, UK) with alumina powder (0.05 μm) and a blank polishing pad. For CV measurements of Co_3O_4, the submicron oxide particles are studied as a 0.8 mg mL^{-1} suspension with 1 hour sonication and of the resulting suspension 2 μL was drop-cast on to a GC electrode.

5.2.3 Stripping Voltammetry of $Co@Co(OH)_2$ NPs

A well-dispersed suspension of $Co@Co(OH)_2$ NPs (0.08 mg mL^{-1}) was prepared by adding 0.4 mg particles into 5 mL of de-ionised water, followed by sonication in an

ultrasonic bath (Fisher Scientific FB15050) for 1 hr. Then 6 µL of the as-prepared suspension was drop-cast onto the GC electrode with a loading of 6.8 µg cm^{-2} and dried under a N_2 atmosphere. Cyclic voltammetry was run on the modified GC electrode in aqueous KOH solution.

5.2.4 Nano-impacts of $Co@Co(OH)_2$ NPs

The above-mentioned 'cobalt metal' NP suspension was prepared and mixed with KOH solutions to a pH of 12.2. To temporarily maintain the dispersity of the NPs during experiments, the suspension was further sonicated for 10 s using a sonic horn (VCX 400, Sonics&Materials, USA) every five scans. Nano-impact experiments were then performed by recording chronoamperometry on a clean carbon microelectrode immersed in the cobalt particle suspension.

5.2.5 Nanoparticle Tracking Analysis (NTA) of $Co@Co(OH)_2$ NPs

The 0.08 mg mL^{-1} $Co@Co(OH)_2$ NP suspension was prepared in deionised water followed by 1 hour of sonication. The sample was injected with a sterile syringe (BsD Discardit II, New Jersey, USA) into the sample chamber at a temperature of 24.0 ± 1.0 °C. NTA sizing measurements were then performed with a measurement time of 60s and automatic exposure settings at 30 frames per second.

5.3 Results and discussion

We first measure and analyse the cyclic voltammetric (CV) response of bulk cobalt using a metallic cobalt disc electrode and second a glassy carbon macroelectrode modified with cobalt oxide (Co_3O_4) particles under alkaline aqueous conditions. The electrochemical responses of the two materials are discussed to comparatively study the dominant cobalt electrode processes. Next, Co@$Co(OH)_2$ NPs are characterised using XRD and TEM, leading to the inferences of their shape, size and compositions. The stripping voltammetry of Co@$Co(OH)_2$ NPs is then performed by drop-casting the nanomaterial on to a GC electrode. On this basis, the chemical surface composition of the 'cobalt' NPs is assessed.

To gain further insights, Co@$Co(OH)_2$ particle aggregates are next studied at the single-entity level. The nano-impact method is applied using a carbon microdisc electrode. Specifically, nanoparticles dispersed in the solution stochastically impact on an electrode held at sufficiently oxidising potentials, enabling electron transfer between the particle and the electrode surface. The charge transfer as a function of applied potential is investigated. As a result, comparison of the potential dependence of the impact charges with the stripping voltammetry further confirms the inferred surface composition of the Co@$Co(OH)_2$ particles. Furthermore, the impact charge data is compared with the sizes of the constituent cobalt particles measured from the TEM images. The measured impact frequency is also discussed. Both lead to inferences regarding the aggregation state of the suspended particles in the solution phase.

5.3.1 Cyclic voltammetry of bulk Co and of Co_3O_4 particles

The cyclic voltammetric response of bulk metallic cobalt was studied between -0.90 V and +0.60 V vs. SCE at a scan rate of 0.05 V s^{-1} using a cobalt disc electrode (ø = 2.0 mm) immersed in a deoxygenated 0.02 M KOH solution. To thoroughly clean the electrode surface of oxides that may form in air, the electrode was electrochemically pre-conditioned by holding the electrode at -1.05 V for 7 seconds prior to the voltammetric scan. Figure 5.1 (solid line) shows three distinct voltammetric features. First, one broad anodic peak is observed at -0.5 V with a shoulder at -0.8 V. Second, a sharp oxidation peak at +0.2 V vs. SCE is noted with the onset of solvent breakdown at nearly + 0.5 V. Third, on the backward scan, a small, sharp cathodic peak is observed at around + 0.2 V. To resolve the observed features, cyclic voltammograms were also run from -0.90 V to different return potentials at the same scan rate of 0.05 V s^{-1}. Apparent in the data shown in Figure 1 is that for the dot-dash line where the scan reverses at +0.21 V the sharp anodic peak is present but the cathodic peak is not. In addition, the back peak is not altered when the applied potential reverses at +0.40 V. Therefore, it is concluded that the sharp peak on the back scan is probably not solely correlated with the sharp peak on the forward scan despite the coincidence in their peak potentials. The inlay (green line) in Figure 5.1 shows a voltammogram of drop-cast Co_3O_4 particles measured using a glassy carbon (GC) macroelectrode under the same conditions. A broad anodic peak at +0.26 V is seen, followed by a sharp peak at +0.56 V. The backward scan shows a nearly symmetric reductive current on the forward scan with similar peak potentials to their anodic counterparts, wave shapes and amount of Faradaic charges.

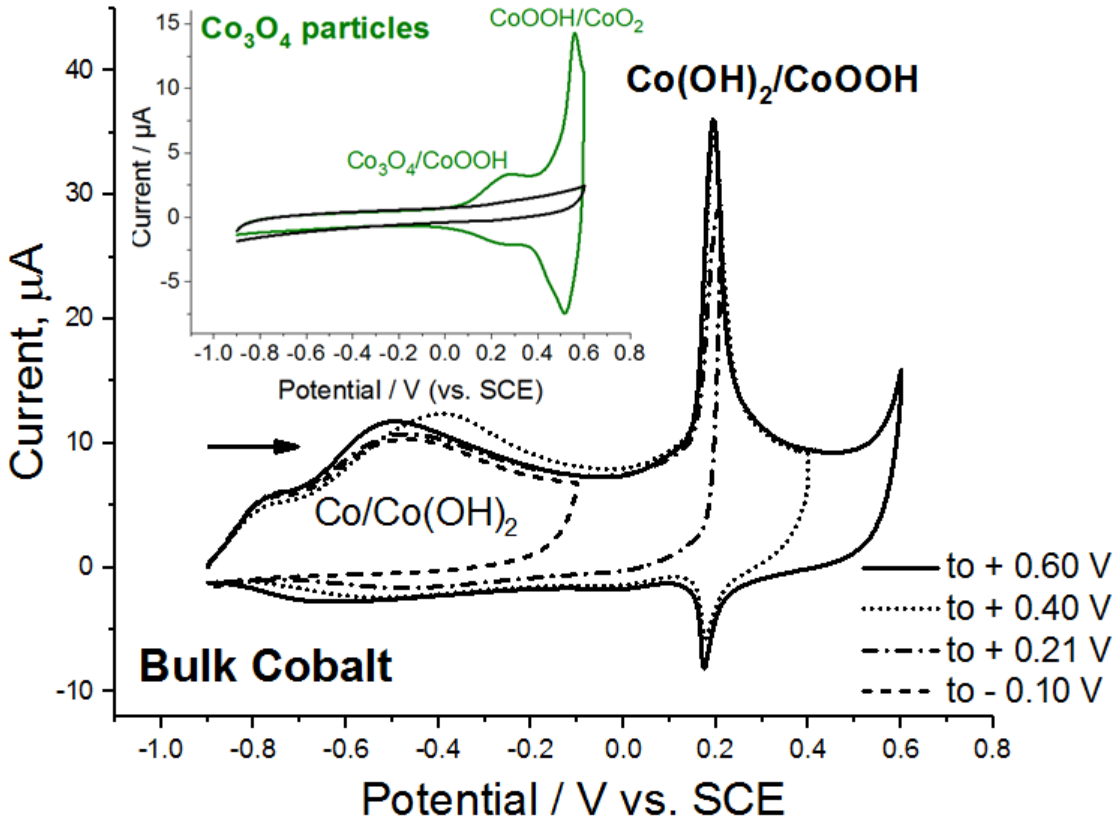

Figure 5.1. Electrochemistry of bulk cobalt in form of pure metallic disc electrode (diameter 2.00 mm) in a N_2-saturated, 20.0 mM KOH solution at a scan rate of 50 mV s^{-1}. The inlay shows a voltammogram of drop-cast Co_3O_4 particles (diameter < 1 µm) on a GC electrode (diameter 3.00 mm) under the same conditions.

Interpretation of the voltammogram of the cobalt materials is made on the basis of the literature which mainly considers bulk CoO, $Co(OH)_2$, Co_3O_4, CoOOH and CoO_2.[44-48] The existence of Co_2O_3 has been previously reported as doubtful.[49] In alkaline conditions, the trivalent compound of cobalt has been exclusively proved using X-ray diffraction to be CoOOH rather than $Co(OH)_3$.[50] A Pourbaix diagram of cobalt (See Figure 5.2) was calculated from the Gibbs energy of formation of the cobalt species at 298 K provided in the literature[51-52], deduced for a fixed total Co concentration of 10^{-2} M. Moreover, a summary of calculated electrode potentials from thermodynamic

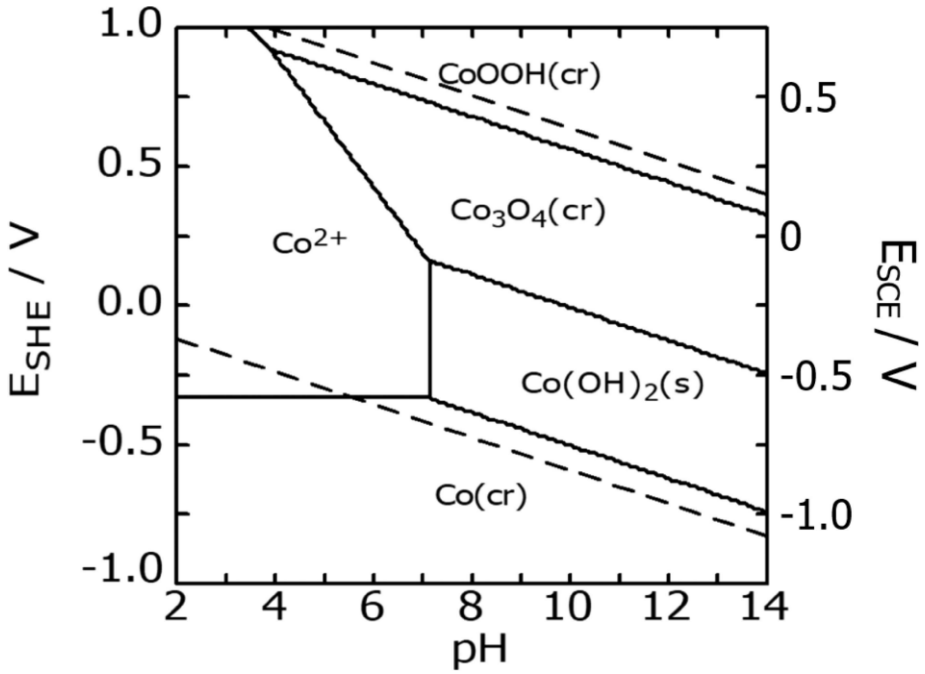

Figure 5.2. Pourbaix diagram (predominant species distribution) calculated for bulk phases of cobalt in aqueous solution. The calculations were performed using the *HYDRA*/*MEDUSA* programmes.[53]

Table 5.1. Calculated electrode potentials for the Co/KOH system.[44]

Half-cell reaction	Electrode couples	E^{o} [a] / V	$E_{cal.}$[b] / V vs. SCE (pH = 12.2)
$Co + 2\ OH^- \rightarrow Co(OH)_2 + 2\ e^-$	$Co/Co(OH)_2$	- 0.71	- 0.86
$Co + 2\ OH^- \rightarrow CoO + H_2O + 2\ e^-$	Co/CoO	- 0.69	- 0.83
$3\ Co + 8\ OH^- \rightarrow Co_3O_4 + 4\ H_2O + 8\ e^-$	Co/Co_3O_4	- 0.56	- 0.70
$3\ Co(OH)_2 + 2\ OH^- \rightarrow Co_3O_4 + 4\ H_2O + 2\ e^-$	$Co\ (OH)_2/Co_3O_4$	- 0.09	- 0.23
$Co(OH)_2 + OH^- \rightarrow CoOOH + H_2O + e^-$	$Co(OH)_2$/CoOOH	+ 0.05	- 0.09
$Co_3O_4 + OH^- + H_2O \rightarrow 3\ CoOOH + e^-$	Co_3O_4/CoOOH	+ 0.33	+ 0.18
$Co_3O_4 + 4\ OH^- \rightarrow 3\ CoO_2 + 2\ H_2O + 4\ e^-$	Co_3O_4/CoO_2	+ 0.58	+ 0.44
$CoOOH + OH^- \rightarrow CoO_2 + H_2O + e^-$	$CoOOH/CoO_2$	+ 0.67	+ 0.52

[a] The symbol E^{o} denotes 'standard electrode potential'; [b] $E_{cal.}$ denotes 'calculated electrode potential'

data at 298 K in alkaline conditions has been given by Behl and Toni[44] and is presented in Table 5.1. The electrode potentials ($E_{cal.}$) are corrected for the pH used in this work (pH = 12.2).

The voltammetry of Co_3O_4 particles is analysed first. As observed in the inlay of Figure 5.1, the reversibility of the electrochemical processes indicates a near Nernstian behaviour of the surface-bound species at the electrode surface. Referring to the calculated electrode potentials ($E_{Co3O4/CoOOH}$ = +0.18 V and $E_{CoOOH/CoO2}$ = +0.52 V vs. SCE), the anodic peaks are correspondingly assigned to the two oxidation reactions respectively. Furthermore, it is noted that the oxidative charge ratio estimated from the currents of these two reactions is around 1/3. This is consistent with the ratio of the number of electron transferred for the redox couple Co_3O_4/CoOOH as compared with CoOOH/CoO_2 and is typical for voltammetry of pure Co_3O_4 oxide.[46, 48]

In the voltammogram of the bulk metal (Figure 5.1), the two shoulders of the first broad peaks at -0.8 V and -0.5 V respectively are almost unresolvable and the electrode potentials of Co/$Co(OH)_2$ and Co/CoO are very close (See Table 5.1). Consequently, clear assignment solely based on the voltammogram is difficult. However, thermodynamically, the Pourbaix diagram (see Figure 5.2) indicates the predominance of $Co(OH)_2$ rather than CoO in the negative potential range against SCE. Moreover, the amphoteric nature of $Co(OH)_2$ that renders it slightly soluble in alkaline solutions (forming $[Co(OH)_4]^{2-}$) implies that the rising portion of the whole broad peak is mainly due to the reaction:

$$Co + 2\ OH^- \rightarrow Co(OH)_2 + 2\ e^- \qquad (5.1)$$

Importantly, Foelske[45] determined by using XPS that in alkaline conditions (pH 13) and after being held at potentials in the same range (i.e. -0.6 ~ +0.2 V vs. SHE) for 5 mins OH^- is the predominant anion on the cobalt surface. The oxidation of Co/Co_3O_4 (E = -0.70 V) is not considered as the major reaction, since the broad peak at -0.5 V is irreversible (see the dashed cycle in Figure 5.1) yet starts from even more negative potentials, although the reaction may be responsible for the subsequent oxidative current at more oxidising potentials as suggested by the Pourbaix diagram. Consequently, the oxidation of Co(0) mainly to $Co(OH)_2$, is assigned to the potential range of -0.90 to -0.10 V.

At higher potentials, a significantly sharp anodic peak at +0.2 V was seen. It has been suggested that the sharp shape is due to fast proton transfer between the electrode couple $Co(OH)_2/CoOOH$ without nucleation of a new phase.[47, 50] The onset potential of this anodic peak is around +0.1 V as compared to the calculated electrode potential -0.09 V. This shows an overpotential of *ca.* 200 mV, indicating the irreversibility of the reaction, which is consistent with the absence of any reductive peak on the dot dash line in Figure 5.1. Moreover, this anodic peak is not considered to be associated with the couple $Co_3O_4/CoOOH$ ($E_{cal.}$ = +0.18 V), since this voltammetric feature differs significantly in terms of wave shape with the corresponding peak in the voltammogram of the cobalt oxide. Therefore, the sharp anodic peak at +0.2 V is assigned to the reaction:

$$Co(OH)_2 + OH^- \rightarrow CoOOH + H_2O + e^- \qquad (5.2)$$

Nevertheless, we note that there may be more than one process responsible for the peak. Detailed discussion can be found in Appendix 1& 2.

5.3.2 Characterisation of Co@$Co(OH)_2$ NPs

Upon the investigation of the electrochemical processes of bulk cobalt, the work now turns to Co@$Co(OH)_2$ NPs. The crystal structure was investigated using X-ray diffraction. The XRD pattern (Figure 5.3a) presents two characteristic diffraction peaks at 44.3° and 51.2°, corresponding to 111 and 200 plane reflections, respectively, of crystalline face-centered cubic (Fm3m) Co metal (inorganic crystal structure database (ICSD): cubic Co (metal), 05–0727),[54] although no diffraction peaks for cobalt hydroxide is observed. Next, TEM measurements were carried out to further evidence the structure and sizes of Co@$Co(OH)_2$ NPs. As observed in Figure 5.3b& c, well-separated single NPs are observed, in which the lattice fringes are visible and thus show good crystallinity of the particles. Probably affected by a poor phase contrast, we did not observe a distinct image of core-shell particle. However, whilst the fringe spacing measured from several HR-TEM images was 0.205 nm that is indexed to the 111 place of cubic Co metal, the d-spacing in a few other regions was measured as 0.46 nm, which is consistent with the reported d-spacing of the (001) plane of β-$Co(OH)_2$[55] or of the (111) plane of Co_3O_4[56]. This indicates the possible presence of $Co(OH)_2$ and/or Co_3O_4 in the core-shell nanoparticles.

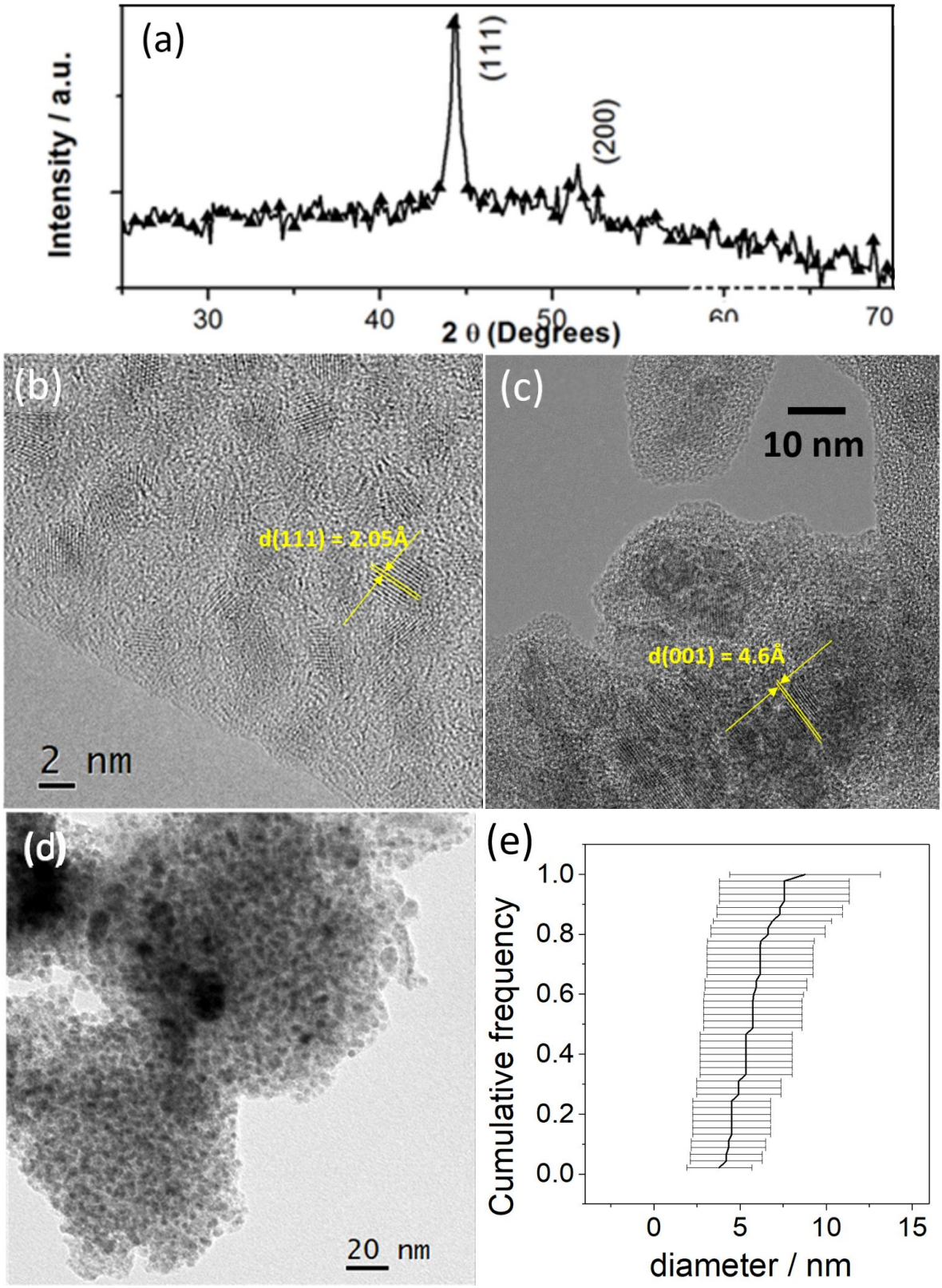

Figure 5.3. (a) XRD pattern of the NPs. (b) and (c) HR-TEM images of individual Co@$Co(OH)_2$ NPs, with highlighted lattice spacing measured for Co metal and $Co(OH)_2$ respectively. (d) TEM image of 'cobalt metal' NPs and (e) corresponding size distribution for the constituent particles inside the aggregates. The error bar denotes the uncertainty estimated for this TEM sizing based on the image resolution.

At a larger scale (Figure 5.3d), more particles are observed giving an average diameter of 5.7 ± 2.9 nm (N = 50). In addition, it is seen at this scale that the small particles are assembled into the bigger entities, which may be considered as aggregates[2] since appearing to be assemblages of those constituent particles which exhibit a discrete, identifiable collective behaviour.[58] The diameters of the aggregates are shown here to be around 100 nm. As such, the electron microscopic measurements indicate a multimodal size distribution of the particles probably consisting of large numbers of constituent particles and fewer aggregates of other sizes.

5.3.3 Stripping voltammetry of drop-cast Co@Co(OH)$_2$ NPs

Having studied the electrochemistry of bulk cobalt and characterised the structure and sizes of Co@Co(OH)$_2$ NPs, and to further examine the surfaces of the NPs, we next measured the anodic stripping voltammetry of the NPs using a GC electrode modified by the drop-cast Co@Co(OH)$_2$. The voltammogram as shown in Figure 5.4 (orange line) was recorded in a deaerated 0.02 M KOH solution at the scan rate of 0.05 V s^{-1}. The loading of the NPs is estimated to be 6.8 μg cm^{-2}. It is noted that the 1 hour's sonication used to improve the particle dispersion, did not alter the voltammetric behaviour (see Appendix 3). For comparison, the voltammetric response of an *unmodified* electrode (black line) is also presented in Figure 5.4. The CV of the 'cobalt' NPs exhibits a sharp and asymmetric anodic peak at around + 0.2 V vs. SCE. Notably,

[2]Note that according to the IUPAC definitions,[57] the difference between aggregation and agglomeration is that aggregation is a physically irreversible process of particles sticking to each other whereas agglomeration is a reversible process. However, herein we use the term 'aggregates' throughout the article to refer to, more accurately, particle assemblages resulting from 'aggregation or agglomeration' for simplicity.

no Faradaic processes are observed at more negative potentials. The backward voltammetric scan also shows a small peak at +0.2 V and a reductive current plateau at higher potentials.

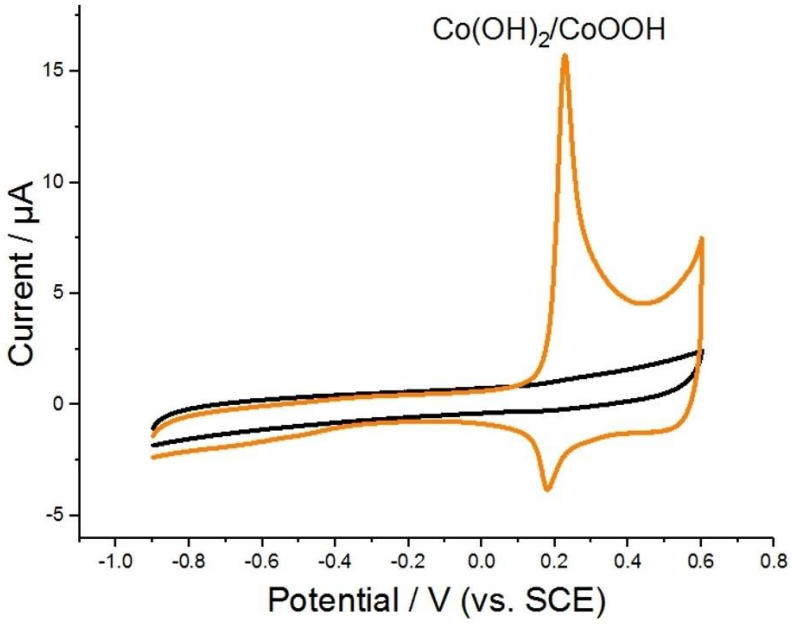

Figure 5.4. Anodic stripping voltammogram of the (orange curve) drop-cast 'cobalt metal' nanoparticles on a glassy carbon (diameter 3.00 mm) electrode in a N_2-saturated, 20.0 mM KOH solution at a scan rate of 50 mV s^{-1}. A (black curve) blank experiment was done with an *unmodified* GC electrode.

The absence of any oxidative peak at negative potentials indicates no metallic cobalt is present at the surface of the nanoparticles. It follows that the metallic core is probably protected by a complete coverage of the oxide/hydroxide shell. Surprisingly, the current between 0.0 V and 0.6 V resembles, in terms of wave shape and peak potential, that seen on the CV of bulk cobalt. This therefore strongly suggested the same reaction $Co(OH)_2/CoOOH$ is occurring at the 'cobalt' NP ensembles. Moreover,

assuming that the 6 nm-diameter particles contains one monolayer of the hydroxide which is oxidised *via* Reaction 5.2, the predicted total charge (as calculated on the basis of the known surface coverage) is found to be 100 μC and is comparable to that measured (*ca.* 40μC), not inconsistent with the inferred electrode reaction. Consequently, also with the TEM observations on the lattice spacing, we suggest that the shell of the 'cobalt' particles is composed of cobalt (II) hydroxide and that this oxidation process is fast as evidence by the voltammetric wave shape.

5.3.4 Nano-impacts of $Co@Co(OH)_2$ NPs

Nano-impact experiments were performed to probe the *in situ* electrochemical behaviour of the suspended particles in solution at the single entity level. To this end, a carbon micro-disc electrode (diameter 33 μm) was inserted in a suspension of $Co@Co(OH)_2$ NPs (0.08 mg mL^{-1}) in aqueous 0.02 M KOH. Chronoamperograms were then recorded at a series of different potentials from +0.1 V to +0.7 V vs. SCE. Figure 5.5a depicts a typical chronoamperogram at 0.3 V vs. SCE with current transients on it, evidencing individual impact events of the cobalt NPs with the potentiostated electrode. The zoom-in Figures 5.5b-f show the representative 'spike' signals obtained at different potentials. No spikes were detected at potentials below 0.3 V vs. SCE. In total, between 100 and 300 of such current spikes were recorded for each potential, and the distribution of their charges is plotted as a function of applied potential in Appendix 4. Across the whole potential range between 0.3 V and 0.7 V, an average charge of around 0.10 pC as seen from Figure 5.6. Herein, it should be noted that from the TEM results, the individual constituent particles are around 6 nm in diameter;

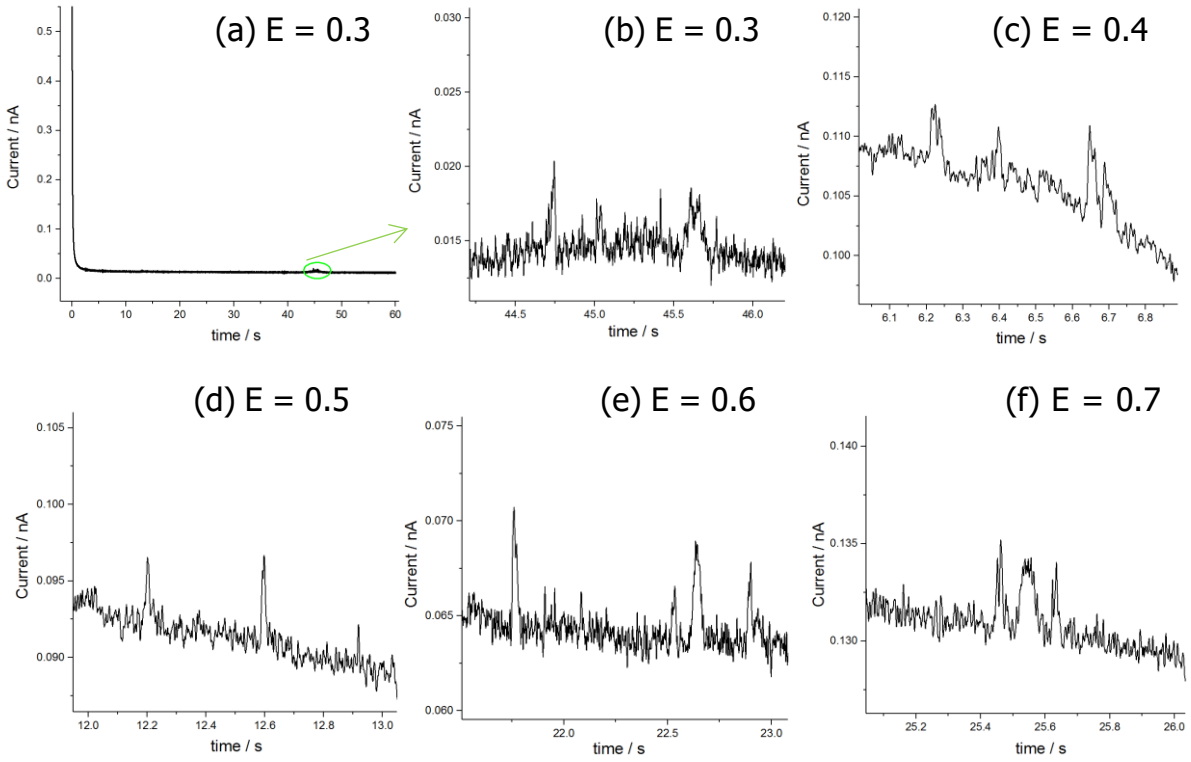

Figure 5.5. (a) Chronoamperograms recorded from a carbon micro-disc electrode (diameter 33 μm) at 0.3 V vs. SCE in a Co@$Co(OH)_2$ nanoparticle suspension containing 20.0 mM KOH. (b-f) Representative transient spikes observed at five different potentials: + 0.3 V, + 0.4 V, + 0.5 V, + 0.6 V and + 0.7 V.

assuming a density of 8.9 g cm^{-3} for these NPs and one-electron-transfer surface oxidation, this predicts an oxidative charge of 0.2 fC per impact event. Consequently, we conclude that the measured charge of 0.1 pC therefore represents impact oxidation of 'cobalt' aggregates or agglomerates rather than that of the single 5.7 nm-diameter constituent particles. In addition, the 'spikes' are found to have an average (by different potentials) impact current of 4.7 ± 0.6 pA and impact duration of *ca*. 55 ± 11 ms. The low variability in these spike features upon potentials applied indicates sufficiently fast electrode kinetics since +0.2 V.

Figure 5.6 is the impact charge plotted as a function of the applied potentials compared to the (overlaid) 'stripping voltammogram' of the NP ensembles. The oxidative spikes are found to onset at potentials comparable to those at which the oxidation of $Co(OH)_2$ is observed in the 'stripping voltammogram'. This shows that the detected spike transients correspond to direct Faradaic current arising from the oxidation of the surface hydroxide of the 'cobalt metal' aggregates. Moreover, the amount of charge transferred during impacts of these suspended particles remains constant above +0.3 V regardless of the increase in the potentials applied. This is consistent with the oxidation $Co(OH)_2/CoOOH$ (Reaction 5.2) as the impact reaction

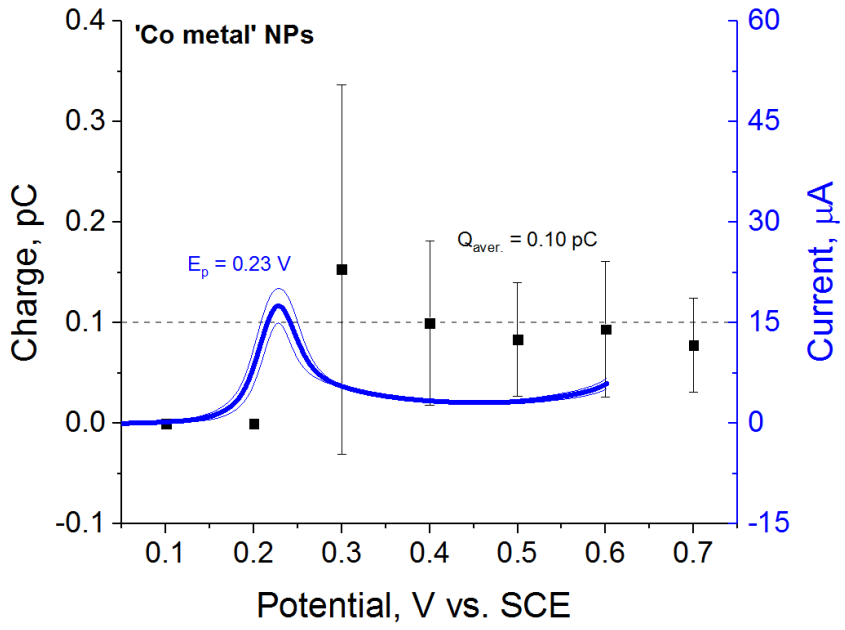

Figure 5.6. Mean charge (black points) obtained from the 'cobalt' particle impact (error bars represent charge variation in the interdecile range) and an overlay with the anodic voltammetry (blue curve) averaged from the dropcasting experiments at 0 to 0.6 V vs. SCE (with a peak potential of + 0.23 V), subtracted by the background curve. The thin lines alongside the middle blue curve denote the experimental errors regarding the voltammogram, while the standard error bars on the black points represent the width of the distribution of their charges.

which has fast electrode kinetics (as discussed in previous sections), and probably occurs to completion at the potentials between +0.3 and +0.7 V given that the reaction already has a considerable overpotential at +0.3 V. Consequently, comparison of the impact experiments with the stripping voltammetry further confirms the surface composition of $Co(OH)_2$ for those individual suspended particles.

Next we consider the question as to whether the 'cobalt' NPs are aggregated in solution, or not? This is addressed by considering the magnitude of the Faradaic charge measured per impact event in comparison with the amount of oxidisable material in the constituent 'cobalt' NPs as measured from TEM. To do so, two *hypothetical* limiting cases are examined both of which conclude that there is significant aggregation in solution. First we consider surface-only oxidation and second we consider full oxidation of the hydroxide shell and the metallic core. In Limiting case 1, the particles are assumed being covered by one monolayer of $Co(OH)_2$, and this hydroxide surface undergoes further oxidation to CoOOH when the particle impacts on the electrode surface. In Limiting case 2, the entire particle is fully oxidised to cobalt oxyhydroxide upon collision. From nano-impact experiments, the *constant* charge transferred per oxidative transient above +0.2 V is 0.10 pC on average. This corresponds to 6×10^5 electrons by using equation:

$$Q = z\, e\, N_{Co} \tag{5.3}$$

where z is the number of electron transferred per cobalt atom; e is the elementary charge (i.e. 1.602×10^{-19} C); N_{Co} is the number of cobalt oxidised per nano-impact event. Assuming a 1 e^- transfer process of $Co(OH)_2$/CoOOH, the number of cobalt

(II) being oxidised per impact event is therefore 6×10^5. In addition, the radius of a constituent particle is 3 nm and the projection dimension of a $Co(OH)_2$ unit cell is 0.32 nm × 0.32 nm. If the particle contains one monolayer of $Co(OH)_2$ (Limiting case 1), the number of cobalt (II) contained in a 6 nm-diameter particle is found to be 1×10^3. Consequently, the number of the constituent particles being oxidised per impact event $N_{NP/impact}$ is 600. In Limiting case 2, the total number of Co atoms contained in a 6 nm-diameter particle is calculated to be 1×10^4 using Equation 6:

$$N_{Co/NP} = \frac{V_p \rho_p}{Ar_{Co}} \quad (5.4)$$

where V_p and ρ_p are the volume and density of the constituent 'cobalt' NPs respectively, herein assuming the unchanged density of the nanoparticles from bulk value; $A_r(Co)$ refers to the molecular mass of the metallic cobalt; N_A is the Avogadro constant (i.e. 6.02×10^{23} mol^{-1}). Similarly, with the assumption of 3 e^- process, the number $N_{NP/impact}$ is then 20. Consequently, with either limiting case, the numbers of the constituent particles being oxidised in the individual impact event are shown to be of a magnitude of tens or hundreds. Therefore, the impact experiment suggests aggregates or agglomerates of the smaller particles (d ~ 6 nm) as the impacting entities.

The formation of aggregates is further supported by NTA data (see Appendix 4) which suggests particles of *ca.* 80 nm in diameter. This particle size is estimated to contain around 1000 constituent particles. Therefore, in Limiting case 1 discussed above, the fewer inferred number of constituent nanoparticles than the NTA result are consistent with partial oxidation of those 80 nm-diameter aggregates. This is highly likely to occur

because the partial oxidation of particle aggregates or big nanoparticles is commonly reported in literature.[59] In Limiting case 2, the discrepancy between the two estimations on the number of the constituent particles inside a particle aggregate from electrochemistry and from NTA is *far* larger. This, though not impossible, suggests this limiting case is much less likely, which is consistent with our conclusion of surface oxidation of the shell only. Both limiting cases point to a significant level of aggregation in the solution phase.

The particle size measured by NTA also allows the estimation of the diffusion coefficients of the particles to be 6.1×10^{-8} cm^2 s^{-1} *via* the Stokes-Einstein equation[60] which in turn allows an estimation of the frequency of impacts to be made using the equation[61]

$$J = 4 D c r \tag{5.5}$$

where J is the diffusional flux towards the electrode, or herein the impact frequency of the 'cobalt' particles; D and c are the diffusion coefficient and the concentration of the particles in the suspension; r is the radius of the micro-disc electrode used. This gives an estimate of 26 s^{-1} which is relatively higher than the value of *ca*. 1 s^{-1} measured as an average frequency over the range of potentials. This may indicate that not all of the particles impacting the electrode become oxidised. Nevertheless, the aggregation of the 6 nm particles is clear for both NTA and impact data.

5.4 Conclusions

The surface composition of $Co@Co(OH)_2$ NPs has been shown to be cobalt (II) hydroxide using *macroelectrode* stripping voltammetry. As X-ray diffraction shows the identity of metallic cobalt and Transmission Electron Microscopy gives the particle sizes, both cannot readily measure the composition of the particle shells. Moreover, as the electrochemistry results of the particle ensembles show a further oxidation of the surface hydroxide to form higher cobalt hydroxide CoOOH, the observations from the particle-electrode impacts indicate, at the single particle level, the same electrode reaction for the individual particles suspended in the alkaline condition. Based on this, in the solution of a low ionic strength ($c(OH^-)$ = 20 mM), the suspended particles are demonstrated by the comparison of impact charge data and the TEM measurements, which is also consistent with the NTA results, to be agglomerates or aggregates of much smaller particles of *ca.* 6 nm in diameter.

Appendices

1. Discussion of the electrode processes associated with the sharp anodic peak in the voltammogram of bulk cobalt

The sharp anodic/cathodic peaks at 0.2 V are assigned to the reversible reactions of the electrode couple $Co(OH)_2$/CoOOH (see main text):

$$Co(OH)_2 + OH^- \rightleftharpoons CoOOH + H_2O + e^- \quad (S1)$$

However, the mismatch of charges in the anodic and cathodic scans and the disappearance of the reduction peak for early scan reversal suggest the possibility of other processes. It is noted that a pre-wave at the potentials between 0.0 and 0.15 V is observed and considered to be a further, slow oxidation of $Co(OH)_2$ formed at preceding more negative potentials. The threshold potential of this pre-wave is close to the calculated electrode potentials of 0.23 V for $Co(OH)_2/Co_3O_4$ as seen from Table 5.1, which suggest an overpotential of more than 200 mV for this reaction. This is consistent with its irreversibility as evident from the dot dash line in Figure 5.1. Consequently, the pre-wave of the main anodic peak at +0.2 V is considered to arise from Reaction S2:

$$3\ Co(OH)_2 + 2\ OH^- \rightarrow Co_3O_4 + 4\ H_2O + 2\ e^- \qquad (S2)$$

At the potentials more positive than the threshold potential of *ca.* +0.15 V above which the sharp anodic peak is observed, Reaction 5.2 is the electrochemical process responsible for the oxidative current, as discussed in the main text. To conclude, the oxidation processes of $Co(OH)_2$ to both Co_3O_4 and CoOOH likely contribute to the current of the anodic peak at *ca.* +0.2 V.

The complexity of the Co/KOH system especially in this range of the positive potentials requires more clarification. First, at the potentials between 0.0 V and 0.4 V, Reaction 5.2 is considered as the predominant process, accounting for the observed sharpness of the anodic peak. However, in this study of bulk cobalt, most of the formed CoOOH is considered to possibly remain blocked beneath the subsequently generated, passive Co_3O_4 oxide.[44] This is supported by the estimation that the charge integrated from the anodic peak at +0.2 V corresponds to electro-oxidation of merely one or a few

layers of $Co(OH)_2$ (see Appendix 2). Such a passivation behaviour explains the vanished reductive peak when the scan reverses at +0.21 V, the very small charge of this cathodic counterpart (Reaction 5.7), as well as no further oxidation of CoOOH to CoO_2 as observed in the voltammogram of the oxide particles. Second, XPS work[45] supports the inference of the simultaneous oxidations of both $Co(OH)_2/Co_3O_4$ and $Co(OH)_2$/CoOOH for the anodic peak, where a large drop of OH^- fraction and a concurrent rise of both spinel O^{2-} and O^{2-} anion fractions were measured at the those potentials. Finally, the assignments of the two peaks are also in good agreement with other literature.[44-45, 50, 62]

2. Estimation of the number of oxidised $Co(OH)_2$ layers in the voltammogram of bulk cobalt

In the voltammogram at potentials between +0.1 V and +0.3 V, the amount of oxidative charge of interest is measured as 6.2×10^{-5} C. Given that the projection dimensions of a $Co(OH)_2$ unit cell is 0.3 nm × 0.3 nm and the radius of the cobalt disc electrode is 1.00 mm, the corresponding number of oxidised $Co(OH)_2$ layers is estimated as follows.

First, the mole of Co^{2+} cations per $Co(OH)_2$ monolayer (assuming an ideally flat monolayer surface with a roughness factor, namely $R = \frac{A_{microscopic}}{A_{geometric}}$, as R = 1) is

$$n_{Co(II)\ atoms/Layer} = \frac{\pi\, r_e{}^2\, R}{r_{Co(II)}\, N_A} = \frac{\pi \times (1.00\ \mathrm{mm})^2 \times 5}{(0.3\ \mathrm{nm})^2 \times 6.02 \times 10^{23} mol} = 6 \times 10^{-11}\ \mathrm{mol}$$

Second, the oxidative charge for the peak at +0.2 V (vs. SCE) measured in the experiment corresponds to the mole of Co^{2+} cations being oxidised

$$n_{Co(II)} = \frac{Q}{z\,F} = \frac{6.2\times 10^{-5}\,\mathrm{C}}{1 \times 96485\ \mathrm{C\ mol^{-1}}} = 6.4 \times 10^{-10}\ \mathrm{mol}$$

Third, the number of $Co(OH)_2$ layers being oxidised is calculated to be

$$N_{Layer} = \frac{N_{Co(II)}}{N_{Co(II)atoms/Layer}} = 11$$

Nevertheless, depending on the roughness of electrode surface (normally 2~3 for a routinely polished metal electrode[63]) and the portion of the Co(II)/Co(III), it is considered that the charge for the sharp anodic peak at around +0.2 V probably corresponds to one or a few $Co(OH)_2$ layers being oxidised.

3 – Possible effects of sonication on the nanoparticle suspension

The 'stripping voltammograms' of 'cobalt metal' NPs under the same measurement conditions as in the bulk cobalt experiment were obtained for three samples: without hour of and with 1 hour of aging, and after 1 hour of sonication. As seen from Figure 5.7, the anodic peak potentials in all the three voltammograms stay *unchanged* at around +0.22 V vs. SCE and so do the cathodic peak potentials at +0.18 V, whereas the oxidative current ascends from nearly 2 μA (fresh) to 5 μA (aging 1 hr) and dramatically to 20 μA (1 hr of sonication). In a drop-cast experiment, such a rise in the current probably represents improved dispersity of the NPs liberated from the particle clumps that usually precipitate. It is therefore concluded that the 'cobalt metal' NPs remains stable against sonication whilst improving the dispersity of the NPs in suspension.

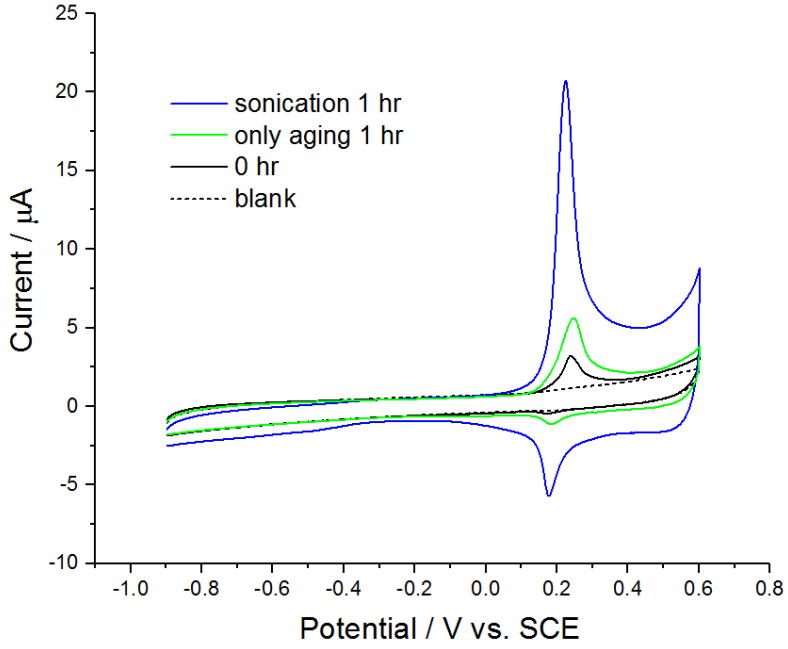

Figure 5.7. Stripping voltammetry from a GC electrode (diameter 3.00 mm) (black solid) modified with fresh 'cobalt' NPs, (green solid) modified with 'cobalt' NPs for 1 hr's aging and (blue solid) modified with 'cobalt' NPs sonicated for 1 hr, and (black curve) with no modification.

4 – Charge distribution from impacts of core-shell nanoparticles at different potentials

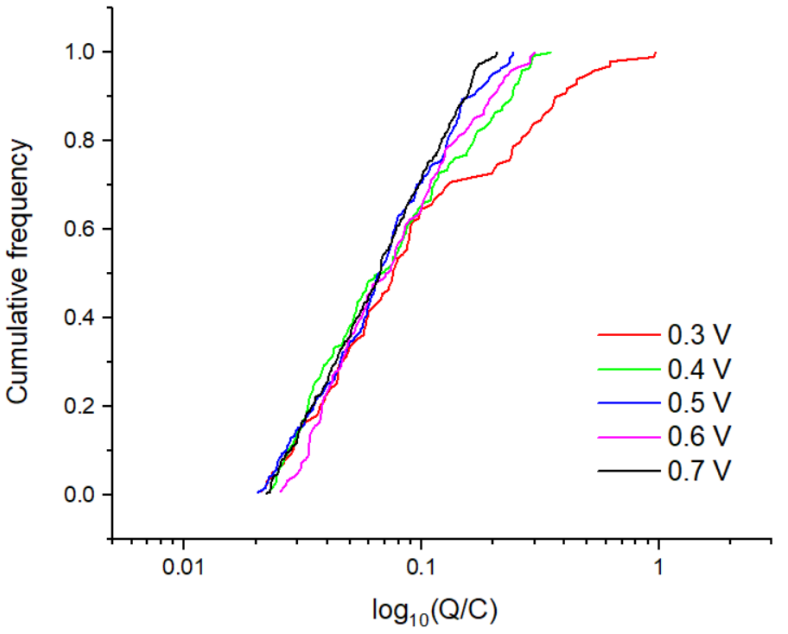

Figure 5.8. Cumulative frequency of impact charges measured as a function of applied potentials from 0.3 V to 0.7 V.

5 – Sizing of the 'cobalt' NPs by Nanoparticle Tracking Analysis (NTA)

NTA sizing measurements of 'cobalt metal' NPs were performed to probe the size of the particles while suspended (0.08 mg mL^{-1}) in deionised water. In the experiments, a number of 'cobalt' particles in form of bright scatters were viewed and over 4,000 tracks in total were obtained for each measurement. As a result shown in Figure 5.9, one single modal diameter for these particles was found to be 55.7 ± 1.5 nm while the mean is 79.3 ± 50.4 nm. This therefore corresponds to the size of the 'cobalt' aggregates present in the particle suspension. Provided that the TEM results show the presence of not only the large aggregates but also individual smaller particles of less than 10 nm in diameter, whereas no particles were detected below 10 nm in NTA measurements, we conclude that NTA is probably not able to measure, due to little light scattered, the constituent particles but shows consistent sizing results for the aggregates with TEM, as well as the inferences from voltammetric experiments.

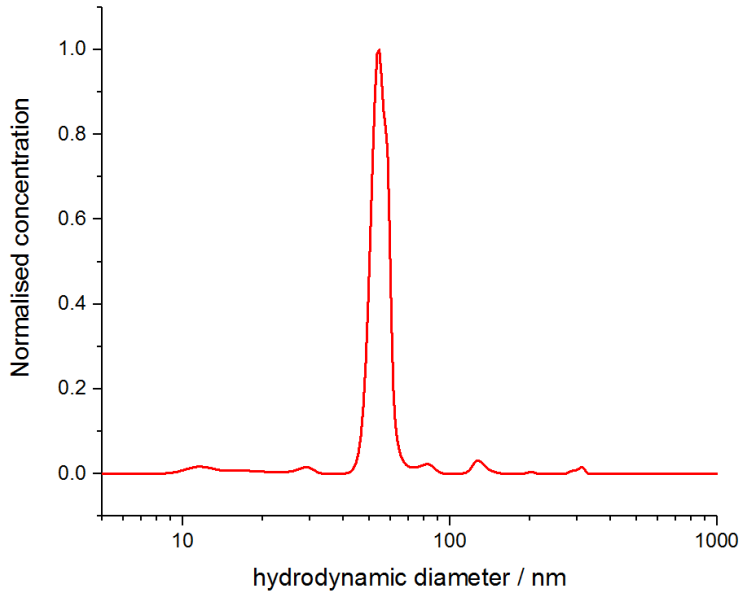

Figure 5.9. Hydrodynamic diameter distribution of the Co@$Co(OH)_2$ NPs suspended in deionised water. Shown is an averaged curve from three parallel experiments.

References

[1] R. Ghosh Chaudhuri, S. Paria, *Chem. Rev.* **2012**, *112*, 2373-2433.

[2] M. B. Gawande, A. Goswami, T. Asefa, H. Guo, A. V. Biradar, D.-L. Peng, R. Zboril, R. S. Varma, *Chem. Soc. Rev.* **2015**, *44*, 7540-7590.

[3] K. Chatterjee, S. Sarkar, K. J. Rao, S. Paria, *Adv. Colloid Interface Sci.* **2014**, *209*, 8-39.

[4] M. A. White, A. Maliakal, N. J. Turro, J. Koberstein, *Macromol. Rapid Commun.* **2008**, *29*, 1544-1548.

[5] G. J. Reynolds, W. O. Martienssen, Google Patents, **2013**.

[6] S.-J. Oh, T. G. Kim, S.-Y. Kim, Y. Jo, S. S. Lee, K. Kim, B.-H. Ryu, J.-U. Park, Y. Choi, S. Jeong, *Chem. Mater.* **2016**, *28*, 4714-4723.

[7] Y. Zhou, L. Zhou, Y. Yan, S.-T. Han, J. Zhuang, Q.-J. Sun, V. Roy, *J. Mater. Chem. C* **2017**, *5*, 8415-8423.

[8] A. Mirzaei, K. Janghorban, B. Hashemi, G. Neri, *J. Nanopart. Res.* **2015**, *17*, 371.

[9] V. Atanasov, V. Sinigersky, M. Klapper, K. Müllen, *Macromolecules* **2005**, *38*, 1672-1683.

[10] B. Jankiewicz, D. Jamiola, J. Choma, M. Jaroniec, *Adv. Colloid Interface Sci.* **2012**, *170*, 28-47.

[11] D. Li, Q. He, J. Li, *Adv. Colloid Interface Sci.* **2009**, *149*, 28-38.

[12] Y. Song, J. Ding, Y. Wang, *J. Phys. Chem. C* **2012**, *116*, 11343-11350.

[13] Y. Bao, K. M. Krishnan, *J. Magn. Magn. Mater.* **2005**, *293*, 15-19.

[14] A. H. Lu, E. e. L. Salabas, F. Schüth, *Angew. Chem. Int. Ed.* **2007**, *46*, 1222-1244.

[15] I. S. Lee, N. Lee, J. Park, B. H. Kim, Y.-W. Yi, T. Kim, T. K. Kim, I. H. Lee, S. R. Paik, T. Hyeon, *J. Am. Chem. Soc.* **2006**, *128*, 10658-10659.

[16] Y. Kobayashi, M. Horie, M. Konno, B. Rodríguez-González, L. M. Liz-Marzán, *J. Phys. Chem. B* **2003**, *107*, 7420-7425.

[17] Y. Ma, Z. Hu, L. Yu, Y. Hu, B. Yue, X. Wang, Y. Chen, Y. Lu, Y. Liu, J. Hu, *J. Phys. Chem. B* **2006**, *110*, 20118-20122.

[18] R. N. Grass, E. K. Athanassiou, W. J. Stark, *Angew. Chem. Int. Ed.* **2007**, *46*, 4909-4912.

[19] Y. K. Kim, S. I. Cha, S. H. Hong, *J. Mater. Chem. A* **2013**, *1*, 9802-9808.

[20] A. Munir, T. Ul Haq, I. Hussain, A. Qurashi, U. Ullah, J. Iqbal, I. Hussain, *ChemSusChem* **2019**, *12*, 5117-5125.

[21] D. Mullangi, D. Chakraborty, A. Pradeep, V. Koshti, C. P. Vinod, S. Panja, S. Nair, R. Vaidhyanathan, *Small* **2018**, *14*, 1801233.

[22] Y. Liu, Z. Fang, L. Kuai, B. Geng, *Nanoscale* **2014**, *6*, 9791-9797.

[23] J. Nishijo, C. Okabe, O. Oishi, N. Nishi, *Carbon* **2006**, *44*, 2943-2949.

[24] B. R. Knappett, P. Abdulkin, E. Ringe, D. A. Jefferson, S. Lozano-Perez, T. C. Rojas, A. Fernández, A. E. Wheatley, *Nanoscale* **2013**, *5*, 5765-5772.

[25] J. L. Lyon, D. A. Fleming, M. B. Stone, P. Schiffer, M. E. Williams, *Nano Lett.* **2004**, *4*, 719-723.

[26] S. Alayoglu, P. Zavalij, B. Eichhorn, Q. Wang, A. I. Frenkel, P. Chupas, *Acs Nano* **2009**, *3*, 3127-3137.

[27] D. E. Newbury, N. W. Ritchie, *J. Mater. Sci.* **2015**, *50*, 493-518.

[28] K. Tschulik, K. Ngamchuea, C. Ziegler, M. G. Beier, C. Damm, A. Eychmueller, R. G. Compton, *Adv. Funct. Mater.* **2015**, *25*, 5149-5158.

[29] N. Muthuswamy, J. L. G. de la Fuente, D. T. Tran, J. Walmsley, M. Tsypkin, S. Raaen, S. Sunde, M. Rønning, D. Chen, *Int. J. Hydrogen Energy* **2013**, *38*, 16631-16641.

[30] P. Ochal, J. L. G. de la Fuente, M. Tsypkin, F. Seland, S. Sunde, N. Muthuswamy, M. Rønning, D. Chen, S. Garcia, S. Alayoglu, *J. Electroanal. Chem.* **2011**, *655*, 140-146.

[31] J. Ghilane, F.-R. F. Fan, A. J. Bard, N. Dunwoody, *Nano Lett.* **2007**, *7*, 1406-1412.

[32] S. J. Cloake, H. S. Toh, P. T. Lee, C. Salter, C. Johnston, R. G. Compton, *ChemistryOpen* **2015**, *4*, 22-26.

[33] H. S. Toh, K. Jurkschat, R. G. Compton, *Chem. Eur. J.* **2015**, *21*, 2998-3004.

[34] B. J. Plowman, B. Sidhureddy, S. Sokolov, N. P. Young, A. Chen, R. Compton, *ChemElectroChem* **2016**, *3*.

[35] L. R. Holt, B. J. Plowman, N. P. Young, K. Tschulik, R. G. Compton, *Angew. Chem. Int. Ed.* **2016**, *55*, 397-400.

[36] R.-C. Xie, M. Volokhova, A. Boldin, L. Seinberg, M. Tsujimoto, M. Yang, B. Rasche, R. G. Compton, *ChemElectroChem* **2020**, *7*, 1216-1276.

[37] B. J. Plowman, K. Tschulik, N. P. Young, R. G. Compton, *Phys. Chem. Chem. Phys.* **2015**, *17*, 26054-26058.

[38] K. Ngamchuea, R. O. Clark, S. V. Sokolov, N. P. Young, C. Batchelor - McAuley, R. G. Compton, *Chem. Eur. J.* **2017**, *23*, 16085-16096.

[39] PRO-1NANOSolutions. Co metal nanoparticles.http://www.pro1nanosolutions.eu/ (Accessed 07 January 2020)

[40] B. Sakmann, *Single-channel Recording*, Springer Science & Business Media, **2013**.

[41] C. Batchelor-McAuley, J. Ellison, K. Tschulik, P. L. Hurst, R. Boldt, R. G. Compton, *Analyst* **2015**, *140*, 5048-5054.

[42] E. Kätelhön, E. E. Tanner, C. Batchelor-McAuley, R. G. Compton, *Electrochim. Acta* **2016**, *199*, 297-304.

[43] On calibration we found the actual diameter of the carbon disc electrode was 39.8 ± 0.04 µm.

[44] W. K. Behl, J. E. Toni, *J. Electroanal. Chem. Interfacial Electrochem.* **1971**, *31*, 63-75.

[45] A. Foelske, H. H. Strehblow, *Surface and Interface Analysis: An International Journal devoted to the development and application of techniques for the analysis of surfaces, interfaces and thin films* **2002**, *34*, 125-129.

[46] R. Boggio, A. Carugati, S. Trasatti, *J. Appl. Electrochem.* **1987**, *17*, 828-840.

[47] L. Burke, M. Lyons, O. Murphy, *J. Electroanal. Chem. Interfacial Electrochem.* **1982**, *132*, 247-261.

[48] R. N. Singh, J. F. Koenig, G. Poillerat, P. Chartier, *J. Electrochem. Soc.* **1990**, *137*, 1408-1413.

[49] A. Earnshaw, N. N. Greenwood, *Chemistry of the Elements, Vol. 60*, Butterworth-Heinemann Oxford, **1997**.

[50] P. Benson, G. Briggs, W. Wynne-Jones, *Electrochim. Acta* **1964**, *9*, 275-280.

[51] J. Chivot, L. Mendoza, C. Mansour, T. Pauporté, M. Cassir, *Corros. Sci.* **2008**, *50*, 62-69.

[52] M. Bajdich, M. García-Mota, A. Vojvodic, J. K. Nørskov, A. T. Bell, *J. Am. Chem. Soc.* **2013**, *135*, 13521-13530.

[53] I. Puigdomenech, in *Stockholm, Sweden*, KHT Royal Institute of Technology, Sweden, **2004**.

[54] S. Liu, J. Zhu, Y. Mastai, I. Felner, A. Gedanken, *Chem. Mater.* **2000**, *12*, 2205-2211.

[55] L. Wang, J. Fu, Y. Zhang, X. Liu, Y. Yin, L. Dong, S. Chen, *Prog. Nat. Sci.: Mater. Int.* **2016**, *26*, 555-561.

[56] H. Jin, J. Wang, D. Su, Z. Wei, Z. Pang, Y. Wang, *J. Am. Chem. Soc.* **2015**, *137*, 2688-2694.

[57] J. Alemán, A. V. Chadwick, J. He, M. Hess, K. Horie, R. G. Jones, P. Kratochvíl, I. Meisel, I. Mita, G. Moad, *Pure Appl. Chem.* **2007**, *79*, 1801-1829.

[58] M. Nic, L. Hovorka, J. Jirat, B. Kosata, J. Znamenacek, *IUPAC compendium of chemical terminology-the gold book*, International Union of Pure and Applied Chemistry, **2005**.

[59] C. A. Little, X. Li, C. Batchelor-McAuley, N. P. Young, R. G. Compton, *J. Electroanal. Chem.* **2018**, *823*, 492-498.

[60] A. Einstein, *Annalen der Physik* **1905**, *322*, 891-921.

[61] R. G. Compton, C. E. Banks, *Understanding Voltammetry* (2nd edition), World Scientific, **2011**.

[62] P. Benson, G. Briggs, W. Wynne-Jones, *Electrochim. Acta* **1964**, *9*, 281-288.

[63] A. J. Bard & L. R. Faulkner, Electrochemical Methods: Fundamentals and Applications, 2nd ed., Wiley New York, 2001.

Chapter 6

Electro-catalytic oxidation of hydroxide ion by Co3O4 and Co3O4@SiO2 nanoparticles both at particle ensemble and single particle level

In this chapter, we report that the Co_3O_4 nanoparticle-mediated electrochemical oxidation under alkaline conditions of hydroxide ion on a glassy carbon macroelectrode leads to hydrogen peroxide as the initial oxidation product of electron transfer. The latter is inferred to subsequently partially decompose to dioxygen by catalytic chemical reaction at the nanoparticles. At the single particle level, electrochemical particle-electrode impacts point out the rate-determining step and the limiting kinetics of the reaction. Further, particles with core-shell structure of a Co_3O_4 core and SiO_2 shell are synthesised, and their electrochemical behaviour is studied and compared with bare Co_3O_4 nanoparticles (NPs), suggesting the very likely broken or highly porous state of the silica shell, which is not otherwise easily distinguished, for example by electron microscopy.

This work has been published in *ChemElectroChem*, 2020, Wiley-Verlag Chemie,[1] and was carried out in collaboration with Ms. Maria Volokhova, Mr. Aleksei Boldin, Dr. Liis Seinberg, from National Institute of Chemical Physics and Biophysics, Estonia, Dr. Masahiko Tsujimoto, from Kyoto University, Japan, Mr. Minjun Yang, and Dr. Bertold Rasche, from University of Oxford. Specifically, Ms. Volokahova, Mr. Boldin and Dr.

Seinberg synthesised the Co_3O_4@SiO_2 and SiO_2 NPs and conducted their XRD measurements. Dr. Tsujimoto imaged the Co_3O_4@SiO_2 and SiO_2 NPs using TEM and obtained the EDS data. Mr. Yang imaged the Co_3O_4 NPs using SEM and obtained the EDS data. Dr. Rasche helped with the interpretation of results mainly regarding crystallography.

6.1. Introduction

Co_3O_4 particles are important electrocatalysts for many reactions in the field of sustainable energy such as the reactions for overall water splitting – hydrogen evolution reaction (HER) and oxygen evolution reaction (OER),[2] for Cl_2 production,[3] and for the electro-oxidation of methanol[4] and glucose in organic fuel cells.[5] As nanoparticles (NPs), they possess large specific surface areas sometimes with an engineered abundance of surface oxygen vacancies,[6-7] leading to high catalytic activity, whilst the intrinsic origin of the latter is considered to be associated with the valencies of the cobalt cations,[8] which in the case of OER catalysis contributes to the formation of strong surface intermediate-bond of Co-OH in the rate determining step.[9] Co_3O_4 NPs have also been considered to be chemically stable in strongly alkaline conditions,[10] and of practical interest due to the relatively low cost and higher abundance.[11] In particular, the NPs have been recently demonstrated to show an excellent electro-catalytic activity towards OER[6-7, 12-18] *via* equation 6.1:

$$4\ OH^- \rightarrow O_2 + 4\ e^- + 2\ H_2O \qquad (6.1)$$

which is comparable to or even superior than the noble-metal based materials (e.g. Pt, Ir).[6] The basis of this comparison is the overpotential at a given current density

relative to the electrode potential of the OH^-/O_2 couple at thermodynamic equilibrium, and/or the turnover frequency of surface Co cations, for which the faradaic current at a certain potential is measured, both assuming a four-electron transfer process generating dioxygen. To this end, mass spectrometry has been applied to confirm the formation of dioxygen, with isotope (^{18}O) labelling used to show its origin as being from the solution phase,[19] and fluorescence-based oxygen sensors to quantify the faradaic yield of O_2 as nearly 100%.[15, 17, 20] The ultimate formation of dioxygen is clear; however, the mechanism by which it is formed remains open and is the focus of the present study. The work focuses on using a glassy carbon electrode as a catalyst support and the analysis of the whole range of potential sweeps, both cathodic and anodic, in contrast to previous studies.[6-7, 14, 21-22] In particular, we consider the possibility that rather than a direct 4 electron process taking place, a mixed electron transfer/chemical disproportionation mechanism occurs via Reactions 6.2& 6.3 as has recently been suggested for oxygen reduction on iron (III) oxide[23] or silver NPs[24]:

$$OH^- \xrightarrow{Co_3O_4(s)} ½\ H_2O_2 + e^- \qquad (6.2)$$

$$H_2O_2 \xrightarrow{Co_3O_4(s)} ½\ O_2 + H_2O \qquad (6.3)$$

in which the catalytic cycling of O_2 leads to the four electron product, H_2O, although the electron transfers lead only as far as H_2O_2, the two-electron product.

Conventionally, drop-cast experiments are performed for the electrochemical studies of solid particles due to the simplicity and ease of operation. However, the surface agglomeration of the drop-casted nanoparticles on the electrode surface has been

demonstrated even in the cases of low particle surface coverages,[25] diminishing the catalytic performance of the NP catalysts.[26] Moreover, the diffusion layer overlap of those particles tends to mask their true catalytic activity[27] and often occurs especially when with a high nanoparticle loading on the electrode surface. Over the last two decades, an emerging technique of particle-electrode impacts, or 'nano-impacts', has been demonstrated to provide insights at the single particle level for many electro-catalysis processes including hydrogen oxidation on Pt NPs[28] and Pd NPs[29-30], methanol oxidation on Pd NPs,[31] oxygen reduction and hydrogen peroxide reduction on single enzymes.[32-34] The area of catalytic impacts has been recently reviewed.[35-38] In a typical catalytic nano-impact experiment, the solid particles are well dispersed in solutions containing appropriate electrolyte, and by virtue of their Brownian motion randomly move and eventually may impact on the electrode surface. The impact is likely to result in a short residence of the NPs at the electrode surface held at suitable potentials, which meanwhile mediates the reactions of redox molecules present in solution phases. Consequently, the impact signals with shapes of 'spikes' or 'steps', depending on the particle residence times, may be recorded in the current-time measurements and, in particular, the analysis of the signal current may be able to provide information regarding the catalytic activity of the *individual* impacting single particles. On this basis, to study the kinetic aspects of Co_3O_4 NPs mediating the OH^- oxidation, single particle electrochemistry will be attempted in addition to the conventional study of the drop-cast particle ensembles. Further, we also investigate the electrochemistry of core-shell Co_3O_4@SiO_2 NPs and compare them with Co_3O_4 NPs, drawing on the successful electrochemical studies of identifying and quantifying

broken shells of metal/metal oxide core-shell NPs[39] using drop-cast experiments, and characterising single core-shell Au@Ag using the nano-impact technique.[40]

6.2. Experimental

6.2.1. Chemicals

Cobalt (II) dicobalt (III) oxide (Co_3O_4) nanoparticles (NPs), potassium hydroxide solutions (0.974 M, purity ≥ 99.0%), calcium hydroxide (95%), hydrogen peroxide (30 wt% in H_2O), potassium chloride (≥ 99.0%), cobalt (II) nitrate hexahydrate ($Co(NO_3)_2 \cdot 6H_2O$, 99.999%), tetraethyl orthosilicate (98%), N,N-Dimethyl formamide (99.8%) and polyvinylpyrrolidone (molecular weight 40000) were purchased from Sigma-Aldrich, UK and used as received. Nitrogen and oxygen gas cylinders was supplied from British Oxygen Company, Surrey, U.K. All solutions were prepared with de-ionised water of resistivity of 18.2 MΩ cm at 298 K (Millipore).

6.2.2. Synthesis of Co_3O_4@SiO_2 NPs and SiO_2 NPs

Prior to the synthesis of the core-shell Co_3O_4@SiO_2 NPs, Co_3O_4 nanoparticles were first synthesized by thermal decomposition of cobalt (II) nitrate hexahydrate ($Co(NO_3)_2 \cdot 6H_2O$) as described in a previous study by Volokhova.[41] Specifically, 0.62 g of $Co(NO_3)_2 \cdot 6H_2O$ was dissolved in 10 mL of anhydrous dimethylformamide and then 0.3 g of polyvinylpyrrolidone was added to the solution, which was stirred for 30 min. The reaction mixture was thermostated at 180°C for four days. The initially transparent purple solution turned black-brown. Then 50 mL of ethanol was added to

the final black-brown colloid solution and washed twice to remove excess surfactant and reaction byproducts. The precipitate of nanoparticles was collected by centrifugation and kept in ethanol solution.

Second, coating of the obtained Co_3O_4 nanoparticles with SiO_2 was carried out according to the similar procedure as previously described.[40, 42] Prior to the synthesis, 100 mL of ethanol and 10 mL of deionised water were stirred at 200 rpm for 10 min. 25 mg of nanoparticles were dissolved in ethanol (2 ml) and added to the mixture of water and ethanol and stirred for 30 min. After that, 25 mL of NH_4OH (28%) were added dropwise to the solution and stirred for 30 min. Meanwhile, tetraethyl orthosilicate (TEOS) solution was made. 1 mL of TEOS was dissolved in 30 mL ethanol and stirred for 30 min. Then 4 mL of TEOS/ethanol mixture was added dropwise for 8 h into the nanoparticle solution. The precipitate was collected by centrifugation and washed twice to remove excess surfactant and reaction byproducts. Collected nanoparticles were stored in ethanol solution. Ms. Volokahova, Mr. Boldin and Dr. Seinberg are thanked for the synthesis of these Co_3O_4@SiO_2 NPs.

The silica nanoparticles were prepared with a modified procedure of a previous study.[43] 6.9 mL of TEOS was hydrolysed in 250 mL of ethanol with continuous stirring with a speed of 230 rpm. After 30 min, a mixture of deionised water (25 mL) and ammonium hydroxide solution (2.5 mL) were added into the reaction solution and kept stirring for 4 hours until the mixture turned into a milky solution. Then, reaction mixture were washed with ethanol twice and dried with rotary evaporator for 1 hour.

Ms. Volokahova, Mr. Boldin and Dr. Seinberg are thanked for the synthesis of these SiO_2 NPs.

6.2.3. Material Characterisation

The scanning electron microscopy (SEM) images of Co_3O_4 NPs were obtained using a Zeiss Sigma 300 FEG-SEM with an accelerating voltage of 2.0 kV. Prior to the measurements, the NPs were suspended in water and drop-casted onto a cleaned glassy carbon stub, which was subsequently dried overnight in vacuum. Energy Diperseive Spectroscopy (EDS) were also performed on those NPs. Mr. Yang is thanked for the SEM imaging and EDS measurement of Co_3O_4 NPs.

Transmission Elecron Microscopy (TEM) images of Co_3O_4@SiO_2 and SiO_2 NPs were obtained using JEOL JEM 2200FS and JEOL JEM 1400EX electron microscope, respectively. Diluted samples for TEM measurements were prepared by drop-cast the pre-suspended NPs on a copper grid and dried overnight in vacuum. EDS were also performed on the specific sites of Co_3O_4@SiO_2 NPs to study the elemental content of core and shell. Dr. Tsujimoto is thanked for the TEM imaging and the EDS measurements of Co_3O_4@SiO_2 and SiO_2 NPs.

Powder X-ray Diffraction (XRD, Panalytica Xpert3) measurements of Co_3O_4@SiO_2 NPs were carried out with Cu Kα radiation (λ = 0.154 nm) with 45 kV beam voltage and 40 mA beam current. Patterns were collected in a range from 20° to 90° with the

steps of 0.02° and the exposure time of 100 sec. Ms. Volokahova, Mr. Boldin and Dr. Seinberg are thanked for the XRD measurements of the Co_3O_4@SiO_2 NPs.

6.2.4. Cyclic voltammetry of hydroxide ion oxidation on a glassy carbon electrode modified with Co_3O_4 and Co_3O_4@SiO_2 NPs

A suspension of Co_3O_4 NPs or Co_3O_4@SiO_2 NPs (0.1 mg mL^{-1}) was prepared by adding 0.5 mg of the particles to 5 mL of water. The particle suspension was vortexed for 10 seconds followed by 30 seconds' resting; this was repeated six times. A glassy carbon (GC) electrode (d = 3.00 mm) was polished with 0.3 and 0.05 μm-sized alumina particles on microcloths in sequence. The as-prepared suspension was then drop-cast on the GC electrode and dried under an N_2 flow.

Cyclic voltammetry was conducted in 0.1 M KCl solutions containing 20 mM KOH, using a three-electrode system under potential control *via* a μAutolab TypeII potentiostat (Metrohm-Autolab BV, The Netherlands) thermostated at 298 K. The modified GC electrode was used as the working electrode, a platinum foil as the counter electrode and a silver/silver chloride electrode (3.4 M KCl, +0.205 V vs. SHE at 298 K) as the reference electrode. For the experiments using oxygen-saturated solutions, pure oxygen gas was bubbled through the solutions for *ca.* 10 mins to reach a steady, saturated condition of the dissolved gas.

6.2.5. Kinetic study of hydrogen peroxide decomposition using UV-vis spectroscopy

The kinetics of hydrogen peroxide decomposition in 20 mM KOH was studied using UV-vis measurements (λ = 240-300 nm) with a Shimadzu UV-1800 spectrophotometer, using quartz cuvettes (Quartz SUPRASIL, Hellma Analytics) with an optical light path of 10 mm.

6.2.6. Nano-impact experiments of Co_3O_4 and Co_3O_4@SiO_2 NPs

An aqueous suspension of either Co_3O_4 NPs (10 mg mL^{-1}) or Co_3O_4@SiO_2 NPs (0.03 mg mL^{-1}) was prepared. Dispersed suspensions were obtained by vortexing as described above. Nano-impact experiments were carried out using a low-noise homemade potentiostat at 298 K which has been described previously.[44] Prior to the measurements, potassium hydroxide and chloride were added to the particle suspensions to give a final concentration of 20 mM KOH + 0.1 M KCl. A clean carbon micro-disc electrode (ALS Co., Ltd, d = 7.0 µm) was inserted to the mixture. In these fresh particle suspensions (ageing time < 15 mins) current-time measurements (or chronamperometry) were made at varying fixed potentials. Counting and analysis of the impact signals were performed in Origin 2017 Pro.

6.3. Results and discussion

We first (Section 6.3.1) characterise the size and chemical composition of cobalt (II) dicobalt (III) oxide (Co_3O_4) particles using Scanning Electron Microscope (SEM) and

Energy Dispersive Spectroscopy (EDS). Second, (Section 6.3.2) we examine the cyclic voltammetric responses (CV) of the Co_3O_4 NPs. Then, (Section 6.3.3) the voltammetry of Co_3O_4-mediated OH^- oxidation on glassy carbon (GC) electrodes modified with drop-cast Co_3O_4 NP ensembles are studied to evidence their catalytic activity towards this oxidative process. (Section 6.3.4) The reaction mechanism is discussed with aid of UV spectroscopy. Third, (Section 6.3.5) we perform nano-impact experiments by making fixed potential, current-time measurements ('chronoamperometry') at a clean glassy carbon micro-disc electrode inserted in a Co_3O_4 nanoparticle suspension, where these particles are on the average spatially well separated with centre to centre distances of *ca.* 1 µm. By virtue of Brownian motion, these particles may stochastically collide with the microelectrode surface held at suitable oxidising potentials. Random current steps were detected in the chronoamperograms, evidencing the catalytic oxidation of hydroxide ions on the *individual* impacting Co_3O_4 NPs for the timescale of their residencies at, or very close to, the electrode surface. Insights into this catalytic process, at the single particle level, are subsequently given. In the Sections 6.3.6-6.3.9, similar experiments were performed on silica-coated cobalt (II) dicobalt (III) oxide nanoparticles (Co_3O_4@SiO_2 NPs). Last, the results of the two types of NPs are compared and discussed.

6.3.1. Characterisation of Co_3O_4 nanoparticles

Co_3O_4 NPs were first imaged by SEM and EDS for size and chemical composition analysis, respectively. Figure 6.1a shows that these NPs are of irregular shapes; for approximate sizing of the particles, the shapes were assumed as perfect spherical and

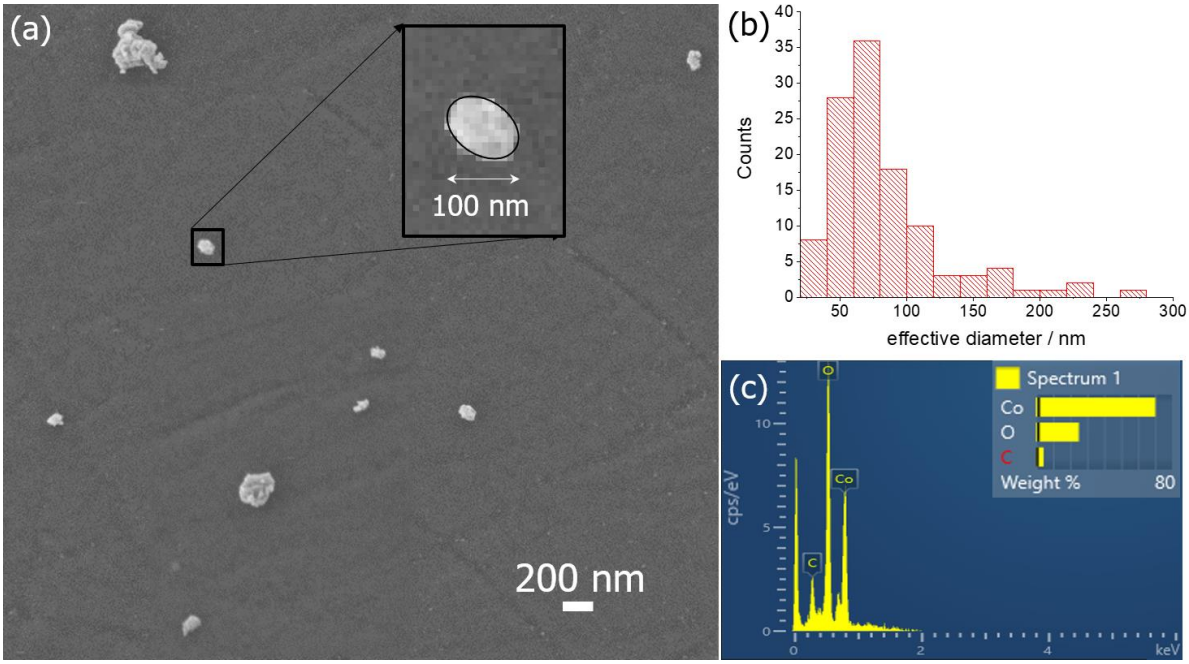

Figure 6.1. (a) SEM image of Co_3O_4 NPs. (b) diameter distribution of the particles. (c) EDS analysis on of the particles with a Co to O molar ratio of 0.72 ± 0.09 average across three different sites. The presence of carbon detected is consistent with the glassy carbon substrate.

accordingly their peripheries in the 2D images were outlined first as an oval shape. The individual oval areas were measured and then converted to the *effective* diameters of circles of same areas. Subsequently, the average diameter of a total number of 115 Co_3O_4 particles were measured as 75 ± 22 nm (Figure 6.1b). Meanwhile, Figure 6.1c illustrates the EDS measured chemical composition of these NPs with weight percentages of cobalt and oxygen elements. The molar ratio of Co to O was calculated as 0.72 ± 0.09, consistent with the expected value of 0.75 for the as-received cobalt (II) dicobalt (III) oxide (Co_3O_4) particles. Note that the existence of Co_2O_3 is thought doubtful.[45] The chemical identity of Co_3O_4 was thus concluded.

6.3.2. Cyclic voltammetry (CV) of Co_3O_4 NP ensembles

The electrochemical behaviour of Co_3O_4 NPs was first investigated. First, the CV of a bare GC electrode immersed in 0.1 M KCl + 20 mM KOH was performed in the potential range of 0.0 V to 0.40 V as shown in Figure 6.2. No voltammetric features were seen. Next, 0.6 µg of Co_3O_4 NPs (corresponding to nearly 35% of a monolayer of close packed particles) was drop-cast onto the GC electrode and dried under an N_2 atmosphere. Cyclic voltammetry was then applied to this Co_3O_4 NP-modified electrode immersed in the same electrolyte. Figure 6.2a shows one small broad oxidation peak at around 0.25 V vs. Ag/AgCl. The inlay presents, after the removal of capacitive current, a better-defined oxidation wave with a peak potential of +0.30 V, with its

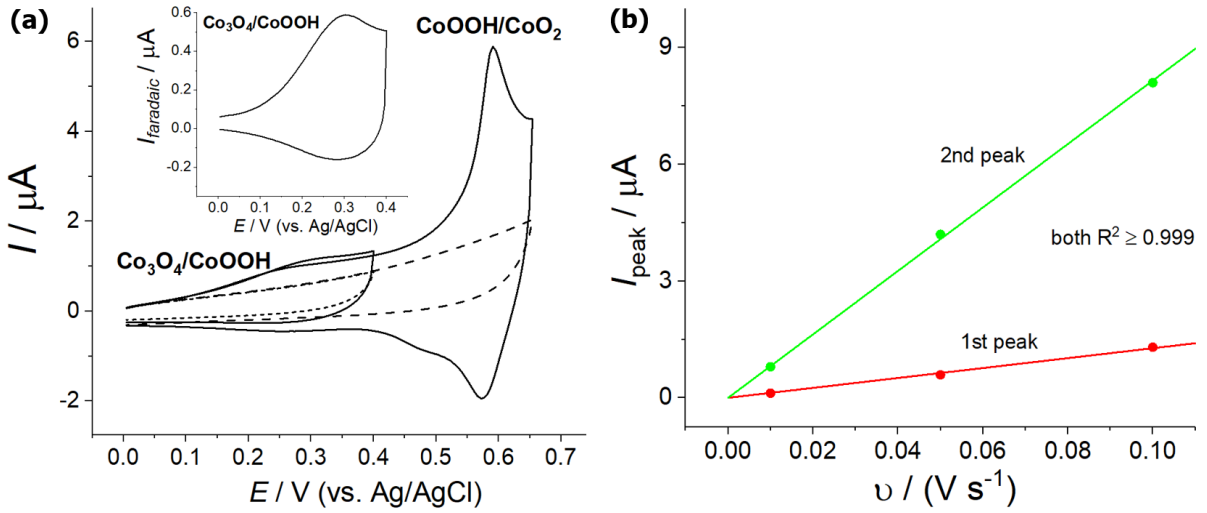

Figure 6.2. (a) Cyclic voltammomgrams of bare GC electrodes (dashed curves) and the ones modified with Co_3O_4 NPs (solid curves) immersed in 0.1 M KCl + 20 mM KOH solutions in the anodic potential ranges of 0.0 V to 0.40 V and to 0.65 V, respectively. A conversion of the potentials against Ag/AgCl to those against reversible hydrogen electrode (RHE) is provided in Appendix 1. Scan rate 50 mV s^{-1}. Inlay: the 'Faradaic current' voltammogram of 0.0 to 0.4 V, obtained from the background current subtraction on the measured drop-cast voltammogram. (b) Plots of peak current of the two oxidation peaks at 0.3 and 0.6 V, respectively, as a function of scan rate.

peak current scaling linearly with the scan rate (Figure 6.2b), suggesting the oxidation of a surface-bound species. Moreover, the reductive counterpart of the oxidative wave occurred at 0.28 V (peak-to-peak separation ΔE_{pp} is *ca*. 20 mV), implying the quasi-reversible behaviour of this oxidation at 0.3 V. According to the Pourbaix diagram of the predominant cobalt species in Figure 5.2 (last chapter), the measured mid-point peak potential of the pair (0.29 V) was found to be close to the thermodynamic potential (+0.22 V vs. Ag/AgCl) for the redox couple Co_3O_4/CoOOH, from the data of Gibbs energy of formation of the cobalt oxide species provided in the literatures at 298 K.[46-47] Therefore, the first peak is attributed to the Reaction 6.4:

$$Co_3O_4 + OH^- + H_2O \rightarrow 3\ CoOOH + e^- \qquad (6.4)$$

Next, the potential region was extended to a more positive value, +0.65 V, and a second sharp oxidation wave with a peak potential of 0.59 V was seen (Figure 6.2a). The peak current of this oxidative wave was again directly proportional to the applied voltage scan rate (Figure 6.2b) and a back peak at *ca.* 0.58 V (with ΔE_{pp} = 15 mV) was observed. These suggest the second wave as also being due to a quasi-reversible surface-bound reaction. The mid-point potential of the redox peaks (0.58 V) was found to be very close to the thermodynamic potential for the redox couple CoOOH/CoO_2, +0.56 V vs. Ag/AgCl. Moreover, the oxidation charges measured from the two oxidative waves at 0.3 V and 0.6 V have a ratio of 1 to 3, agreeing with the number ratio of electrons transferred per cobalt atom of the two reactions. Therefore, the second oxidation was attributed to the Reaction 6.5:

$$CoOOH + OH^- \rightarrow CoO_2 + H_2O + e^- \qquad (6.5)$$

Nevertheless, we note that the total charge measured from the two oxidative waves was 8.8 ± 2.0 μC, significantly smaller than the expected charge for complete oxidation of drop-cast Co_3O_4 NPs (*ca.* 1 mC) *via* the two-step oxidation to CoO_2, yet comparable to the value of 31 μC estimated for the oxidation of only the NP surfaces assuming a monolayer of the surface of the Co_3O_4 NPs was oxidised (to CoO_2) (see Appendix 2a). This suggests the oxidation of the NPs only occurs at the particle surfaces compounded with the incomplete stripping effects[26].

6.3.3. Cyclic voltammetry of hydroxide ion oxidation mediated by Co_3O_4 nanoparticles

To investigate the possible hydroxide ion oxidation, the CVs measured above were further extended to a positive potential of +1.2 V and to a more negative potential region (-1.4 V). For the dropcast Co_3O_4 NPs, the particle surface coverage was calculated to be *ca.* 35% of a monolayer, assuming the particles were evenly distributed on the electrode surface (see Appendix 2b), although in practice, the NPs likely form agglomerates on the electrode surface through the drying process.[25] Figure 6.3 shows in the anodic region the CV of the Co_3O_4-modified electrode shows, apart from the NP oxidation peaks between 0.1 and 0.6 V, a large oxidative wave peaking at 1.0 V. The peak current of the latter was found to scale linearly with the square root of voltage scan rate as seen from Figure 6.4a and to be proportional to the concentration of hydroxide ion in solutions (Figure 6.4b), with no peak observed in the absence of the deliberately added hydroxide ions. These suggest the process is attributed to diffusion-controlled oxidation of OH^-. In the absence of the NPs, no

voltammetric features were observed in the extended potential region of 0.65 to 1.20 V, indicating that the oxidative wave at 1.0 V is OH^- oxidation catalysed by Co_3O_4 NPs.

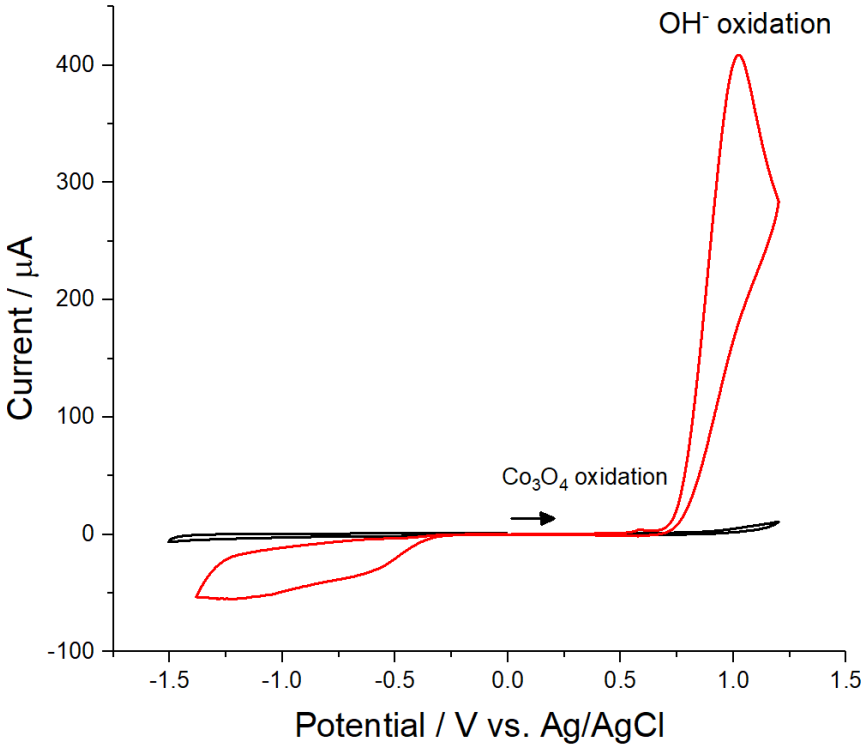

Figure 6.3. Cyclic voltammomgrams of a bare GC electrode (d = 3.00 mm) and one modified with Co_3O_4 NPs (particle surface coverage of 35%) immersed in 0.1 M KCl + 20 mM KOH solutions. Scan rate 50 mV s^{-1}. The scans start from 0.0 V.

Further upon the study of the OH^- oxidation peak, an average anodic transfer coefficient (β) of 0.47 ± 0.06 was obtained by Tafel analysis (see Figure 6.16 in the Appendix 3) in the region of 20%-30% of the peak current.[48] From the slope of the fitted straight line in Figure 6.4a, one can derive the number of electron transferred via the Randles-Sevcik equation for 298 K

$$\mathrm{I}_p = 2.99 \times 10^5 \sqrt{n' + \beta_{n'+1}}\, n\, D^{1/2}\, c^* A\, v^{1/2} \qquad (6.6)$$

where I_p is the peak current, n' the number of electrons transferred before the rate determining step, $\beta_{n'+1}$ the transfer coefficient of the rate determining step, n the total

number of electrons transferred, D the diffusion coefficient (4.60×10^{-9} m^2 s^{-1})[49-50] of OH^-, c^* the bulk concentration of OH^-, A the electrode surface area and v the scan rate. The total number of electrons transferred was thus calculated to be 0.96 ± 0.14, indicating a one-electron-transfer process for the oxidation of hydroxide ion, very probably to H_2O_2 (see the next section).

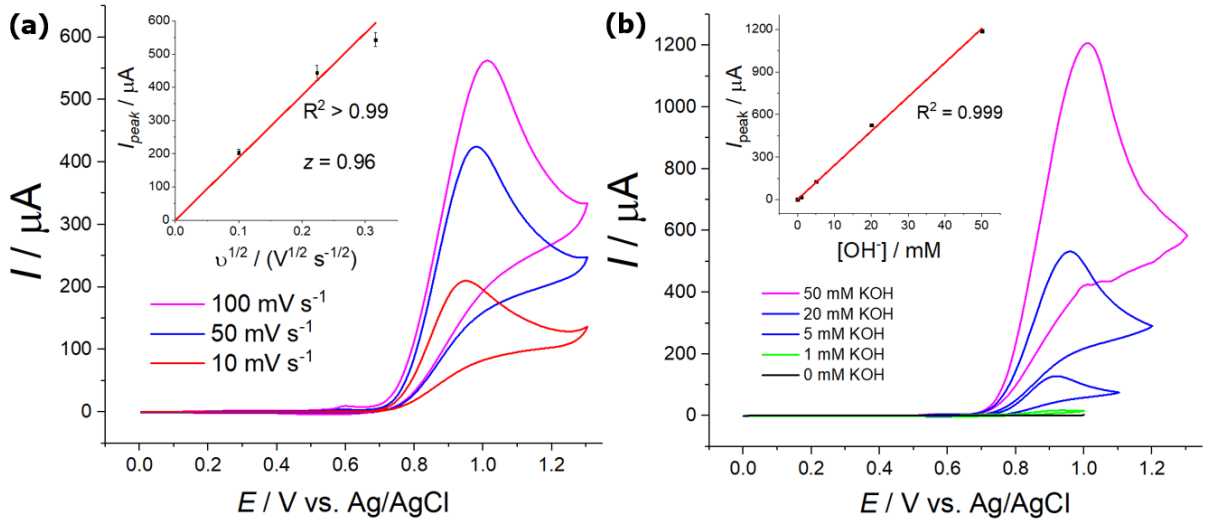

Figure 6.4. (a) Anodic voltammograms of a Co_3O_4 NP-modified electrode in 0.1 M KCl + 20 mM KOH. Scan rate varies from 10, 50 to 100 mV s^{-1}. Inlay shows the linearity between the peak current and the square root of scan rate. (b) Voltammograms of a Co_3O_4 NP-modified GC electrode (d=3.00 mm, NP surface coverage 35%) in 0.1 M KCl containing varying concentrations of KOH from 0 mM to 50 mM. Scan rate 50 mV s^{-1}. Inlay shows the linearity between the peak current and the hydroxide ion concentration.

6.3.4. Mechanistic studies of the hydroxide ion oxidation

To further elucidate the mechanism of the hydroxide ion oxidation catalysed by cobalt (II) dicobalt (III) oxide nanoparticles, the negative potential region in Figure 6.3 was first studied. As seen from Figure 6.5a, on the reverse scan to a very negative potential (-1.4 V), a peaked broad reductive wave was seen with a peak potential of -1.2 V,

with a small shoulder peak at *ca.* -0.6 V. To study the origin of this reduction current, in an N_2-saturated 0.1 M KCl + 20 mM KOH solution, the CVs of Co_3O_4 NP-modified

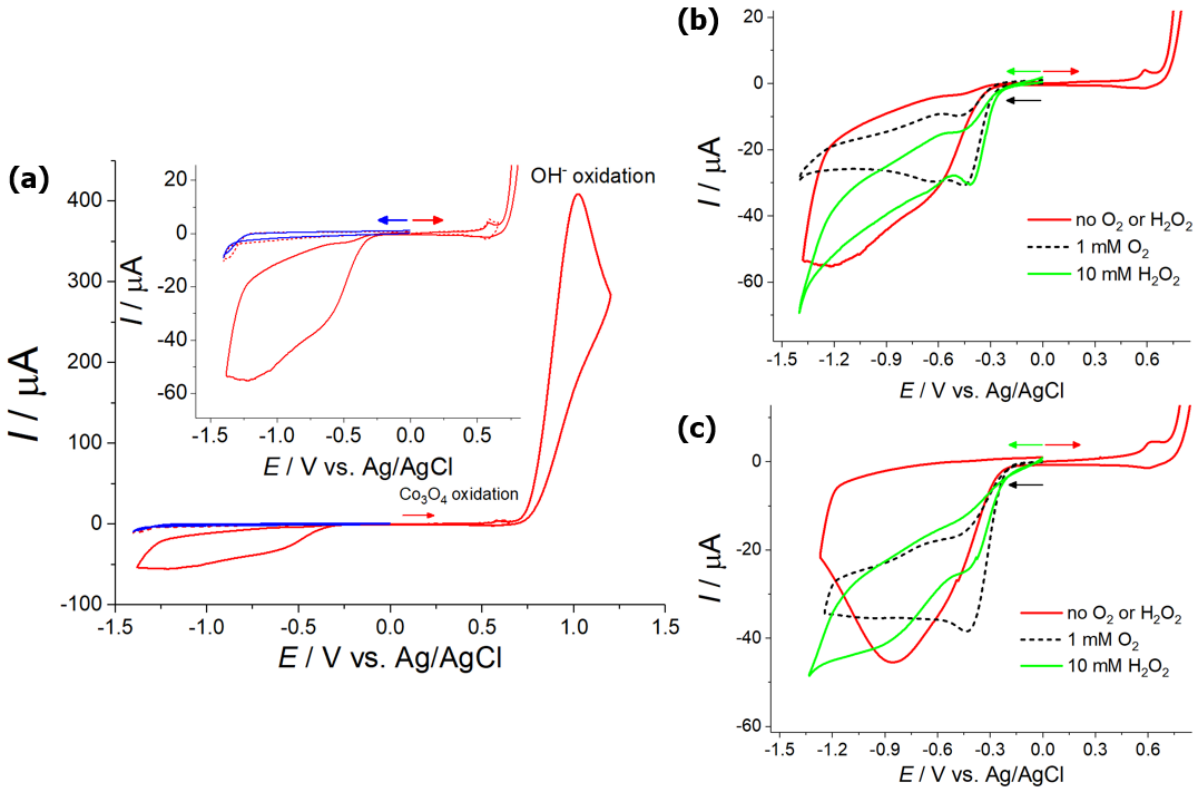

Figure 6.5. a) Voltammograms of a Co_3O_4 NP-modified electrode in degassed 0.1 M KCl + 20 mM KOH. Inlay shows the enlarged region of the broad reduction wave and the additional two cycles for comparison. Fingerprinting voltammograms of O_2 reduction and H_2O_2 reduction in b) 20 mM KOH and c) 10 mM $Ca(OH)_2$ alkaline solutions.

GC electrode was additionally performed from 0 V to +0.65 V to -1.4 V (red dashed curve) and also directly to -1.4 V (blue curve). Consequently, the broad reductive wave was not found in either of the two cycles, indicating that the reduction was related to the generated species from the OH^- oxidation.

It is noteworthy that in the anodic region at around +1.0 V, gas bubble formation was visually observed on the GC electrode surface. This was inferred to be possible generation of gaseous O_2. Nevertheless, as the OH^- oxidation process has been shown as a one-electron-transfer process, hydrogen peroxide (H_2O_2) is very likely the immediate, direct electrolysis product, whereas the gaseous oxygen may result from the chemical process of the disproportionation of H_2O_2 under the prevailing conditions, given that H_2O_2 is prone to disproportionating under alkaline conditions encouraged by the formation of HO_2^-,[51] and more importantly Co_3O_4 NPs have been suggested as a heterogeneous catalysts for H_2O_2 decomposition.[2, 52] In order to investigate which of the two (H_2O_2 or O_2) was the predominant final product or their proportions in the product mixture, the broad reductive wave was fingerprinted by recording the CVs of Co_3O_4 NP-modified GC electrodes in the same electrolyte saturated with dissolved oxygen (*ca.* 1 mM) and in the one thoroughly degassed using N_2 but containing 10 mM of hydrogen peroxide, respectively. Figure 6.5b shows that in the voltammogram of oxygen reduction, two peaks were seen at -0.45 and -0.6 V, respectively, followed by a quasi steady-state current. It is clear that except the minor feature of the small peak at -0.6 V, the overall voltammetric features differed significantly from those of interest, precluding dioxygen as a major, direct oxidation product of the OH^- oxidation.

For hydrogen peroxide reduction (green curve in Figure 6.5b), the wave shows a peak at -0.45 V, which is almost identical to the peak at -0.45 V found in the oxygen reduction voltammogram and therefore suggests the possible chemical decomposition

of H_2O_2 catalysed by Co_3O_4 NPs upon immersion of the electrode; further interestingly, a small peak at -0.6 V is seen followed by an ever increasing reductive current prior to solvent breakdown. The absence of any peak features at potentials more negative than -0.6 V may result from the changed mass transport conditions. Unlike the condition in the hydroxide ion oxidation voltammogram where the electro-generated species was only present locally near the electrode surface, the conditions in the H_2O_2 reduction voltammogram always provide a bulk concentration that can constantly supply peroxide to the electrode surface by diffusion. Nonetheless, the voltammogram of hydrogen peroxide reduction is broadly consistent in terms of wave shape with the reductive current recorded after OH^- oxidation, suggesting H_2O_2 as the major product from the OH^- oxidation. Moreover, similar but more distinct voltammograms for the fingerprinting study were also obtained in alkaline conditions using $Ca(OH)_2$ rather than KOH (Figure 6.5c). At -0.85 V, A distinct broad reduction peak recorded after OH^- oxidation was observed. In the voltammogram for H_2O_2 reduction, apart from the small peak at *ca.* -0.45 V of probably the same origin as in the case of KOH, a reductive wave at a very similar potential of close to -0.9 V was seen, whilst the oxygen reduction voltammogram stays almost the same to that seen in KOH solutions. The consistency in the peak potentials of *ca.* -0.85 V, together with the observations discussed above, further confirmed that the major product of OH^- oxidation was H_2O_2, *via* the Reaction 6.7:

$$OH^- \xrightarrow{Co_3O_4(s)} \tfrac{1}{2}\, H_2O_2 + e^- \qquad (6.7)$$

It follows that although the gas bubbles were seen on the electrode surface, the decomposition of electro-generated H_2O_2 to O_2, catalysed by Co_3O_4 NPs, occurred only

to a marginal extent as they are subject to slow chemical kinetics relative to the OH^- oxidation and on the timescale of the experiments. This inference was supported by the subsequent UV spectroscopic study of the kinetics of the catalytic decomposition of H_2O_2 as next reported.

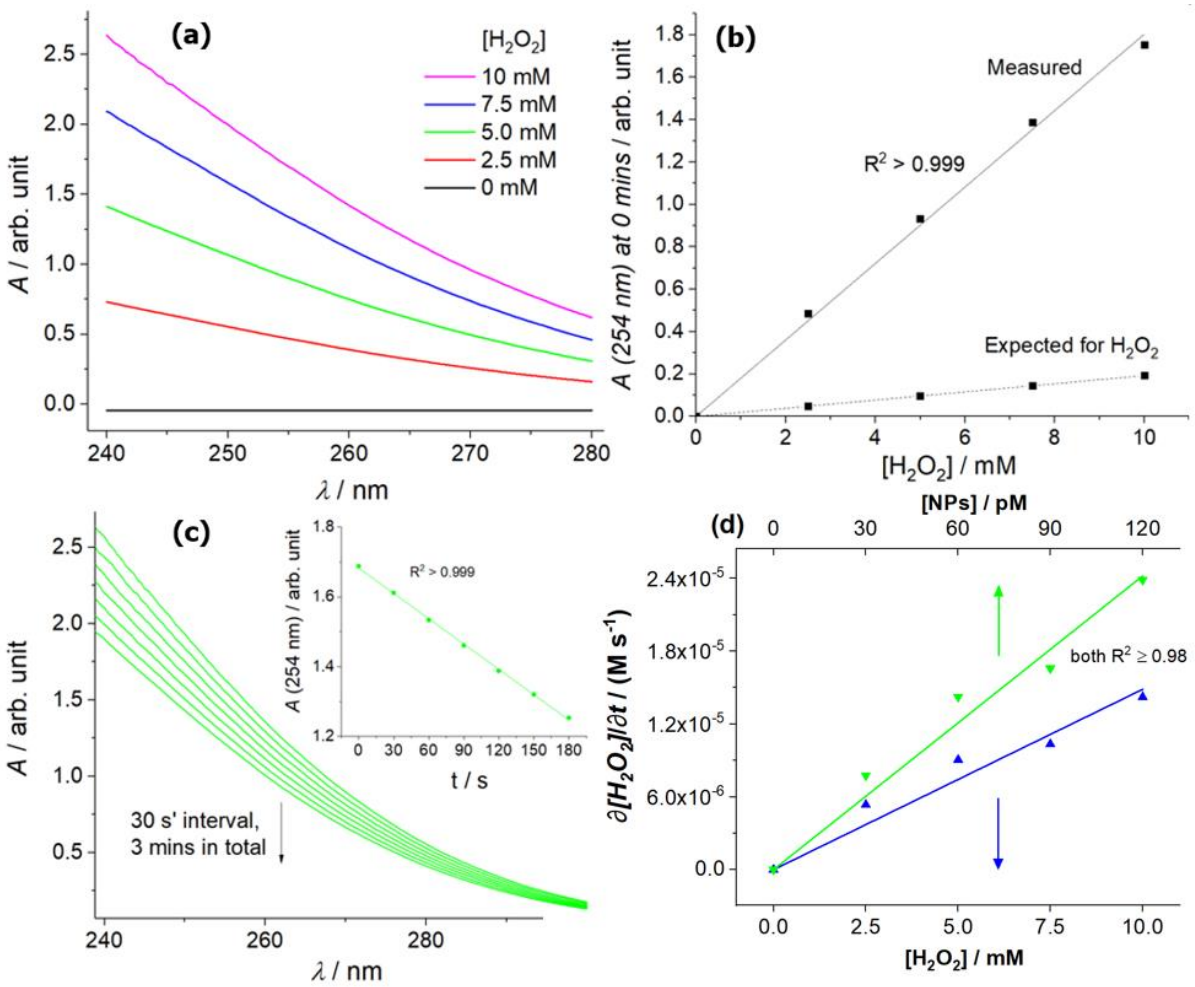

Figure 6.6. a) UV spectra of 0-10 mM H_2O_2 in 20 mM KOH in absence of Co_3O_4 NPs. b) UV absorbance at 254 nm plotted as a function of H_2O_2 concentration. c) UV spectra of 10 mM H_2O_2 in the presence of 60 pM Co_3O_4 NPs over time. Inlay shows the measured absorbance at 254 nm plotted as a function of time. d) The rate of H_2O_2 decomposition plotted as a function of nanoparticle concentration (green) and of hydrogen peroxide concentration (blue).

Experimentally, in absence of Co_3O_4 NPs the UV spectra (Figure 6.6a) of hydrogen peroxide of varying concentrations from 0 to 10 mM in 20 mM KOH solutions were first obtained. No decline over time in the UV absorbance was observed. Figure 6.6b shows that the absorbance (at 254 nm) scaled linearly with H_2O_2 concentration, but the spectra are consistent with HO_2^- rather than H_2O_2, reflecting the pK_a of 11.6 for the H_2O_2/HO_2^- equilibrium at 298 K.[53], [54], [55] Next, in the presence of Co_3O_4 NPs, the UV aborbance (Figure 6.6c) of HO_2^- was found to linearly decrease with time (measured within 3 mins), showing the catalytic activity of the NPs towards the chemical decomposition under the alkaline condition via Equations 6.8& 6.9

$$H_2O_2 + OH^- \rightleftharpoons H_2O + HO_2^- \quad (6.8)$$

$$HO_2^- \xrightarrow{Co_3O_4(s)} ½\ O_2 + OH^- \quad (6.9)$$

From the initial slope of absorbance over time plot, the rate of decomposition was calculated. Subsequently, Figure 6.6d shows that the decomposition rate scaled linearly with the concentration of Co_3O_4 NPs, suggesting a first order chemical process with respect to the concentration of the NPs. Likewise, the linearity between the decomposition rate and H_2O_2 concentration suggests a first order chemical process with respect to the peroxide concentration. Therefore, an overall second order kinetics of the peroxide decomposition catalysed by Co_3O_4 NPs was inferred:

$$J = k_0\,[NP]\,[HO_2^-] \quad (6.10)$$

where J is the reaction flux (M s^{-1}), k_0 the rate constant (M^{-1} s^{-1}), [NP] the particle concentration of Co_3O_4 NPs (M) and $[HO_2^-]$ the bulk concentration of the deprotonated

H_2O_2 (M). As such, the k_0 was calculated as 2.7 (± 0.3) × 10^7 M^{-1} s^{-1}. For a direct comparison in the reaction rates of this heterogeneous catalysis process with the electrochemical process of OH^- oxidation, knowing the total NP surface area, the reaction flux J can be converted to an interfacial reaction flux J_i (M m^{-2} s^{-1}) of the peroxide to the NP surfaces by

$$J_i = \frac{J}{[S_p]} \tag{6.11}$$

where $[S_p] = S_p^o \times [\mathrm{NP}]$, $[S_p]$ is the total NP surface area per unit volume (m^2 L^{-1}) and S_p^o is the total NP surface area per mole of Co_3O_4 NPs estimated from the average size (m^2 mol^{-1}). Then we have

$$J_i = \frac{k_0[HO_2^-]}{S_p^o} \tag{6.12}$$

So that we define an equivalent interfacial rate constant k_i as

$$k_i = \frac{k_0}{S_p^o} \tag{6.13}$$

Consequently, assuming the diameter of the Co_3O_4 NPs is 75 ± 22 nm as measured from SEM, k_i is determined as 2.5 ± 1.5 × 10^{-4} cm s^{-1}, which is significantly slow as compared to the *limiting* electrochemical rate constant (2.0 ± 1.0 × 10^{-2} cm s^{-1}) for OH^- oxidation measured from the single particle electrochemistry results as will be derived in next section. Hence, the UV spectroscopy results support the conclusion of O_2 as a marginal product due to the rather slow formation kinetics from hydrogen peroxide that was consequently considered as the predominant product of the electro-oxidation of OH^- at Co_3O_4 NP surfaces.

6.3.5. Single particle electrochemistry of Co_3O_4 NPs

Having discovered and studied the hydroxide ion oxidation catalysed by Co_3O_4 NP ensembles, we next conducted nano-impact experiments to probe this electro-catalytic process at the single particle level. Experimentally, a freshly polished carbon micro-disc electrode (d=7 μm) was first dipped in a 20 mM KOH + 0.1 M KCl solution, to

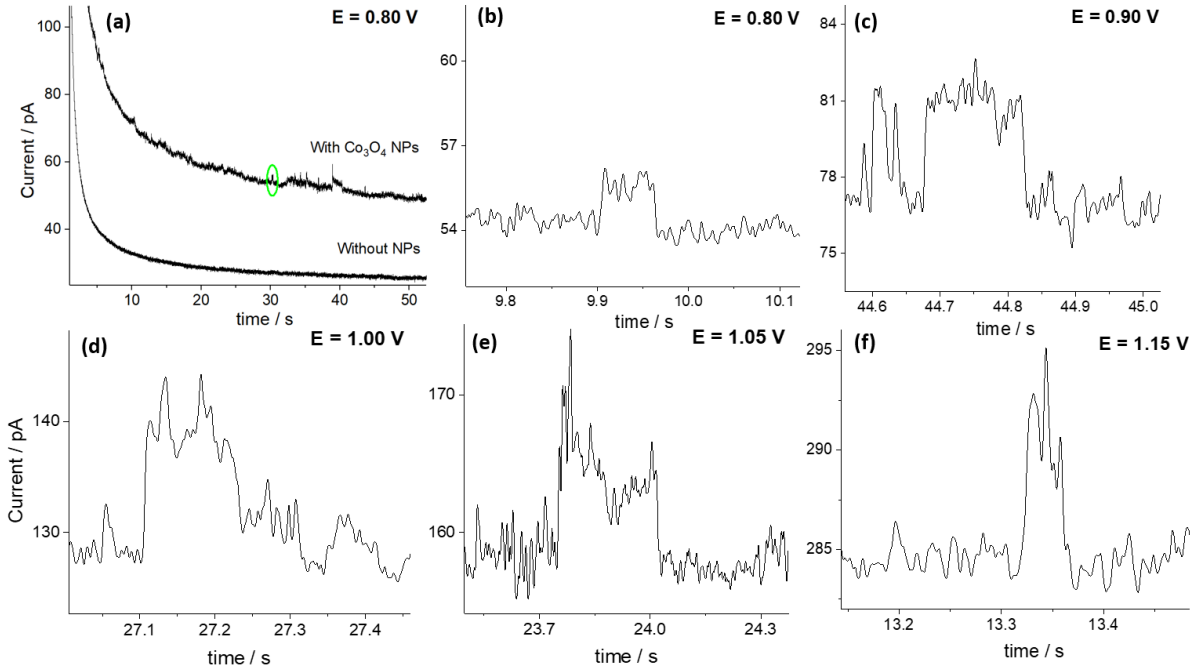

Figure 6.7. (a) Chronoamperograms of a carbon micro-disc electrode (d=7 μm) immersed in a 20 mM KOH + 0.1 M KCl solution containing 10 mg mL^{-1} Co_3O_4 NPs, held at a potential of 0.80 V vs. Ag/AgCl. Current steps are seen (outlined by the green circle) as enlarged in **(b)**. Examples of representative steps at higher potentials (0.90~1.15 V) are shown in **c-f**. No steps are detected below/at 0.70 V.

which chronoamperometry was recorded at 0.80 V vs. Ag/AgCl for 60 seconds. No features was observed as seen from Fig. 6.7a. Next, 10 mg mL^{-1} (or 12 nM) Co_3O_4 NPs were added into the solution, where individual suspended particles randomly move by virtue of Brownian motion, although many particles were seen sedimenting out from

the suspension. Upon particle collisions with the electrode held at the oxidising potentials (0.8-1.2 V), clear current steps were observed in the chronoamperograms (Fig. 6.7b-f), evidencing the impacts of the individual Co_3O_4 NPs. Below +0.7 V inclusive, no impact signals regarding the oxidation of Co_3O_4 NPs were detected (see Figure 6.17 in Appendix 4).

On the average, 50 current steps were obtained at each of these potentials (Figure 6.8a). The mean impact frequencies as a function of potentials were plotted (Figure 6.8b), from which over the potential range of 0.80 to 1.15 V the impact frequency was found to stay nearly the same with a mean value of 0.20 ± 0.13 s^{-1}. Each step was assumed to result from the impact events of individual 75 nm diameter NPs and their diffusion coefficient in the aqueous solution was estimated as 6.5 × 10^{-12} m^2 s^{-1} *via* Stokes-Einstein equation,[56] which allows an estimation of the bulk particle concentration to be made using the equation[57]

$$J = 4 D c^* r \qquad (6.14)$$

where J is the diffusional flux (or herein the impact frequency) of the NPs towards the electrode surface, D the diffusion coefficient of the NPs in the suspension, c^* the bulk concentration of the NPs and r the electro-active radius of the carbon microelectrode. As a result, this frequency suggested a suspended Co_3O_4 particle concentration of 4 ± 3 pM (*ca.* 0.3% of the initial amounts). This is consistent with the experimental observation mentioned above that only a tiny fraction of the particles remained suspended, giving an estimate of an average inter-particle distance of *ca.* 1 μm that indicates those suspended particles were well-separated.

The average step height (current) at +0.8 V were measured as 1.1 ± 0.2 pA, with a step duration of *ca*. 130 ± 40 ms. This duration may be limited by the oxygen bubble formation and collapse (agitation) upon the catalysis process of the impacting particles, or simply result from the diffusional departure of the particles from the interface.[37] At more positive potentials, increasingly higher steps were measured from 0.80 to 1.00 V with a current plateau at *ca.* 5.7 ± 1.5 pA, as shown in Figure 6.8a that depicts the average impact step currents as a function of applied potentials in comparison with the anodic voltammogram of the drop-cast Co_3O_4 nanoparticle ensembles. The threshold potential above which the current steps were found is shown to superpose with that of the catalytic current of hydroxide ion oxidation on the drop-cast Co_3O_4 NPs; and the impact step currents starts to plateau out at 1.00 V, agreeing well with the peak potential of the anodic voltammogram. These observations strongly indicate the catalytic oxidation of OH^- occurring on the individual impacting Co_3O_4 NP surfaces.

Further insights regarding the catalysis of OH^- oxidation on *individual* single NP surfaces can then be discussed on the basis of the impact current measured. Given that the catalytic process is a first order catalytic reaction of hydroxide ion (as $I_{peak} \propto [OH^-]$ observed from Figure 6.4b), the limiting rate constant k_{lim} under the condition was derived from the average step currents I_{step} from 1.00 to 1.15 V using the equation:

$$I_{step} = n\,F\,A\,k_{lim}\,[OH^-] \qquad (6.15)$$

where n is the number of electrons transferred, F is the Faraday constant (96485 C mol^{-1}), A is the catalysing surface area of the impacting NP and $[OH^-]$ the bulk

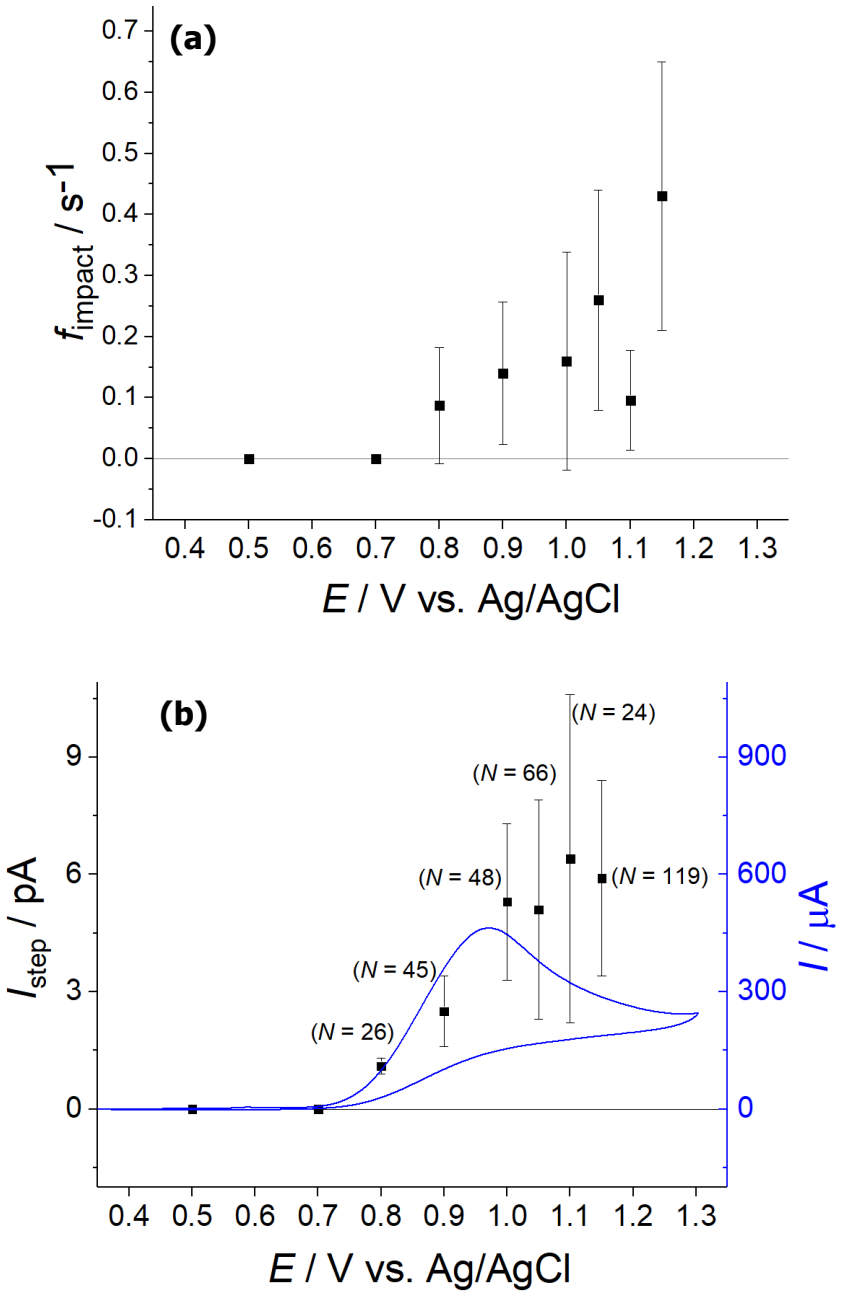

Figure 6.8. (a) Overlay of the plot (black) of average impact step currents (error bars represent the interdecile range) as a function of applied potentials with the anodic voltammogram (blue) of Co_3O_4 NP ensembles immobilised on a GC electrode. (b) Impact frequency plot as a function of applied potentials.

concentration in solutions. As such, the rate constant k_{lim} was found to be $2 \pm 1 \times 10^{-2}$ cm s^{-1}. By contrast, the estimated mass transport coefficient m_T was approximately given by the equation:

$$m_T = \frac{D_{OH^-}}{\delta} \sim \frac{D_{OH^-}}{r_p} \quad (6.16)$$

where D_{OH^-} is the diffusion coefficient in the electrolyte condition, δ is the diffusion layer thickness of OH^- on the NP surfaces, r_p is the Co_3O_4 nanoparticle radius. As such, the mass transport coefficient was calculated to be *ca.* 10 cm s^{-1}, which is significantly larger than the k_{lim}. This suggests, at single particle level, that the reaction at the individual impacting NP surfaces is a surface reaction rate limited process. However, as seen above for the particle ensembles on a macroelectrode, where a linear regime of mass transport prevails, a diffusion controlled process was observed, consistent with the relatively fast heterogeneous rate constant measured.

6.3.6. Characterisation of Co_3O_4@SiO_2 NPs

Based on the successful study of hydroxide ion oxidation catalysed by bare Co_3O_4 NPs, our research turned to the novel core-shell NPs with Co_3O_4 cores and SiO_2 shells (Co_3O_4@SiO_2). First, these nanoparticles were synthesised and imaged using TEM. Figure 6.9a shows the image of a single Co_3O_4@SiO_2 NP. The core-shell structure and their quasi-spherical shapes of both parts were clearly revealed after appropriate adjustments of the image brightness and contrast, allowing the size measurements of the two different compositions. A number of synthesised particles were imaged (Figure 6.9e) and few particles were found without a core (2 out of 26), giving an average

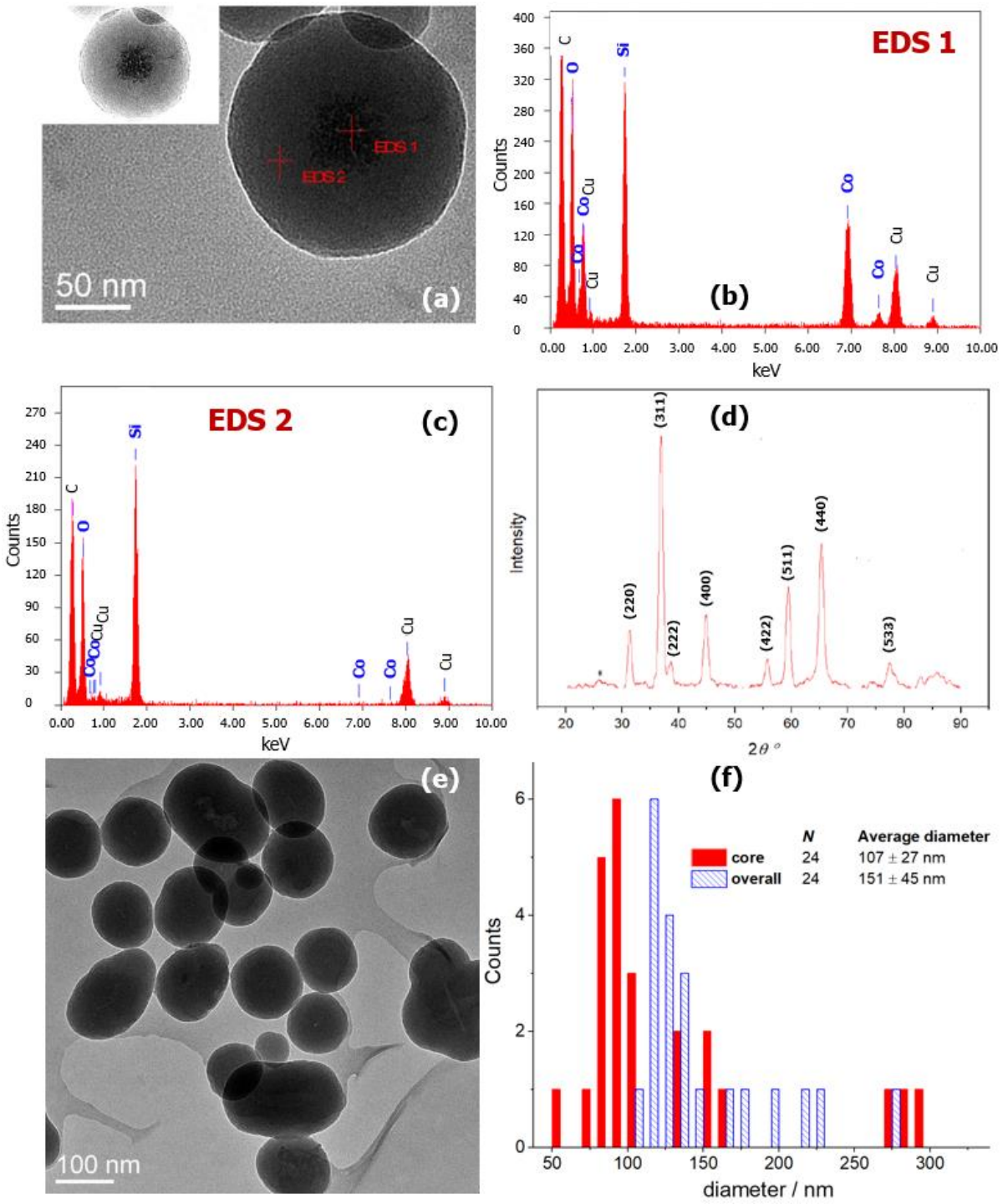

Figure 6.9. (a) TEM image of a single Co_3O_4@SiO_2 nanoparticle. Inlay shows the clear intensity profile of its core-shell structure after brightness and contrast adjustments. (b) 'EDS1' and (c) 'EDS2' are the EDS analysis measured at the correspondingly labelled spots in (a). (d) XRD pattern of Co_3O_4@SiO_2 NPs. (e) TEM images of more Co_3O_4@SiO_2 nanoparticles and (f) the measured diameters for both the cores and the entire particles.

core diameter of 107 ± 27 nm and an overall (core + shell) diameter of 151 ± 45 nm (N = 24).

Next, the chemical composition and structure of the Co_3O_4@SiO_2 NPs were measured by EDS and XRD. As labelled with 'EDS1' and 'EDS2' in Figure 6.9a, corresponding to the locations of Co_3O_4 core and SiO_2 shell, respectively, EDS measurements were performed on the two separate sites on this two-dimensional TEM image. The results (Figure 6.9b and 6.9c) showed that the element of cobalt was found only in the core position (EDS1), not in the shell position (EDS2). Both positions showed the presence of the elements of silicon and oxygen, consistent with the presence of silica. The detection of SiO_2 in the image of the core is anticipated as the silica shell will be present above and below the cores on the third spatial dimension. Moreover, the relative amount of oxygen element in the core position was higher than that in the shell position, as expected with the Co_3O_4 cores having a higher density of atomic oxygen (1.0×10^5 mol m^{-3}) than that of SiO_2 (7.2×10^4 mol m^{-3}) assuming the density of the material is not significantly altered from that of the bulk. These observations are consistent with a composite structure of the cobalt oxide cores with silica shells. Further, the measured XRD pattern (Figure 6.9d) confirmed the chemical identity of the cobalt oxide cores as Co_3O_4.

6.3.7. Cyclic voltammetry of Co_3O_4@SiO_2 NPs

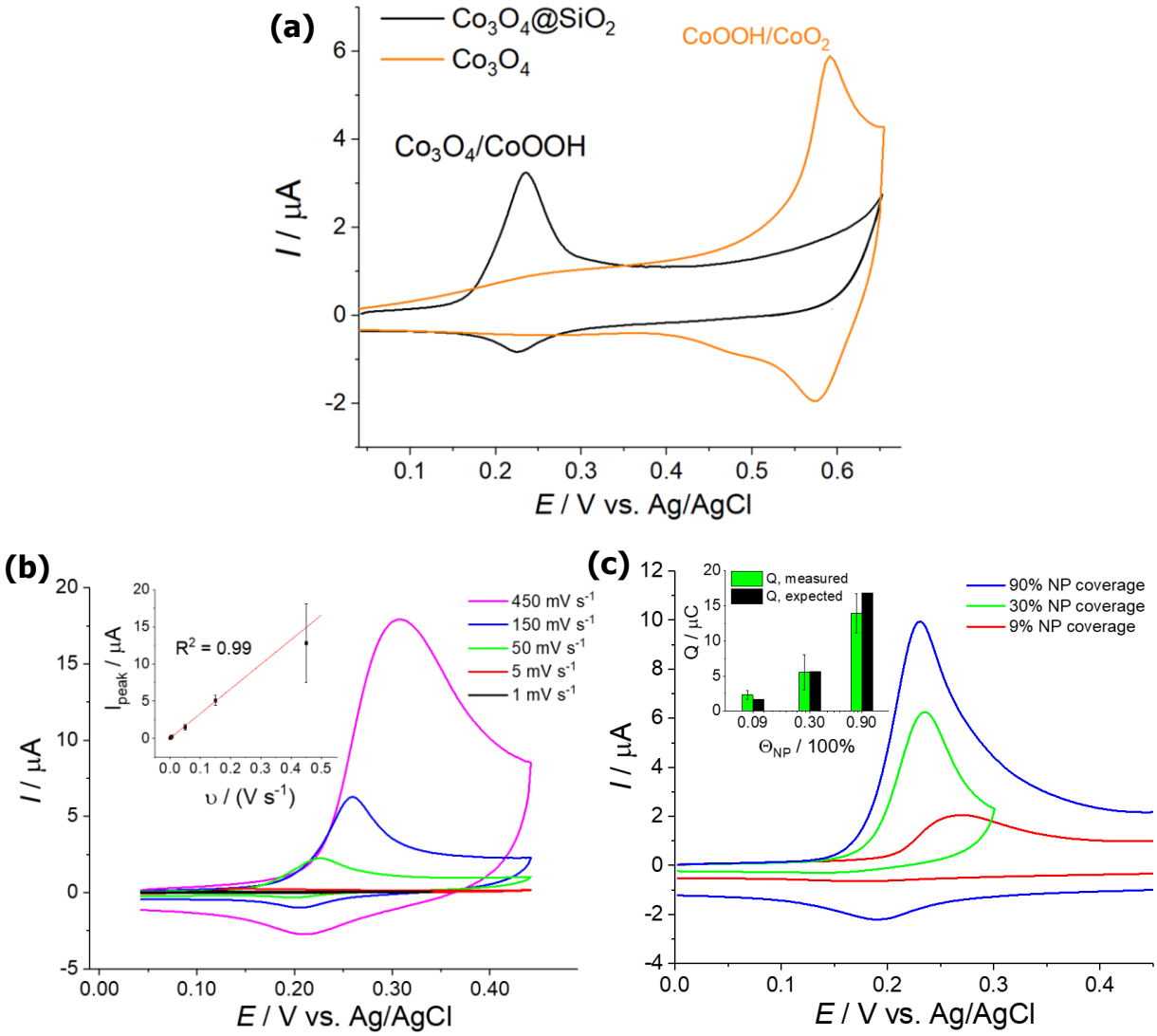

Figure 6.10. (a) Anodic CVs of a 3 mm-diameter GC electrode modified with Co_3O_4@SiO_2 NPs immersed in 0.1 M KCl + 20 mM KOH solutionsm, in comparison with that of the bare Co_3O_4 NPs. Scan rate 50 mV s^{-1}. (b) The CVs measured at varying scan rates of 5 to 450 mV s^{-1}. Inlay is the plot of peak current as a function of scan rate. (c) The CVs measured at varying NP surface coverages of 9% to 90% of a monolayer with a scan rate of 50 mV s^{-1}. Inlay is the plot of charge measured from the peak area as a function of NP coverage.

To check for electro-activity of the synthesised Co_3O_4@SiO_2 NPs, we performed cyclic voltammetry first from 0 V to +0.65 V. Specifically, the CV of a glassy carbon macroelectrode modified with 0.6 μg of Co_3O_4@SiO_2 NPs, equivalent to an NP coverage of *ca.* 30% (See Appendix 5a), was recorded in the same electrolyte as used above, namely 20 mM KOH + 0.1 M KCl. Surprisingly, a single oxidation peak was observed occurring at *ca.* +0.2 V (Figure 6.10a), a very similar potential to that of the oxidation peak of Co_3O_4 to CoOOH found in the CVs of drop-cast Co_3O_4 NPs. Further studies show that (Figure 6.10b) the peak current was found to be directly proportional to the scan rate, indicating the oxidation of a surface-bound species. Moreover, a small reduction peak in the backward scan was seen, with a peak-to-peak separation of 10 mV with the oxidation peak, suggesting the quasi-reversibility of the surface oxidation process. The mid-potential ($E_{1/2}$ = 0.230 V) of the peak pair was close to the thermodynamic potential (+0.22 V vs. Ag/AgCl) for the electrode couple of Co_3O_4/CoOOH. Also importantly, Figure 6.10c shows that the oxidative charge transferred was proportional to the nanoparticle surface coverage/loading on the carbon electrode surface; and the amounts of the charge measured were consistent with the assumption that only one monolayer of the surfaces of the Co_3O_4 cores was oxidised to CoOOH (See Appendix 5b). These observations strongly confirmed that the oxidation peak at 0.2 V was due to the reaction 6.4. That said, the Co_3O_4 cores remained electro-active despite the present silica shells. Given that the average shell thickness is 22 nm, much bigger than the usual electron tunnelling distance (1~2 nm), the shells were considered either highly porous and/or at least some were broken.[39]

On the other hand, an unusual behaviour associated with the pH dependence of this process was discovered. Figure 6.11a shows that the peak potential shift with pH was found to be -80 ± 30 mV / pH, which deviated from the Nernstian slope of -59 mV /

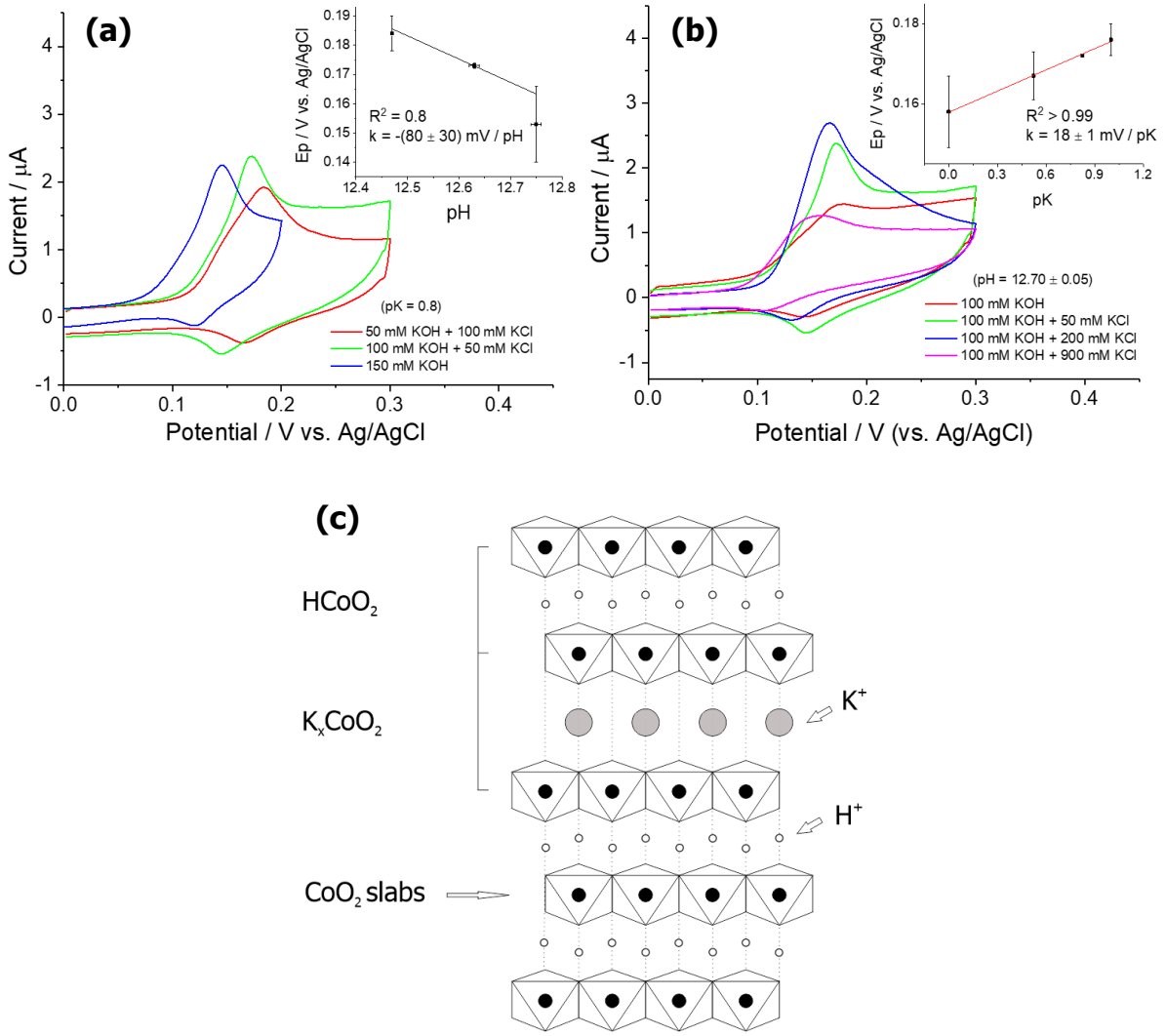

Figure 6.11. (a) Voltammograms of the oxidation of Co_3O_4@SiO_2 NPs using GC electrodes at varying pH from 12.30 to 12.75 with a fixed potassium cation concentration of 0.15 M. (b) Voltammograms of the oxidation of Co_3O_4@SiO_2 NPs using GC electrodes at varying pK (pK = -log[K^+]) from 0 to 1.0 with a fixed pH of 12.70 ([KOH] = 0.1 M), measured by a pH meter. (c) Schematic illustration of the suggested interstratified slab packing in the alkali-metal cation inserted cobalt oxyhydroxide structure. Adapted from Ref [58] for K^+ cations.

pH (298 K). This suggested a possible involvement of another chemical process. It is proposed in the literature[58] that, as shown in the Figure 6.11c, an alkali-metal cation intercalated structure may exist for cobalt oxyhydroxide (CoOOH). To explore whether the oxidation process was accompanied with the insertion of K^+ used in our experiements forming the intercalated structure, the CVs were also recorded in the solutions of different KCl concentrations at a fixed pH of 12.70. Consequently, Figure 6.11b shows that the peak potential indeed varied in a way the electrode reaction was favoured by a higher concentration of potassium cation at a slope of 18 ± 1 mV per pK ($pK = -\log[K^+]$). It follows that the formation of CoOOH on the surface of the NP cores probably involves partial K^+ insertion. Therefore, the oxidation mechanism of Co_3O_4 cores was modified to

$$Co_3O_4 + (0.31\pm0.02)\ K^+ + (0.64\pm0.51)\ H_2O + (1.36\pm0.51)\ OH^- \rightarrow$$
$$3\ CoOO(H_{0.88\pm0.43}K_{0.11\pm0.1}) + e^- \qquad (6.17)$$

Possibly, the formation of the K^+ inserted CoOOH inhibited their further oxidation to CoO_2. Similar experiments were attempted on the CVs of drop-cast Co_3O_4 NPs but unsuccessful due to the difficulty in defining the precise peak potential of the not well-defined peaks.

6.3.8. Cyclic voltammetry of OH^- oxidation mediated by $Co_3O_4@SiO_2$ NPs

To investigate the activity of the Co_3O_4 cores towards OH^- oxidation, the potential region of the CV was extended to a more positive potential of +1.2 V and then to the

negative potential of -1.5 V. Strikingly, an almost identical oxidation wave with a peak potential of 1.0 V to the one found in the CV of bare Co_3O_4 NPs was seen (see Figure 6.12). No peaks were observed in the potential region when using modified electrodes with SiO_2 NPs of a similar size (see Figure 6.18 in Appendix 6) to those of the two types of 'cobalt' particles. These observations therefore evidenced that the cobalt oxide cores were also electro-active towards the OH^- oxidation despite the silica shell which was thus inferred to be imperfect. In the cathodic potential region of 0 to -1.5 V, a very similar reduction wave with a peak potential of -1.1 V, with a shoulder peak at -0.6 V, was seen. The peak potentials were consistent with those found in the CVs of bare Co_3O_4 NPs (see Section 6.3.4), therefore indicating that the product of OH^- oxidation catalysed by the Co_3O_4 cores was also very likely H_2O_2.

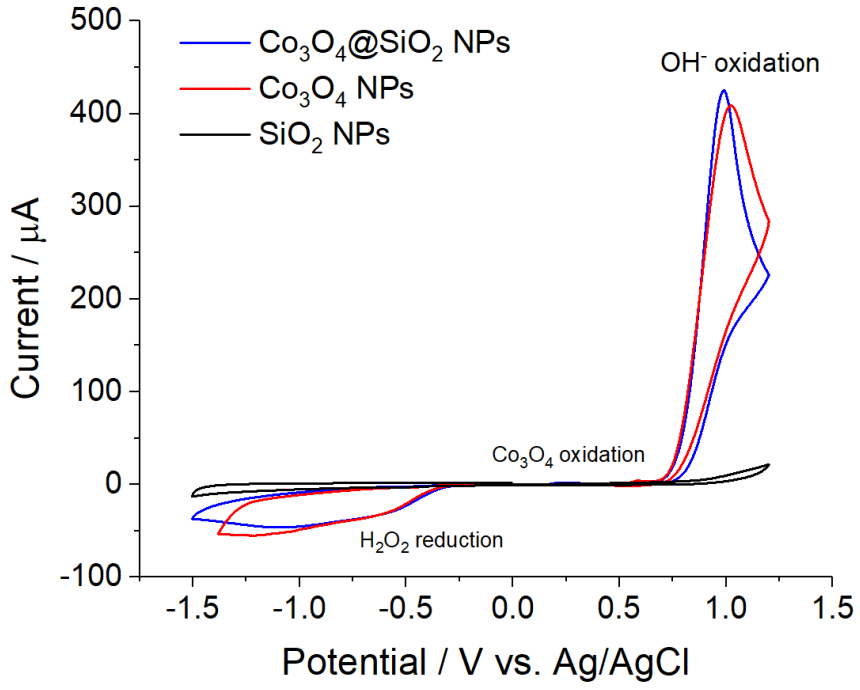

Figure 6.12. Overall CVs of modified GC electrodes (*d* = 3.00 mm, NP surface coverage *ca.* 30% of a monolayer) with Co_3O_4@SiO_2 NPs (blue), Co_3O_4 NPs (red) and SiO_2 NPs (black) in N_2-saturated 0.1 M KCl + 20 mM KOH solutions. Scan rate 50 mV s^{-1}.

Considering the reaction process of the core oxidation, we discovered that the oxidation mechanism of OH^- on the Co_3O_4@SiO_2 may be slightly different from the one for the mediated reaction by bare Co_3O_4 NPs. In the KOH solutions with a concentration of 20 mM, the voltammograms at a much higher scan rate of 0.5 V s^{-1} (Figure 6.13a) remained similar with no more features observed. However, using a KOH solution with a much lower concentration of 1 mM and at the higher scan rates of 0.5 V s^{-1}, a reductive counterpart of the oxidation wave with a peak potential of nearly +0.75 V was observed (Figure 6.13b)! This was tentatively attributed to the immediate reduction of the electro-generated HO• radicals from OH^- oxidation (see below). In contrast, for the voltammograms of bare Co_3O_4 NPs (Figure 6.13c and 6.13d) under the same conditions, apart from the increase of the seemingly adsorption peak (at +0.45 V in 20 mM KOH and +0.55 V in 1 mM KOH) which was associated with NP oxidation as seen before, the back peak of the OH^- oxidation was not observed. This may suggest that the silica shell is not passive but rather may be able to stabilise the short-lived HO•, as supported by the observations on SiO_2 of this radical as an reaction intermediate in the literature.[59-60] Hence, the reaction mechanism of OH^- oxidation mediated by Co_3O_4@SiO_2 NP was modified to

$$OH^- \xrightarrow{Co_3O_4(s)} HO\bullet + e^- \quad (6.18)$$

$$HO\bullet \overset{SiO_2}{\rightleftharpoons} HO\bullet\ (ads) \quad (6.19)$$

$$HO\bullet\ (ads) + e^- \rightarrow OH^-\ (\text{at fast scan rates}) \quad (6.20)$$

$$HO\bullet\ (ads) \rightarrow \tfrac{1}{2}\ H_2O_2\ (\text{at slow scan rates}) \quad (6.21)$$

where the observation of the concentration dependence of the visibility of the back peak is consistent with the likely second order kinetics for HO• dimerisation.

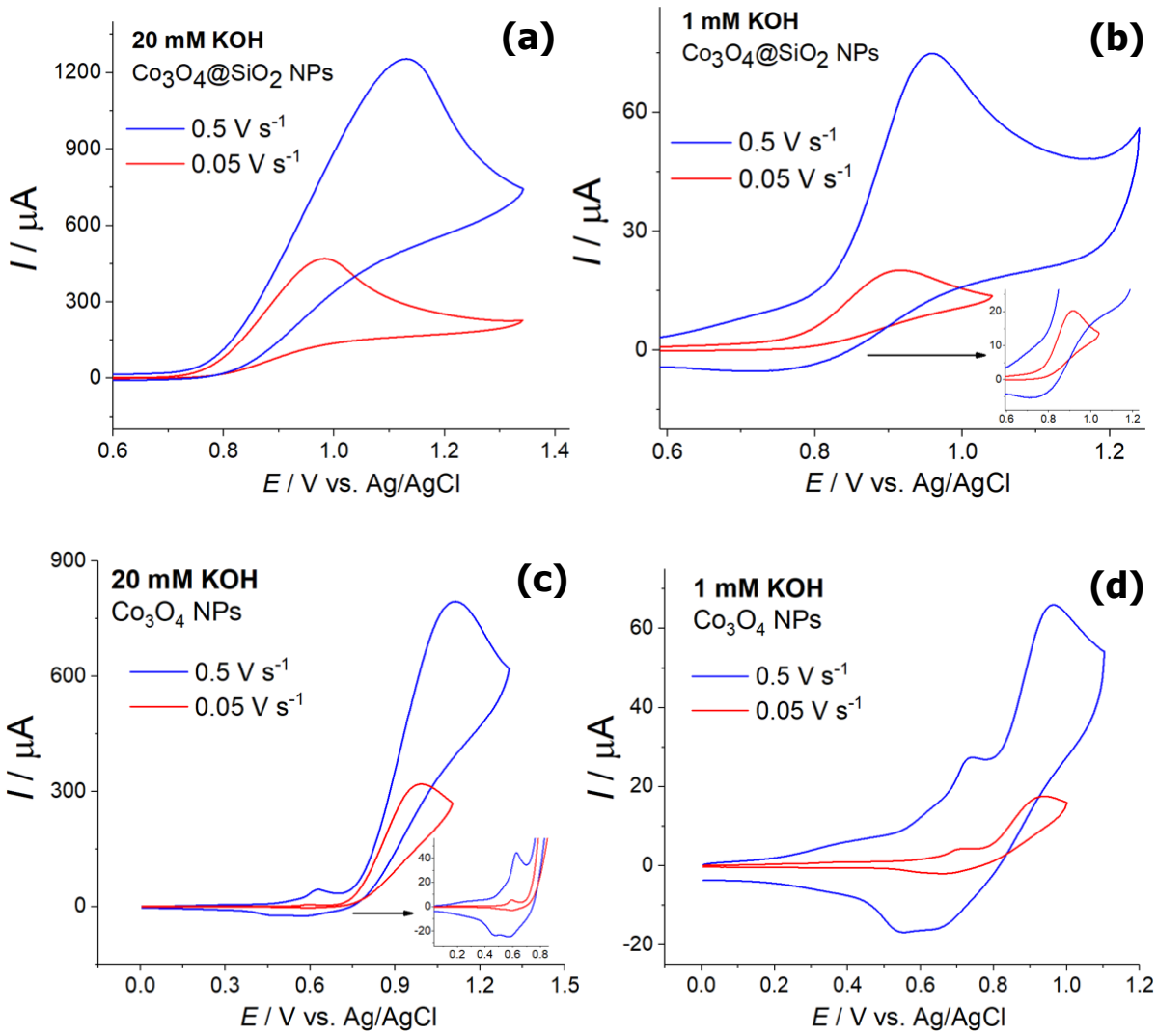

Figure 6.13. Anodic voltammograms of modified GC electrodes with Co_3O_4@SiO_2 NPs in 0.1 M KCl solutions containing (a) 0.1 M KCl + 20 mM KOH, (b) 0.1 M KCl + 1 mM KOH; and with bare Co_3O_4 NPs in (c) 0.1 M KCl + 20 mM KOH, (d) 0.1 M KCl + 1 mM KOH. Scan rate 0.05 and 0.5 V s^{-1}.

6.3.9. Single particle electrochemistry of Co_3O_4@SiO_2 NPs

Having evidenced that the silica-coated Co_3O_4 NPs catalysed the OH^- oxidation in a similar way to the bare Co_3O_4 particles, and that the impact step currents of single

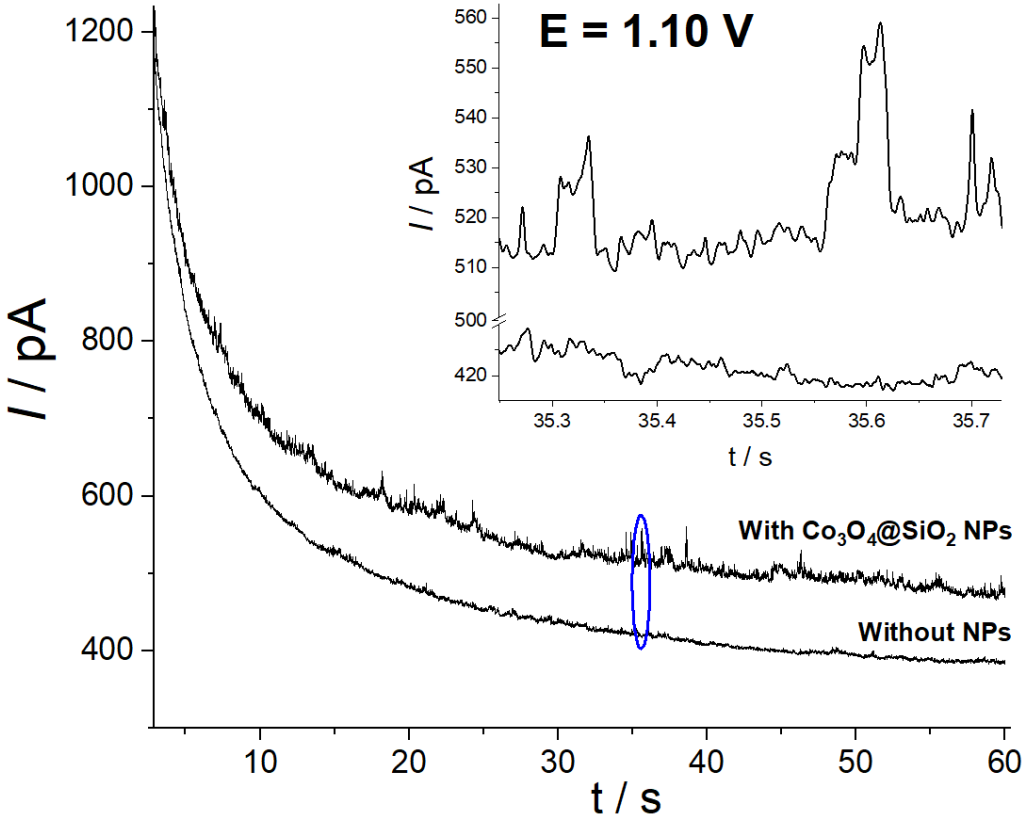

Figure 6.14. (a) Chronoamperograms (at 1.10 V vs. Ag/AgCl) of a clean carbon micro-disc electrode (d=7 μm) immersed in a 20 mM KOH + 0.1 M KCl solution with and without 42 pM Co_3O_4@SiO_2 NPs. Inlay shows the examples of current spikes and steps from the current-time traces highlighted by the blue circle.

Co_3O_4 NPs levelled out above +1.0 V vs. Ag/AgCl (i.e. the peak potential as seen from the voltammograms of drop-cast Co_3O_4), we briefly performed the nano-impacts of the core-shell NPs at a very oxidising potential of 1.1 V to compare their *limiting* catalytic activity with that of the bare Co_3O_4 NPs at the single particle level. Experimentally, chronoamperometry of a clean carbon micro-disc electrode dipped in a solution of 20 mM KOH + 0.1 M KCl in the absence of Co_3O_4@SiO_2 NPs at a fixed potential of 1.10 V was recorded. Very few signals (in total N = 3 within 180 s) were found on the fluctuating baseline (Figure 6.14). In the presence of *ca.* 40 pM

Co_3O_4@SiO_2 NPs, a total number of 151 current transients were detected, evidencing the impacts of the core-shell NPs with the electrode surface. The distribution of the impact durations for both spike- and step-shaped transients shows a continuum with no obvious discreteness in the cumulative frequency plot (see Figure 6.19 in Appendix 7), and therefore the spike-shaped transients were considered simply as the step-shaped transients of a shorter duration. Moreover, these transients have much shorter durations of 39 ± 24 ms than those of the current steps for the impacts of the bare Co_3O_4 NPs (130 ± 40 ms) despite the lower diffusional mobility of the larger coated particles. This may result from the coating of insulating silica on the Co_3O_4 cores that possibly leads to a decreased quality of electrical contact formed upon the impacts between the particles and the carbon electrode surface. At the potentials more negative than +0.7 V, No impact signals were found (see Figure 6.20 in Appendix 8). As such, the threshold potential, above which the current steps were found in the impact experiments of individual Co_3O_4 NPs, is found to be almost that of the catalytic current in the CV of drop-cast Co_3O_4 ensembles. The latter is also very similar to the potential found in the CV of drop-cast Co_3O_4@SiO_2 NPs. Consequently, it is inferred that those current transients were due to the catalysis of the impacting NPs towards the OH^- oxidation.

The catalytic impact responses of the core-shell NPs have an average frequency of 0.84 ± 0.16 s^{-1}, consistent with the predicted 0.70 s^{-1} assuming a steady-state diffusional flux of the NPs towards the electrode surface. This confirms the impacts of individual *single* core-shell NPs, as well as no sedimentation in their colloidal

suspension, unlike the bare Co_3O_4 NPs, which is consequently attributed to the SiO_2 shells preventing particle agglomeration.[61]

Figure 6.15 (blue curve) depicts the current distribution of the impact transients, giving a mean impact current of 12.2 ± 3.5 pA. Since the catalysis reaction occurred at the particle-solution interface, the current measured is expected to be proportional to the electro-active surface area of the individual impacting NPs. At this time, it is reminded that from the electron microscopic measurements, the core diameter of the Co_3O_4@SiO_2 NPs was 107 ± 27 nm and the particle diameter of Co_3O_4 NPs 75 ± 22 nm, giving a surface area ratio of 2.0 ± 0.8. Then for a straight comparison on the relative sizes of the two types of particles based on the impact currents, the current height distribution of the transient responses measured from the impact experiments of Co_3O_4 NPs is also plotted (the red curve in Figure 6.15), giving an average impact current of 6.4 ± 4.2 pA. As such, the current of the Co_3O_4 cores was found to be 1.9 ± 1.4 times that of the bare Co_3O_4 NPs, suggesting the same ratio of the surface area of a single Co_3O_4 core to that of a bare Co_3O_4 NP, which agrees well with that measured using electron microscopy. Summarily presented in the inlay is the strong correlation between the measured impact currents and the estimated particle surface areas of the two types of particles. These results, therefore, show at the single particle level, the preserved electro-activity of the silica-coated Co_3O_4 NPs from the bare ones and hence further supports the inference of the imperfection of the silica shells.

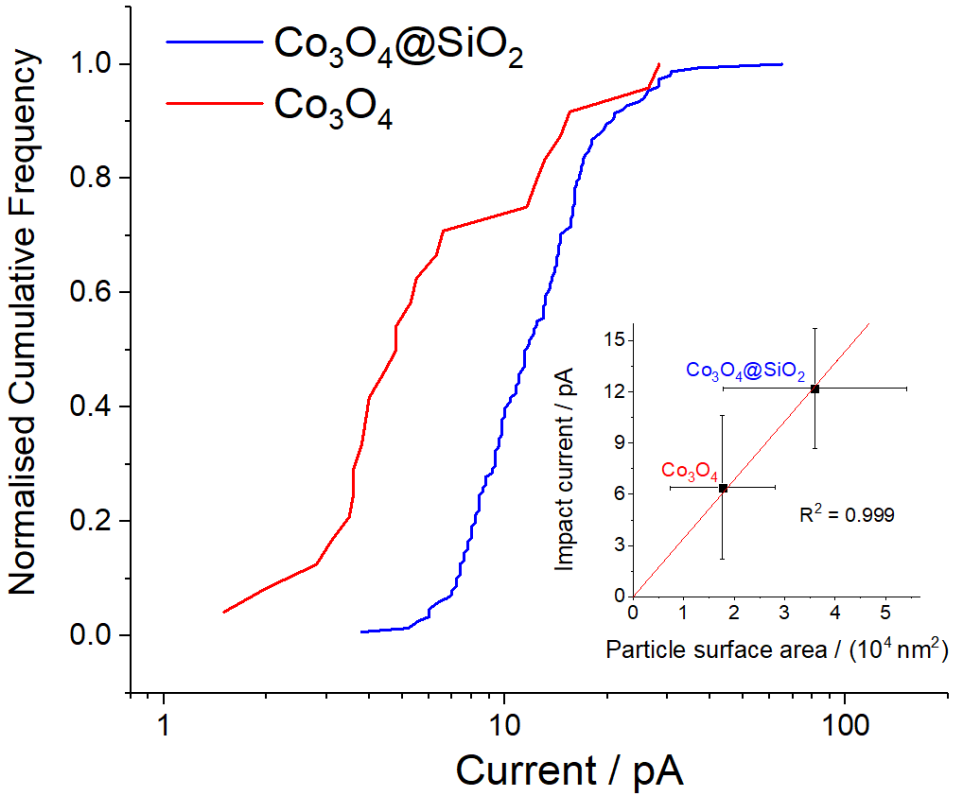

Figure 6.15. (a) Cumulative frequency (normalised to the total number of impact events) as a function of measured current for the impact transients measured in the impact experiments of Co_3O_4@SiO_2 NPs (blue) and Co_3O_4 NPs (red). Inlay is the correlation chart between the impact current and the Co_3O_4 surface area of individual particles. Note that the standard deviation bars reflect more the width of the current/surface area distribution than the measurement errors. The linear fitting shows a coefficient of determination (R^2) as 0.999.

6.4. Conclusions

Co_3O_4 nanoparticles have been shown to be an effective electro-catalyst for hydroxide ion oxidation with *hydrogen peroxide* rather than dioxygen as the predominant initial oxidation product of the electron transder. Single particle electrochemistry further indicated that the rate of this catalysis is limited by the rate of the surface catalytic process. Further, silica-coated Co_3O_4 nanoparticles were synthesised and their

structures were characterised *via* a combination of TEM, EDS and XRD techniques. Similar electrochemistry results to those of bare Co_3O_4 nanoparticles were obtained and our studies demonstrated generally unchanged electro-catalytic activity towards OH^- oxidation, therefore suggesting the imperfect coating of the Co_3O_4@SiO_2 NPs. Last, but not least, the UV spectroscopy shows the catalytic activity of Co_3O_4 NPs towards the chemical decomposition of H_2O_2. As studies have also shown their electro-catalytic activity towards oxygen reduction reaction, this may in turn offer a mechanistic pathway for a 4-electron reduction to water *via* hydrogen peroxide as an initial reaction intermediate, with Co_3O_4 NPs thus acting as bifunctional electrochemical and chemical catalysts, as shown for Fe_2O_3 NPs.[23]

Appendices

1. Conversion of the potentials against Ag/AgCl to those against Reversible Hydrogen Electrode (RHE)

For convenience, a conversion of the potentials against Ag/AgCl to those against RHE is provided:

$$E_{RHE} = E_{Ag/AgCl} + E^o_{Ag/AgCl} + 0.0591 \times pH$$

where E_{RHE} is the potentials against RHE, $E_{Ag/AgCl}$ is the potential against Ag/AgCl applied directly in the experiments and $E^o_{Ag/AgCl}$ is the standard electrode potential of the silver/silver chloride reference electrode used in the experiment that equals to +0.205 V in the 298 K.

2. Calculations regarding drop-cast voltammograms of Co_3O_4 NPs

(a) Charge estimation

In the case of complete oxidation, 0.60 μg of Co_3O_4 NPs contains 1.5×10^{15} Co_3O_4 molecules, and assuming complete oxidation of the NPs *via* the one electron transfer process to CoOOH, using the Faraday law of electrolysis the expected total oxidation charge is calculated to be 240 μC.

In the case of surface-only oxidation, assuming perfect spheres of the NPs, one 75 nm-diameter Co_3O_4 NP is calculated to contain 3.4×10^6 Co_3O_4 molecules; and knowing the dimensions of the crystal structure is $(8.0\ Å)^3$ for the occupations of 8 $Co^{II}Co^{III}_2O_4$ such that on average each Co_3O_4 molecule has a projection area of 16 $Å^2$, one 75 nm-diameter Co_3O_4 NP is calculated to contain 1.1×10^5 surface Co_3O_4 units. In the experiments, 0.60 μg of Co_3O_4 particles corresponds to 4.4×10^8 such NPs and therefore 4.8×10^{13} surface Co_3O_4 molecules. As such, using the Faraday law of electrolysis the total expected oxidation charge for surface-only process of the 4-electron transfer (per Co_3O_4 molecule) oxidation reaction of Co_3O_4 to CoO_2 is 31.4 μC.

(b) Surface coverage

The average diameter of the Co_3O_4 NPs was characterised by SEM as 75 nm (Figure 1c). Provided that the total drop-cast weight is 0.6 μg, and assuming the nanoparticles were perfect spheres and evenly distributed throughout the GC electrode surface (d=3.00 mm), the total projection area occupied by these NPs is then calculated to be

2.5 × 10^{-6} m^2. Therefore, the NP surface coverage on this electrode is 35% (of a monolayer).

3. Tafel analysis

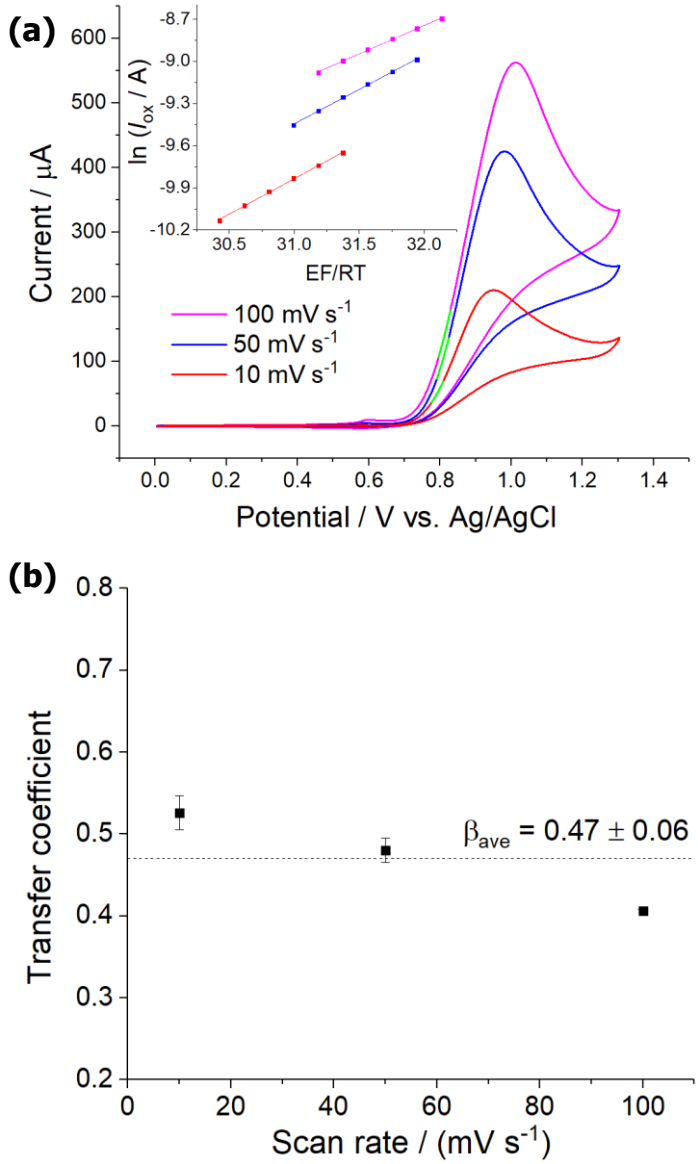

Figure 6.16. a) Cyclic voltammograms of the hydroxide ion oxidation with the Tafel regions highlighted by green segments (20-30% of peak currents). Scan rates 10, 50, 100 mV s^{-1}. Inlay shows the linearity between the natural logarithm of oxidative current and the applied potentials in the Tafel plots. b) Transfer coefficients (β) plot as a function of scan rate.

4. Blank experiments of nano-impacts of Co_3O_4 nanoparticles

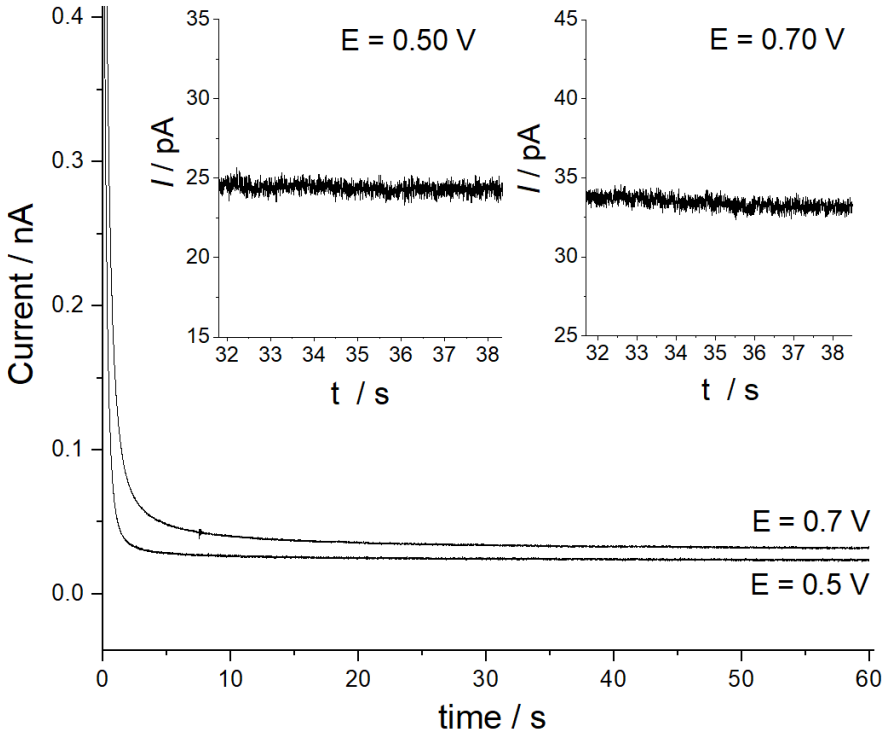

Figure 6.17. Chronoamperograms of a carbon microdisc electrode at +0.7 and +0.5 V vs. Ag/AgCl in a 10 mg mL^{-1} suspension of Co_3O_4 NPs containing 20 mM KOH and 0.1 M KCl. Inlay shows typical enlarged regions from *ca.* 32-38 seconds measured at 0.7 and 0.5 V, respectively.

5. Calculations regarding drop-cast voltammograms of Co_3O_4@SiO_2 NPs

(a) Surface coverage

As TEM characterisation has shown the shapes of both overall particles and the cores as quasi-spherical, for calculation the shapes were assumed as perfect spheres. Having the data of the radius of the overall particles (75.5 nm) and the cores (53.5 nm), density and molecular weight of Co_3O_4 and SiO_2, which were assumed not altered from their bulk form, we can calculate the mass fraction of a Co_3O_4 core in a single core-shell particle *via* the equation

$$\varepsilon = \frac{\frac{4}{3}\pi {r_{Co3O4}}^3 \rho_{Co3O4}}{\frac{4}{3}\pi {r_{Co3O4}}^3 \rho_{Co3O4} + \frac{4}{3}\pi \left({r_{overall}}^3 - {r_{Co3O4}}^3\right) \rho_{SiO2}} \quad (6.22)$$

where ε is the mass fraction of a Co_3O_4 core in a single core-shell particle, r_{Co3O4} and $r_{overall}$ are the average radius of the particle cores and the entire particles measured from TEM; ρ_{Co3O4} and ρ_{SiO2} are the densities of the particle cores (6.11 g cm^{-3}) and the shells (2.20 g cm^{-3}) assuming unchanged values from those of their bulk forms. Consequently, the mass fraction was calculated to be 60.6%. Provided that the total drop-cast weight is 0.6 μg, corresponding to a total number of 9.3×10^7 core-shell NPs, and assuming the nanoparticles were evenly distributed throughout the GC electrode surface (d=3.00 mm), the total projection area occupied by these NPs is then calculated to be 2.1×10^{-6} m^2. Therefore, the NP surface coverage on this electrode is 30% of a monolayer.

(b) Charge estimation

In the case of Co_3O_4 surface-only oxidation, assuming perfect spheres of the NPs, one 107 nm-diameter Co_3O_4 NP was calculated, in a same way to the calculation for the bare Co_3O_4 NPs, to contain 2.2×10^5 surface Co_3O_4 molecules. The amount of drop-cast core-shell NPs (total weight is 0.6 μg for the 30% coverage for instance) on the GC macroelectrode was calculated to be 9.3×10^7. Consequently, the expected oxidation charge for one monolayer of surface Co_3O_4 of all the drop-cast particle, in the case of 30% coverage, through their one-electron oxidation to CoOOH was 3.3 μC.

6. TEM sizing of SiO_2 nanoparticles

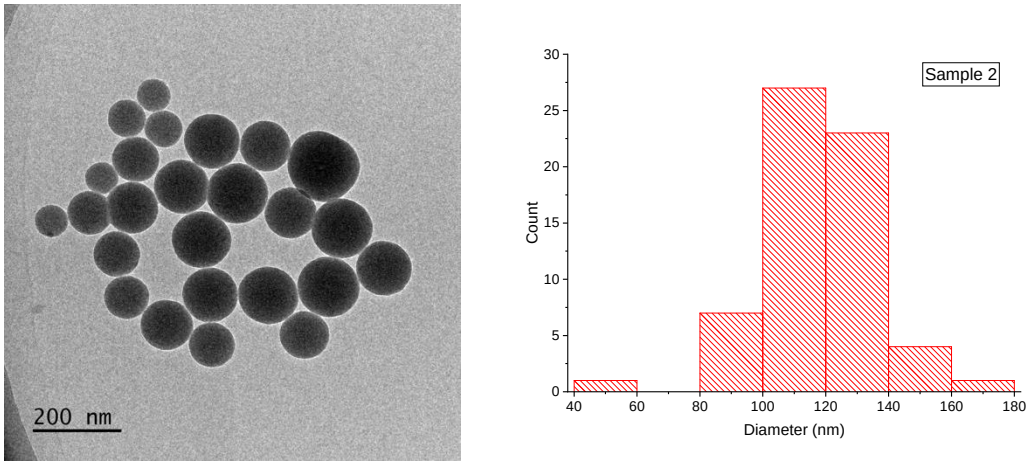

Figure 6.18. TEM image and size distribution of SiO_2 NPs with an average diameter of *ca.* 120 nm.

7. Duration distribution of impacts of Co_3O_4@SiO_2 nanoparticles

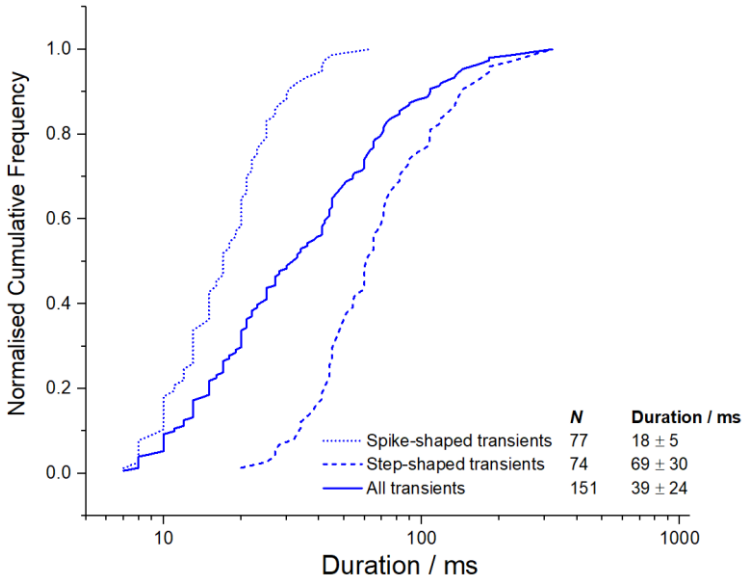

Figure 6.19. Distributions of impact duration of spike-shaped transients (dotted curve) and step-shaped transients (dashed curve) and all measured transients (solid curve).

8. Blank experiments of nano-impacts of Co_3O_4@SiO_2 nanoparticles

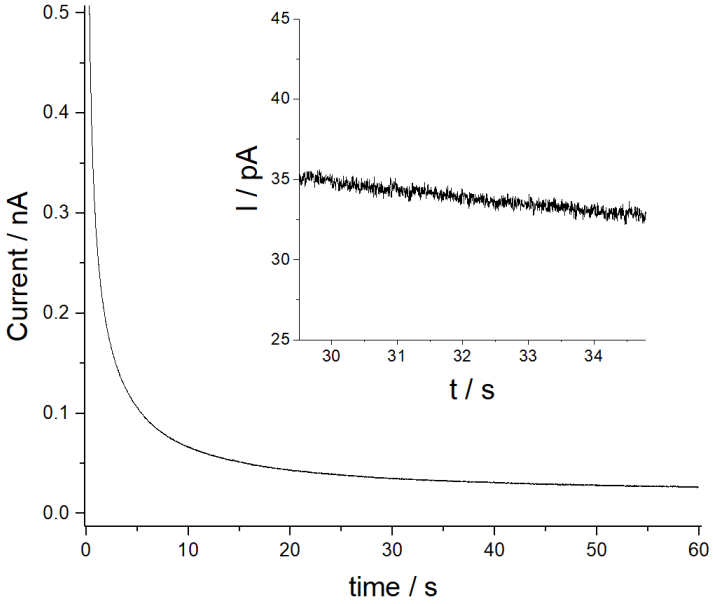

Figure 6.20. Chronoamperogram of a carbon microdisc electrode at +0.7 V vs. Ag/AgCl in a 42 pM suspension of Co_3O_4 NPs containing 20 mM KOH and 0.1 M KCl. Inlay shows typical enlarged regions from *ca.* 32-34 seconds.

References

[1] R.-C. Xie, M. Volokhova, A. Boldin, L. Seinberg, M. Tsujimoto, M. Yang, B. Rasche, R. G. Compton, *ChemElectroChem* **2020**, *7*, 1216-1276.

[2] T. Zhang, C. He, F. Sun, Y. Ding, M. Wang, L. Peng, J. Wang, Y. Lin, *Sci. Rep.* **2017**, *7*, 43638.

[3] H. Ha, K. Jin, S. Park, K.-G. Lee, K. H. Cho, H. Seo, H.-Y. Ahn, Y. H. Lee, K. T. Nam, *J. Phys. Chem. Lett.* **2019**, *10*, 1226-1233.

[4] G. Rajeshkhanna, G. R. Rao, *Int. J. Hydrogen Energy* **2018**, *43*, 4706-4715.

[5] E. Zhang, Y. Xie, S. Ci, J. Jia, Z. Wen, *Biosens. Bioelectron.* **2016**, *81*, 46-53.

[6] Y. Liang, Y. Li, H. Wang, J. Zhou, J. Wang, T. Regier, H. Dai, *Nat. Mater.* **2011**, *10*, 780.

[7] L. Xu, Q. Jiang, Z. Xiao, X. Li, J. Huo, S. Wang, L. Dai, *Angew. Chem. Int. Ed.* **2016**, *55*, 5277-5281.

[8] M. Hamdani, R. Singh, P. Chartier, *Int. J. Electrochem. Sci.* **2010**, *5*, 556-577.

[9] I.-H. Yeo, PhD thesis, Iowa State University (US), 1987.

[10] C. C. McCrory, S. Jung, J. C. Peters, T. F. Jaramillo, *J. Am. Chem. Soc.* **2013**, *135*, 16977-16987.

[11] B. Su, Z.-C. Cao, Z.-J. Shi, *Acc. Chem. Res.* **2015**, *48*, 886-896.

[12] B. S. Yeo, A. T. Bell, *J. Am. Chem. Soc.* **2011**, *133*, 5587-5593.

[13] Z. Zhuang, W. Sheng, Y. Yan, *Adv. Mater.* **2014**, *26*, 3950-3955.

[14] S. Liu, L. Li, H. S. Ahn, A. Manthiram, *J. Mater. Chem. A* **2015**, *3*, 11615-11623.

[15] J. Wu, Y. Xue, X. Yan, W. Yan, Q. Cheng, Y. Xie, *Nano Res.* **2012**, *5*, 521-530.

[16] Y.-R. Liu, G.-Q. Han, X. Li, B. Dong, X. Shang, W.-H. Hu, Y.-M. Chai, Y.-Q. Liu, C.-G. Liu, *Int. J. Hydrogen Energy* **2016**, *41*, 12976-12982.

[17] J. D. Blakemore, H. B. Gray, J. R. Winkler, A. M. Müller, *ACS Catal.* **2013**, *3*, 2497-2500.

[18] J. A. Koza, Z. He, A. S. Miller, J. A. Switzer, *Chem. Mater.* **2012**, *24*, 3567-3573.

[19] A. J. Esswein, M. J. McMurdo, P. N. Ross, A. T. Bell, T. D. Tilley, *J. Phys. Chem. C* **2009**, *113*, 15068-15072.

[20] N. H. Chou, P. N. Ross, A. T. Bell, T. D. Tilley, *ChemSusChem* **2011**, *4*, 1566-1569.

[21] S. Chen, Y. Zhao, B. Sun, Z. Ao, X. Xie, Y. Wei, G. Wang, *ACS Appl. Mater. Interfaces* **2015**, *7*, 3306-3313.

[22] T. Watanabe, Y. Einaga, *Anal. Chem.* **2017**, *89*, 7139-7144.

[23] K. Shimizu, L. Sepunaru, R. G. Compton, *Chem. Sci.* **2016**, *7*, 3364-3369.

[24] C. C. Neumann, E. Laborda, K. Tschulik, K. R. Ward, R. G. Compton, *Nano Res.* **2013**, *6*, 511-524.

[25] H. S. Toh, C. Batchelor-McAuley, K. Tschulik, M. Uhlemann, A. Crossley, R. G. Compton, *Nanoscale* **2013**, *5*, 4884-4893.

[26] S. J. Cloake, H. S. Toh, P. T. Lee, C. Salter, C. Johnston, R. G. Compton, *ChemistryOpen* **2015**, *4*, 22-26.

[27] X. Li, H. Hodson, C. Batchelor-McAuley, L. Shao, R. G. Compton, *ACS Catal.* **2016**, *6*, 7118-7124.

[28] X. Jiao, C. Batchelor-McAuley, C. Lin, E. Kätelhön, E. E. Tanner, N. P. Young, R. G. Compton, *ACS Catal.* **2018**, *8*, 6192-6202.

[29] X. Li, C. Batchelor - McAuley, S. A. Whitby, K. Tschulik, L. Shao, R. G. Compton, *Angew. Chem. Int. Ed.* **2016**, *55*, 4296-4299.

[30] X. Li, C. Lin, C. Batchelor-McAuley, E. Laborda, L. Shao, R. G. Compton, *J. Phys. Chem. Lett.* **2016**, *7*, 1554-1558.

[31] C. Lin, R. G. Compton, *J. Phys. Chem. C* **2017**, *121*, 2521-2528.

[32] A. N. Sekretaryova, M. Y. Vagin, A. P. Turner, M. Eriksson, *J. Am. Chem. Soc.* **2016**, *138*, 2504-2507.

[33] L. Han, W. Wang, J. Nsabimana, J.-W. Yan, B. Ren, D. Zhan, *Faraday Discuss.* **2016**, *193*, 133-139.

[34] E. Kätelhön, L. Sepunaru, A. A. Karyakin, R. G. Compton, *ACS Catal.* **2016**, *6*, 8313-8320.

[35] T. Albrecht, S. Horswell, L. Allerston, N. Rees, P. Rodriguez, *Curr. Opin. Electrochem.* **2018**, *7*, 138-145.

[36] N. V. Rees, *Electrochem. Commun.* **2014**, *43*, 83-86.

[37] S. V. Sokolov, S. Eloul, E. Kätelhön, C. Batchelor-McAuley, R. G. Compton, *Phys. Chem. Chem. Phys.* **2017**, *19*, 28-43.

[38] K. J. Stevenson, K. Tschulik, *Current Opinion in Electrochemistry* **2017**, *6*, 38-45.

[39] K. Tschulik, K. Ngamchuea, C. Ziegler, M. G. Beier, C. Damm, A. Eychmueller, R. G. Compton, *Adv. Funct. Mater.* **2015**, *25*, 5149-5158.

[40] L. R. Holt, B. J. Plowman, N. P. Young, K. Tschulik, R. G. Compton, *Angew. Chem. Int. Ed.* **2016**, *55*, 397-400.

[41] Maria Volokhova, Aleksei Boldin, Joosep Link, Masahiko Tujimoto, Raivo Stern , Liis Seinberg. Submitted to Chem. Comm. in January 2020.

[42] K. Kohara, S. Yamamoto, L. Seinberg, T. Murakami, M. Tsujimoto, T. Ogawa, H. Kurata, H. Kageyama, M. Takano, *Chem. Commun.* **2013**, *49*, 2563-2565.

[43] D. Green, J. Lin, Y.-F. Lam, M.-C. Hu, D. W. Schaefer, M. Harris, *J. Colloid Interface Sci.* **2003**, *266*, 346-358.

[44] C. Batchelor-McAuley, J. Ellison, K. Tschulik, P. L. Hurst, R. Boldt, R. G. Compton, *Analyst* **2015**, *140*, 5048-5054.

[45] A. Earnshaw, N. N. Greenwood, *Chemistry of the Elements, Vol. 60*, Butterworth-Heinemann Oxford, **1997**.

[46] J. Chivot, L. Mendoza, C. Mansour, T. Pauporté, M. Cassir, *Corros. Sci.* **2008**, *50*, 62-69.

[47] M. Bajdich, M. García-Mota, A. Vojvodic, J. K. Nørskov, A. T. Bell, *J. Am. Chem. Soc.* **2013**, *135*, 13521-13530.

[48] D. Li, C. Lin, C. Batchelor-McAuley, L. Chen, R. G. Compton, *J. Electroanal. Chem.* **2018**, *826*, 117-124.

[49] S. Daniele, M. A. Baldo, C. Bragato, G. Denuault, M. E. Abdelsalam, *Anal. Chem.* **1999**, *71*, 811-818.

[50] S. H. Lee, J. C. Rasaiah, *J. Chem. Phys.* **2013**, *139*, 124507.

[51] Z. M. Galbács, L. J. Csányi, *J. Chem. Soc., Dalton Trans.* **1983**, 2353-2357.

[52] S. Sharifi, H. Shakur, A. Mirzaei, M. Hosseini, *Int. J. Nanosci. Nanotechnol.* **2013**, *9*, 51-58.

[53] R. C. Taylor, P. C. Cross, *J. Am. Chem. Soc.* **1949**, *71*, 2266-2268.

[54] Y.-S. Shen, C.-C. Lin, *Water Environ. Res* **2003**, *75*, 54-60.

[55] J. Rabani, S. O. Nielsen, *J. Phys. Chem.* **1969**, *73*, 3736-3744.

[56] A. Einstein, *Annalen der Physik* **1905**, *322*, 891-921.

[57] R. G. Compton, C. E. Banks, *Understanding Voltammetry*, 3rd ed., World Scientific, New Jersey, **2018**.

[58] M. Butel, L. Gautier, C. Delmas, *Solid State Ionics* **1999**, *122*, 271-284.

[59] E. Giamello, B. Fubini, M. Volante, D. Costa, *Colloids Surf.* **1990**, *45*, 155-165.

[60] Y. Gong, D. P. Wang, R. Wu, S. Gazi, H. S. Soo, T. Sritharan, Z. Chen, *Dalton Trans.* **2017**, *46*, 4994-5002.

[61] H. D. Ackler, R. H. French, Y.-M. Chiang, *J. Colloid Interface Sci.* **1996**, *179*, 460-469.

Chapter 7

Substrate mediated dissolution of redox active nanoparticles; electron transfer over long distances

Whilst previous chapters 3-6 investigate the physiochemical properties of metal-based nanoparticles with a major focus on the study and the use of electrochemical impacts, this chapter focuses on probing the electrochemical activity of metal nanoparticles mainly using an optical approach. Reflective dark field microscopy is used to observe the decrease in the light scattered from Ag nanoparticles immobilised on differing solid substrates. The nanoparticles are exposed to solutions containing halide ions, both at open circuit and under potentiostatic control, leading to the loss of the nanomaterial. By coupling optical and electrochemical techniques the physical origin of this transformation is demonstrated to be the electrochemical dissolution of the metal nanoparticles driven by electron transfer to ultra-trace dissolved oxygen. The dissolution kinetics of the surface-supported metal nanoparticles are compared on four substrate materials (i.e. glass, indium titanium oxide, glassy carbon and platinum) with varying electrical conductivity. The three conductive substrates catalyse the redox-driven dissolution of Ag nanoparticles with the electrons transferred from the nanoparticles, via the macroscopic electrode to the dioxygen electron acceptor.

This work has just been accepted in *Nano Research*, 2021, Tsinghua University Press and Springer Nature Switzerland AG and was accomplished in collaboration with Dr. Christopher Batchelor-McAuley, from the Department of Chemistry, University of

Oxford, who offered help with some experimental design and the interpretation of the results. Dr. Minjun Yang from the Department of Chemistry, University of Oxford conducted the SEM measurements.

7.1. Introduction

Probing the redox chemical behaviour of metal nanomaterials is critical to understanding their corrosion and dissolution. These chemical transformations have important implications for various scenarios including nano-toxicity in aquatic environments [1-3], electronics [4-5] and cell [6-8] degradation. In particular, the chemical stability of the metal against oxidation is a key factor. The oxidation of metal nanoparticles often leads to the direct or ultimate production of dissolved metal species , where the resulting speciation depends on the identity of the used electrolyte and its concentration[9]. The dissolution process is therefore intimately associated with the nanoparticles' redox chemistry. Consequently, much work has focused on the study of the solution phase redox behaviour of NPs [10-13]. For instance, in the case of silver, the release kinetics of Ag^+ from Ag nanoparticles has been studied to evidence the size-dependent equilibrium of their oxidation based on the measurement of the equilibrated silver ion concentrations [12]. However, solution phase studies are often complicated by the need to use relatively high concentrations of nanoparticles and the dynamic process of their agglomeration in the presence of dissolved salts. The critical coagulation concentration of a monovalent electrolyte for Ag nanoparticles is some 10 mM and of divalent ions is 0.1-1 mM [13-14] and such electrolyte concentrations routinely occur in real world environments. Consequently, decoupling information

regarding the chemical transformation for the physical agglomeration/aggregation of the particles in solution can be challenging.

Despite problems in studying the process in the solution phase, electrochemistry remains an attractive candidate method for investigating nanoparticle redox behaviour using an electrode to support the particles. For example, stripping voltammetry is commonly used to study the effects of particle apparent size [15], agglomeration [16], coverage [17] and assembly methods [18] on the nanoparticle oxidation. In this way, the influence of electrolyte [19] and the interactions of the metal NPs with the substrate electrode [20] or their attached surface functional groups have also been investigated [21]. Such electrochemical methods necessarily require the polarisation of the electrode to drive/control the particles' oxidation. However, we speculate that nanoparticle oxidation might also be driven by electroactive species in the solution (see Figure 7.1) in a similar way to which metal corrosion occurs spontaneously under open circuit conditions especially in the presence of molecular oxygen. Under both conditions no external currents flow with the oxidative dissolution flux matched by that of the oxygen reduction on a macroscopic conductive solid surface. However, typical corrosion of a bulk metal results from the electron transfer from itself to dissolved oxygen, destroying the macroscopic metal surface, whereas in the proposed nanoparticle oxidation the electron transfer is mediated by the supporting conductive substrate which suffers no change and is therefore catalytic. The aim of this paper is to validate this latter speculation.

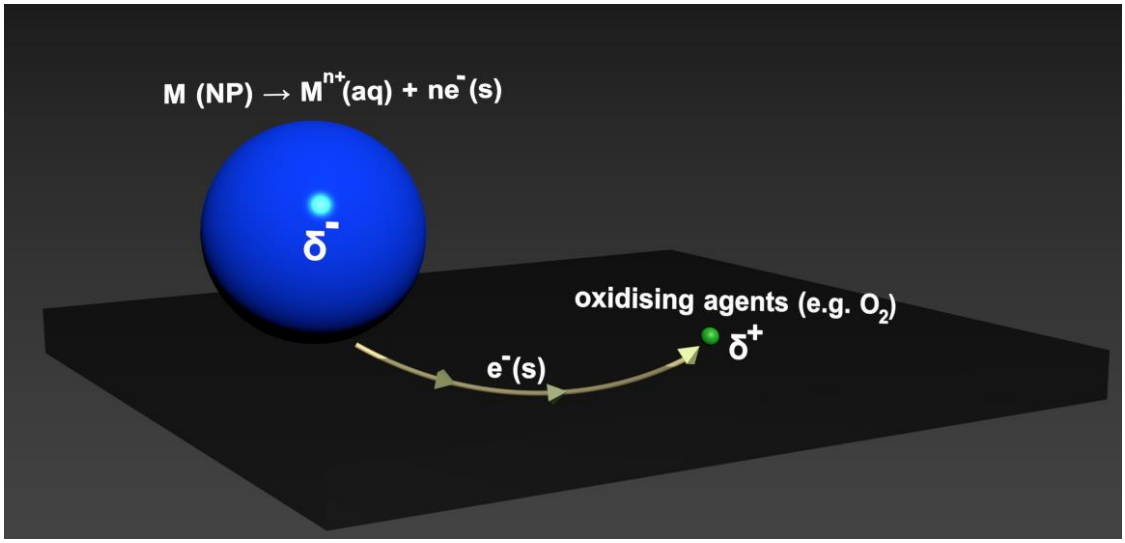

Figure 7.1. Schematic of a redox-driven dissolution of metal nanoparticles by electron transfer over macroscopic distances. Molecular oxidising agents notably dissolved oxygen in trace amounts may oxidise the nanoparticles by electron transfer *via* a conductive substrate with charge injection from the latter at any point on the electrode surface.

Metallic nanoparticles are visible using a dark-field optical microscope within a wide size limit between *ca.* 10 and 100 nm in diameter [22-23] and under suitable conditions individual particles or their clusters can be separately monitored [24]. This is in contrast to many other experimental techniques which are often limited to measuring the average response across a nanoparticle population. Optical microscopy can not only allow the position of each particle to be identified [25-29] but also enables changes in the chemical identity of solid particles to be monitored on the basis of the differences in their spectral properties [30-36]. Due to the ability to provide complementary information recent work has focused on the coupling of optical and electrochemical techniques to facilitate the investigation of redox processes at the nanoscale [37-45].

In a typical electrochemical study of the redox behaviour of metal nanoparticles, the electrode is assumed to be neither chemically nor catalytically active in the studied conditions. Little attention has thus been paid to examining the potential influence of the substrate on the nanoparticles' redox behaviour. Recent work [21] has reported a clear dependence of the oxidation potential of Ag nanopartices on the chemical nature of the underlying electrode material. Despite the lack of a well-understood origin of the observations, these results imply the possible influence of the substrate on the reaction mechanism of the redox processes. Moreover, it is important to note that even on a same conductive substrate surface, the interfacial potential difference at different locations can vary due to, for instance, the size-dependent surface energy of Ag nanoparticles [46] as in electrochemical Ostwald ripening [47] where larger particles grow at the expense of smaller particles through the electron transfer *via* the substrate. However the role of the substrate has been largely overlooked in the numerous studies of nanoparticle chemistry but maybe in fact be decisively influential. As will be shown in this work the presence of a conductive substrate under commonly encountered conditions can catalyse nanoparticle dissolution. The effect is accentuated by the usually larger area of the substrate compared to that of the nanoparticles.

In the following we combine electrochemistry and optical microscopy to study the oxidative dissolution kinetics of supported silver nanoparticles under open circuit conditions, demonstrating a significant role of the substrate. We further discuss what comprises a sufficiently 'good' electrical connection to facilitate the mediated dissolution.

7.2. Experimental

7.2.1. Chemicals

Citrate-capped nominally 100 nm-diameter spherical Ag nanoparticles are purchased from nanoComposix, USA (NanoXact, 0.02 mg mL^{-1} silver, 2 mM sodium citrate). The particle diameters have been characterised by TEM as 89 ± 12 nm (see Appendix Section 1 for further details). Potassium iodide, potassium bromide, chloride and potassium nitrate were purchased from Sigma-Aldrich and used as received (all ≥ 99.9%). Argon and oxygen gas cylinders were purchased from British Oxygen Company, Surrey, U.K. All solutions were prepared with deionised water (Millipore, USA) of an electrical resistivity of 18.2 MΩ cm at 25 °C.

7.2.2. Optical microscopy

Optical measurements were conducted on a Zeiss Axio Examiner A1 microscope. The objective lense has a magnification of 10× with a numerical aperture of 0.3 (EC Plan-Neofluar). 2D black-and-white optical images were acquired by a Hamamatsu ORCA-Flash 4.0 Digital CMOS camera (Hamamatsu, Japan), giving 16 bit images with 4 megapixel resolution.

7.2.3. Optical measurements and data analysis

The optical measurements as a function of immersion times were done *ex situ* on a glassy carbon substrate surface throughout the work. The surface of a GC electrode (d=3.00 mm, electrical resistivity 50 μΩ ▪ m, BASi, USA) was cleaned and mechanically

smoothened by polishing on two micro-cloths loaded with very dilute alumina powder suspensions (0.2 g solid mixed with 5 mL DI water) of decreasing diameters of 0.3 μm and 0.05 μm. In addition, lens tissues were used to wipe off the residual alumina particles from the surface. Then the Ag nanoparticles were dropcast onto the cleaned substrate with a loading of 0.9±0.1 μg cm^{-2} (or 2.4×10^{8} particles cm^{-2}) and dried under a nitrogen flow. The drop-cast area on the modified substrates was then visually focused using dark field illumination with a exposure time of 500 ms and the mean scattering light intensity of Ag nanoparticles was measured as the value for t = 0 s. Subsequently, the same modified substrate was immersed in the 0.2 M KI for a time period of directly 6 minutes (or 50 minutes in the study of halide identity effects in Section 7.3.3) at 25 °C, followed by rinsing with deionised water (to avoid the formation of salt microcrystals) before drying. The dried substrate was placed in the same position in the chamber for measuring the scattering light intensity at t = 6 minutes (or 50 minutes).

For monitoring the dissolution kinetics of the silver particles in varying concentrations of iodide in Section 7.3.3, the same modified substrate was immersed in the 0.2 M KI for a time interval cumulatively to reach t = 5, 10, 30, 60, 120, 240, 360 s, and the subsequent procedure described above is repeated until the cumulative immersion times reached the final 6 minutes.

For the study of the substrate influence in Section 7.3.4, three other different materials of glass, ITO and Pt were used as the substrates. The disc substrate of single crystal

platinum with a crystal facet (110) was fabricated by fastening the metal piece at a sheared thin end of a micropipette tip with an exposed 2.00 mm-diameter disc area, whilst the pipette tip acts as a 'leakless' sheath. The cleaning of this Pt disc surface is the same as that of the GC, whereas the surfaces of the coverslip substrates, glass (22×22mm, 0.13-0.17 mm thick, Sigma-Aldrich) and indium titanium oxide (ITO, 25×25mm, 1.1 mm thick, surface resistivity 8-12 Ω/square, SPI, USA) were cleaned by washing with acetone and deionised water thoroughly. As such, after being modified with the Ag nanoparticles of a same loading, the substrate was immersed in 0.2 M KI or deionised water for 6 minutes at 25 °C. The scattered light intensity of the particles were measured before and after the immersion time.

Zen 2 Pro (Carl Zeiss Ltd., Cambridge, UK) was used for imaging processing and intensity analysis. The data was normalised to the initial value of t = 0 s and averaged over at least three repeat measurements for the plotted remaining fractions of the scattering light intensity.

7.2.4. Combined Optical and Electrochemical Measurements

Potentiostating and cyclic voltammetry were performed using a μ-Autolab type II potentiostat (Eco-Chemie, Netherlands) with a three-electrode set-up in a home-built Faradaic cage. For studying the effects of potentiostating in Section 7.3.2, the GC electrode was used as the working electrode, a platinum foil as the counter electrode and a leakless Ag/AgCl (3.4 M KCl) electrode as the reference electrode. A cleaned GC electrode was modified with Ag NPs of a same surface coverage as above. The

modified electrode was inserted in air-saturated 0.2 M KI solutions and held at the fixed potential between -0.73 V and +0.25 V vs. Ag/AgCl for 6 minutes. Last, the electrode surface was rinsed with deionised water and dried for the optical measurements of the dropcast nanoparticles. The cyclic voltammetry of the nanoparticle-modified electrode, the freshly modified electrode was polarised in an Ar-saturated 0.2 M KI solution in the potential range between -0.75 V and +0.25 V (vs. Ag/AgCl) at a scan rate of 0.1 V s^{-1}.

For studying the effects of oxygen concentration in Section 7.3.2, 0.2 M iodide solutions were purged with O_2 and argon thoroughly for 30 minutes. The air saturation was obtained by air equilibration with a freshly prepared iodide solution. Cathodic cyclic voltammetry of a clean macrodisc glassy carbon electrode was carried out in O_2 and air saturated solutions, and of a carbon microfibre electrode (d=7 μm and l=1 mm) was conducted in an Ar-saturated solution at a scan rate of 0.05 V s^{-1}, to measure their oxygen concentration respectively. Next, a GC electrode was modified with silver nanoparticle as described above and the same modified substrate surface was immersed in the freshly degassed 0.2 M KI in a rubber-sealed three-necked glass bottle for a time interval cumulatively to reach t = 5, 10, 30, 60, 120, 240, 360 s. A gas atmosphere was constantly kept above the liquid surface with a very slow flow of the gas. During the intermission of the immersion of the modified electrode, once the electrode was taken out from the three-necked bottle a block of pressure-sensitive adhesive was used for the temporary sealing. The electrode rinsing and drying and optical measurements of the dropcast nanoparticles after each immersion were repeated until the cumulative immersion times reached the final 6 minutes.

7.3. Results and discussion

We first demonstrate how silver nanoparticles can be readily visualised on an opaque carbon support using reflective dark field microscopy. Optical measurements from the presented dark field images provide a quantitative route by which the surface supported nanoparticles population can be monitored. Exposure of the surface supported nanoparticles to a halide containing solution leads to their more rapid disappearance from the surface. This catalysed removal is evidenced to arise due to the electrochemical dissolution of the nanomaterial driven by electron transfer through the substrate to trace dissolved dioxygen. Subsequently, the role and influence of the supporting substrate upon this dissolution process is evidenced.

7.3.1. Optical measurements of scattering from silver nanoparticles

Silver nanoparticles are plasmonic and both strongly scatter and adsorb light in the range of 400-500 nm. The surface plasmon resonance peak position depends on a number of factors including the particle size, shape and agglomeration state [14, 48]. Under dark field illumination individual silver nanoparticle as small as 10-15 nm in diameter can be observed under optimal conditions [22-23]. If the dimensions of the nanoparticle are below the wavelength of the light, on a microscope image a single nanoparticle appears as an individual diffraction-limited spot. This imaging technique can be used to visualise particles both in the solution and supported on a substrate [40-41]. In this work we drop-cast silver nanoparticles on to a glassy carbon macrodisc electrode (d = 3.0 mm) and visualise the interface under dark field illumination (see Appendix section 2 for further details on the microscopy setup).

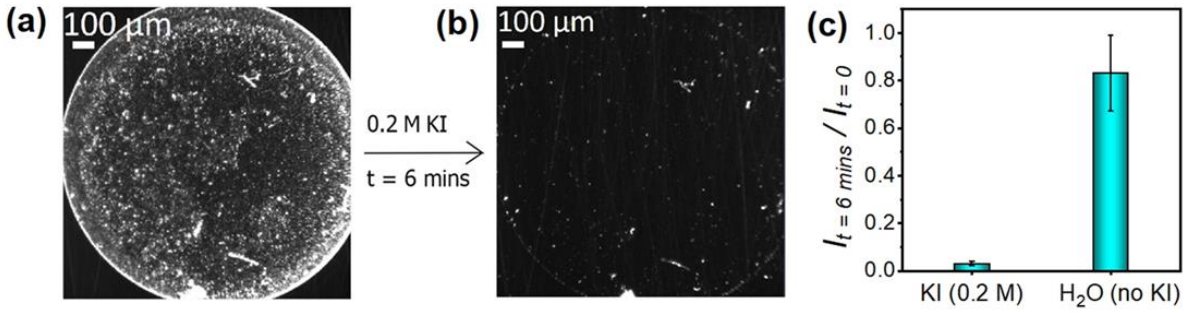

Figure 7.2. Optical microscopy images of the drop-cast AgNPs on a dried glassy carbon surface (a) before and (b) after the 6 minutes' immersion in a (non-degassed) 0.2 M KI solution under open circuit conditions. (c) Light scattering intensity measured at the 6 minutes relative to the initial value in the presence and absence of 0.2 M KI, respectively.

Figure 7.2 a shows a representative microscope image of a glassy carbon surface dropcast with silver NPs (loading: 0.9±0.1 µg cm^{-2}, or 2.4±0.3 $\times 10^8$ particles cm^{-2}). Due to the distinctive 'coffee ring' effect [49-50] the edge of the dropcast area is clearly visible on the microscope image. At the corners of the image the glassy carbon appears black due to only minimal light scattering by the surface. In contrast the central area of the image is bright due to the presence of the nanoparticles. As can be seen in Figure 7.2 a, the light intensity across the dropcast area is highly heterogeneous with brighter patches representing clusters of nanoparticles on the electrode surface (see Appendix section 3 for more details). Previous work has evidenced that drop-casting of nanoparticles leads to significant surface agglomeration of the material during the drying process [16]. Consequently, although the microscope image can yield information about the presence of the nanoparticles on the electrode surface, given the *average* inter-particle separation (estimated to be 560 nm for a uniform distribution) is comparable to or less than the wavelength of light, the

microscope images cannot be used to provide detailed information regarding individual nanoparticles, but the images can be used to provide quantitative information regarding the overall nanoparticle population.

The silver nanoparticle modified electrode was immersed into an iodide (0.2 M) solution for 6 minutes under open circuit conditions. After the immersion process the surface was reimaged and the resulting micrograph is shown in Figure 7.2 b. A noticeable decrease in the light scattering intensity is observed. If the electrode is submerged into pure DI water containing no dissolved iodide then this large decrease in the light scattering intensity does not occur.

To quantify this change in the microscope image, the mean light scattering intensity was measured across the drop cast area and background corrected (see Appendix section 2 for details) to account for light scattered by the underlying carbon substrate. Prior to immersion of the electrode the mean light intensity was found to be reproducible with a 20% standard deviation (see Appendix section 4). This variation in light intensity may at least in part result from a minor change from the particle surface coverage (11% calculated from the error of nanoparticle loading). This therefore indicates that the mean light intensity when averaged over a larger area is relatively insensitive to the specific surface morphology and agglomeration state of the nanoparticles on the interface and hence can be used to quantify changes in the nanoparticle population. After 6 minutes of immersion of the electrode, the modified electrode was subsequently rinsed in DI water before air drying and imaging of the

interface. The remaining fraction of the scattered light intensity was therefore calculated as the ratio of light intensity measured before and after exposure to the solution.

Figure 7.2 c depicts the ratio of the scattered light intensity before and after the electrode has been immersed into either DI water or a 0.2 M iodide solution. In the case where the electrode was exposed to de-ionised water for a period of 6 minutes. After the immersion process the microscope image light intensity decreased by < 20%. This loss of light intensity was found to occur immediately upon immersion of the electrode into the DI water and most likely arises due to the desorption and physical removal of a small fraction of the drop-cast material from the electrode surface. Note the exposure of the electrode to the DI water also results in surface redistribution of the particles but longer immersion times or further washing of the interface in DI water does not lead to any further loss in the light scattering intensity (see Appendix section 5). This further indicates the around 80% of the nanoparticle have a mechanically stable connection to the glassy carbon electrode surface.

In contrast to the case where the electrode is immersed into the DI water, immersion of the electrode into the 0.2 M iodide solution results in a major decrease in the light scattering intensity where only *ca.* 3% of the light scattering remains after this immersion process. This implies the near complete removal of Ag NPs from the electrode surface, which is confirmed by scanning electron microscopy imaging (see Appendix section 6) of samples after immersion in water and in the iodide containing

media. This observation is further evidenced in Section 7.3.3. The physical cause of this transformation is the focus of the following two sections.

7.3.2. Opto-electrochemical investigations of the redox processes

A silver nanoparticle modified electrode was submerged into an iodide containing solution. Upon immersion, the electrode was polarised with fixed potentials in the range of -0.75 V to +0.25 V vs. Ag/AgCl. The mean scattering light intensity of the silver nanoparticles was measured before and after the 6 minutes immersion.

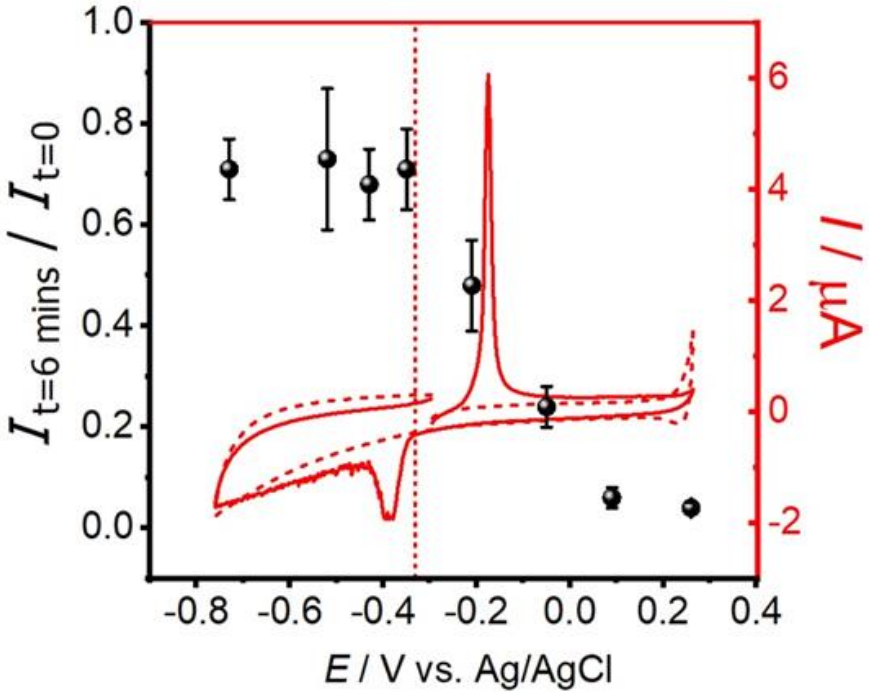

Figure 7.3. The average remaining fractions of scattering intensity of the immobilised Ag particles on a GC electrode held at each different fixed potentials after 6 minutes' immersion in an air-saturated 0.2 M KI solution. The overlaid cyclic voltammograms of (solid) a freshly immersed, modified GC electrode and (dashed) a bare GC electrode in an Ar-saturated 0.2 M KI solution. Note that the vertical dashed line labels out the expected electrode potential for Ag/AgI under the condition. Scan rate 0.1 V s^{-1}.

Figure 7.3 (black dots) plots the remaining fraction of the scattered light intensity as a function of the applied holding potential. Most notably, holding a potential below a threshold of *ca* ~ -0.3 V (vs Ag/AgCl) essentially completely inhibits the nanoparticle removal from the electrode surface, where approximately 71±8% of the light scattering intensity remains after exposure of the electrode. This value of 71±8% is consistent with that obtained when the electrode is immersed solely in DI water (83±16%). All the potentials above -0.3 V lead to a quantitatively similar (within experimental error) loss of nanoparticles from the electrode surface.

The observation that the nanoparticle dissolution can be inhibited by the application of a potential to the underlying substrate provides strong evidence that immersion of the nanoparticles into the iodide solution leads to the loss of the nanoparticles via the occurrence of a redox reaction. Further Appendix section 7 demonstrates how the required threshold potential to avoid nanoparticle dissolution is sensitive to the ionic composition of the solution. For comparison in Figure 7.3, overlaid with the optical data, is a voltammogram of a drop-cast silver nanoparticle modified electrode measured in a solution containing 0.2 M potassium iodide. On the forward sweep of the voltammogram a clear stripping peak is observed at -0.22 V, corresponding to the oxidation of the surface adhered silver to silver iodide. On the reverse scan a corresponding reduction wave is observed at -0.45 V. In the presence of 0.2 M iodide the Ag/AgI redox couple has a reduction potential of -0.33 V, this potential is marked on Figure 7.3 and is good agreement with both the position of the voltammetric peaks and the threshold potential at which the iodide driven dissolution of the nanoparticles is inhibited.

Consequently, we infer that the dissolution of the silver nanoparticles from the modified electrode following immersion into the solution involves the oxidation of the silver:

$$Ag(NP) \rightleftharpoons Ag^{+}(aq) + e^{-}(s) \qquad (7.1)$$

where the chemical products are either silver cations or silver salts (as discussed in Section 7.3.3). In addition, the evolution of the open circuit potential of the NP-modified electrode over the six minutes of immersion in the iodide solution shows a conspicuous change only in the first 60 seconds (Appendix section 8). This period of time is similar to that for the major decrease (ca 90%) in the light scattering intensity of the silver particles. This observation likely supports the occurrence of the electrochemical redox process.

Accepting that the nanoparticle loss originates from the oxidation of the nanoparticles, it is important to consider the identity of the counter reaction for which an obvious candidate oxidant is atmospheric oxygen. To investigate possible effects of dissolved dioxygen on the nanoparticle dissolution process, we prepared the iodide (0.2 M) solutions with different concentrations of oxygen corresponding to O_2, air or Ar gas saturation conditions by purging each pure gas (except air) thoroughly for 30 minutes to the solutions in a well-sealed three-necked bottle. For measuring the concentration of dissolved dioxygen in these degassed solutions, a glassy carbon macrodisc electrode (d=3.00 mm) was inserted into the O_2 and air-saturated solutions and was then scanned voltammetrically using applied potentials from -0.1 V to -1.0 V vs. Ag/AgCl, whilst a carbon microfibre electrode (d=7 μm and l=1 mm) was preferred under argon saturation so as to probe the ultra-low concentrations encountered [51],

leading to currents of the order of nA recorded by scanning a potential range from -0.1 to -1.5 V after immersion in the solution.

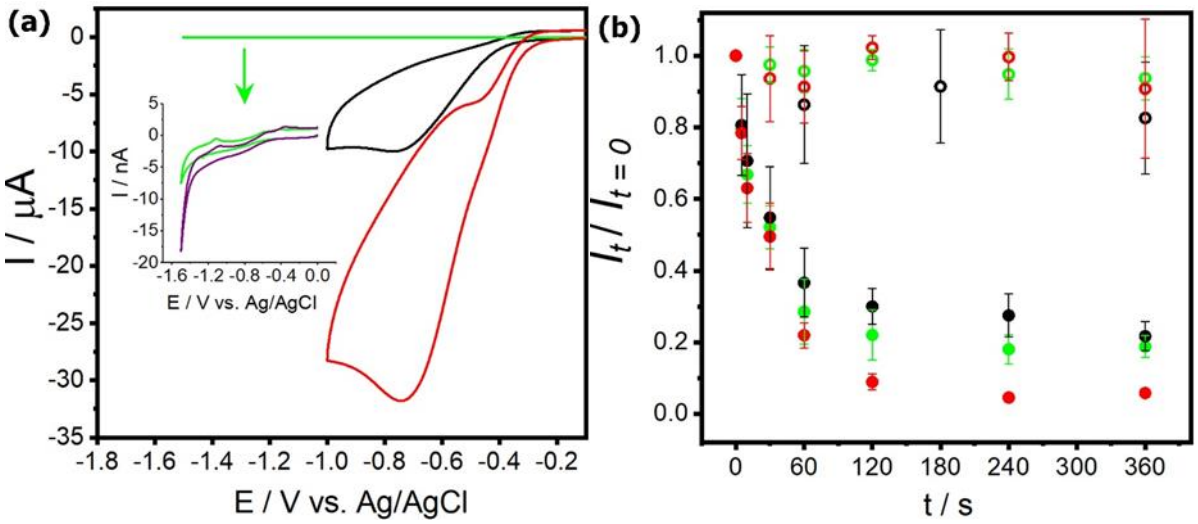

Figure 7.4. (a) Voltammetric responses of the reduction of dissolved dioxygen using a glassy carbon macrodisc electrode (d=3.00 mm) immersed in (red) oxygen-saturated and (black) air-saturated 0.2 M KI solutions and using a carbon microfibre electrode (d=7 µm and / =1 mm) in (green) an argon-saturated solution. The inset presents the enlarged version of the green curve for zero aging time while the purple curve denotes the voltammogram after an aging time of 6 minutes. Scan rate 0.05 V s^{-1}. **(b)** Light scattering intensity relative to the initial value as a function of time (within 6 minutes' total immersion time: 0, 5, 10, 30, 60, 120, 240, 360 seconds) measured in (hollow spots) non-iodide containing solutions and (solid spots) 0.2 M KI solutions with varying concentrations of dissolved oxygen: (green) 1-2 µM with Ar saturation, (black), 0.3 mM with air saturation and (red), 1.2 mM with O_2 saturation.

Figure 7.4 a shows an irreversible reduction peak at -0.7 V for both O_2 and air saturated solutions, which is due to the two-electron reduction of O_2 to H_2O_2 under the neutral condition [52]. The peak currents for oxygen and air saturation conditions are measured to be 30.4±3.4 µA and 8.6±0.7 µA, respectively. Using the Randles-Secvik equation for irreversible peak currents [53], the reduction currents correspond

to 1.20±0.1 mM and 0.31±0.02 mM of dissolved O_2 in the respective bulk solutions (see Appendix section 9 for detail calculations and for those below regarding the oxygen concentration), which are consistent with literature [52]. In the case of argon saturation, the microelectrode voltammogram as seen in the inlay of Figure 7.4 a shows a tiny quasi-steady-state current of oxygen reduction in the potential range between -1.0 V and -1.2 V, where no significant solvent breakdown is observed. Using linear extrapolation from the capacitive current at potentials above -0.5 V, the quasi-steady-state current is background subtracted and measured to be 1.2±0.7 nA. This is then calculated to correspond to an oxygen level of 1.2±0.7 µM. An aging time of 6 minutes still retained a reduction current of 2.3±0.4 nA and thus an O_2 concentration of 2.3±0.4 µM, indicating a desired air tightness of the vessel.

For the subsequent optical measurements, a GC surface modified with Ag nanoparticles was immersed in the three solutions each containing one of the different levels of dissolved dioxygen described above. Control experiments in the deionised water with the O_2, air and Ar saturation, respectively, were also done. The scattering light intensity of the particles were monitored as a function of time at each oxygen concentration of 1.2 mM, 0.3 mM and 1-2 µM. In the absence of iodide, the light intensity was generally essentially constant although in few cases including some of the experiments in Figure 4 b) there was a ca 5-10% variation in the measured light intensity. Figure 7.4 b shows in the presence of iodide, however, the greatly lowered O_2 concentration to few micromolar did not markedly influence the dissolution process. Although one may anticipate that the removal of oxygen might inhibit the reaction, the *complete* removal of oxygen from the solution by gas purging is not feasible.

Indeed in this work the use of denser inert gas of argon than dinitrogen and an airtight container has enabled to reach a significantly low level of dissolved oxygen, 1-2 μM. This level of dissolved oxygen is further improved compared to that reported in the literature (7-14 μM using N_2 outgassing) [51, 54]. Nevertheless despite the inconclusive result for dissolved oxygen we note that other candidate oxidising agents, notably protons or triiodide ions (which may form upon the aging of iodide solutions), are excluded on the basis of the results presented in Appendix section 10. Therefore, we believe that the only likely oxidising agent is the trace oxygen. First, the trace amount of O_2 at μM levels is considered to be sufficient for the reaction given the tiny mass of silver (0.1 nmol) to be oxidised. Second, micromolar levels of oxygen would be insignificant in many reactions but in the present case the oxygen only needs to be present in the diffuse layer *at any point of the conductive electrode surface* to be effective (see Section 7.3.4). Even oxygen molecules which are close to the electrode but remote from the particles by some millimetres can oxidised them *via* the conductive substrate mediating the electron transfer as in classical models of corrosion, and as explored and discussed further below. Hence, the influence of oxygen is much amplified because of the possibility of the oxidising agent acting remotely. Consequently, the lack of sensitivity of the silver nanoparticle dissolution to the 'removal' of oxygen most likely reflects the fact that the oxygen reduction processes is, in this case, not the rate determining step.

7.3.3. Optical study of the Ag nanoparticle dissolution process

The above results provide evidence that the nanoparticle loss involves the oxidation of the nanoparticles in accordance with Equation 7.1. Given halide ions have a strong

affinity towards argentous ions, the rate of this dissolution process is likely sensitive to both the halide identity and concentration. To investigate this experimentally, silver nanoparticle modified electrodes were immersed for a period of 50 minutes into differing halide containing solutions (KI, KBr and KCl) and also into a solution containing 0.2 M KNO_3 under open circuit conditions. In a further experiment the concentration of the iodide was varied from 0.2 to 0 M and the silver nanoparticle light scattering intensity monitored as a function of time at each concentration.

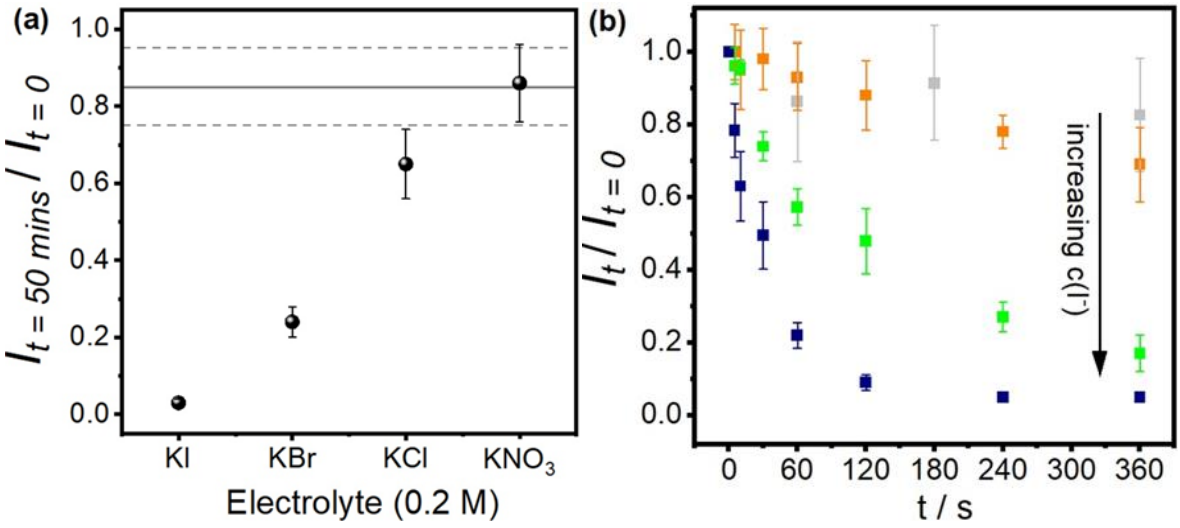

Figure 7.5. (a) Optical measurements of the remaining fraction of the total scattering of drop-cast Ag NPs on a glassy carbon electrode surface at open circuit potentials after 50 minutes' immersion in 0.2 M halide, KNO_3 solutions; the solid line denotes that measured in deionised water, along with the dashed lines represent the upper and lower limits from the standard deviation. **(b)** Light scattering intensity relative to the initial value as a function of time (within 6 minutes' total immersion time: 0, 5, 10, 30, 60, 120, 240, 360 seconds) measured in KI solutions with varying concentrations of (grey) 0 M, (orange) 0.05 M, (green) 0.1 M and (navy) 0.2 M.

Figure 7.5 a demonstrates that in the nitrate containing solution, the scattered light intensity after exposure is essentially unaltered from that found with DI water.

However in the other solutions, a significant reduction of intensity was observed in the order KI<KBr<KCl<KNO_3. This ordering directly relates to high halide-containing media (0.2 M) where the soluble Ag(I) halide complexes, $AgX_n^{(n-1)-}$ are formed via the reaction

$$Ag^+(aq) + nX^-(aq) \rightleftharpoons AgX_n^{(n-1)-}(aq) \quad (2)$$

where (X=I, Br or Cl, and 2≤ n≤ 4) and for which

$$K(AgX_n^{(n-1)-}) = \frac{[AgX_n^{(n-1)-}]}{[Ag^+][X^-]^n} \quad (3)$$

where, for instance when n=2, log[$K(AgX_2^-)$] = 11.5 (X = I) > 7.5 (X = Br) > 5.2 (X = Cl) at 25°C [59] as discussed below. The same trend is also found for the soluble higher silver halide complexes [59]. This sensitivity to the halide ion is also reflected in the kinetic data shown in Figure 7.5 b where the rate at which the nanoparticle dissolution occurs is shown to be sensitive to the iodide concentration.

The observed halide effects strongly suggest that the final products of the silver oxidation in the iodide solutions are iodide compounds of silver (I). We infer that either, despite the volume expansion, the solid particles of silver monoiodide scatter less light than metallic silver or, alternatively, that further soluble silver iodide complexes account for the observed scattering loss by dissolution of the particles leading to their reduction in size. We experimentally exclude the possibility of $AgI_{(s)}$ formation due to both observations of very few particles seen by SEM (Appendix section 6) and no voltammetric fingerprint of this solid (see Appendix section 11) on the NP-modified glassy carbon surfaces after 6 minutes' immersion in 0.2 M KI. Soluble silver iodide

complexes are $AgI_n^{-(n-1)}$ where the integer n≤4 and have increasing cumulative formation constants with log[$AgI_n^{-(n-1)}$] of 6.6 < 10.7 < 13.4 < 14.1 from n=1 to n=4 at 25°C [55]. It can be calculated that ***all*** the AgI formed from the dropcast nanoparticles would, under thermodynamic control, dissolve to form the soluble complexes given the magnitude of the formation constants of the latter. Consequently, it is inferred that the oxidised silver in the iodide solutions most likely dissolve into soluble silver iodide compounds *via*

$$Ag^+(aq) + nI^-(aq) \rightleftharpoons AgI_n^{-(n-1)}(aq) \quad (7.2)$$

7.3.4. Influence of the substrate on the dissolution kinetics

Having verified that the loss of the surface supported nanoparticles is due to their oxidative dissolution and demonstrated how this reaction can be controlled by the application of a potential to the substrate or changing the halide concentration and/or identity, we next turn to consider the possible influence of the substrate upon this dissolution reaction under open-circuit conditions. Silver nanoparticles were drop-cast on to four different substrate materials: platinum, glassy carbon, indium-tin oxide (ITO) and glass. These four substrates have markedly different conductivities. The surface-bound nanoparticles were subsequently exposed to either deionised water or a solution containing 0.2 M KI for a period of 6 minutes. As done previously the light scattering intensity was measured prior to and after exposure of the material to the solution.

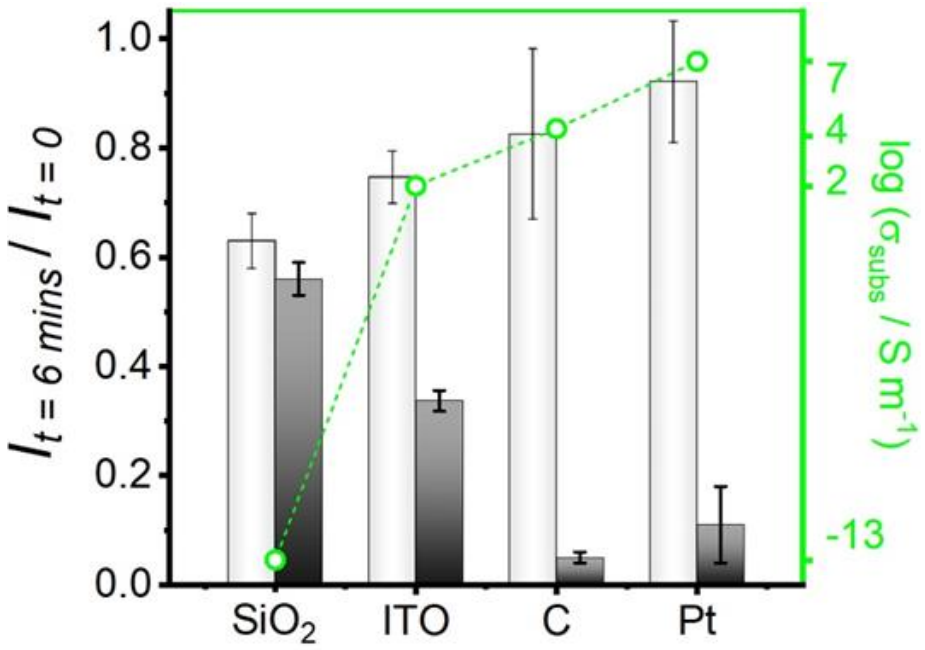

Figure 7.6. Optical measurements of the remaining fractions of Ag scattering, after 6 minutes' immersion in (white) pure water or (black) 0.2 M KI solutions under the open circuit condition, as a function of differently conducting substrates. The green data presents the specific values of the substrate conductivity.

Figure 7.6 plots the scattered light normalised to its initial value for the four substrates, with and without the presence of the halide ions. In the absence of halide, the remaining fraction of the scattered light intensity varies with the substrate identity – 63±5% for glass, 75±5% for ITO, 83±16% for glassy carbon and 92±11% for platinum. This relatively smaller variation in the fraction of the remaining scattered light intensity where the nanoparticle have been exposed to DI water most likely reflects the different adhesion strengths of the nanoparticles to the substrate materials [56]. However, adhesion strength cannot solely explain the comparative rates of loss in the presence of iodide which varies markedly across the different substrates. For the glass supported nanoparticles, immersion into a solution containing iodide reduced the nanoparticle scattering light intensity by only a further 7±5% such that after

immersion 56±3% of the scattering light intensity remained. This is in stark contrast to the platinum and carbon substrates where exposure to the iodide solution decreased the scattering light intensity by a further 78±16% and 81±13% respectively. The ITO substrate was found to show a response in between these two limits where exposure of the nanoparticles to the iodide solution led to a further 41±5% decrease in the light scattering intensity. It is of importance to note that in the case of the glass substrate, the substitution of the glass does not completely inhibit the iodide driven dissolution mechanism. For the nanoparticles supported on a glass substrate, when they are exposed to the iodide solution for longer periods of time *ca.* 1.5 hours (see Appendix section 12) the nanoparticles are found to be completely removed from the surface, this removal does not occur in the absence of the iodide in the solution phase. This result evidences that the oxidative dissolution reaction proceeds even without the presence of a conductive substrate albeit slowly but the presence of the electrode much increases the dissolution rate.

The results presented in Figure 7.6 are consistent with the idea that the substrate can significantly influence the rate at which the nanoparticle oxidative dissolution occurs. Given that the nanoparticle loss has already been demonstrated above to be an electrochemical process that can be directly controlled if a potential is held on the supporting substrate, it is reasonable to consider that the nature of the electrode support can influence the dissolution kinetics *via* two factors: the conductivity of the supporting material and the quality of the electrical connectivity of the particle to the surface. Overlaid on Figure 7.6 is the variation in the conductivity of the materials used. At one limit glass is a near ideal insulator, ITO and glassy carbon have higher

conductivities whilst platinum has the highest high conductivity, where the influence of the substrate material is found to be clearly correlated to its inherent conductivity. More precisely, we infer that the major effects of the substrate is to provide a threshold conductivity for either the dissolution via electron transfers within the electrode or not. Glass does not have sufficient conductivities whereas the others do, such that the 'switch-on' of the substrate-mediated oxidative dissolution is observed as the substrate becomes more conductive. However, the conductivity differences between ITO, glassy carbon and platinum are so much that they cannot all be close to the threshold value. As such, the differences between the rates of the reaction observed on these electrode supports must also reflect differing NP/substrate contact resistances.

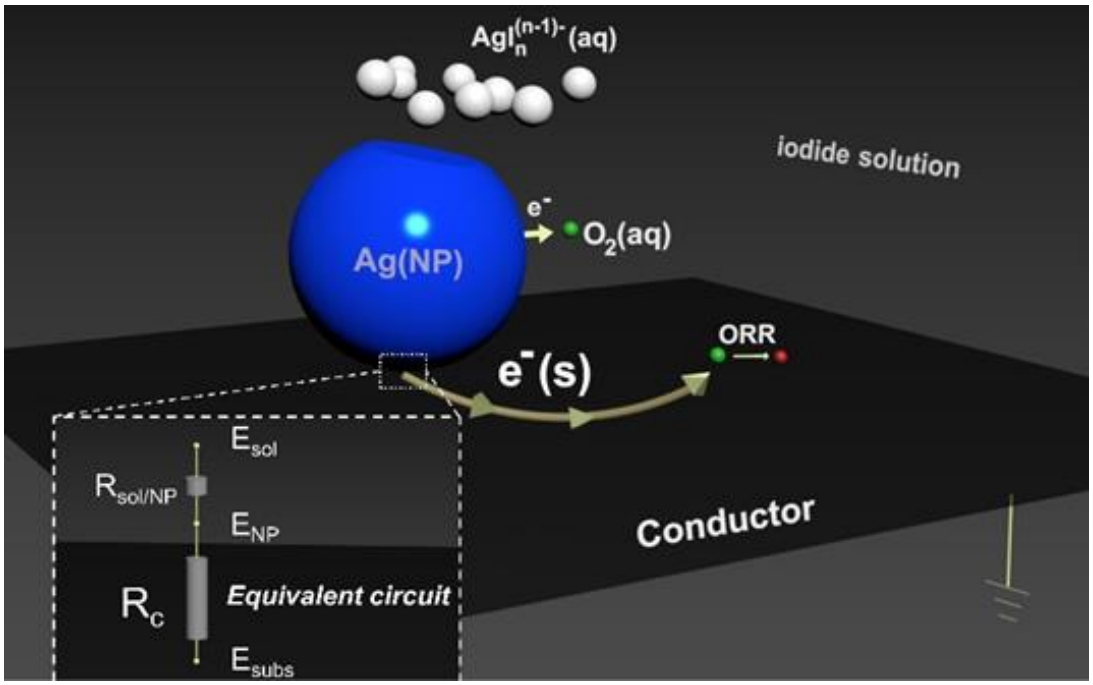

Figure 7.7. Proposed mechanism for the electrochemical oxidative dissolution of Ag NPs under the open circuit condition, and the concept of a 'voltage divider' for viewing the NP/substrate electrical contact. 'ORR' stands for 'oxygen reduction reaction'. E_{sol}, E_{NP} and E_{subs} are the electrical potential at the solution phase, the nanoparticle, and the local point of substrate respectively, whilst $R_{sol/NP}$ and R_c are the solution/nanoparticle interfacial resistance and the nanoparticle/substrate contact resistance respectively.

The increased nanoparticle dissolution that occurs on the conductive substrates (ITO, GC and Pt) indicates that electron transfer through the substrate is likely an important mechanism for the loss of the nanomaterial. Figure 7.7 presents a schematic for the proposed overall mechanism of the oxidative dissolution under open circuit conditions. Specifically it is envisaged that on a conductive supporting substrate the counter reaction – in this case likely oxygen reduction – occurs not at the nanoparticle but remote from it. Consequently, it is concluded that by providing an additional large area interface, much greater than the total surface area of all the nanoparticles (see Appendix section 13 for detailed calculations), at which the oxygen reduction reaction is able to occur, the substrate is able to essentially catalyse the nanoparticle oxidative dissolution!

Finally, it is of interest to reflect on previous work [57-59] which has shown that for nanomaterial that has been drop-cast on to an electrode surface, when the particles are studied voltammetrically – either by stripping voltammetry [57-58] or by investigating metal deposition on to the nanomaterial [59] – it has been concluded that in many cases only a small fraction of the nanoparticle sample is in 'good' electrical contact with the electrode surface [60]. Conversely, in the present results the presence of a conductive substrate has a marked effect on a very large proportion of the nanoparticles. Importantly, the application of a cathodic potential can, as shown in Figure 7.3, completely inhibit the dissolution process, thus indicating that a very high fraction of the nanoparticles are in fact in electrical contact with the substrate. At first sight these two results are contradictory. However, it is illuminating to consider the timescales involved for each process, a voltammetric experiment is often run over the

course of a few seconds, whilst conversely the present dissolution experiments span a time frame of minutes to hours. As schematically highlighted in Figure 7.7 a voltage divider [61] can be a useful analogy for viewing the electrical contact of a surface supported nanoparticle with the substrate electrode where a redox reaction occurs at the nanoparticle interface and the electrons are provided through the supporting substrate. From this we can recognise that even if a nanoparticle has an ohmic contact with an electrode, the potential held on the nanoparticle is not necessarily the same as that of the electrode and will depend upon both the reaction occurring at the nanoparticle/solution interface and the contact resistance between the particle and the electrode. A relatively resistive contact between the nanoparticle and the electrode may not be sufficient to drive a reaction to occur on the timescale of seconds but may be sufficient, as is the case in the present work, to allow a reaction to occur over a longer timescales of minutes to hours. As such, what constitutes a 'good' electrical contact depends upon the experimental timeframe.

7.4. Conclusions

Under reflective dark field illumination the scattered light from silver nanoparticles immobilised on a glassy carbon substrate is found to reduce over time under open-circuit conditions in a halide-containing solution (X^-, X=I, Br, Cl). By coupling the electrochemical actuation and optical monitoring we demonstrate that the scattering decrease arises from a redox-driven dissolution of the metal nanoparticles into soluble halide complexes by electron transfer to trace dissolved dioxygen. Further, the comparison of the dissolution kinetics of the surface-supported Ag nanoparticles on

four differently conducting materials – glass, ITO, GC, and Pt – reveals that the presence of a conductive substrate is able to catalyse the oxidative dissolution. On this basis, the assessment of particle/electrode electrical connectivity is critically discussed with recent relevant studies and suggested to rely on the experimental timeframe.

Appendices

1. TEM images and sizing of the silver nanoparticles

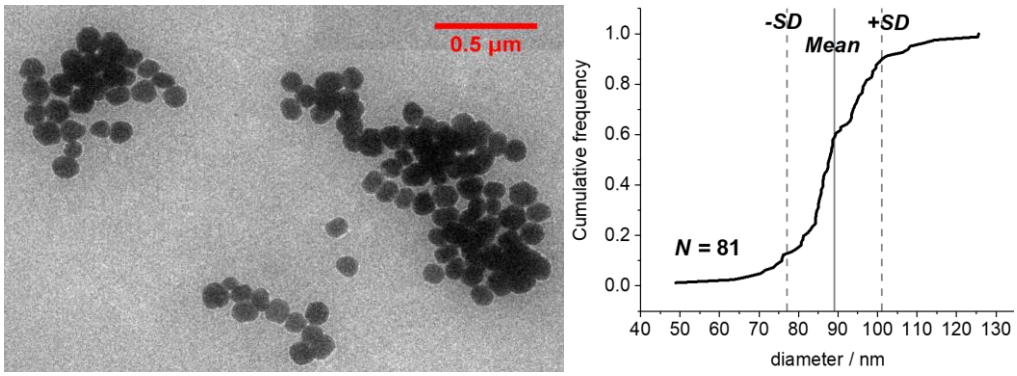

Figure 7.8. TEM image of the nominally 100 nm Ag NPs and their size distribution. Mean diameter with standard deviations is marked by the vertical lines.

2. Microscopy set-up for reflective dark field illumination

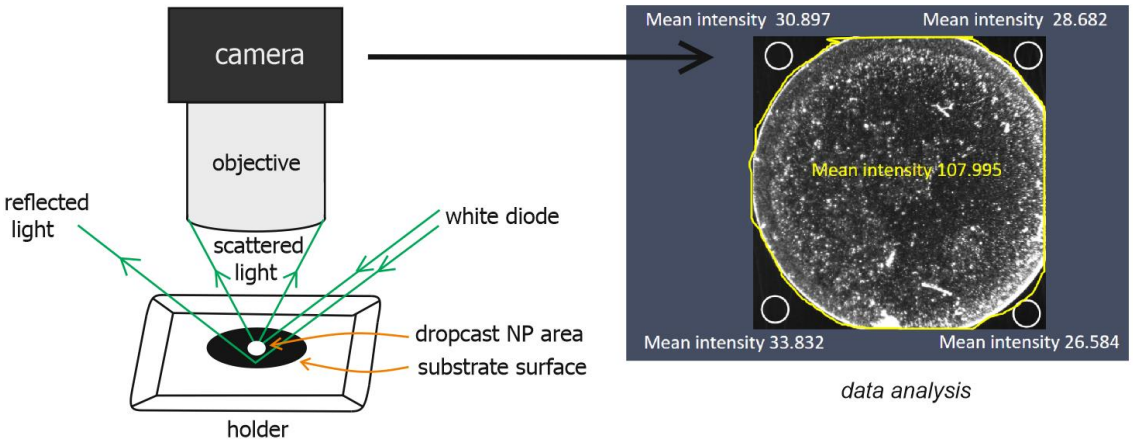

Figure 7.9. Schematic illustration of reflective dark field illumination microscopy and data analysis.

Figure 7.9 shows the microscopy set-up for the optical measurements under reflective dark field illumination. The position of the substrate is held fixed by a holder and exposed to the objective above. A white diode light source is maintained in a fixed position from which the incident light is directed to the substrate surface at an angle from the above. Consequently, in contrast to the light reflected away by the flat and smooth substrate surface which therefore appears minimal light intensity at the corners of the produced image, the silver nanoparticles located in the in-focus dropcast area scatters light which partly enters the objective and so this central area appears very bright.

Using the camera, the image described above is obtained and the optical intensity is analysed. Specifically, the mean light intensities over the whole central dropcast area (I_{tot}) highlighted by the yellow outline and the bare substrate at the corners (I_s) were measured respectively. Assuming the substrate scatters homogeneously across the whole imaged area, the scattered light intensity from the Ag nanoparticles was thus measured by subtracting the average I_s over the four corners from the I_{tot}.

3. Optical analysis of the scattering features from a glassy carbon surface

In this section we report the individual scattering features observed on the electrode surface. First, a total number of 23 separate bright scatters were selected as the representative features on the basis that their half maximum intensity (29 ± 6 a.u.) is approximately the mean intensity (31 a.u.) of all the particles across the drop-cast area. Five of them in a local region of Figure 7.2 a are presented in Figure 7.10 a and

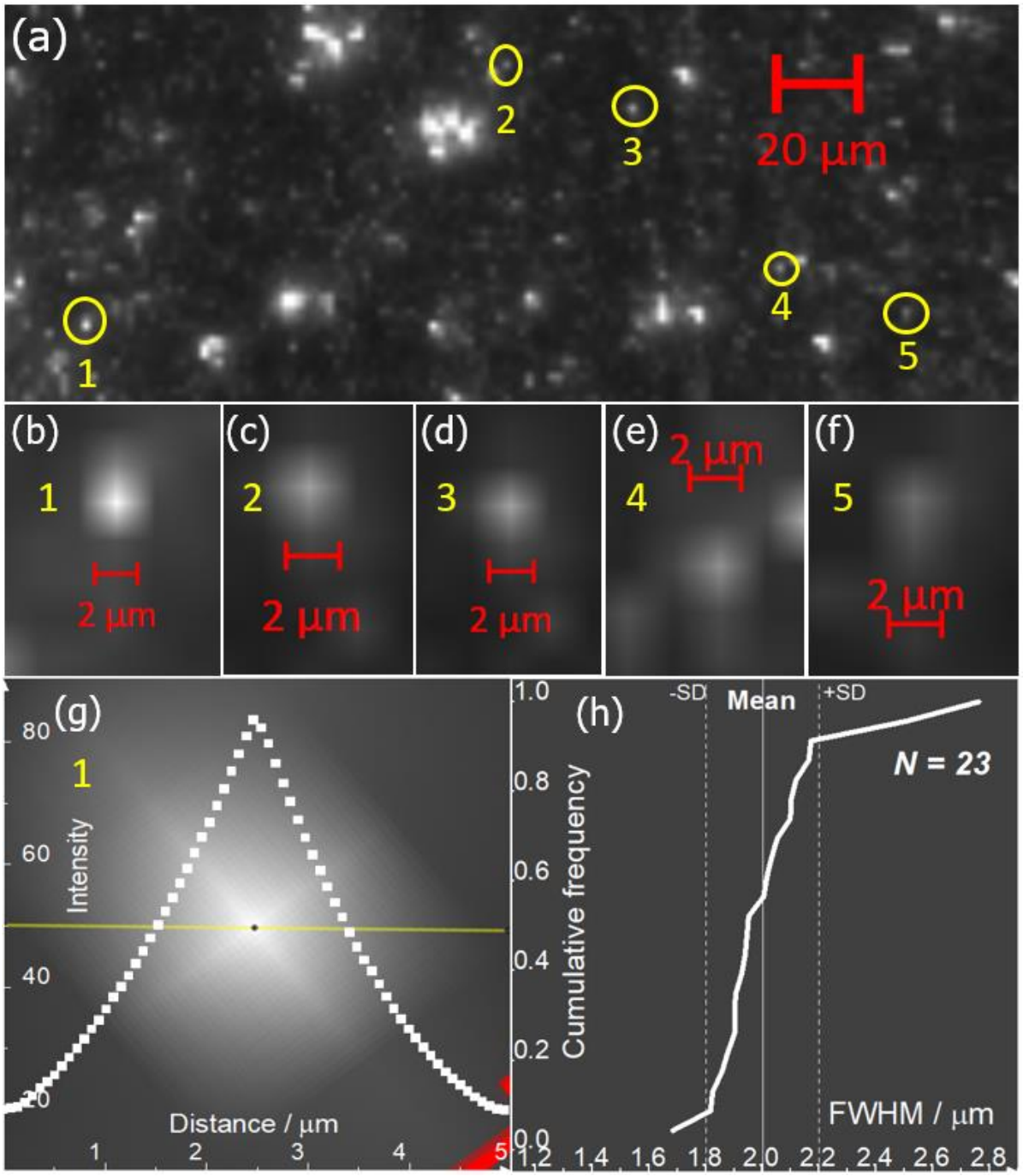

Figure 7.10. (a) Local region of Figure 1a containing 5 optical images of the representative scattering features 1-5. (b)-(f) Scattering patterns of individual optical features. (g) Line profile of the scattering intensity across Feature 1. (h) Size distribution of the 23 optical features. The mean FWHM with standard deviations is marked by the vertical lines.

clear images of their individual spreading scattering are shown in Figure 7.10 b-f. The scattering appears quasi-spherical with a central maximum intensity. Note that here we only focus on the Airy-type diffraction pattern resulting from the circular aperture of the objective; therefore the four-spike diffraction patterns forming upon the additional light diffraction by the square-shaped aperture of the camera sensor is avoided in the following measurement of the line-profile intensity for accuracy. The line profiles of intensity distribution across the selected optical features, e.g. that of Feature 1, were plotted (Figure 7.10 g), from which the full widths at half maximum (FWHM) were measured, giving an average value of 2.0 ± 0.2 μm (Figure 7.10 h). This value is used as the approximate mean size of all the observed scattering features.

Due to the Abbe diffraction limit of an optical system using a visible light source, the size of the scattering spots of a single 100 nm-diameter spherical NPs is expected to be significantly larger than their own geometry size. Previous work [62] has simulated the point spread function of the optical microscopy. According to the equations given in that work

$$l_0 = \alpha\sqrt{|\log(\tfrac{1}{4})|} \qquad \text{(S1)}$$

where l_0 is the radius at half maximum of the point spread function of the particles, and $\alpha \sim 0.435\frac{\mathrm{n}\lambda}{2\,NA}$ [62] (λ is the wavelength of incident light, here we take 550 nm as the average wavelength for the white light source, *n* is the refractive index of the medium (~1.33) and *NA* is the numerical aperture of the microscope objective). Accordingly the expected FWHM of the diffraction limited pattern for a single

nanoparticle is calculated to be 0.8 μm. This is significantly smaller than the measured mean size of 2.0 ± 0.2 μm. It follows that the drop-cast nanoparticles in fact form large surface clusters due to the particle agglomeration during the electrode drying process.

4. Reproducibility of the measured mean scattered light intensity of dropcast Ag NPs

To evaluate the reproducibility of the mean intensity of the scattered light from the dropcast silver particles, the measurements were repeated for five times. On glassy carbon surfaces, as the light intensity of the substrate corners was kept at around 31 a.u., the total scattering intensity of the five drop-cast areas with different surface morphology (see Figure 7.11) was measured to range from 107 to 138 a.u. Consequently, the mean scattered light from Ag NPs averaged over these five repeats are calculated to be 85 ± 15 a.u., indicating an 18% reproducibility. Similarly, on all the other substrates used in this work, the reproducibility is found to be around 20% as shown in Table 7.1.

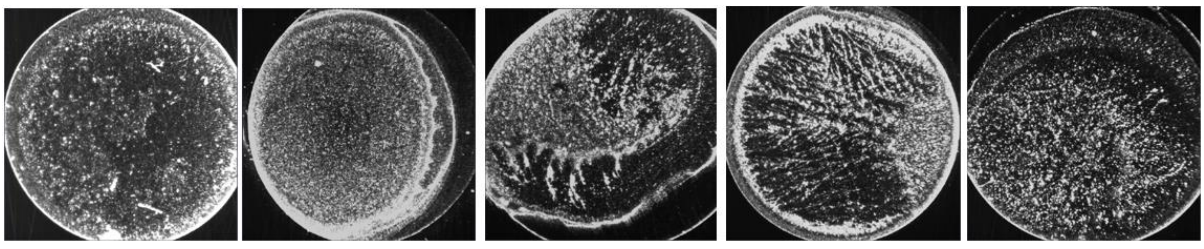

Figure 7.11. Images of the drop-cast areas in 5 repeat experiments on a glassy carbon surface.

Table 7.1. Particle scattering light intensity in 5 repeat experiments on the different substrates.

Sample code	Total intensity	Substrate intensity	NP intensity	Mean±SD and SD/mean ratio
GC1	108	30	78	
GC2	126	33	93	85 ± 15
GC3	104	33	71	(18%)
GC4	138	31	107	
GC5	107	31	76	
Glass1	114	39	75	
Glass2	119	42	77	73 ± 15
Glass3	99	43	56	(21%)
Glass4	135	40	95	
Glass5	102	40	62	
ITO1	67	26	41	
ITO2	72	25	46	37 ± 7.1
ITO3	60	28	32	(19%)
ITO4	57	29	28	
ITO5	64	26	38	
Pt1	66	29	37	
Pt2	63	27	36	35 ± 6.0
Pt3	55	30	25	(17%)
Pt4	65	26	39	
Pt5	67	27	40	

5. Effects of electrode washing by deionised water on the scattering pattern and intensity

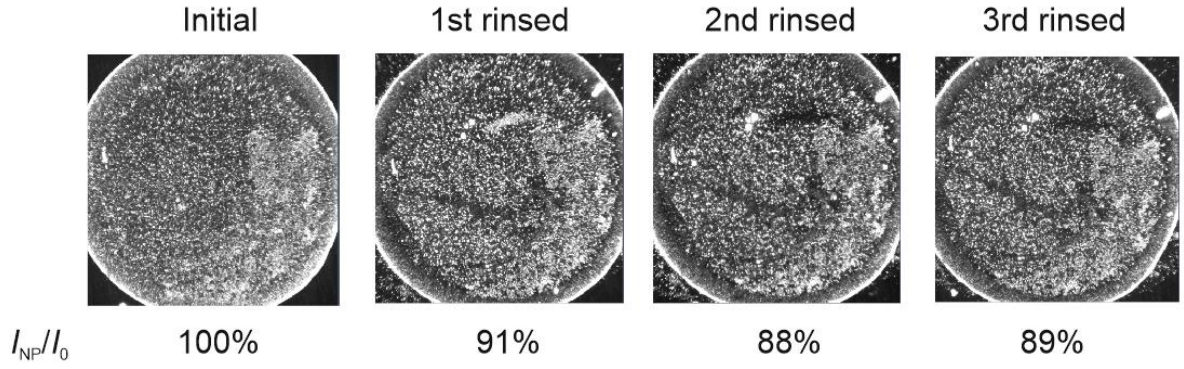

Figure 7.12. Optical image of the dropcast Ag NPs as a function of rinsing times.

6 – SEM imaging of the dropcast silver nanoparticles after immersion in water and in iodide solutions

To examine the fate of the dropcast silver nanoparticles, mainly the presence or absence of solid particles on the NP-modified substrate surfaces, after immersion in iodide solutions, SEM imaging of the silver nanoparticles supported on GC and glass substrates after immersion in water or in the iodide solution was conducted. Specifically, GC and glass substrates were first thoroughly cleaned by immersing in Aqua Regia for 1 hour, and the silver nanoparticles were dropcast onto the two substrates, respectively, with a same surface coverage ($2.4\pm0.3 \times 10^8$ nanoparticles cm^{-2}) as that used in this work and dried. Next, the NP-modified substrate surfaces were immersed in deionised water or a 0.2 M KI solution for 6 minutes. For the latter, the substrate surfaces were subsequently rinsed with deionised water. The modified substrate surfaces were dried under a nitrogen atmosphere overnight. Finally, the particles were located and imaged using SEM (Sigma 300, FEG-SEM, Zeiss) with an accelerating voltage of 2.0 kV at representative sites.

Figure S6 a shows after immersion in water many (herein 86 in total) individual particles with a diameter of mainly 150-200 nm in most imaging regions of the dropcast area. In addition, very close to the edge of the dropcast area (see Figure S6 b) the presence of micron-sized agglomerates was observed and appear to be formed from the 90 nm-diameter nanoparticles. The surface coverage was estimated to be around 2×10^8 nanoparticles cm^{-2}, which is consistent with the dropcast loading of $2.4\pm0.3 \times10^8$ nanoparticles cm^{-2} with a small loss of the particles due to their physical detachment upon immersion. In stark contrast, after immersion in the iodide solution,

as shown in Figure S6 c bare surfaces only are observed! On glass substrates, however, despite the difference in the agglomeration states (single nanoparticles in Figure S6 d and diameter ranges of 100-400 nm in Figure S6 e), no significant difference in the nanoparticle surface coverages is observed between the surfaces after immersion in pure water and 0.2 M KI solutions. Consequently, these observations strongly confirm that the substrate-mediated silver dissolution, rather than the formation of solid AgI particles, is the physical origin of the optical disappearance of the dropcast silver nanoparticles.

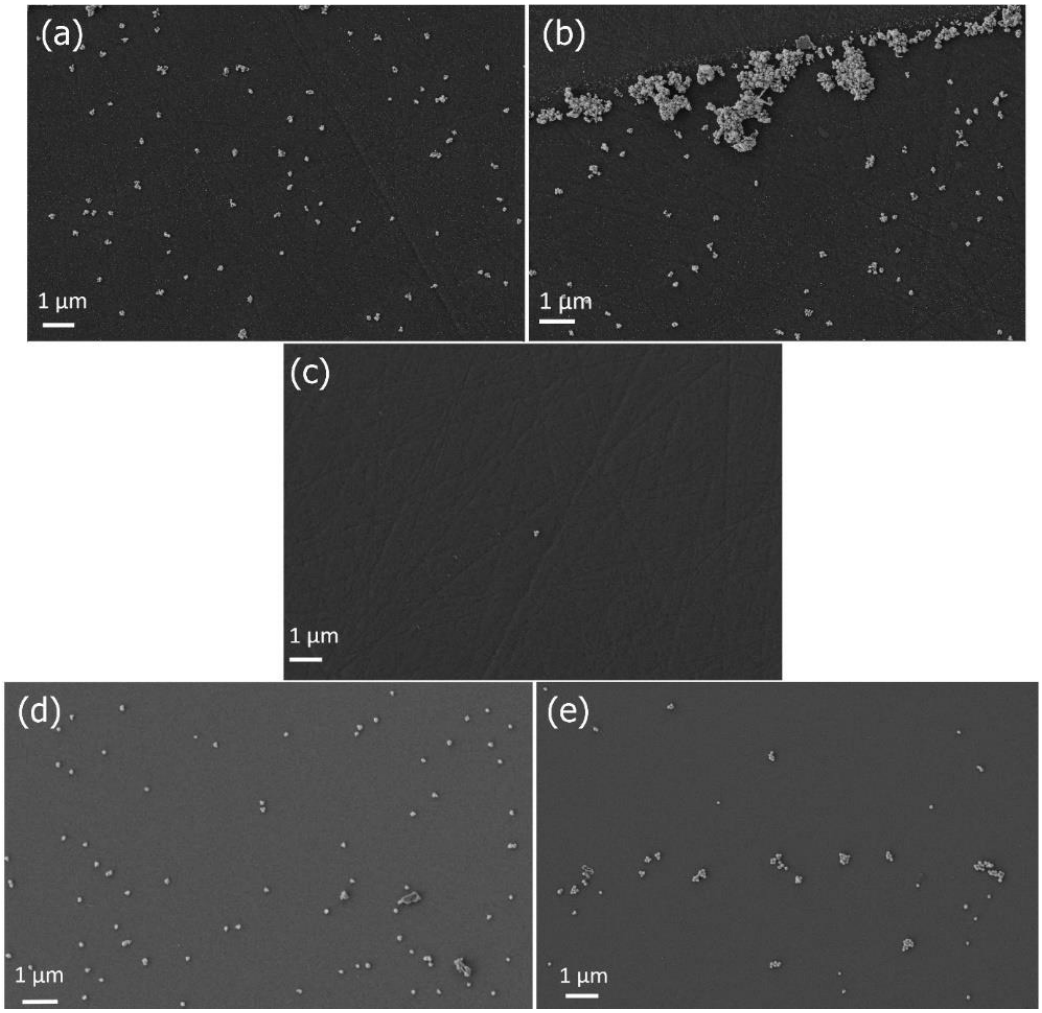

Figure S6. SEM images of silver nanoparticles supported on a glassy carbon surface after immersion in (a) and (b) water or (c) a 0.2 M KI solution for 6 minutes, and those supported on a glass substrate after immersion in (d) water or (e) a 0.2 M KI solution for 6 minutes.

7. Comparison of the substrate potentials for avoiding the nanoparticle dissolution in nitrate solutions with that in iodide solutions

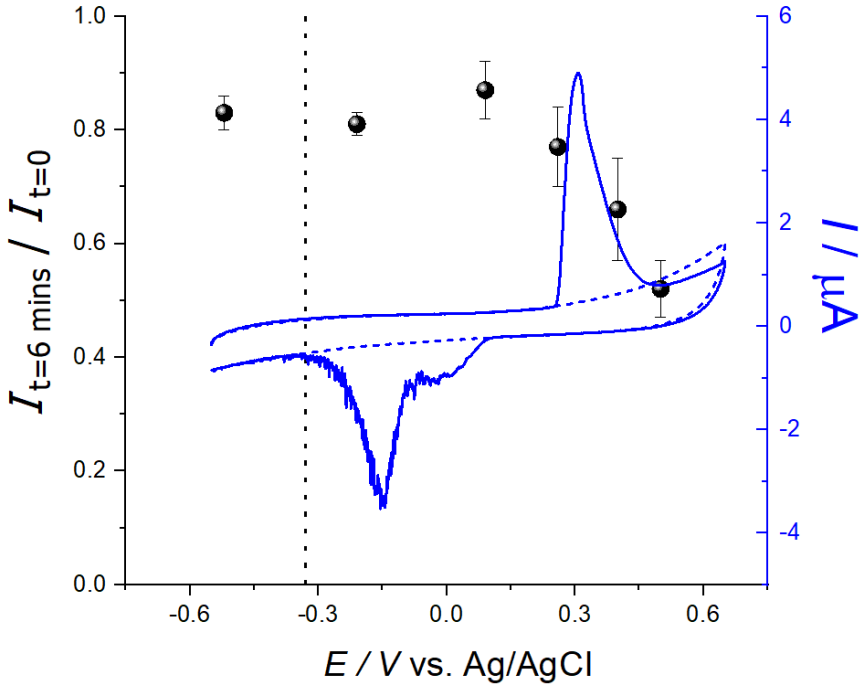

Figure 7.13. Scatter plots of the average remaining fractions of scattering intensity of the immobilised Ag particles on a GC electrode held at each different fixed potentials after 6 minutes' immersion in an air-saturated 0.2 M KNO_3 solution. The overlaid cyclic voltammograms of (solid) a freshly immersed, modified GC electrode and (dashed) a bare GC electrode in an N_2-saturated 0.2 M KNO_3 solution. Scan rate 0.1 V s^{-1}. Note that in order to facilitate the comparison for different electrolyte conditions, the vertical dashed line labels out the expected electrode potential for Ag/AgI (0.2 M KI), which is consistent with the threshold potential for inhibiting the nanoparticle dissolution under the condition (see main text Section 7.3.2).

The remaining fraction of scattering as a function of applied substrate potential was also measured in 0.2 M nitrate solutions. It is evident that in this nitrate solution, holding the electrode potential below *ca.* +0.3 V vs. (Ag/AgCl) can retain over 80% of total scattering whilst the lost 18±4% scattering intensity is very close to that

observed when the nanoparticles are exposed to nitrate solutions (i.e. 14±10%, see Figure 7.5 a). In contrast, when the electrode potential is more positive than +0.3 V, more particles are lost from the interface with increasingly positive potentials. Therefore, this clearly shows a substrate potential more negative than +0.3 V is required in the nitrate solutions to avoid nanoparticle dissolution.

For comparison in Figure 7.13, the overlaid voltammogram of a freshly modified electrode in 0.2 M KNO_3 shows in the forward scan an oxidation peak at +0.31 V, corresponding to silver oxidation to silver ions, whilst in the reverse scan a reduction peak at -0.15 V is seen resulting from the reverse process. The threshold potential above which the oxidation of Ag NPs is observed (+0.25 V) is consistent with that for avoiding the dissolution (<+0.3 V). The latter potential differs significantly from the inhibiting potential in iodide solutions (≤-0.35 marked in the figure below) and the observation of this difference is in excellent agreement with the shift from the threshold potential for the Ag oxidation in 0.2 M KNO_3 (> +0.25 V) to that for the oxidation (>0.33) in 0.2 M KI. Consequently, the experiments in nitrate solution further shows the sensitivity of the substrate potentials required for avoiding nanoparticle dissolution towards the solution ionic composition.

8 – Open circuit potential measurements of the silver nanoparticle-modified glassy carbon electrode during the immersion in iodide solutions

We performed the open circuit potential measurements (OCP) of silver nanoparticle modified electrodes in iodide containing solutions over a period of 6 minutes'

immersion. Measurements were also made at bare GC electrodes for comparison. Figure S8 a shows that in absence of dropcast nanoparticles, the GC electrode has an almost constant OCP at +0.2 V vs. Ag/AgCl throughout the 6 minutes' immersion in a 0.2 KI solution. However, the silver nanoparticle-modified electrode shows an obvious increase of OCP from -0.15 V to about +0.08 V over the first 60 seconds, and maintains a nearly constant OCP afterwards. The timescale of the change is in good agreement with that of the measured scattering light intensity decrease by optical microscopy where nearly 90% decrease occurred in the first minute, as shown in Figure S8 b. This is not inconsistent with the inferred electrochemical dissolution of silver nanoparticles which is expected to significantly vary the electrode potential.

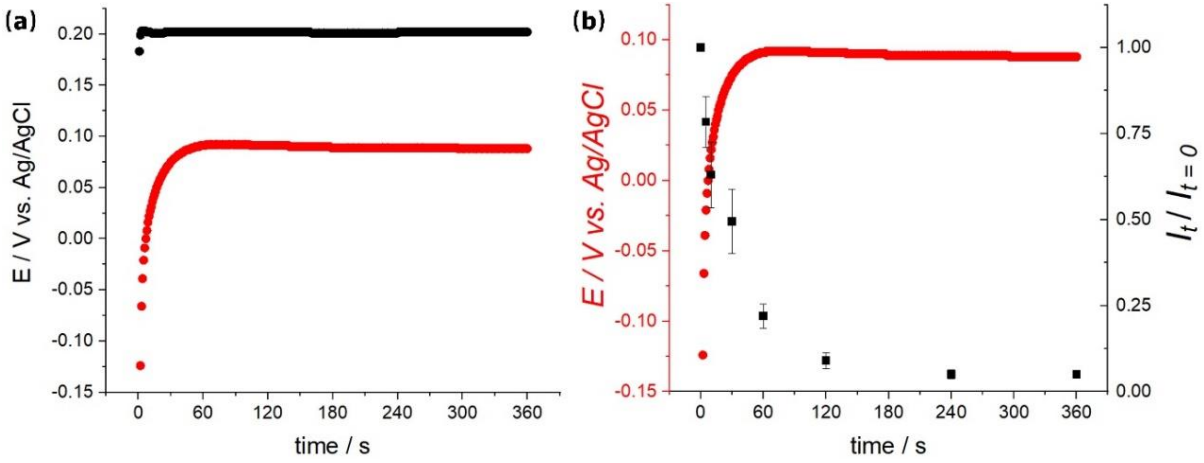

Figure S8. (a) Open circuit potentials of (black) a bare GC electrode and (red) a silver nanoparticle-modified GC electrode as a function of time in 0.2 M KI solutions. (b) Comparison between the changes in the measured OCP and scattering light intensity relative to the initial value over the 6 minutes' immersion in the iodide solution.

9. Calculations of dissolved dioxygen concentration based on the electrochemical sensing

The concentration of dissolved O_2 can be calculated from the voltammetric current of oxygen reduction on a sensing electrode. In O_2 or air saturated solutions, the macroelectrode voltammogram shows irreversible peak currents for oxygen reduction of 30.4±3.4 μA and 8.6±0.7 μA, respectively as described in the main text. The bulk concentrations of dissolved dioxygen in those solutions can therefore be calculated according to Randles-Sevcik equation at 25 °C

$$c^* = \frac{2.99 \times 10^5 \sqrt{n' + \beta_{n'+1}}\, n\, D^{1/2}\, A\, v^{1/2}}{\mathrm{I}_p} \qquad \text{(S2)}$$

where c^* is the bulk concentration of O_2, I_p is the peak current, n' is the number of electrons transferred before the rate determining step (n'=0 in this case), $\beta_{n'+1}$ is the transfer coefficient of the rate determining step (discussed below), n is the total number of electrons transferred (n=2), D is the diffusion coefficient (2.69 ×10^{-9} m^2 s^{-1}) [63] of dissolved O_2, A is the electrode surface area (m^2) and v is the scan rate (0.05

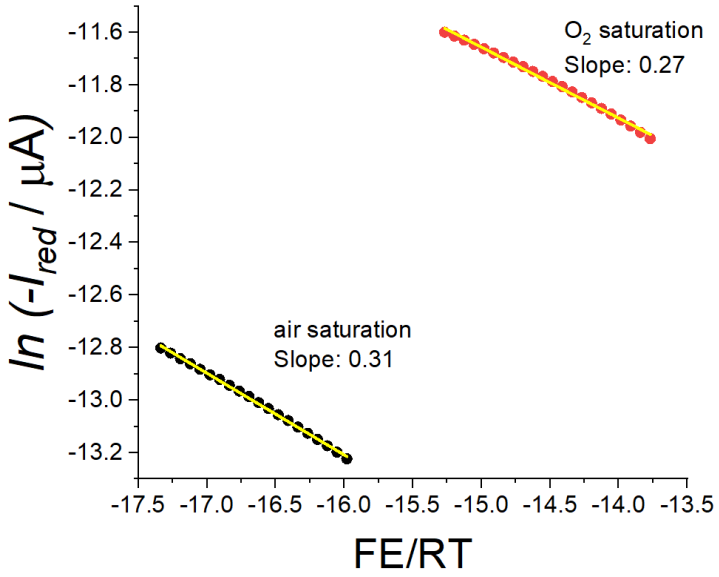

Figure 7.14. Tafel slopes of oxygen reduction current for air and O_2 saturation conditions.

V s^{-1}). The transfer coefficient $\beta_{n'+1}$ was derived to be 0.31 and 0.27 from the Tafel slope in the region of 20%-30% of the peak current [64], as shown in Figure 7.14. Consequently, the O_2 and air saturated solutions are found to contain 1.20±0.10 mM and 0.31±0.02 mM of dissolved dioxygen respectively.

In the argon-saturated solution, the microelectrode voltammogram shows a quasi-steady-state current of 1.2±0.7 nA. The concentration of oxygen in the bulk solution can therefore be calculated based on the following equation for a cylindrical microwire electrode geometry [65]

$$c^* = \frac{I_{qss}}{2\pi nFDl\,(0.446\,p+0.335p^{0.15})}, with\ p = \left(\frac{nFr^2v}{RTD}\right)^{0.5} \quad \text{(S3)}$$

where I_{qss} is the quasi-steady-state current (A), l and r are the length (m) and the diameter (m) of the microwire electrode, F is the Faraday constant (96485 C mol^{-1}), R is the gas constant (8.314 J K^{-1} mol^{-1}), and T is the measurement temperature (K). Consequently, the bulk concentration of O_2 dissolved in the Ar-saturated solution is calculated to be 1.2±0.7 μM. Similarly, the 2.3±0.4 nA of quasi-steady-state current measured after 6 minutes' aging suggests an oxygen level of 2.3±0.4 μM.

10. Discussions on other possible oxidising agents, protons and triiodide ions

In the main text dissolved oxygen is inferred to be the cause of the particle dissolution. Here we consider other possible oxidising agents notably protons and triiodide ions.

For protons, the possibility of the cell reaction is considered in terms of thermodynamics. The half reaction on the anode is $Ag_{(s)} + I^-_{(aq)} = AgI_{(s)} + e^-$ (E^o = -0.152 V vs. SHE); therefore, in 0.2 M KI, the anodic potential for the voltaic cell is -0.111 V. For an oxidation involving one I^- ion per Ag atom, the shift in the oxidation potential is +59 mV per unit of $\log_{10}([I^-])$ according to Nernst equation. Therefore, the potential depends on what complexes form upon the oxidation. Nevertheless, it is clear that the anodic potential for the voltaic cell would be more positive than -0.111 V. The half reaction on the cathode is $H^+_{(aq)} + e^- = ½\ H_{2(g)}$ (E^o = 0.00 V vs. SHE). As pH was measured to be around 7 – in between 6.8 (solutions are air-equilibrated after around 30 s) and 7.9 (initially upon gas bubbling), so the concentration of protons is approximately 10^{-7} M. The partial pressure of gas H_2 in the atmosphere is $P_{H2} = 5.55 \times 10^{-7}$ atm [66]. Using the Nernst equation, the cathodic potential for the voltaic cell is calculated to be -0.229 V vs. SHE. Consequently, due to a negative cell potential the reaction cannot be thermodynamically driven by the H_2/H^+ couple for pH *ca.* 7.

I_3^- is not necessarily present in our experiments using iodide solutions fresh (< 3 days) and stored in dark and 4-6 °C, since its presence only becomes visible, by the advent of a yellow colour, after several days at room temperature for 0.2 M KI, following exposure of iodide solutions to light. Nevertheless, we discuss the possibility of it being the oxidising agent for completeness of argument given that thermodynamically the oxidation of silver by tri-iodide is possible ($E^o_{I3-/I-}$ = 0.54 V > -0.15 V, $E^o_{Ag/AgI}$ vs. SHE[67]). To clarify the non-involvement of iodine or tri-iodine species present by virtue of the aerial oxidation of the aqueous iodide solutions, we compared fresh and aged

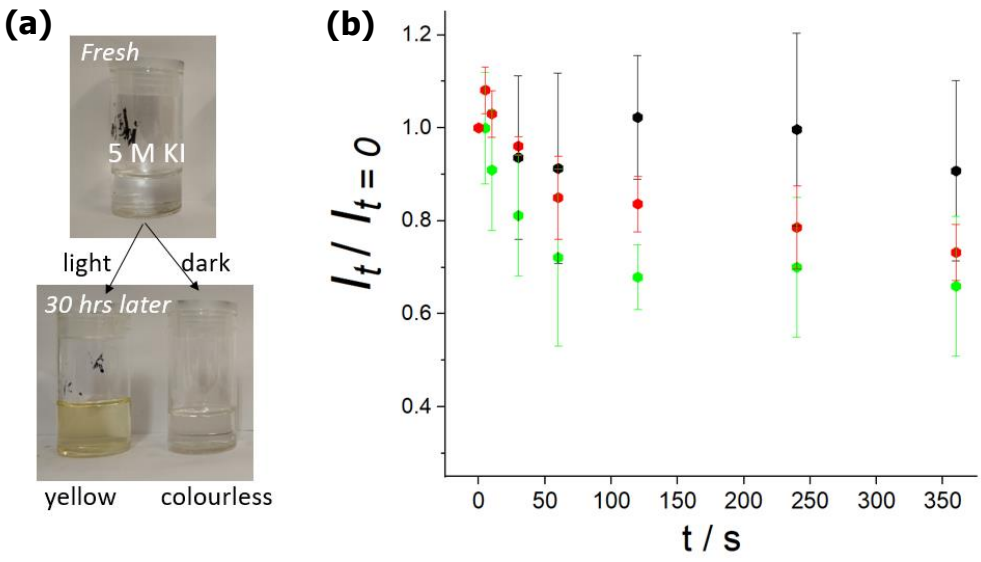

Figure 7.15. (a) Colours of the iodide solutions before and after the 30 hrs' exposure to light at room temperature. **(b)** Scattering intensity normalised to the initial value of the dropcast Ag NPs on GC substrates as a function of time within the 6 minutes in (black) pure water, (green) a fresh and (red) the aged 0.05 M KI solution, respectively.

solutions. 5 M KI solutions were prepared, which were colourless. The solutions was then exposed to light at room temperature for 30 hrs. As a result, the solution became yellow (see Figure 7.15 a); in contrast, the solution stored in dark for 30 hrs did not turn yellow. This indicates the presence of triiodide ions in the aged yellow solution. To next compare the dissolution kinetics of interest, the aged solutions were diluted 100 fold to contain 0.05 M iodide but with trace I_3^-. Dissolution experiments were conducted using a fresh and the aged 0.05 M iodide solutions, respectively. Optical intensity of the dropcast Ag NPs was monitored within 6 minutes. As seen from Figure 7.15 b, no major differences in the dissolution kinetics were observed between the triiodide containing and non-triiodide containing KI solutions. This suggests that in addition to the unlikely presence of I_3^- in our studied solution, the triiodide ions are not considered to be the oxidising agent for our dissolution experiments.

11. Voltammetry of NP-modified electrodes after immersion in the iodide

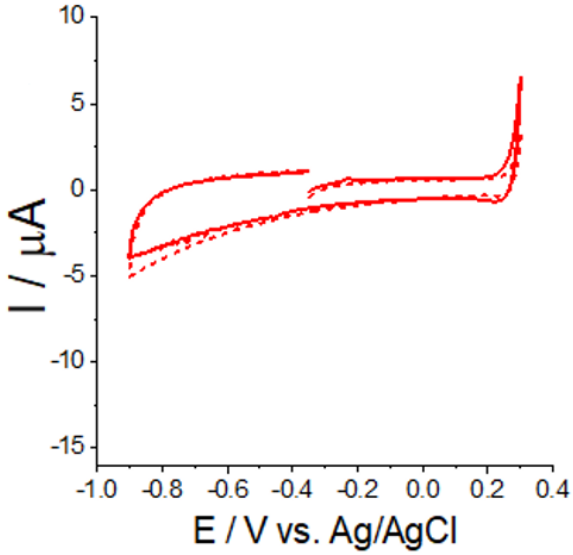

Figure 7.16. Cyclic voltammograms of (dashed) a bare GC electrode and (solid) an Ag NP-modified GC electrode after the 6 minutes' immersion in a 0.2 M KI solutions. Scan rate 0.1 V s^{-1}.

12. Full-time optical measurements of the dissolution on glass substrates

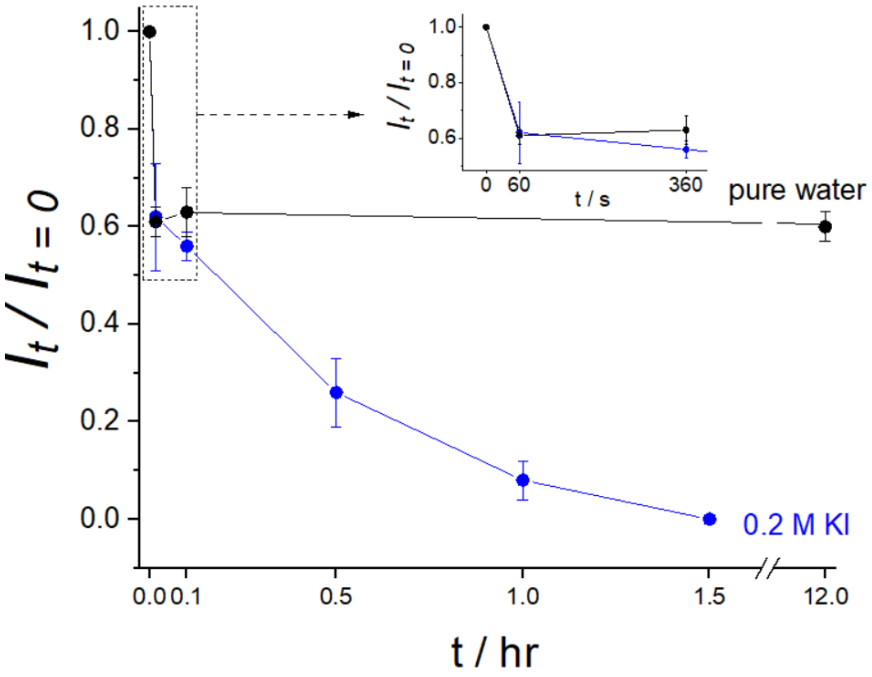

Figure 7.17. Scattering intensity, of the dropcast Ag NPs on a glass substrate relative to the initial value, as a function of time within the 12 hrs in (black) pure water and (blue) 0.2 M KI solutions, respectively.

13. Calculations for surface area comparison between nanoparticle ensembles and the substrate

The surface areas between the ensembles of the dropcast silver nanoparticles and the substrate are compared based on the following estimation. For a single silver nanoparticle with an average diameter of 90 nm (see Appendix section 1), the surface area is 2.5×10^{-14} m^2. The amount of dropcast silver nanoparticles is 10 ng, so the number of nanoparticles across the whole dropcast area is calculated to be 2.5×10^6. Therefore, the total surface area of the silver nanoparticle ensemble is 6.4×10^{-8} m^2. For the GC electrode with a disc diameter of 3.00 mm, the geometric area is 7.1×10^{-6} m^2. The substrate surface used in this work is polished to be very smooth for the reflective dark field illumination, so the roughness factor (i.e. ratio of the microscopic area to geometric area) is considered to be below 2 [68]. Even so, it is evident that despite the large surface-to-volume ratio of nanoparticles, due to the tiny amount of silver to be oxidised, the surface area of GC electrode is substantially larger (2-3 higher orders of magnitude) than the total surface area of all the silver nanoparticles across the dropcast area.

References

[1] K. Ngamchuea, C. Batchelor-McAuley, R. G. Compton, *Nanotoxicology* **2018**, *12*, 305-311.

[2] C. Batchelor-McAuley, K. Tschulik, C. C. Neumann, E. Laborda, R. G. Compton, *Int. J. Electrochem. Sci.* **2014**, *9*.

[3] C. Batchelor-McAuley, K. Tschulik, R. G. Compton, *Port. Electrochim. Acta* **2013**, *31*, 249-256.

[4] H. Kang, Y. Kim, S. Cheon, G.-R. Yi, J. H. Cho, *ACS Appl. Mater. Interfaces* **2017**, *9*, 30779-30785.

[5] D.-Y. Shin, G.-R. Yi, D. Lee, J. Park, Y.-B. Lee, I. Hwang, S. Chun, *Nanoscale* **2013**, *5*, 5043-5052.

[6] G. Liang, F. Mo, D. Wang, X. Li, Z. Huang, H. Li, C. Zhi, *Energy Stor. Mater.* **2020**, *25*, 86-92.

[7] B. Vanrenterghem, P. Jovanovič, M. Šala, M. Bele, V. S. Šelih, N. Hodnik, T. Breugelmans, *Electrochim. Acta* **2018**, *286*, 123-130.

[8] Y. Shao, J. P. Dodelet, G. Wu, P. Zelenay, *Adv. Mater.* **2019**, *31*, 1807615.

[9] C. Levard, E. M. Hotze, G. V. Lowry, G. E. Brown Jr, *Environ. Sci. Technol.* **2012**, *46*, 6900-6914.

[10] T. S. Peretyazhko, Q. Zhang, V. L. Colvin, *Environ. Sci. Technol.* **2014**, *48*, 11954-11961.

[11] M. N. Martin, A. J. Allen, R. I. MacCuspie, V. A. Hackley, *Langmuir* **2014**, *30*, 11442-11452.

[12] W. Zhang, Y. Yao, N. Sullivan, Y. Chen, *Environ. Sci. Technol.* **2011**, *45*, 4422-4428.

[13] X. Li, J. J. Lenhart, H. W. Walker, *Langmuir* **2010**, *26*, 16690-16698.

[14] K. Ngamchuea, C. Batchelor-McAuley, S. V. Sokolov, R. G. Compton, *Anal. Chem.* **2017**, *89*, 10208-10215.

[15] O. S. Ivanova, F. P. Zamborini, *J. Am. Chem. Soc.* **2010**, *132*, 70-72.

[16] H. S. Toh, C. Batchelor-McAuley, K. Tschulik, M. Uhlemann, A. Crossley, R. G. Compton, *Nanoscale* **2013**, *5*, 4884-4893.

[17] S. E. Ward Jones, F. W. Campbell, R. Baron, L. Xiao, R. G. Compton, *J. Phys. Chem. C* **2008**, *112*, 17820-17827.

[18] D. K. Pattadar, J. N. Sharma, B. P. Mainali, F. P. Zamborini, *J. Phys. Chem. C* **2019**, *123*, 24304-24312.

[19] K. Ngamchuea, R. O. Clark, S. V. Sokolov, N. P. Young, C. Batchelor - McAuley, R. G. Compton, *Chem. Eur. J.* **2017**, *23*, 16085-16096.

[20] X. Li, C. Batchelor - McAuley, S. A. Whitby, K. Tschulik, L. Shao, R. G. Compton, *Angew. Chem. Int. Ed.* **2016**, *55*, 4296-4299.

[21] R. A. Masitas, I. V. Khachian, B. L. Bill, F. P. Zamborini, *Langmuir* **2014**, *30*, 13075-13084.

[22] K. Wonner, C. Rurainsky, K. Tschulik, *Front. Chem.* **2019**, *7*.

[23] J. F. Lemineur, J. M. Noël, D. Ausserré, C. Combellas, F. Kanoufi, *Angew. Chem.* **2018**, *130*, 12174-12178.

[24] W. Wang, *Chem. Soc. Rev.* **2018**, *47*, 2485-2508.

[25] J.-F. Lemineur, T. J. Stockmann, J. Médard, C. Smadja, C. Combellas, F. Kanoufi, *J. Anal. Test.* **2019**, *3*, 175-188.

[26] S. Nizamov, V. M. Mirsky, in *In-situ Characterization Techniques for Nanomaterials*, Springer, Berlin, **2018**, pp. 61-105.

[27] S. Nizamov, V. Scherbahn, V. M. Mirsky, in *Optical Sensors 2017, Vol. 10231*, International Society for Optics and Photonics, **2017**, p. 102312F.

[28] I. Sidorenko, S. Nizamov, R. Hergenröder, A. Zybin, A. Kuzmichev, B. Kiwull, R. Niessner, V. M. Mirsky, *Microchim. Acta* **2016**, *183*, 101-109.

[29] S. Nizamov, O. Kasian, V. M. Mirsky, *Angew. Chem. Int. Ed.* **2016**, *55*, 7247-7251.

[30] L. Sun, Y. Fang, Z. Li, W. Wang, H. Chen, *Nano Res.* **2017**, *10*, 1740-1748.

[31] J.-G. Wang, J. S. Fossey, M. Li, T. Xie, Y.-T. Long, *ACS Appl. Mater. Interfaces* **2016**, *8*, 8305-8314.

[32] S. Munteanu, N. Garraud, J. P. Roger, F. Amiot, J. Shi, Y. Chen, C. Combellas, F. Kanoufi, *Anal. Chem.* **2013**, *85*, 1965-1971.

[33] J.-F. Lemineur, J.-M. Noël, A. Courty, D. Ausserré, C. Combellas, F. Kanoufi, *J. Am. Chem. Soc.* **2020**, *142*, 7937-7946.

[34] J.-M. Noël, M. M. Vieira, V. Brasiliense, J.-F. Lemineur, C. Combellas, F. Kanoufi, *Nanoscale* **2020**, *12*, 3227-3235.

[35] V. Sundaresan, J. W. Monaghan, K. A. Willets, *J. Phys. Chem. C* **2018**, *122*, 3138-3145.

[36] J.-F. Lemineur, J.-M. Noël, C. Combellas, F. Kanoufi, *J. Electroanal. Chem.* **2020**, 114043.

[37] L. Sun, D. Jiang, M. Li, T. Liu, L. Yuan, W. Wang, H.-Y. Chen, *Anal. Chem.* **2017**, *89*, 6050-6055.

[38] C. Batchelor-McAuley, A. Martinez-Marrades, K. Tschulik, A. N. Patel, C. Combellas, F. Kanoufi, G. Tessier, R. G. Compton, *Chem. Phys. Lett.* **2014**, *597*, 20-25.

[39] K. Wonner, M. V. Evers, K. Tschulik, *Electrochim. Acta* **2019**, *301*, 458-464.

[40] V. Brasiliense, A. N. Patel, A. Martinez-Marrades, J. Shi, Y. Chen, C. Combellas, G. Tessier, F. Kanoufi, *J. Am. Chem. Soc.* **2016**, *138*, 3478-3483.

[41] C. A. Little, C. Batchelor - McAuley, K. Ngamchuea, C. Lin, N. P. Young, R. G. Compton, *ChemistryOpen* **2018**, *7*, 370-380.

[42] S. Munteanu, J. P. Roger, Y. Fedala, F. Amiot, C. Combellas, G. Tessier, F. Kanoufi, *Faraday Discuss.* **2013**, *164*, 241-258.

[43] A. N. Patel, A. Martinez-Marrades, V. Brasiliense, D. Koshelev, M. Besbes, R. Kuszelewicz, C. Combellas, G. Tessier, F. Kanoufi, *Nano Lett.* **2015**, *15*, 6454-6463.

[44] V. Brasiliense, J. Clausmeyer, A. L. Dauphin, J. M. Noël, P. Berto, G. Tessier, W. Schuhmann, F. Kanoufi, *Angew. Chem. Int. Ed.* **2017**, *56*, 10598-10601.

[45] J.-F. Lemineur, J.-M. Noël, C. Combellas, F. Kanoufi, *Nanoscale* **2020**, *12*, 15128-15136.

[46] W. Plieth, *J. Phys. Chem.* **1982**, *86*, 3166-3170.

[47] P. L. Redmond, A. J. Hallock, L. E. Brus, *Nano Lett.* **2005**, *5*, 131-135.

[48] J. A. Scholl, A. L. Koh, J. A. Dionne, *Nature* **2012**, *483*, 421-427.

[49] Y. Zhang, A. K. Selva Kumar, D. Li, M. Yang, R. G. Compton, *ChemElectroChem* **2020**, *7*, 4614-4624.

[50] A. K. S. Kumar, Y. Zhang, D. Li, R. G. Compton, *Electrochem. Commun.* **2020**, 106867.

[51] K. Cinková, M. Clark, S. V. Sokolov, C. Batchelor - McAuley, Ľ. Švorc, R. G. Compton, *Electroanalysis* **2017**, *29*, 1006-1013.

[52] H. Zhang, C. Lin, L. Sepunaru, C. Batchelor-McAuley, R. G. Compton, *J. Electroanal. Chem.* **2017**, *799*, 53-60.

[53] H. Matsuda, Y. Ayabe, *Zeitschrift für Elektrochemie, Berichte der Bunsengesellschaft für physikalische Chemie* **1955**, *59*, 494-503.

[54] M. A. A. S. a. D. T. R. Ian B. Bulter, *Talanta* **1994**, *41*, 211-215.

[55] C. H. Gammons, Y. Yu, *Chem. Geol.* **1997**, *137*, 155-173.

[56] S. Joo, D. F. Baldwin, *Nanotechnology* **2009**, *21*, 055204.

[57] W. Wei, T. Yuan, W. Jiang, J. Gao, H.-Y. Chen, W. Wang, *J. Am. Chem. Soc.* **2020**.

[58] S. J. Cloake, H. S. Toh, P. T. Lee, C. Salter, C. Johnston, R. G. Compton, *ChemistryOpen* **2015**, *4*, 22-26.

[59] M. W. Glasscott, A. D. Pendergast, M. H. Choudhury, J. E. Dick, *ACS Appl. Nano Mater.* **2018**, *2*, 819-830.

[60] M. E. Hyde, C. E. Banks, R. G. Compton, *Electroanalysis* **2004**, *16*, 345-354.

[61] E. Kätelhön, R. G. Compton, *ChemElectroChem* **2015**, *2*, 64-67.

[62] C. Batchelor-McAuley, C. A. Little, S. V. Sokolov, E. Kätelhön, G. Zampardi, R. G. Compton, *Anal. Chem.* **2016**, *88*, 11213-11221.

[63] Y. Guo, M. Yang, R.-C. Xie, R. G. Compton, *Chem. Sci.* **2020**.

[64] D. Li, C. Lin, C. Batchelor-McAuley, L. Chen, R. G. Compton, *J. Electroanal. Chem.* **2018**, *826*, 117-124.

[65] K. Aoki, K. Honda, K. Tokuda, H. Matsuda, *J. Electroanal. Chem. Interfacial Electrochem.* **1985**, *182*, 267-279.

[66] D. R. Bates, M. Nicolet, *Publ. Astron. Soc. Pac.* **1950**, *62*, 106-110.

[67] P. Vanysek, in *CRC Handbook of Chemistry and Physics, Vol. 8*, 93rd ed., CRC Press, **2000**.

[68] A. J. Bard & L. R. Faulkner, Electrochemical Methods: Fundamentals and Applications, 2nd ed., Wiley New York, 2001.

Conclusions and future work

Current electrochemical techniques enable a *careful* examination of nanomaterials not only in a tiny volume of particle ensembles but also at the single nanoparticle level. The latter has been well exemplified with the sizing of individual 40 nm-diameter silver nanoparticles in Chapter 3. Therein, a quantitative methodology of the emerging technique nano-impact is importantly established for *in situ* sizing nanoparticles, highlighting the use of low filtering frequency (e.g. 100 Hz) for conserving the total charge of the impact events for each nanoparticle, and the weighing of nanoparticle diffusion coefficients to obtain an *accurate* size distribution of the nanoparticle sample. As such, in Chapter 4, we concluded that even compared to the existing well-established methods based on light scattering, the 'nano-impacts' show an advantage in accurately sizing small (≤30 nm-diameter) and polydisperse nanoparticles.

Detailed characterisation on the physical and chemical states of the shell of a core-shell nanoparticle can also be done using mainly comparative electrochemistry, despite the very limited knowledge of the structures of the particles and the electrode-solution interface. The work of Chapter 5 infers the chemical composition and its integrity of the thin cell of $Co@Co(OH)_2$ NPs and Chapter 6 the broken shell of $Co_3O_4@SiO_2$ NPs by comparing the voltammetric features of relevant cobalt materials at both the particle ensemble and single entity level. Also importantly, in Chapter 6, the reaction mechanism of hydroxide ion oxidation mediated by Co_3O_4 is discovered by comparing the derived kinetic rate constants to undergo a mixed electrochemical/chemical pathway, rather than a direct four electron transfer pathway, for producing dioxygen, which is yet likely to be a minor product. The conclusion contradictory to most literature originates from a careful

revisit to the voltammetric studies of the electrode reaction and therefore highlights the necessary *caution* for elucidating reaction mechanisms *via* voltammetry.

Most interestingly, combined methodology of optical microscopy and electrochemistry allows a synergistic study that extracts *both* spatial and chemical information at the electrochemical interface, to work out a new and important nano-corrosion mechanism at an open circuit condition, where the substrate electrode can even catalyse the electro-dissolution of redox active nanomaterials.

From the above microscopic research on the nanomaterial or related phenomena at the electrified solid-solution interface, an accurate depiction of the focused aspect is shown to be possible (as for the sizing of silver nanoparticles). However, when it comes to more complicated electrode processes of cobalt materials, the study necessarily requires many assumptions of other aspects for investigating at the highly complex chemical environment of the interface, and may thus limit the reliability of the conclusions and sometimes even show contradictory results among literature. Nevertheless, it should not be doubted that the interfacial phenomena are extremely interesting due to its controllable activity and great potential insights into understanding the physical world and fundamental biological processes. Whilst measurements of electrochemical interfacial phenomena are challenging, last chapter in particular supports that a combined strategy of complementary and synergistic techniques may be required to probe overall electrode processes for its increased capacity and desirable reliability. As a note from the third chapter again, the comparison between different techniques needs to be carefully done. As such, combining various analytical methods such as optical microscopy and spectroscopy with electrochemistry for better measuring the complex phenomena at an electrode-solution interface in a microscopic level shall be a nice direction to pursue next.